RADIOFLUORINATED AMINO ACIDS FOR ONCOLOGICAL POSITRON EMISSION TOMOGRAPHY IMAGING

by

Milena Čolović

B.Sc., Simon Fraser University, 2015

A THESIS SUBMITTED IN PARTIAL FULFILLMENT OF

THE REQUIREMENTS FOR THE DEGREE OF

DOCTOR OF PHILOSOPHY

in

THE FACULTY OF GRADUATE AND POSTDOCTORAL STUDIES

(Interdisciplinary Oncology)

THE UNIVERSITY OF BRITISH COLUMBIA

(Vancouver)

December 2019

© Milena Čolović, 2019

The following individuals certify that they have read, and recommend to the Faculty of Graduate and Postdoctoral Studies for acceptance, the dissertation entitled:

Radiofluorinated Amino Acids for Oncological Positron Emission Tomography Imaging

submitted by Milena Čolović in partial fulfillment of the requirements for

the degree of Doctor of Philosophy

in Interdisciplinary Oncology

Examining Committee:

Dr. François Bénard
Co-supervisor

Dr. Paul Schaffer
Co-supervisor

Dr. Mads Daugaard
Supervisory Committee Member

Dr. Urs Häfeli
Supervisory Committee Member

Dr. Michel Roberge
University Examiner

Dr. Marcel Bally
University Examiner

Abstract

Cancer progression and metastasis are driven by certain molecular features that are either non-existent or abnormally active in normal cells. These features are often exploited by medical scientists for the development of targeted therapies and/or imaging probes to better diagnose and stratify patients. In this thesis, we report the investigation of novel radiotracers designed to measure oxidative stress and the use of amino acids as alternative sources of energy, both associated with malignant transformation and resulting in upregulation of different amino acid transporters (AATs).

Oxidative stress has been implicated as a feature of aggressive cancer types, particularly those with poor prognosis. System x_C^- is an antiporter of cystine and glutamate, which is upregulated under oxidative stress and overexpressed in many cancers including triple-negative breast cancer and glioblastoma. System x_C^- provides cells with a substrate for antioxidant synthesis. This transporter can be studied by positron emission tomography (PET) using ^{18}F-fluoroaminosuberic acid ([^{18}F]FASu). [^{18}F]FASu is hypothesized to be a specific substrate for system x_C^- activity. The work herein explores the relationship between [^{18}F]FASu uptake and system x_C^- transporter activity, and whether this can be used for cancer diagnosis and treatment response monitoring. We studied system x_C^- activity and overexpression *in vitro* and used [^{18}F]FASu *in vivo* to monitor intratumoural changes following radiotherapy. We evaluated a novel [^{18}F]FASu analogue, [^{18}F]ASu-BF_3, synthesized *via* an alternative radiolabelling method. Additionally, we compared [^{18}F]FASu to two other PET radiopharmaceuticals *in vivo*, one of which also targets system x_C^-.

Finally, this thesis also explores a novel radiolabelling methodology and biological characterisation of a number of radiofluorinated leucine derivatives, substrates for another AAT, LAT1. LAT1 is highly upregulated in several cancers and at metastatic sites. LAT1 is a poor prognostic biomarker in cancer patients. It is associated with mTOR pathway activation, through which amino acids are being imported and used as substrates for protein biosynthesis. This research presents effective methodology for producing LAT1 substrates for the purposes of cancer imaging with PET. Collectively, this research provides a non-invasive platform for the characterization of two AAT proteins, both of which play a role in cancer development and progression.

Lay Summary

In this thesis, radioactive amino acids are used to study how cancers use nutrients other than glucose. The main theme of my thesis is a compound called [^{18}F]FASu, which is a modified amino acid, determined to be specific for an amino acid transporter protein system x_C^-, which is very active in many cancers. We sought to understand the properties and purpose of this activation of system x_C^-, by using [^{18}F]FASu as a probe. We also modified the structure of [^{18}F]FASu to make a new probe, [^{18}F]ASu-BF_3, but this approach did not result in improved imaging properties. Additionally, [^{18}F]FASu was compared with [^{18}F]FDG, the radioactive glucose molecule, and another labelled amino acid specific for system x_C^-, [^{18}F]FSPG, in a series of studies. Finally, in the last part of this project, a large number of labelled amino acids are tested as novel imaging probes for their ability to target cancer cells.

Preface

A version of Chapter 2 has been published in *Molecular Imaging and Biology* [**M Čolović**, H Yang, H Merkens, N Colpo, F Bénard, P Schaffer. Non-invasive Use of Positron Emission Tomography to Monitor Chemo- and Radiation- Induced Changes in System x_C^- Expression in Breast Cancer]. I was the lead investigator, responsible for all major areas of concept formation, data collection and analysis, as well as the manuscript composition. H Yang was responsible for tracer radiosynthesis and was involved in concept formation and manuscript composition. H Merkens was responsible for Western blot and siRNA knockdown experimentation. N Colpo performed PET/CT image acquisition. F Bénard and P Schaffer were the supervisory authors and were involved throughout the project in concept formation and manuscript composition.

A version of Chapter 3 has been published in *Bioorganic & Medicinal Chemistry Letters* [**M Čolović**, É Rousseau, Z Zhang, J Lau, CC Zhang, HT Kuo, H Yang, P Schaffer, F Bénard and KS Lin. Synthesis and Evaluation of an ^{18}F-labeled boramino acid analog of aminosuberic acid for PET imaging of the antiporter system x_C^-]. Myself and É Rousseau were the lead investigators on this project, responsible for all major areas of concept formation and manuscript composition. I was responsible for all *in vitro* uptake studies, biodistribution and imaging studies of tumour-bearing mice, and data analysis. É Rousseau and J Lau performed imaging and biodistribution studies with and without probenecid treatment, with the help of HT Kuo. CC Zhang performed mass analysis of the compounds. H Yang, together with the supervisory authors: P Schaffer, F Bénard and KS Lin, was involved throughout the project in concept formation. All authors participated in the manuscript composition.

A version of Chapter 4 has been published in *Molecular Imaging and Biology* [**M Čolović**, H Yang, H Merkens, N Colpo, F Bénard, P Schaffer. The Effect of Chirality on the Application of [^{18}F]5-Fluoroaminosuberic Acid ([^{18}F]FASu) for oxidative stress imaging]. H Yang and I were the lead investigators on this project. I was responsible for all *in vivo* and *in vitro* data collection, analysis and manuscript composition. H Yang was involved in concept formation and responsible for radiotracer synthesis. H Merkens helped with biodistribution data collection. N Colpo performed PET/CT imaging. F Bénard and P Schaffer were the supervisory authors involved throughout the project in concept formation.

The work presented in Chapter 5 is currently in preparation for submission. I was the lead investigator on this project, responsible for all major areas of concept formation. H Yang was responsible for radiotracer synthesis. I was responsible for all other experimentation, data collection and analysis. H Merkens and N Colpo were involved in biodistribution studies and image acquisition. F Bénard and P Schaffer were the supervisory authors on this project and were both involved in experimental design.

A version of Chapter 6 has been published [M Nodwell, H Yang, **M Čolović**, Z Yuan, H Merkens, RE Martin, F Bénard, P Schaffer and R Britton. ^{18}F-Fluorination of Unactivated C-H Bonds in Branched Aliphatic Amino Acids: Direct Synthesis of Oncological Positron Emission Tomography Imaging Agents] and [M Nodwell, H Yang, H Merkens, N Malik, **M Čolović**, B Wagner, RE Martin, F Bénard, P Schaffer and R Britton. ^{18}F-Branched-Chain Amino Acids: Structure-Activity Relationship and PET Imaging Potential]. Part of the publications presented herein is the product of my efforts, including all cell uptake and animal experiments, and relevant manuscript input. Figures 6.1 and 6.2 and Table 6.1 were designed by M Nodwell and H Yang and used herein with permission. All other data presented herein I am responsible for. H Merkens assisted with biodistribution data collection. N Colpo and N Hundal-Jabal performed PET/CT image acquisition. The studies were designed by the lead investigators, M Nodwell and H Yang, with critical input from the supervisory authors F Bénard, P Schaffer and R Britton, who were involved in manuscript composition.

Experimental work in this thesis was performed at British Columbia Cancer (BC Cancer) and TRIUMF in collaboration with Simon Fraser University, Vancouver Canada. All the animal studies performed in this thesis were under animal protocols A16-0236, “Amino Acid Radiotracers for Oncology Imaging”, A17-0112, “Tumour Radiation Treatment Monitoring with PET (SARRP-PET)” and A16-0128, “Preclinical Evaluation of Radiotracers for Cancer Imaging” that were approved by the Institutional Animal Care Committee of the University of British Columbia and was performed in compliance with the Canadian Council on Animal Care Guidelines.

Table of Contents

Abstract ..... **iii**

Lay Summary ..... **iv**

Preface ..... **v**

Table of Contents ..... **vii**

List of Tables ..... **xiv**

List of Figures ..... **xvi**

List of Symbols and Abbreviations ..... **xxi**

Acknowledgements ..... **xxviii**

Dedication ..... **xxx**

Chapter 1: Introduction **1**

1.1 Molecular imaging in nuclear medicine 1

1.1.1 Positron emission tomography 2

1.1.1.1 [^{18}F]FDG oncological imaging 4

1.1.1.2 Impact of [^{18}F]FDG PET on cancer patient care 5

1.1.1.3 Role of molecular imaging in personalised treatment 5

1.2 Cancer and tumour microenvironment 7

1.2.1 The hallmarks of cancer 7

1.2.2 The role of tumour microenvironment in cancer progression 8

1.3 Reactive oxygen species 8

1.3.1 Sources and scavengers of reactive oxygen species 8

1.3.2 Function of reactive oxygen species in normal and cancer cells 11

1.3.2.1 ROS-response mechanisms in cancer 12

1.3.3 Detection of intracellular ROS 14
1.4 Physiological function of system x_C^- in cancer 17
1.4.1 System x_C^- as a marker of oxidative stress 17
1.4.2 Biochemical structure of system x_C^- 19
1.4.2.1 Maintenance of cystine/cysteine redox cycle 20
1.4.2.2 Regulation of ferroptosis 20
1.4.3 Regulation of system x_C^- activity and abundance 22
1.4.4 Distribution of system x_C^- in normal tissues and malignancies 22
1.4.5 Functional interactions of xCT 23
1.4.6 System x_C^- nuclear imaging agents 24
1.4.6.1 4-[^{18}F]fluoroglutamate 25
1.4.6.2 (*4S*)-4-(3-[^{18}F]fluoropropyl)-*L*-glutamate 25
1.4.6.3 [^{18}F]5-Fluoroaminosuberic acid 27
1.4.6.4 [^{18}F]-hGTS13 27
1.5 Breast cancer 28
1.5.1 Triple-negative breast cancer 29
1.5.1.1 PET imaging of TNBC 30
1.5.2 System x_C^- in breast cancer 31
1.6 Amino acid transporters as targets for molecular imaging of cancer 32
1.6.1 Amino acid radiopharmaceuticals 32
1.6.1.1 Amino acid radiopharmaceuticals for cancer imaging 33
1.6.2 Amino acid radiolabelling 33
1.6.2.1 Radiofluorination (^{18}F) 34
1.7 System L targeting in oncological PET imaging 36
1.7.1 LAT1 as a cancer biomarker 37
1.8 Thesis theme and rationale 39

1.8.1 Hypotheses 39

Chapter 2: ^{18}F-labelled cystine analog, [^{18}F]5-fluoroaminosuberic acid ([^{18}F]FASu), for oxidative stress imaging with positron emission tomography 40

2.1 Introduction 40

2.2 Materials & methods 41

2.2.1 General 41

2.2.2 Radiosynthesis of [^{18}F]-fluoroaminosuberic acid ([^{18}F]FASu) 41

2.2.3 Cell culture and *in vitro* [^{18}F]FASu uptake experiments 42

2.2.3.1 siRNA knockdown experiments 43

2.2.3.2 qPCR 43

2.2.4 Western blotting 44

2.2.5 Glutatione level measurements 44

2.2.6 ROS detection 45

2.2.7 Animal studies 45

2.2.7.1 *Ex vivo* biodistribution of [^{18}F]FASu 45

2.2.7.2 Small animal PET/CT imaging and radiation therapy 46

2.2.8 Statistical analysis 46

2.3 Results 47

2.3.1 [^{18}F]FASu uptake, *SLC7A11* and xCT expression vary in response to prolonged DEM treatment 47

2.3.2 System x_C^- activity changes with DEM incubation in a time-dependent manner 48

2.3.3 System x_C^- response to short (1 h) *vs.* long (overnight) DEM treatment in MDA-MB-231 cells 49

2.3.4 Determination of GSH content and [^{18}F]FASu uptake in additional, ER+/PR+, breast cancer cell lines after 1 h and overnight treatment with DEM 50

2.3.5 *Ex vivo* qPCR and Western blot experiments 51

2.3.6 *In vivo* radiotherapy and [^{18}F]FASu-PET/CT imaging 52

2.3.7 [^{18}F]FASu as a gauge for oxidative stress level monitoring in TNBC 57
2.3.8 *In vivo* radiotherapy and [^{18}F]FASu-PET/CT imaging – Part 2 58
2.4 Discussion 59
2.5 Conclusion 62
Chapter 3: Synthesis and evaluation of an ^{18}F-labelled boramino acid analogue of aminosuberic acid for PET imaging of the antiporter system x_C^- 63
3.1 Introduction 63
3.2 Materials & methods 65
3.2.1 Chemicals and instrumentation 65
3.2.2 Chemical syntheses 66
3.2.2.1 Synthesis of methyl 7-[(*R*)-2-methyl-propane-2-sulfinylimino]heptanoate (2) 66
3.2.2.2 Synthesis of methyl (*S*)-[7-(4,4,5,5-tetramethyl-1,3,2-dioxaborolan-2-yl)-7-((*R*)-2-methyl-propane-2-sulfinylamino)]heptanoate 66
3.2.2.3 Synthesis of (*S*)-(7-trifluoroboryl-7-ammonio)heptanoic acid (ASu-BF_3)..... 67
3.2.3 Radiosynthesis of [^{18}F]ASu-BF_3 67
3.2.4 *In vivo* stability in mouse plasma 67
3.2.5 Cell uptake assays 68
3.2.6 Biodistribution and PET/CT imaging studies in PC-3 tumour-bearing mice 68
3.2.7 Biodistribution studies of [^{18}F]ASu-BF_3 in mice with/without probenecid treatment 70
3.2.8 Quantification of metabolites of [^{18}F]ASu-BF_3 in mouse urine 70
3.3 Results & discussion 70
3.4 Conclusion 79
Chapter 4: The effect of chirality on the application of [^{18}F]5-fluoro-aminosuberic acid ([^{18}F]FASu) for oncological PET imaging.....80
4.1 Introduction 80

4.2 Materials & methods 82
4.2.1 Tracer synthesis and purification 82
4.2.2 Cell culture 82
4.2.3 Western blotting 83
4.2.4 Animal studies 84
4.2.4.1 Tumour inoculation 84
4.2.4.2 Preclinical PET/CT imaging 84
4.2.4.3 Biodistribution studies 85
4.2.5 Statistical analysis 85
4.3 Results 85
4.4 Discussion 96
4.5 Conclusion 97
Chapter 5: Comparison of two xCT-targetting imaging agents, [^{18}F]5- fluoroaminosuberic acid ([^{18}F]FASu) and (4S)-4-(3-[^{18}F]fluoropropyl)-L-glutamate ([^{18}F]FSPG) 98
5.1 Introduction 98
5.2 Materials & methods 99
5.2.1 Chemicals and instrumentation 99
5.2.2 Syntheses of radiotracers 99
5.2.2.1 [^{18}F]-fluoroaminosuberic acid ([^{18}F]FASu) 99
5.2.2.2 (4S)-4-(3-[^{18}F]fluoropropyl)-*L*-glutamate ([^{18}F]FSPG) 100
5.2.3 *In vitro* uptake specificity studies 100
5.2.4 Western blotting 101
5.2.5 Animal studies 102
5.2.5.1 Tumour inoculation 102
5.2.5.2 Biodistribution studies 102

5.2.5.3 PET imaging and data analysis 102
5.2.6 Statistical analysis 103
5.3 Results & discussion 103
5.4 Conclusion 121
Chapter 6: ^{18}F-labelled system L substrates for imaging with positron emission tomography 122
6.1 Introduction 122
6.2 Materials & methods 125
6.2.1 Reagents and instrumentation 125
6.2.2 Photo-catalyzed fluorination: radiochemistry 125
6.2.2.1 Synthesis of 4-[^{18}F]FL, 5-[^{18}F]FHL, 5-[^{18}F]FBAHL, 3-[^{18}F]FV and α-Me-[^{18}F]FL 125
6.2.2.2 Determination of specific activity 126
6.2.3 *In vitro* experiments 127
6.2.3.1 Tissue culture 127
6.2.3.2 *In vitro* uptake studies 127
6.2.4 Animal studies 128
6.2.4.1 Biodistribution studies 128
6.2.4.2 PET/CT imaging 129
6.2.5 Statistical analysis 129
6.3 Results & discussion 129
6.4 Conclusion 143
Chapter 7: Conclusion 145
7.1 Summary of study and findings 145
7.2 Strengths and limitations of this study 147

7.3 Future research directions 150
7.3.1 Chemo- and radiation therapy monitoring *in vivo* 150
7.3.2 Using CRISPR as an alternative approach for the tracer specificity studies 151
7.4 Clinical translation of [^{18}F]FASu 152
7.5 Overall significance and implications of research findings 153
Bibliography 154
Appendices 177
Appendix A 177
Appendix B 179
Appendix C 180
C.1 AWARDS AND SCHOLARSHIPS 180
C.2 PUBLICATIONS 180

List of Tables

Table 1.1 Overview of imaging systems 1

Table 1.2 Overview of some commonly used isotopes for PET imaging 3

Table 1.3 Fluorescent probes used to detect ROS with the use of microplate reader 16

Table 1.4 Breast cancer subtypes and clinicopathological markers 29

Table 1.5 System L transporter subtypes and their respective substrates 36

Table 2.1 Biodistribution data of [^{18}F]FASu at 1 h post-injection collected at 24 h post-radiation therapy of MDA-MB-231 xenografts in NRG mice 55

Table 2.2 Biodistribution data of [^{18}F]FASu at 1 h post-injection collected at 16 h post-radiation therapy of MDA-MB-231 xenografts in NRG mice 58

Table 2.3 Tumour weight and [^{18}F]FASu uptake data at 1 h post-injection from the two biodistribution studies collected at 24 h and 16 h post-radiation therapy of MDA-MB-231 xenografts in NRG mice 59

Table 3.1 Biodistribution data of [^{18}F]ASu-BF_3 in PC-3 tumour-bearing mice at 1 h post-injection 75

Table 3.2 Biodistribution data (mean ± SD %ID/g, n = 4) of [^{18}F]ASu-BF_3 in mice without (control) or with probenecid treatment (50 mg/kg) 10 min before the tracer injection……..... 78

Table 4.1 Summary of quality control data for each [^{18}F]FASu production run 82

Table 4.2 Biodistribution data of 2*S*,5*R/S*-[^{18}F]FASu at 2 h post-injection (p.i.) in breast cancer (MDA-MB-231) and at 1 h p.i. glioblastoma (U-87) and prostate cancer (PC-3) xenograft-bearing Rag2M mice 89

Table 4.3 Biodistribution data of 2*S*,5*S*-[^{18}F]FASu and 2*S*,5*R*-[^{18}F]FASu at 2h p.i. in triple-negative breast cancer (MDA-MB-231) xenograft-bearing Rag2M mice 90

Table 4.4 Biodistribution data of 2*S*,5*R*-[^{18}F]FASu and 2*S*,5*S*-[^{18}F]FASu at 1h p.i. in glioblastoma (U-87) xenograft-bearing Rag2M mice 92

Table 4.5 Biodistribution data of 2*S*,5*R*-[^{18}F]FASu and 2*S*,5*S*-[^{18}F]FASu at 1h p.i. in prostate cancer (PC-3) xenograft-bearing Rag2M mice 95

Table 5.1 Biodistribution and tumour-to-non-target ratios of [^{18}F]FDG, [^{18}F]FASu and [^{18}F]FSPG in A549 xenograft-bearing Rag2M mice 109

Table 5.2 Biodistribution and tumour-to-non-target ratios of [^{18}F]FDG, [^{18}F]FASu and [^{18}F]FSPG in U-87 xenograft-bearing Rag2M mice 113

Table 5.3 Biodistribution and tumour-to-non-target ratios of [^{18}F]FDG and [^{18}F]FASu in U-87 xenograft-bearing NSG mice that had been subjected to fasting for 12-14 h. 116

Table 6.1 ^{18}F-fluorination of unprotected branched aliphatic amino acids 127

Table 6.2 Biodistribution of (*L*)-5-[^{18}F]FHL, (*L*)-5-[^{18}F]FBAHL and (*L)*-4-[^{18}F]FαML in U-87 tumour bearing mice at 60 min post injection 142

List of Figures

Figure 1.1 Enzymatic and non-enzymatic intracellular sources of reactive oxygen species 9

Figure 1.2 Antioxidants have both beneficial and harmful roles in tumourigenesis 11

Figure 1.3 Redox regulation is crucial for physiological outcomes and cancer cell proliferation and survival 12

Figure 1.4 Cellular mechanism of xCT expression induced by oxidative stress and promoting increased glutathione synthesis 19

Figure 1.5 A) Graphic representation of system x_C^- B) Crystal structure of xCT 21

Figure 1.6 Chemical structures of [^{18}F]FGlu, [^{18}F]FSPG, [^{18}F]FASu and [^{18}F]-hGTS13 24

Figure 1.7 mTOR signalling regulation 38

Figure 2.1 Radiosynthesis of [^{18}F]FASu 42

Figure 2.2 [^{18}F]FASu uptake and xCT expression with siRNA knockdown or OS-inducer treatment 48

Figure 2.3 [^{18}F]FASu uptake over time with DEM treatment 49

Figure 2.4 *SLC7A11* expression, [^{18}F]FASu uptake, GSH levels and ROS levels in MDA-MB-231 cells after 1 h or overnight DEM treatment 51

Figure 2.5 [^{18}F]FASu *in vitro* uptake is positively correlated to xCT expression and intracellular GSH levels in three breast cancer cell lines 53

Figure 2.6 Flow cytometry CM-H_2DCFDA staining shows a partial shift in fluorescence peak after 1 h treatment with DEM (red) in MDA-MB-231 and MCF-7, but not in ZR-75-1 cells 54

Figure 2.7 The TNBC line, MDA-MB-231, shows significantly higher *SLC7A11* and xCT expression levels, both *in vitro* and *ex vivo* 55

Figure 2.8 Biodistribution data and maximal intensity projections of PET/CT images with [^{18}F]FASu at 1 h post-injection taken 24 h before and post-radiation therapy of MDA-MB-231 xenografts in NRG mice 56

Figure 2.9 [^{18}F]FASu uptake post-radiation treatment 57

Figure 3.1 Chemical structures of glutamate and cystine, and their respective derivatives [^{18}F]FSPG and [^{18}F]FASu for imaging the system x_C^- transporter with positron emission tomography 64

Figure 3.2 Chemical structures of ^{18}F-labeled boramino acid derivatives of Phe, Leu, Met, Ala, Pro and ASu. 64

Figure 3.3 Synthesis of (A) nonradioactive and (B) ^{18}F-labeled ASu-BF_3 71

Figure 3.4 HPLC chromatograms of (A) [^{18}F]ASu-BF_3 QC sample, and [^{18}F]ASu-BF_3 samples after being incubated in mouse plasma for (B) 5 min; (C) 30 min and (D) 60 min..... 72

Figure 3.5 *In vitro* evaluation of [^{18}F]ASu-BF_3 73

Figure 3.6 *In vivo* evaluation of [^{18}F]ASu-BF_3 74

Figure 3.7 Biodistribution data of ^{18}F[ASu]BF_3 in selected organs for PC3 tumour-bearing mice at 1 h post-injection..... 74

Figure 3.8 Uptake values of [^{18}F]ASu-BF_3 in blood and kidneys with/without probenecid treatment 77

Figure 3.9 HPLC chromatograms of (A) [^{18}F]ASu-BF_3 QC sample, and urine samples collecetd from three separate mice (B-D) at 30 min post-injection. 77

Figure 4.1 Chemical structures of fluorinated aminosuberic acid stereoisomers in four stereoisomeric configurations 81

Figure 4.2 *In vitro* experimentation. 86

Figure 4.3 *In vivo* evaluation of the 5-position racemate. 87

Figure 4.4 Tumour uptake of [^{18}F]FASu 5-position diastereomers, 2*S*,5*S*-[^{18}F]FASu and 2*S*,5*R*-[^{18}F]FASu. 88

Figure 4.5 Studies with glioblastoma xenograft-bearing mice. 91

Figure 4.6 Studies with PC-3 xenograft-bearing mice. 93

Figure 4.7 Dynamic images of PC-3 tumour-bearing mice with all three 5-position tracer configurations. 94

Figure 5.1 Chemical structures of ^{18}F-labelled FASu, FSPG and FDG. 99

Figure 5.2 [^{18}F]FSPG *in vitro* uptake at 20, 40 and 60 min in the absence and presence of xCT inhibitor sulfasalazine (SSZ). 105

Figure 5.3 [^{18}F]FASu *in vitro* uptake at 20, 40 and 60 min in the absence and presence of xCT inhibitor sulfasalazine (SSZ). 105

Figure 5.4 [^{18}F]FASu and [^{18}F]FSPG *in vitro* uptake blocked with SSZ 106

Figure 5.5 Validation study: biodistribution of [^{18}F]FASu in two different formulations 107

Figure 5.6 Western blot image of tumour lysates indicating 35 kDa xCT protein expression in U-87 and A549 tumour lysates 108

Figure 5.7 Comparative study: uptake of [^{18}F]FDG, [^{18}F]FASu and [^{18}F]FSPG in A549 tumour-bearing mice at 1 h post – injection 110

Figure 5.8 Two-way ANOVA analysis of tumour-to-muscle and tumour-to-brain ratios, tumour and brain uptake for [^{18}F]FDG, [^{18}F]FASu and [^{18}F]FSPG in A549 tumour-bearing mice at 1 h post – injection 110

Figure 5.9 Comparative study: uptake of [^{18}F] FDG, [^{18}F]FASu and [^{18}F]FSPG in U-87 tumour-bearing mice at 1 h post – injection 111

Figure 5.10 Two-way ANOVA analyses of tumour-to-muscle and tumour-to brain ratios, tumour and brain uptake for [^{18}F]FDG, [^{18}F]FASu and [^{18}F]FSPG in U-87 tumour-bearing mice at 1 h post – injection 112

Figure 5.11 Dynamic PET maximum intensity projection of [^{18}F]FDG uptake 45-60 min after injection in U-87 tumour-bearing Rag2M mouse 115

Figure 5.12 Comparative study: uptake of [^{18}F]FDG and [^{18}F]FASu in U-87 tumour-bearing mice at 1 h post – injection 117

Figure 5.13 Comparative study: uptake of [^{18}F]FDG and [^{18}F]FASu in U-87 tumour-bearing mice at 1 h post – injection 118

Figure 5.14 Two-way ANOVA analysis of tumour-to-muscle and tumour-to-brain ratios, tumour and brain uptake for [^{18}F]FDG and [^{18}F]FASu in U-87 tumour-bearing fasted NSG mice at 1 h post – injection 118

Figure 5.15 Two-way ANOVA analysis of 1h uptake of [^{18}F]FASu and [^{18}F]FSPG in A549, U-87 and MDA-MB-231 cells 120

Figure 5.16 Dose-dependent competition cell assays in A549 cell line 120

Figure 6.1 Radiotracers for PET imaging in oncology and ^{18}F-labelled analogues of leucine ..122

Figure 6.2 Decatungstate-catalyzed C-H fluorination applied to the production of 4-[^{18}F]fluoroleucine (4-[^{18}F]FL (7)). 124

Figure 6.3 Uptake of 4-[^{18}F]FL in LNCaP, PC-3 and MCF-7 cells at 20, 40 and 60 min in the presence (+) and absence (-) of the LAT1 inhibitor BCH (10 mM). 131

Figure 6.4 Biodistribution at 60 min p.i. of 4-[^{18}F]FL, 5-[^{18}F]FHL and 5- [^{18}F]FBAHL in healthy mice. 132

Figure 6.5 Uptake of 5-[^{18}F]FHL in LNCaP, PC-3, U-87 and MCF-7 cells at 20, 40 and 60 min in the presence (+) and absence (-) of the LAT1 inhibitor BCH (10 mM). 134

Figure 6.6 PET imaging of 5-[^{18}F]FHL in mice bearing human glioma (U-87) xenografts..... 134

Figure 6.7 Time-activity curves of the accumulation of 5-[^{18}F]FHL in selected organs..... 135

Figure 6.8 Biodistribution of 5-[^{18}F]FHL in selected organs at 1 h p.i. in NSG mice bearing U-87 and PC-3 xenograft tumours 135

Figure 6.9 Whole-body maximum intensity projection images overlaid on CT of the biodistribution of 5-[^{18}F]FHL at 50-60 minutes for the U-87 tumour xenografts and for the PC-3 tumour xenografts 136

Figure 6.10 Uptake of *L*- [^{18}F]FHL, *D*- [^{18}F]FHL, *L*- [^{18}F]FBAHL, *D*- [^{18}F]FBAHL and *L*-α-Me-[^{18}F]FL in PC-3 cells at 60 min in the presence of substrates/inhibitors of a wide array of amino acid transporters 138

Figure 6.11 Percent inhibition of *L*- [^{18}F]FHL, *D*- [^{18}F]FHL, *L*- [^{18}F]FBAHL, *D*- [^{18}F]FBAHL and *L*-α-Me-[^{18}F]FL uptake by PC-3 cells at 60 min..... 138

Figure 6.12 Substrates/inhibitors used in the cell study and their respective transporters 139

Figure 6.13 Biodistribution of *L*- and *D*- isomers of [^{18}F]FL at 1 h p.i. in healthy mice 140

Figure 6.14 Biodistribution of *L*- and *D*- isomers of [^{18}F]FBAHL at 1 h p.i. in healthy mice.. 140

Figure 6.15 Biodistribution of *L*-α-Me-[^{18}F]FL at 1 h p.i. in healthy mice 141

Figure 6.16 A) *In vivo* dynamic PET imaging of (*L*)-5-[^{18}F]FHL in NSG mouse bearing U-87 xenograft at 60 min post injection. B) Time-activity curve of (*L*)-5-[^{18}F]FHL in the U-87 tumour, brain and muscle tissues over 55 min p.i. 143

Figure 7.1 MDA-MB-231 tumour analysis data..... 149

List of Symbols and Abbreviations

$	Dollar
%	Percentage
%ID/g	Percent injected dose per gram
[^{11}C]MET	[^{11}C]-Methionine
[^{18}F]ASu-BF$_3$	[^{18}F]-labelled (*S*)-(7-trifluoroboryl-7-ammonio)heptanoic acid
[^{18}F]DOPA	3,4-Dihydroxy-6-[^{18}F]fluoro-*L*-phenylanine
[^{18}F]FASu	5-[^{18}F]Fluoro-aminosuberic acid
[^{18}F]FDG	^{18}F-Fluorodeoxyglucose
[^{18}F]FET	*O*-(2-[^{18}F]Fluoroethyl) tyrosine
[^{18}F]FGlu	4-[^{18}F]Fluoroglutamate
[^{18}F]Leu-BF$_3$	Boramino acid derivative of fluoroleucine
[^{18}F]FMISO	[^{18}F]Fluoromisonidazole
[^{18}F]FSPG	(*4S*)-4-(3-[^{18}F]Fluoropropyl)-*L*-glutamate
[^{68}Ga]DOTA	[^{68}Ga]-1,4,7,10-Tetraazacyclododecane-*N*,*N′*,*N″*,*N‴*-tetraacetic acid
°	Degree
° C	Degree Celsius
•OH	Hydroxyl radical
^{18}F$^-$	^{18}F-Fluoride anion
^{19}F-NMR	^{19}F-Nuclear magnetic resonance
^{1}H-NMR	Proton nuclear magnetic resonance
2D	Two-dimensional
3-[^{18}F]FV	3-[^{18}F]Fluorovaline
3D	Three-dimensional
3D OSEM – MAP	3D ordered subset-expectation maximization (3D OSEM) – Maximum a priori (MAP) algorithm
4-[^{18}F]FL	3-[^{18}F]Fluoroleucine
4F2hc	Heavy chain of the surface antigen 4F2

5-[^{18}F]FBAHL	5-[^{18}F]Fluoro-β-amino-homoleucine
5-[^{18}F]FHL	5-[^{18}F]Fluoro- homoleucine
AAT	Amino acid transporter
***anti*-[^{18}F]FACBC**	*Anti*-1-amino-3-[^{18}F]fluorocyclobutane-1-carboxilic acid
AP-1	Activator protein 1
ApcT	Amino acid, polyamine, organo-cation transporter
ARE	Antioxidant response element
ASu	Aminosuberic acid
BC	British Columbia
bp	Base pairs
Bq	Becquerel
BSA	Bovine serum albumin
CA	Carbonic anhydrase
CD44v	Tumour-associated antigen CD44v isoform
cDNA	Complementary DNA
CH_3CN	Acetonitrile
CM-H_2DCFDA	5-(and 6)-Chloromethyl-2',7'-dichlorohydrofluorescein diacetate
CO_2	Carbon dioxide
CPG	*p*-Carboxy-phenylglycine
cpm	Counts per minute
CSC	Stem-like cancer cell
C_t	Threshold cycle
CT	Computed tomography
Cys	Cysteine
d	Day
D_2O	Deuterium water
Da	Dalton
DCF	Dichlorohydrofluorescein
DCFDA	Dichlorohydrofluorescin diacetate
DEM	Diethylmaleate

DHE	Dihydroethidium
DMEM	Dulbecco Modified Eagle Medium
DNA	Deoxyribonucleic acid
DOTA	1,4,7,10-Tetraazacyclododecane-*N*,*N*′,*N*″,*N*‴-tetraacetic acid
dsDNA	Double-stranded DNA
EAAT	Excitatory amino acid transporter
EC	Electron capture
EPO	Erythropoietin
ER	Oestrogen receptor
ER	Endoplasmic reticulum
etc.	*Et cetera*
eV	Electron volt
FBS	Fetal bovine serum
FDA	U.S. Food and Drug Administration
G	Giga
GE	General Electric
GEP	Gene expression profiling
GF	Growth factor
GLUT	Glucose transporter protein
GPx	Glutathione peroxidase
GSH	Glutathione
h	Hour
H^+	Proton / hydrogen ion
H_2DCFDA	2',7'-Dichlorohydrofluorescein diacetate
H_2O	Water
H_2O_2	Hydrogen peroxide
HBSS	Hepes basal salt solution
HEPES	4-(2-Hydroxyethyl)-1-piperazineethanesulfonic acid
HER2	Human epidermal growth factor 2 receptor
HGF	Hepatocyte growth factor

HIF-1	Hypoxia-inducible factor 1
HNO_2	Nitrous acid
HOCl	Hypochlorous acid
HPLC	High-performance liquid chromatography
HPRT1	Hypoxanthine phosphoribosyltransferase 1
HRP	Horseradish peroxidase
IC_{50}	Half maximal inhibitory concentration
i.v.	Intravenous
IgG	Immunoglubulin
IHC	Immunohistochemistry
IL-1b	Interleukin-1b
IRW	Inveon Research Workplace software
K_{222}	Kryptofix-222
K_2CO_3	Potassium carbonate
KEAP1	Kelch ECH associating protein 1
keV	Kilo electron volt
K_i	Inhibition constant
KO	Knockout
L	Liter
LCFA	Long-chain fatty acid
LD_{50}	Lethal dose
LPS	Lipopolysaccharide
M	Molar concentration (mol/L)
MAPK	MAP kinase
Met	Methionine
MeV	Megaelectron volt
mg	Milligram
min	Minute
mm	Millimeter
mol/L	Moles per liter

MRI	Magnetic resonance imaging
mRNA	Messenger RNA
mTOR	Mammalian target of rapamycin
mTORC1	Mammalian target of rapamycin complex 1
MUC-1	Mucin-1 transmembrane glycoprotein
n	Neutron
Na^+	Sodium cation
NADPH	Dinicotinamide-adenine dinucleotide phosphate
$NaHCO_3$	Sodium bicarbonate
NaOH	Sodium hydroxide
NET	Neuroendocrine tumour
NF-kB	Nuclear factor kappa-light-chain-enhancer of activated B cells
NFSI	N-Fluorobenzenesulfonimide
nm	Nanometer
NO•	Nitric oxide
NRF2	Nuclear factor erythroid 2-related factor 2
NRG	Mouse strain: NOD-*Rag1*^{null} *IL2rg*^{null}
NSG	Mouse strain: NOD-*scid* IL2Rg^{null}
O_2	Dioxygen
$O_2•^-$	Superoxide radical
$ONOO^-$	Peroxynitrite
OS	Oxidative stress
p	Proton
p.i.	Post-injection
PBS	Phosphate buffered saline
PCR	Polymerase chain reaction
PDGF	Platelet-derived growth factor
PET	Positron emission tomography
PI3K	Phosphoinositide 3-kinase
PKA	Protein kinase A

PR	Progesterone receptor
Prx	Peroxiredoxin
PTEN	Phosphatase and tensin homolog
PTP1B	Protein-tyrosine phosphatase 1B
qPCR	Quantitative polymerase chain reaction
Rag2M	Mouse strain: 129S6/SvEvTac-*Rag2*^{tm1Fwa}
RCP	Radiochemical purity
RCY	Radiochemical yield
RNA	Ribonucleic acid
RNS	Reactive nitrogen species
ROI	Region of interest
ROS	Reactive oxygen species
rpm	Rotations per minute
RPMI	Rowell Park Memorial Institute medium
SA	Specific activity
SARRP	Small animal radiation research platform
SD	Standard deviation
Ser	Serine
siRNA	Small interfering RNA
SLC2A3	Solute carrier family 2 member 3
SLC7A11	Solute carrier family 7 member 11
S_N2	Bimolecular nucleophilic substitution reaction
S_NAr	Nucleophilic aromatic substitution
SOD	Superoxide dismutase
SPECT	Single photon emission computed tomography
SSZ	Sulfasalazine
System ASC	Alanine-serine-cysteine transporter system
$t_{1/2}$	Half-life
TBS-T	Tris-buffered saline - tween
TFA	Trifluoroacetic acid

TLC	Thin-layer chromatography
TNBC	Triple-negative breast cancer
TNFα	Tumour necrosis factor alpha
Trx	Thioredoxin
UBC	University of British Columbia
UV	Ultraviolet
VEGF	Vascular endothelial growth factor
VEGFR	Vascular endothelial growth factor receptor
***xCT*$^{-/-}$**	xCT knockout mice
α-Me-[^{18}F]FL	Alpha-methyl-[^{18}F]fluoroleucine
β^+	Positron
γ	Gamma ray
γ-GCS	Gamma-glutamylcysteine synthetase
λ_{em}	Emission wavelength
λ_{ex}	Excitation wavelength
μ	Micro
μPET/CT	MicroPET/CT scanner

Acknowledgements

I would like to offer my sincere gratitude to my supervisors, Drs. Paul Schaffer and François Bénard, for their guidance and support towards this project. Thank you, Dr. Schaffer for always believing in me and for giving me the opportunity to explore my curiosity-turned-passion for medical research. Thank you for always holding me in high esteem. Dr. Bénard, your creativity, immense knowledge and passion for research continue to inspire me to pursue my dreams. Thank you for giving me this opportunity and for always expecting the best of me.

I offer my enduring gratitude to the professors on my supervisory committee, Drs. Urs Häfeli and Mads Daugaard. Thank you for enhancing my understanding of nuclear medicine and molecular signalling, and for all your advice. Special thanks to Dr. Kuo-Shyan Lin, for always being there to answer my numerous chemistry questions and giving me the opportunity to do chemistry, and to Dr. Corina Andreoiu, for introducing me to the field of nuclear medicine and for being a magnificent role model. I would like to acknowledge our collaborators, Drs. Nodwell, Britton, and Yapp, and the generous scholarship support from IsoSiM CREATE NSERC Program. The work presented herein was funded by the Canadian Institute of Health Research.

My sincere thanks to the Life Sciences team at TRIUMF - especially to Dr. Hua Yang for her guidance and mentorship during the past years. Thank you, Hua, for your continuous support and advice, and for encouraging me to pursue a graduate degree and beyond. You have been a great mentor and friend, in good times and especially during hardships. Thanks to the TR13 Team: David, Linda and Samuel, for all their hard work and dedication. Thank you, Gayle, for your patience and guidance towards overcoming my murophobia and thanks to the rest of the ARC team for making our animal studies possible. Thank you to all past and present Bénard and Lin lab members: Helen, Joseph, Iulia, Gemma, Julie, Jutta, Chengcheng, Carlos, Étienne, Johnson, Ting, Guillaume, Frederic, Jinhe, Jason, Aron, Marin, Daniel, Ivica, Teresa, Shreya, Sara, for your support. Special thanks to Silvia, who taught me hands-on lab skills, and to Nadine and Nav for helping me complete my imaging studies. Without your support and friendship this project would have been a lot more difficult to pursue.

Finally, I would like to thank my loving family for their unceasing support throughout the years of my education abroad, always encouraging me to be the best version of myself and strive for excellence. Special thanks to my brothers Milan and Nikola, and my husband and best friend Nikola for their unconditional support without which I would not have been where I am today. To my parents, Dženana and Miloje Čolović, thank you for all your sacrifices. To them I dedicate this thesis.

Scientia potestas est.

Chapter 1: Introduction

1.1 Molecular imaging in nuclear medicine

Nuclear medicine is a multidisciplinary medical field which entails the use of radioactive isotopes to diagnose, stage, treat and monitor diseases of various nature.[1] This approach enables clinicians and scientists to quantitatively measure physiological and biochemical processes *in vivo*, using non-invasive imaging.[2–4] The term 'molecular imaging' has been coined to refer to imaging methods that probe *in vivo* biochemistry.[5] The molecular imaging techniques used primarily in clinical practice are planar gamma imaging, single photon emission computed tomography (SPECT) and positron emission tomography (PET).[2] All three of these imaging modalities use radioactive isotopes attached to biomolecules to non-invasively evaluate the physiological function and biochemical changes of molecular targets.[6] Anatomical information is obtained by pairing PET and/or SPECT images with computed tomography (CT) or magnetic resonance imaging (MRI), which provide high-resolution tissue density map of the patient in 3D,[7] allowing co-registration of the functional and anatomical information. Table 1.1 outlines the main properties of these four imaging modalities.

Table 1.1 Overview of imaging systems. Adapted with permission from Weissleder and Pittet.[7]

Modality	Resolution*	Quantitative	Imaging agents	Target	Cost[§]	Main small-animal use	Clinical use
PET	1 -2 mm	Yes	^{18}F-, ^{64}Cu- or ^{11}C-labeled compounds	Physiological, molecular	$2.5M for PET/CT	Versatile imaging modality with many tracers	Yes
SPECT / planar gamma imaging	0.4 – 2 mm	Yes	^{99m}Tc- or ^{111}In-labeled compounds	Physiological, molecular	$750k for SPECT or $1-1.2M for SPECT/CT	Imaging labelled antibodies, proteins and peptides	Yes
MRI	10 -100 μm	Yes	Paramagnetic chelates, magnetic particles	Anatomical, physiological, molecular	$2-3M	Versatile imaging modality with high soft-tissue contrast	Yes
CT	50 μm	Yes	Iodinated molecules	Anatomical, physiological	$750k	Imaging lungs and bone	Yes

*For high-resolution, small-animal imaging systems; (clinical systems differ). §Cost is based on purchase price of imaging systems in Canada (in Canadian dollars ($)).[8]

Molecular imaging techniques aid physicians in disease detection, diagnosis and management;[9] particularly PET, due to its high sensitivity of 10^{-11}-10^{-12} mol/L,[3,10–12] has become an indispensable tool for drug development and discovery,[3,13,14] as well as cancer treatment, staging, and determination of prognostic information and detection of recurrent disease.[9,12]

1.1.1 Positron emission tomography

PET is based on the use of radiopharmaceuticals labelled with a positron–emitting isotope, which is usually intravenously injected into a patient's body. Ideally, the radiopharmaceutical is specific to a molecular target whose location and/or activity is revealed on the PET scan due to the decay of the radioisotope. The emitted positrons travel a short distance through nearby tissue or organ, annihilating with atomic electrons. Upon annihilation, two 511 keV gamma rays are emitted nearly 180° apart, and caught by the ring detectors in coincidence.[10,15] The distance travelled by the emitted positron, called the positron range, results in an uncertainty in determining the origin of the source, which limits the resolution of PET to 5-8 mm in standard clinical PET cameras, and 1 – 2 mm in small-animal PET systems.[10] The need for collimators is obviated in PET by the assumption that the source is positioned along the line that connects the two detectors which had recorded the annihilation photons, called the "line of response".[15] The detected signals are reconstructed using computer algorithms to generate 2D projections or 3D data sets.[10]

Commonly used PET isotopes include ^{18}F, ^{11}C, ^{68}Ga, ^{124}I and ^{89}Zr, all of which have different half-lives, production modes and biological compatibilities[16] (listed in Table 1.2), allowing for labelling of a wide range of biomolecules including small molecules, peptides, antibodies etc. When selecting an appropriate radioisotope, the physical half-life of the isotope should be aligned with its biological half-life. For example, shorter-lived isotopes such as ^{18}F and ^{11}C are often used for labelling of small molecules, which have shorter biological half-lives, allowing for injection of higher amount of tracer activity which in turn increases signal-to-noise ratio.[1] Additionally, since the physical half-lives are short, patients can participate in multiple scans. However, an important complication when using shorter-lived tracers is that the radiosynthesis methods must also be rapid and efficient. On the other hand, longer-lived isotopes such as ^{124}I and ^{89}Zr are particularly suitable for antibody labelling because they match well to

their biological half-lives, giving optimal contrast for imaging purposes at later time points.[1] Furthermore, since monoclonal antibodies are highly target-specific and tend to circulate in the bloodstream for days while accumulating at the target site; radiolabelling them with a high energy beta or alpha emitter would make them very useful therapeutic agents.

Table 1.2 Overview of some commonly used isotopes for PET imaging.[2,4,16–21]

Isotope	Half-life	Decay mode	Production mode	Common PET tracer	Molecular target / metabolic process	Tumour type / Disease
^{11}C	20.36 min	β^+ (100 %)	Cyclotron, $^{14}N(p,\alpha)^{11}C$	^{11}C-choline	Choline transporter	Various[§]
				^{11}C-nicotine	Cortical nicotinic receptors	Alzheimer's disease
				^{11}C-methionine	AAT[§] & protein synthesis	Brain & other tumours
^{18}F	109.77 min	β^+ (97 %) EC (3 %)	Cyclotron, $^{18}O(p,n)^{18}F$	[^{18}F]FDG	GLUT1	Various
				[^{18}F]NaF	Bone metabolism	Bone metastasis
				[^{18}F]DOPA	Dopamine uptake & metabolism	NETs[§] Parkinson's disease
				[^{18}F]FMISO	Tumour hypoxia	Various tumours
^{68}Ga	67.71 min	β^+ (89 %) EC (11 %)	$^{68}Ge/^{68}Ga$ generator	^{68}Ga-DOTApeptides	Somatostatin receptors	NETs
^{124}I	4.2 d	β^+ (23 %) EC (77 %)	Cyclotron, $^{124}Te(p,n)^{124}I$	^{124}I-cG250	CA-IX[§]	Clear-cell renal carcinoma
^{89}Zr	3.27 d	β^+ (23 %) EC (77 %)	Cyclotron, $^{89}Y(p,n)^{89}Zr$	^{89}Zr-bevacizumab	VEGFR[§]	Various tumours

[§]Prostate, bladder, colorectal, oesophageal, lung and brain cancer. [21]

[§] AAT – amino acid transport; NETs – neuroendocrine tumours; CA-IX – carbonic anhydrase IX; VEGFR – vascular endothelial growth factor receptor;

Table 1.2 lists some commonly used PET radiopharmaceuticals, but is by no means exhaustive. Examples include ^{11}C-choline for the imaging of recurrent prostate cancer, bladder, colorectal, lung and brain cancers;[21] [^{18}F]-fluoromisonidazole ([^{18}F]FMISO), which is used to assess tumour hypoxia in lung, head-and-neck and brain cancer patients and for imaging myocardial ischemia;[1,19] [^{68}Ga]-DOTA-peptides for somatostatin receptor imaging in neuroendocrine tumours,[19] and [^{89}Zr]-avastin for imaging tumour angiogenesis.[20] However, ^{18}F

remains the most commonly used PET isotope,[22] primarily because 2-[^{18}F]-fluoro-2-deoxy-*D*-glucose ([^{18}F]FDG) is the most used PET radiopharmaceutical in clinical practice.[18,22]

1.1.1.1 [^{18}F]FDG oncological imaging

2-fluoro-2-deoxy-*D*-glucose (FDG) was originally synthesized in 1968 by Pacák *et al.*,[23] and radiofluorinated in the 1970s by Wolf and colleagues in the Brookhaven National Laboratory,[24,25] with the first in-human use soon to follow.[26] Originally developed for the specific purpose of mapping glucose metabolism in the living human brain,[25] [^{18}F]FDG has become the most widely used radiopharmaceutical for PET cancer imaging.[19,24]

[^{18}F]FDG enters the cells *via* glucose transporter proteins (GLUT), gets phosphorylated by hexokinase into [^{18}F]FDG-6-phosphate, trapping it intracellularly, due to the lack of hydroxyl group at the C2 position (where ^{18}F atom is attached to the ring) preventing glucose-6-phosphate isomerase from converting it into the next substrate of glycolytic pathway.[22] This "metabolic trapping" of [^{18}F]FDG-6-phosphate provides the means for tracer accumulation and enhanced contrast and signal for image acquisition[22,27] and is based on enhanced glycolytic and metabolic rates in malignant tumours (Warburg effect) compared to non-malignant tissues.[27–29] [^{18}F]FDG-PET has thus become an indispensable tool for diagnosis, staging, restaging and assessment of response to treatment of a wide variety of cancers.[30,31]

The main limitation of [^{18}F]FDG as a PET radiopharmaceutical is that it is not cancer-specific tracer.[32] It is taken up by hypermetabolic cells with high demand for glucose such as brain cells, brown adipocytes, and also by kidney and bladder cells, which restricts its use for imaging gliomas, prostate and bladder cancers.[33] Furthermore, some non-neoplastic inflammatory processes such as tuberculosis, sarcoidosis and fungal infections may result in false-positive PET signal.[32,34] In addition, small lesions (<8mm), unless they are very hypermetabolic, are difficult to visualise by [^{18}F]FDG-PET and slow-growing malignant lesions have poor avidity for [^{18}F]FDG. Examples include low-grade sarcomas, low-grade non-Hodgkin's lymphomas, bronchoalveolar cell carcinoma.[32] For these reasons, development of novel PET radiopharmaceuticals that attempt to address the above limitations is an active area of research.

1.1.1.2 Impact of [^{18}F]FDG PET on cancer patient care

Numerous studies have demonstrated that PET/CT plays an important role in cancer patient management,[30,35–37] and is beneficial for cancer diagnosis, staging and evaluation of treatment response.[3] In their study of more than 8,200 patients who had undergone more than 10,400 [^{18}F]FDG PET scans combined, Hillner and colleagues reported that PET enabled physicians to avoid additional medical tests and procedures in 90.6% of the time.[36] The same group also reported that in >70% cases invasive surgical procedures were avoided thanks to PET imaging,[35] and that the intended cancer management was adjusted in almost 50% of patients, based on treatment-monitoring scans.[36] A Canadian study from 2010 reported similar findings, with PET/CT contributing to the changing of cancer treatment plans in ~50% of the cases and improved decision making in more than 80% of the cases.[37]

In Canada, cancer is the leading cause of death and the leading cause of premature mortality,[38] which poses a growing challenge for the Canadian healthcare system.[39] Nuclear imaging infrastructure varies province to province, but as of September 2015, Canada has 45 publicly-funded PET cameras, across 34 centres.[40] Our facility, the British Columbia Cancer (BC Cancer), currently has three operational PET/CT scanners which now perform over 10,000 scans per annum.[40] With plans for expansion of the provincial scanning capacity, it can be expected that the outcomes for ~200,000 newly diagnosed cancer patients[38] every year will be improved and the long-term cost will be reduced overall by avoiding unnecessary surgical and testing procedures.

1.1.1.3 Role of molecular imaging in personalised treatment

Whether the impact of PET on cancer patient care results in the change in therapy regimen or intent of treatment (curative/palliative), its impact on cancer management is vast. What gives PET even more potential to improve cancer management is its application in individualized treatment. Cancer has long been recognized as a complex and dynamic disease,[41] requiring subtype determination and targeted treatments for the specific diagnosis, reliable prognosis and best outcomes. Molecular imaging enables us to study cancer biology *in vivo* and optimize personalized patient treatment.[1]

With the development of molecular biology, particularly DNA sequencing technology, we are now able to use the information about the genetic makeup of tumours to strategically plan prevention and/or treatment. An example of this is the improvement in management of stage IV malignant melanoma, a disease with meagre prognosis - the median patient survival is 7.5 months and estimated five-year survival rate of a mere 6%.[42,43] With the discovery that 66% of malignant melanomas harbour a *V600E* mutation in the *BRAF* oncogene, which is indicative of increased disease severity and poor response to standard chemotherapy,[44,45] a RAF kinase inhibitor, vemurafenib, was developed to target cancers with this specific mutation, subsequently reducing the relative risk of death or disease progression by 74% in these patients as compared to the standard of care.[44,46] Another benefit of personalized cancer medicine is genetic screening to predict the risk of developing certain cancers – which may enable physicians to reduce disease occurrence *via* the action of prophylactic procedures. Examples include mastectomy, oophorectomy or chemical estrogen deprivation for *BRCA1/2* mutation carriers[44] – which increase the risk of developing breast cancer and ovarian cancer.[47] With the increased accessibility of whole genome and exome sequencing as a clinical diagnostic tool, personalized cancer medicine is quickly becoming a mainstay in large medical centres throughout the world. While these preventative procedures do not completely eliminate the risk of cancer occurrence,[44] it was found precautionary mastectomy was effective in reducing the incidence of deaths from breast cancer.[48]

Molecular imaging has the potential to influence personalized treatment strategies because it enables the non-invasive visualization of drug biodistribution *in vivo*, as long as a radioactive isotope can be attached to it, without compromising its active/binding site(s) and thus changing biological function of the drug.[12] The downstream applications of this approach include a non-invasive platform for stratifying tumours into marker-positive *versus* marker-negative, patients into responders and non-responders, ability to diagnose the tumour correctly, plan treatment and also effectively deliver treatment (in the case of targeted radiotherapy). Physicians need to be able to monitor physiological and genetic changes in the tumours, particularly because cancers tend to evolve and adapt to changing environment[41,49] (e.g., due to treatment). While this is accomplished *via* biopsies and other biomarkers (e.g., prostate-specific antigen), new non-invasive imaging methods represent the next effective cancer diagnostics and monitoring. This

will require development of novel tracers specific for cancers with different molecular signatures, enabling features such as a new route to monitoring a patient's response to therapy and surveillance for cancer recurrence.[12] While [^{18}F]FDG and other available radiopharmaceuticals play a key role in clinical cancer management, there is still room for substantial improvement.

1.2 Cancer and tumour microenvironment

1.2.1 The hallmarks of cancer

Tumourigenesis is a complex and multistep process, driven by a set of underlying traits that the progenitor cells need to acquire in order to be able to progress to become cancerous and ultimately metastasize. These traits can be thought of as the hallmarks of cancer, a concept originally proposed by Hanahan and Weinberg in 2000,[41] and were put forward with a goal to rationalize and deepen the understanding of complexities of cancer progression. Six hallmarks were originally proposed: sustaining proliferative signalling, evading growth suppressors, resisting cell death, enabling replicative immortality, inducing angiogenesis and activating invasion and metastasis.[41] A decade later, as the understanding of cancer biology deepened, two additional hallmarks were added, namely: reprogramming of the cellular metabolism and evading immune destruction,[49] along with two characteristics of neoplasia that facilitate acquisition of both core and emerging hallmarks. One of these tumour-promoting characteristics is genomic instability a consequence of which is increased mutation burden resulting in advantage of subclones of cells, enabling their survival and eventual genetic makeup that confers selective dominance in a local tissue environment. The other enabling characteristic is tumour-promoting inflammation, which can contribute to multiple hallmark capabilities by supplying bioactive molecules (including growth factors, survival factors, proangiogenic factors and extracellular matrix-modifying enzymes) to the tumour microenvironment. This also shed light on the evidently greater role of the tumour microenvironment in cancer progression.[50]

1.2.2 The role of tumour microenvironment in cancer progression

The local microenvironment provides extrinsic barriers that are evolutionarily conserved to preserve normal tissue structure and function,[51] however, cancer cells are active and responsive cells, in constant communication with one another and their surrounding milieu. They recruit vasculature and stroma through production and secretion of stimulatory growth factors and cytokines.[52] Additionally, proliferating cancer cells alter the metabolic composition of the extracellular niche around them as well, causing alterations to the extracellular matrix and cell-to-cell interactions. In turn, the locally activated microenvironment affects the metabolism and signalling responses of cancer cells themselves[53] which can lead to changes in the proliferative and invasive behaviour of the tumour cells.[54,55] This dynamic interaction between cancer cells and their microenvironment greatly influences most of the hallmark capabilities needed for the tumourigenesis, and it has become clear that cancer cells do not act alone in elaborating the disease.

One interesting example of this interaction between cancer cells and their surrounding stroma are reactive oxygen species (ROS), which can be secreted by both cancer cells and inflammatory cells of the stroma, and are involved in multiple aspects of tumourigenesis[50]. ROS are DNA-damaging agents that can also act as signalling molecules and as such are an example of both an extrinsic barrier that tumour microenvironment is imposing on cancer cells, and intrinsic factors that cancer cells use to their advantage.[50]

1.3 Reactive oxygen species

1.3.1 Sources and scavengers of reactive oxygen species

ROS are defined as oxygen-containing, chemically reactive molecules, which can be classified into two main groups, based on whether or not they contain unpaired electrons in their molecular orbits: radical and non-radical molecules.[56] Free radicals are species which contain one or more unpaired electrons and are capable of independent existence, such as superoxide ($O_2^{\bullet -}$), hydroxyl radicals (•OH), and nitric oxide (NO•), and are highly reactive. Non-radical ROS are easily converted to free radicals in living systems and thus are also highly-reactive.

Examples of non-radical ROS include hydrogen peroxide (H_2O_2), hypochlorous acid (HOCl), and nitrous acid (HNO_2).[56]

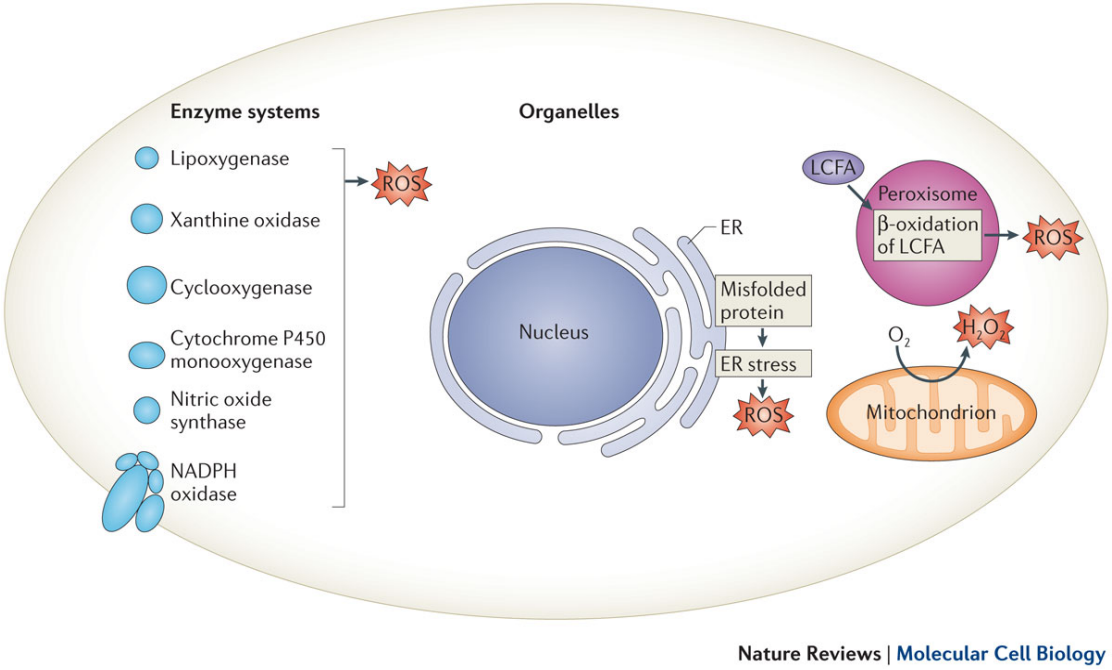

Figure 1.1 Enzymatic and non-enzymatic intracellular sources of reactive oxygen species (ROS). ROS are generated within various cellular organelles. These include the mitochondria (electron transport chain), endoplasmatic reticulum (ER; particularly in the setting of ER stress) and peroxisomes (during catabolism of long-chain fatty acids (LCFA)). In addition, various enzymes, including oxidases and oxygenases, generate ROS as part of their enzymatic reaction cycles. Reprinted with permission from Macmillan Publishers Limited: *Nat Rev Mol Cell Bio* (Cellular mechanisms and physiological consequences of redox-dependent signaling. Holmström and Finkel[57]) Copyright 2014. doi: 10.1038/nrm3801.

ROS are produced in all cells as a normal by-product of metabolic processes, whether it be *via* non-enzymatic or enzymatic routes[57] (Figure 1.1). The main endogenous non-enzymatic source of ROS is the mitochondrial respiratory chain. Most intracellular ROS are derived from superoxide ($O_2^{\bullet -}$),[58] which is generated by the one electron reduction of O_2 from the electron transport chain.[59] The endoplasmic reticulum (ER) constitutes another source of ROS production as it provides an oxidizing environment that favours disulphide bond formation and protein folding. Another organelle in which ROS are generated as integral feature of their normal metabolism is peroxisome,[60] where organic peroxides are generated as normal products of the biological reduction of molecular oxygen in the process of β-oxidation of long-chain fatty

acids.[59] In addition, ROS, more specifically superoxide, are produced not as byproducts but as the primary function of NADPH oxidase complex, a membrane-bound enzyme system which catalyzes conversion of oxygen to superoxide, as an integral part of innate immune response of phagocytes against invading microorganisms.[61]

Since there are many active endogenous sources of ROS, in addition to all exogenous sources (pollution, alcohol, radiation, heavy metals, certain drugs[56] – to name a few) it is clear that, if left intact, this accumulated ROS burden will become detrimental to cell survival as excess ROS can result in disruption of biological function due to irreversible damage to DNA, proteins and lipids.[56] ROS have a plethora of downstream effects, depending on the concentrations at which they are present and therefore the balance between production and scavenging of ROS is of critical importance.[62] The cellular redox balance is maintained by a battery of antioxidant systems that is comprised of enzymatic antioxidants such as superoxide dismutase (SOD), catalase, peroxiredoxins (Prxs), thioredoxins (Trx), and glutathione peroxidases (GPx), as well as non-enzymatic antioxidants, which include glutathione (GSH), Vitamin C (ascorbic acid), Vitamin E (α-tocopherol), carotenoids, and flavonoids.[63] The action of antioxidants can have both beneficial and detrimental effects on cell survival, particularly in the case of cancer cells, depending on which step in the process of maintaining redox balance they step in: on the one hand, neutralizing ROS can reduce DNA damage and thus genetic instability; on the other hand, decreasing ROS burden on the verge of the limit for triggering cellular senescence or death can in fact contribute to cell survival – or in the case of cancer, tumourigenesis[57] (Figure 1.2).

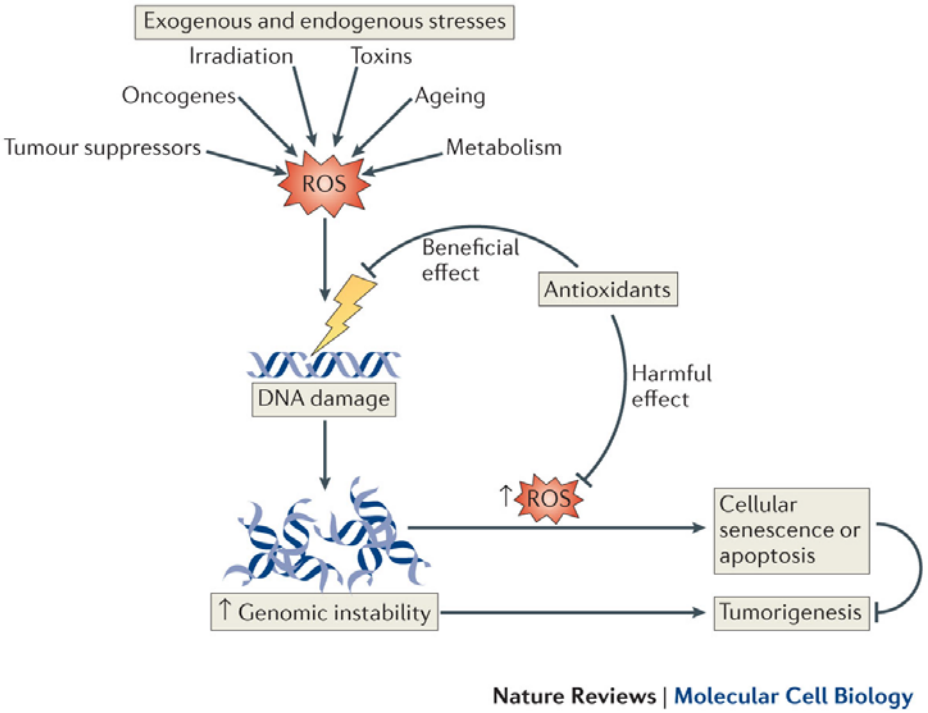

Figure 1.2 Antioxidants can have both beneficial and harmful roles in tumourigenesis. ROS result from various endogenous and exogenous factors, and can contribute to genomic instability by damaging DNA. If the accumulation of ROS is too high, this can trigger cellular senescence and apoptosis, which limit genetically damaged cells from further proliferation and hence limit tumour formation. Antioxidants can function in two separate but antagonistic parts of these pathways. They can be beneficial to cell survival by neutralizing ROS and thereby preventing further DNA damage. Conversely, antioxidants can contribute to tumorigeneris by enabling cells to withstand the induction of senescence or apoptosis. Reprinted with permission from Macmillan Publishers Limited: *Nat Rev Mol Cell Bio* (Cellular mechanisms and physiological consequences of redox-dependent signaling. Holmström and Finkel[57]) Copyright 2014. doi: 10.1038/nrm3801.

1.3.2 Function of reactive oxygen species in normal and cancer cells

At low to moderate levels, ROS play a crucial role in various signalling pathways to support cellular proliferation and differentiation, or to engage in stress-response survival pathways to ensure cell survival. Production of ROS can be promoted by cytokines and growth factor receptor signalling to act as second messengers that propagate molecular signals to downstream effectors.[64,65] For example, ROS act as inhibitors of protein phosphatases such as PTEN and PTP1B, as well as activators or Src family kinases and MAPK.[53,66–69] Furthermore, the role of ROS in cell signalling extends downstream to the regulation of nuclear transcription

factors, including AP-1, NF-KB, p53, and HIF-1, thus influencing a myriad of cellular processes.[64] However, excessive amounts of ROS can have deleterious effects on macromolecules including DNA, RNA, lipids and proteins, which can gradually lead to the onset of disease states including cancer, neurodegenerative diseases, atherosclerosis and the aging process itself.[57,62,70] Also, high concentrations of ROS can induce cellular senescence and/or apoptosis.[71,72] Therefore, modulation of ROS homeostasis is fundamental in maintaining normal cellular function,[73] and it is of particular importance in diseased state, such as in cancer cells, whose survival and progression is greatly influenced by a various pathways in which ROS act as signalling molecules (Figure 1.3).

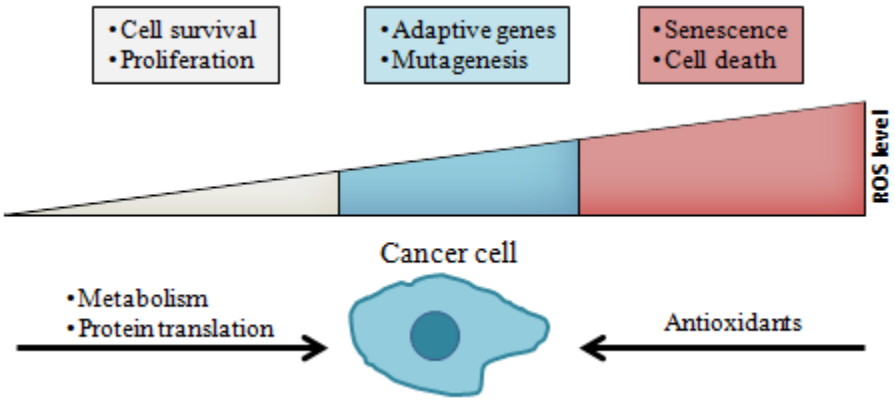

Figure 1.3 Redox regulation is crucial for physiological outcomes and cancer cell proliferation and survival. ROS have a variety of functions depending on concentration. Redox balance is crucial for cell survival. Modified from Macmillan Publishers Limited: *Nat Rev Can* (Regulation of cancer cell metabolism. Cairns, Harris & Mak[62]) Copyright 2011. doi: doi: 10.1038/nrc2981.

1.3.2.1 ROS-response mechanisms in cancer

ROS activity is related to several mechanisms underlying cancer. These can be crudely divided into three main categories: promoting oxidative stress; contributing to cancer pathophysiology by regulating several redox sensitive signalling pathways; and ROS-dependent modulation of the hallmarks of cancer.

The imbalance between the production of ROS and their elimination by antioxidants results in oxidative stress,[59] and it leads to damage of important biomolecules and cells, with potential to impact the whole organism. High levels of ROS are generally detrimental to cells,

whether they be normal or cancerous, however the redox status of cancer cells differs from that of normal cells.[74] Cancer cells are deemed to be less sensitive to high levels of ROS than normal cells[59] due to the fact that cancer cells have upregulated antioxidant mechanisms that protect them against ROS.[74,75] With this reduced sensitivity to ROS, cancer cells are capable of enduring higher levels of oxidative stress than normal cells, which gives them another prominent characteristic.[62,74]

The MYC and RAS proto-oncogenes, when activated, contribute to genesis of many cancers.[76–80] As a result of this activation, cancers cells are stimulated to proliferate and grow uncontrollably and hence their metabolic rates and energy demands are increased – which results in increased production of ROS. Consequently, the master regulator of antioxidant response element, Nuclear factor erythroid 2-Related Factor 2 (NRF2), is stimulated to enable the cancer cells to undergo extensive metabolic reprogramming to ensure adequate availability of a non-enzymatic antioxidant, NADPH.[78,80] This reprogramming, in turn, supports proliferation and promotes survival of cancer cells.

Another example of how oxidative stress affects signalling pathways is presented by a study that delineated a relationship between phosphatidylinositol-4,5-bisphosphate-3-kinase (PI3K) signalling and the NRF2 –regulated antioxidant response in human breast cancers.[81] Gorrini and colleagues demonstrated that dysregulation of PI3K-AKT signaling, whether it be due to estrogen stimulation or oncogenic stimulation, results in upregulation of NRF2 gene targets associated with GSH biosynthesis to support resistance to oxidative stress, initiation of anchorage-independent growth, and tumour spheroids.

In addition to helping cancer cells resist cell death and deregulate cellular energetics, promoting genome instability and tumour-promoting inflammation, examples of which were discussed above, oxidative stress contributes to a few more cancer-defining hallmarks. For instance, compelling evidence suggests that oxidative stress plays a key role in activating invasion and metastasis as well as inducing angiogenesis. There is significant experimental evidence for the existence of positive feedback loops between ROS and growth factor (GF) activation (vascular endothelial (VEGF), platelet-derived (PDGF), hepatocyte (HGF)) as well as between ROS and integrin signalling, which is a key contributor to cancer cell invasion leading to metastasis.[82] Alternatively, ROS participates in cancer cell motility and invasion through

proteolytic degradation of glycosaminoglycan and other components of the extracellular matrix such as through the induction of various matrix metalloproteases.[82]

1.3.3 Detection of intracellular ROS

Presently, ROS-sensitive fluorescent probes are one of the fastest, most user-friendly and accessible methods for monitoring ROS production in live cells.[83] Usually, non-fluorescent precursors diffuse into cells, oxidize upon reacting with ROS and form intermediate probe-derived radicals that generate fluorescent products.[84] This fluorescent emission can then be assessed by flow cytometry, a standard fluorescence plate reader or fluorescence microscopy using appropriate filter.[85] There are several approaches used to detect and characterize different ROS, a few of which are discussed herein and outlined in Table 1.3 along with their emission and excitation wavelengths.

Dihydroethidium (DHE) is the reduced form of ethidium bromide and it is known to be the most specific fluorescent probe for superoxide detection.[86] DHE passively diffuses into cells where it reacts with cytosolic superoxide, which causes it to form a red fluorescent product, 2-hydroxyethidium.[87] The downside of this probe, however, is that aside from reacting with cytosolic superoxide, DHE can also be oxidized by cytochrome *c* and it can undergo unspecific oxidation by $ONOO^-$ or •OH into enhidium.[88] Fluorescence spectra of ethidium and 2-hydroxyethidium differ very slightly and are thus indistinguishable by fluorometric measurements, which is why the result interpretation should be performed with caution when using DHE for monitoring superoxide production.

MitoSOX Red dye is used to measure superoxide production in the mitochondrial matrix.[83] Being a cationic derivative of DHE, MitoSOX Red exhibits similar behaviour as DHE, with the difference that its reaction with superoxide radicals is faster and it is rapidly targeted to the mitochondria, where it is oxidized to form 2-hydroxymitoethidium.[89] The main limitation of this probe is its potential to cause cyto- and mito-toxicity, and to cause alterations of mitochondrial morphology and redistribution of fluorescence to the nuclei at higher probe concentrations.[88] In addition, and similarly to DHE, MitoSOX Red can also undergo unspecific reactions with other oxidants to form mito-ethidium, whose fluorescence peak overlaps with that

of 2-hydroxymitoethidium.[87] Therefore, is it recommended that for more detailed and complex analyses, additional methods such as fluorescence spectroscopy be used.

5-(and 6)-chloromethyl-2',7'-dichlorohydrofluorescein diacetate (CM-H_2DCFDA) is known as a hydrogen peroxide-detecting probe for the measurement of hydrogen peroxide in intact cells,[83] however, the range of the oxidative species it detects is much broader. It has been shown that CM-H_2DCFDA reacts with hydroxyl and peroxyl oxidative radicals, as well as with reactive nitrogen species (RNS) such as NO• and $ONOO^-$.[88] Therefore, it has been suggested that this probe should be used as an indicator of the degree of general oxidative stress,[90] rather than as a gauge specific for ROS-production monitoring. CM-H_2DCFDA is a modified version of the original compound, dichlorohydrofluorescin diacetate (DCFDA), allowing for a longer retention inside the cells, as the added chloromethyl group enables covalently bind to intracellular components.[85,91] Otherwise, the principle behind using this probe is the same: CM-H_2DCFDA diffuses into cells where it is cleaved by intracellular esterases forming a nonfluorescent product, which is then trapped intracellularly, and whose subsequent oxidation yields the highly fluorescent dichlorofluorescin (DCF).[92] Accumulation of DCF in cells may be measured by an increase in fluorescence, which is proportional to the increase in cytosolic ROS levels.

Despite criticism and the limitations described in the literature, the presented methods can be useful for rapid screening experiments to provide an overview of general ROS production.[83] As CM-H_2DCFDA is extremely sensitive to changes in the redox state of a cell and can be used to follow changes in ROS over time, we chose to use it for the purposes of monitoring intracellular oxidative stress in Chapter 2 of this study.

Table 1.3 Fluorescent probes used to detect ROS with the use of microplate reader. Modified from Wojtala *et al.* (2014).[83]

Probe	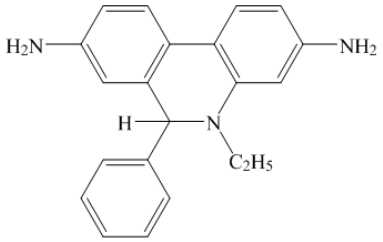 **Dihydroethidium (DHE)**	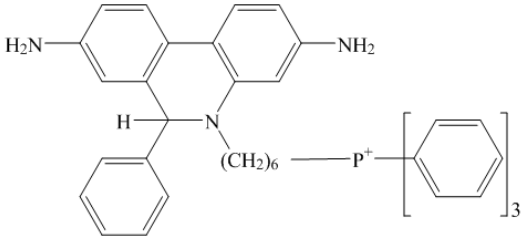 **MitoSOX Red**	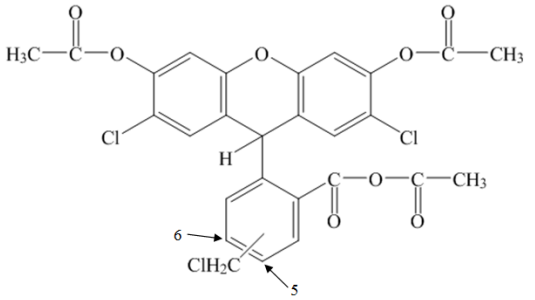 **CM-H_2DCFDA**
ROS detected	Primarily cytosolic superoxide, but also $ONOO^-$, •OH, $•NO_2$, H_2O_2 and M^+-based oxidants[70]	Mitochondrial superoxide, but also other oxidants	H_2O_2 but also $•O_2^-$, •OH, carbonate radical, NO•, $ONOO^-$ and NO_2[70,88]
λ_{ex} / λ_{em}	535/635 nm	510/595 nm, alternatively: 400/595 nm	~492–495 / 517–527 nm
Fluorescent product(s)	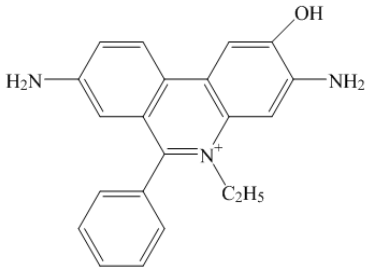 2-Hydroxyethidium 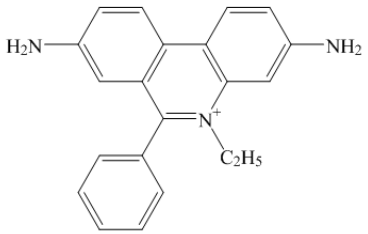 Ethidium	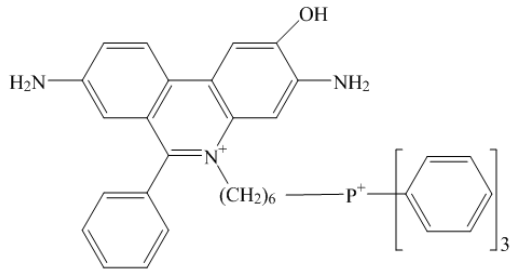 2-Hydroxy-5-(triphenylphosphonium) hexylethidium (2-hydroxymitoethidium) 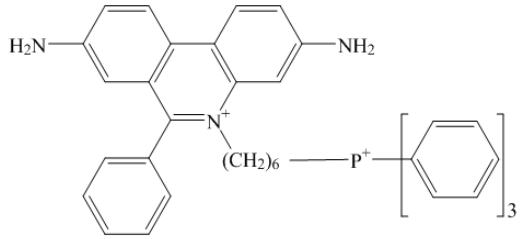 Mito-ethidium	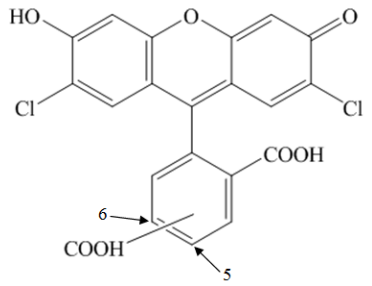 Dichlorofluorescein (DCF)

1.4 Physiological function of system x_C^- in cancer

System x_C^- is a transmembrane transporter of cystine and glutamate. The directionality of substrate trafficking is concentration-dependent and thus, due to high intracellular glutamate concentrations, normally a molecule of cystine is imported across the plasma membrane in exchange for a molecule of glutamate.[93–96] System x_C^- has three major physiological functions. It plays a crucial role in cellular protection from oxidative stress and xenobiotics by mediating cellular uptake of cystine which is necessary for GSH synthesis. In addition, the x_C^- antiporter is instrumental in maintaining the redox balance between extracellular cystine and cysteine,[97] which is the major disulfide/thiol redox couple in human plasma.[98] More recently, it has been reported that system x_C^- plays a role in regulation of non-apoptotic form of regulated cell death, termed ferroptosis.[99]

1.4.1 System x_C^- as a marker of oxidative stress

To cope with endogenous and exogenous stresses caused by ROS and other electrophiles, cancer cells undergo substantial gene expression changes. Nuclear factor erythroid-2-related factor (NRF2) – antioxidant response element (ARE) (NRF2-ARE) signalling pathway is the principal regulator of this homeostatic response.[79] Under basal conditions, NRF2 is dimerized with Kelch ECH associating protein 1 (KEAP1) and continuously targeted for degradation *via* ubiquitination by CuI3[100] (Figure 1.4). Under oxidative stress, electrophiles and antioxidants disrupt this NRF2-KEAP1 dimerization either by enabling phosphorylation of NRF2 at Ser-40 by protein kinases or by modifying cysteine residues (Cys-151, Cys-273 and/or Cys-288) on the KEAP1 active site.[100] This results in nuclear translocation of NRF2. Once in the nucleus, NFR2 binds to an adaptor protein (Maf or ATF4) and acts as a transcription factor driving the expression of ARE-driven genes, including solute carrier family 7 member 11 (*SLC7A11*) which encodes the cystine/glutamate transporter xCT.[79,100–103]

xCT is a light chain subunit of an anionic amino acid antiporter protein system x_C^-.[97,104] System x_C^- was first described by Bannai and Kitamura, as sodium-independent antiporter of cystine and glutamate, in 1:1 stoichiometry[94,95,105] (Figure 1.5A). xCT imparts the substrate specificity of system x_C^- and it maintains very low basal expression in most normal tissue,[93,106]

with the exception of the thymus, pancreas, spleen and brain, but it is universally upregulated as cells respond to oxidative stress.[102] As a member of the heteromeric amino acid transporters, xCT is paired up with a heavy chain subunit 4F2hc, encoded by solute carrier family 2 member 3 (*SLC2A3*), which serves for stabilisation and membrane localization. 4F2hc is an integral membrane protein with a single-membrane spanning domain, classified as a type II membrane glycoprotein.[107] Aside from xCT, it has been associated with many other light chain subunits forming a number of amino acid transporters with different substrate specificities. Systems L, y^+L, x_C^- and ASC have been shown to require 4F2hc for their functional expression.[107]

Literature reports show that the activity of system x_C^- is associated with xCT expression,[93,103] which plays a vital role in intracellular ROS modulation and maintaining redox balance. System x_C^- is the primary cellular source of intracellular cystine,[100] which upon import into the cell is reduced to cysteine, the rate-limiting precursor for the synthesis of GSH,[74] which is important for the maintenance of intracellular redox balance and protection from oxidative stress.[93,108] Upon the upregulation of xCT as a result of oxidative stress, an influx of cystine results, which is then reduced to cysteine, hence enabling the cell to meet the demand for GSH synthesis (Figure 1.4). System x_C^- is thus believed to be cellular oxidative stress marker imaging of which could potentially be used as an *in vivo* reporter for ARE activation.[102]

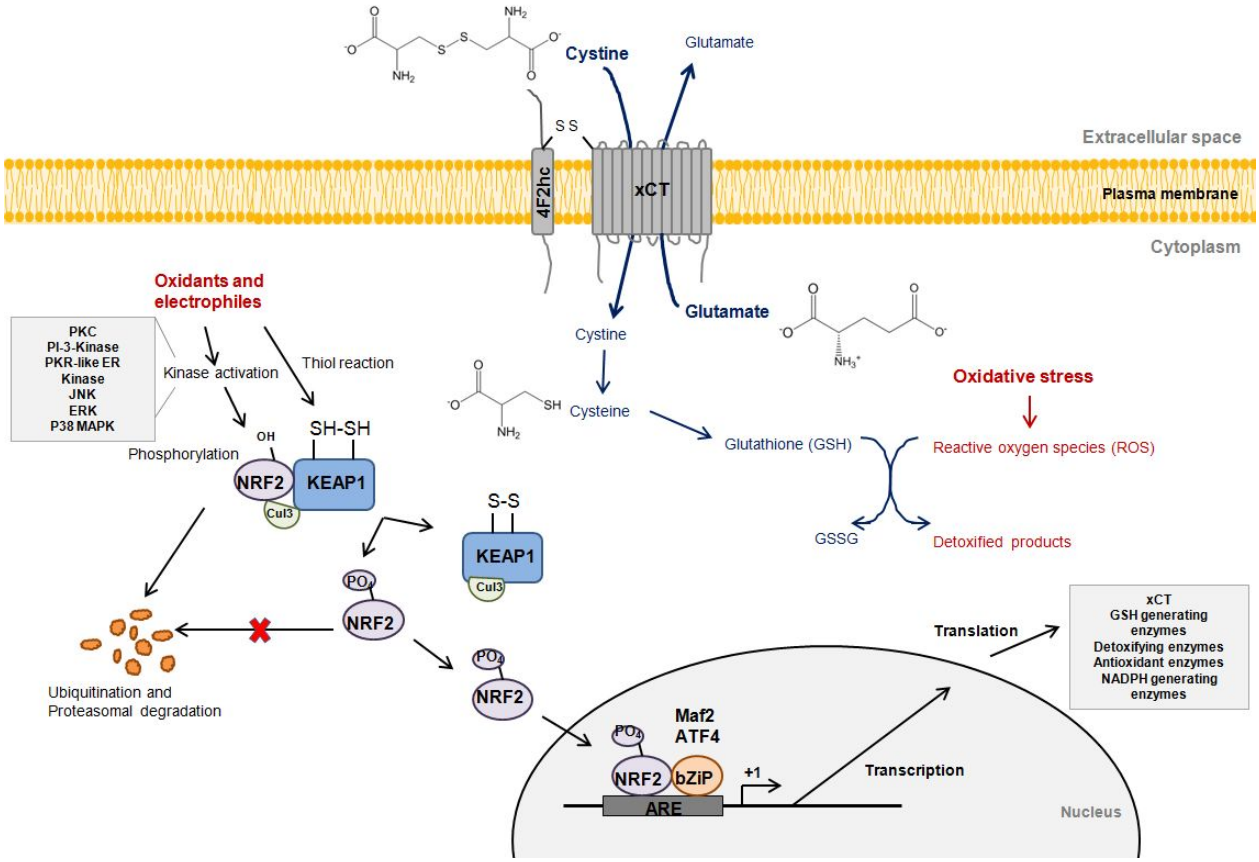

Figure 1.4 Cellular mechanism of xCT expression induced by oxidative stress and promoting increased glutathione synthesis. Adapted from Webster *et al.*[102] and Bridges *et al.*[100]

1.4.2 Biochemical structure of system x_C^-

System x_C^- is a heterodimeric protein comprised of two subunits: a cell surface glycoprotein 4F2hc (also known as CD98), and xCT – the light chain subunit[104,108] (Figure 1.5A). 4F2hc, heavy chain of the surface antigen 4F2, is less hydrophobic and contains a single transmembrane domain which is, presumably, incapable of the transport activity by itself.[104,109] It is connected to the light chain subunit by a disulfide bridge between Cys-109 residue of 4F2hc and Cys-158 residue of xCT.[104,110] Human xCT protein is made up of 501 amino acids,[111] is highly hydrophobic and it spans across the plasma membrane *via* twelve domains[104] with intracellular N- and C- termini.[97,100] The re-entrant loop between 2nd and 3rd transmembrane domain is believed to participate in substrate binding.[109,112] In addition, it was found that Cys-327 residue in the 8th transmembrane domain of xCT is functionally important, because it is

accessible from the aqueous extracellular compartment and structurally linked to the permeation pathway and/or substrate binding site.[112] Figure 1.5B shows a homologous structure for xCT that was constructed by threading the human xCT sequence through the ApcT (amino acid, polyamine, organo-cation transporter) structure.

1.4.2.1 Maintenance of cystine/cysteine redox cycle

Substrate profile of system x_C^- is narrow, involving only two amino acids, cysteine and glutamate, trafficking direction of which is determined by the concentration gradient of each substrate. Glutamate is more abundant intracellularly than in the extracellular space, since it is actively taken up by excitatory amino acid transporter (EAAT) protein family. In contrast, the intracellular pool of cystine is negligibly small because the disulfide is rapidly reduced once inside the cell. Hence, system x_C^- generally imports cystine while exporting glutamate.[113] The reduction of cystine takes place due to the action of thioredoxin reductase 1 and/or GSH itself. The resulting cysteine can be exported into the extracellular space *via* system ASC.[113]

This cycle of cystine uptake by system x_C^-, its intracellular reduction, and subsequent export by system ASC seems to be the mechanism through which cells modify the redox state of the extracellular cystine/cysteine redox cycle.[113] This regulation seems to be vital, as a more oxidized redox state of the cysteine/cystine redox couple in human plasma is associated with risk factors for cardiovascular diseases. Cell and rodent studies indicate that the extracellular cysteine/cystine redox state can play a vital role in controlling cardiovascular disease through proinflammatory signalling.[98] xCT knockout mice ($xCT^{-/-}$) have been reported to have a more oxidized state of the cysteine/cystine redox couple in their plasma, and thus system x_C^- activity seems to be crucial for maintenance of cystine/cysteine redox balance.[114]

1.4.2.2 Regulation of ferroptosis

Ferroptosis is a unique iron-dependent type of cell death, different from apoptosis, necrosis and autophagy, in that it is characterized by the accumulation of intracellular soluble and lipid reactive ROS.[99,115] It was found that inhibition of cystine uptake *via* system x_C^- with known inhibitors sulfasalazine and erastin induced ferroptotic cell death by inducing intracellular accumulation of lipid hydroperoxides in an iron-dependent manner.[115,116] Normally, these lipid

hydroperoxides are converted to lipid alcohols by the action of glutathione peroxidase 4 (GPX4).[116] Since GSH is used for this process, ferroptosis can be induced by cystine deprivation and/or pharmacological inhibition of system x_C^-. Therefore, by importing cystine and promoting GSH biosynthesis, system x_C^- prevents accumulation of lipid peroxides and protects cells from undergoing ferroptosis.[116]

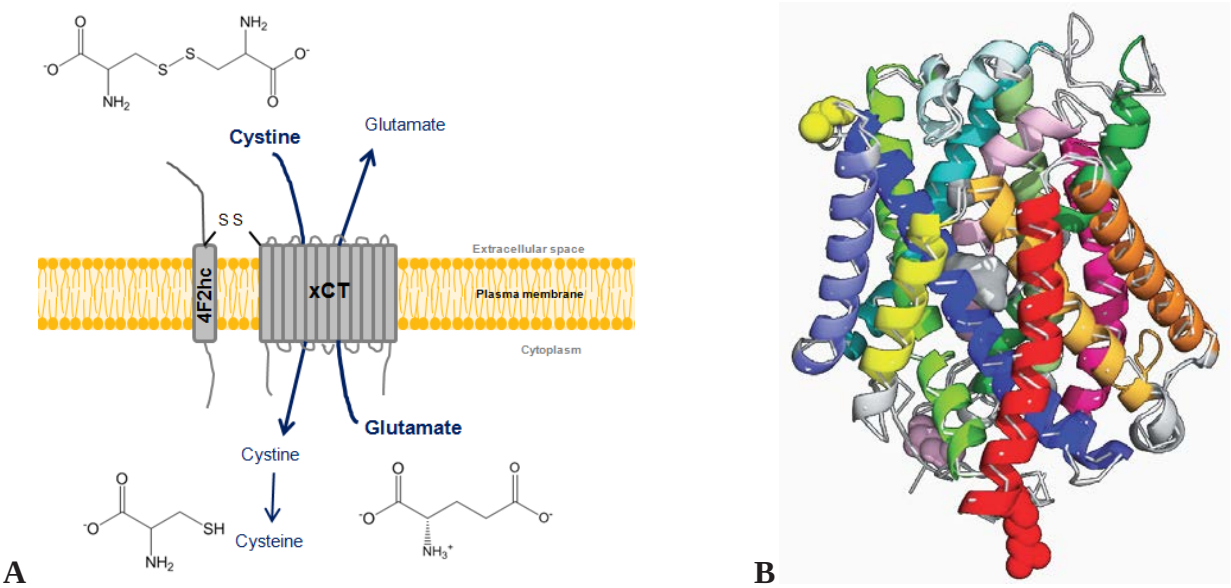

A **B**

Figure 1.5 A Graphic representation of system x_C^-. B Crystal structure of human xCT: an xCT homology model was constructed by threading the human xCT sequence over the crystal structure of ApcT structure from the thermophile *Methanocaldoccus jannaschii* as reported by Goaux and co-workers[117] using FASTA[118] followed by multiple sequence alignments with ClustalW.[119] The structure of ApcT is shown as a white thread overlayed with the helical ribbons of the 12 transmembrane domains (TMDs) of xCT: TMD 1A/B in light pink; TMD2 in dark pink; IL1 in dark blue; TMD3 in bright blue; TMD4 in light purple; TMD5 in teal, TMD6A/B in dark green; TMD7 in olive green; EL4A/B in silver; TMD8 in light green; TMD9 in yellow; TMD10 in gold; TMD11 in orange and TMD12 in red. Truncated intracellular N (light pink) and C (red) termini are shown with spheres. The Cys-158 that participates in the disulphide bond with 4F2hc is highlighted with yellow spheres. The protein is shown in its inwardly facing Apo-form. A hypothetical substrate is depicted by the centrally located white surface as predicted by Shaffer *et al.*[117] Reprinted with permission from Bridges *et al.* (2012).[100]

1.4.3 Regulation of system x_C^- activity and abundance

In addition to oxidative stress, amino acid deprivation and xenobiotics have been shown to trigger the upregulation of system x_C^-.[95,120] For example, system x_C^- activity can be induced by cystine depletion and by agents that reduce intracellular GSH, like oxidants, electrophilic agents (e.g., diethylmaleate (DEM)), and γ-glutamylcysteine synthetase (γ-GCS) inhibitors.[105,113] This upregulation is, at least in part, mediated by the ARE.[105] Moreover, there have been reports suggesting that system x_C^- activity is also regulated by NF-kB (nuclear factor kappa-light-chain-enhancer of activated B cells) transcription factor, which plays a central role in regulation of numerous genes involved in cellular defense mechanisms and cytokine production.[108] Both ARE and NF-kB binding sites have been identified in the of *SLC7A11* (xCT) promoter.[105] More recently, Lim and colleagues reported that xCT is essential for RAS-induced tumourigenicity by enhancing GSH synthesis. Their results uncovered that the oncogenic RAS activation promotes the transcription of *SLC7A11* in response to oxidative stress, by a synergistic cooperation between ETS-1 transcription factor downstream of the RAS-RAF-MEK-ERK signalling cascade and ATF4.[121]

It is thought that ROS act as intermediate second messengers involved in the activation of NF-κB by interleukin-1b (IL-1b) and tumour necrosis factor alpha (TNFα),[108,113] however no detailed information about the intracellular signalling pathways involved has been published. Other inflammatory stimuli that strongly induce xCT expression and system x_C^- activity *in vitro* include lipopolysaccharide (LPS) and erythropoietin (EPO).[113,122] Sato and colleagues demonstrated that post-transcriptional regulation of xCT mRNA expression takes place in the cells primed with LPS under hypoxic conditions.[108]

1.4.4 Distribution of system x_C^- in normal tissues and malignancies

Under normal physiological conditions, system x_C^- expression is restricted to pancreatic islet cells, the central nervous system, thymus and spleen.[113] Northern blot analyses have identified very low or no expression of *SLC7A11* in heart, liver, lung and kidney.[113] xCT in the brain is highly expressed in astrocytes,[103] which protects neurons from damage[123] by maintaining neuronal GSH levels.[124] Moreover, embryonic neuronal/glial cultures rely on x_C^- activity to

remain viable.[125] It has been reported that the expression of xCT is induced in cultured cells, even though the organ of origin may not express xCT under normal physiological conditions.[113,126] There are two possible explanations for this induction: 1) the partial pressure of oxygen is higher under cultured conditions;[113] and 2) normal cell culture medium provides cysteine only in the form of cystine, which is primarily transporter *via* system x_C^-.[126]

Cancer cells possess higher levels of ROS compared with those of normal cells due to their rapid metabolic rates.[74,127] Therefore, it does not come as a surprise that system x_C^- expression and activity are upregulated in a number of different cancers including breast,[128] pancreatic[129] cancers and gliomas.[126] System x_C^- seems to play a key role in cancer cell survival, as inhibition of xCT *in vivo* lead to lymphoma tumour growth arrest in rats[130] and attenuation in triple-negative breast cancer (TNBC) xenograft growth in mice.[128] Furthermore, it was shown that xCT inhibition can sensitize patient-derived TNBC tumour samples to carboplatin *ex vivo*.[128]

1.4.5 Functional interactions of xCT

Recent reports indicate that, in addition to 4F2hc, xCT expression might be associated with two other transmembrane proteins: a tumour-associated antigen CD44v[131] and mucin-1 (MUC-1) transmembrane glycoprotein.[132] CD44 is a major adhesion molecule for the extracellular matrix and it plays a role in many physiological processes including leukocyte homing and activation, wound healing, and cell migration, as well as in tumour cell invasion and metastasis.[131] Its variant isoform CD44v is a marker of stem-like cancer cells (CSCs)[132] and it is shown to interact with the extracellular region of xCT and stabilize it at the plasma membrane.[131] Ishimoto and colleagues demonstrated that ablation of CD44v resulted in loss of expression of xCT and depletion of intracellular GSH, while the expression of 4F2hc remained unchanged.[131] MUC1-C is the oncogenic C-terminal subunit of MUC-1, intrinsically disordered oncoprotein, with a plethora of downstream cancer-driving effectors.[133] MUC1-C overexpression has been shown to induce anchorage-independent tumour growth, and self-renewal of breast cancer cells.[134] Moreover, MUC1-C has been linked to maintenance of redox balance and GSH regulation.[133] Hasagawa and colleagues showed that xCT/CD44v expression is correlated to MUC1-C expression, and that MUC1-C interacts with CD44v *via* its intracellular domain,[132] thereby promoting the stabilization of xCT in the plasma membrane in TNBC cells. The study

did not demonstrate the mechanistic nature of these interactions, nor did it exclude the possibility of a direct interaction between MUC1-C and xCT nor 4F2hc.

1.4.6 System x_C^- nuclear imaging agents

System x_C^- has become an appealing target for therapeutic and imaging purposes. In the past decade four ^{18}F-labeled tracers have been developed, with ongoing research on a number of other compatible structures. This section is meant to provide an overview of the different system x_C^- substrates for PET imaging that have been reported to date. Further characterisation and direct comparison of specific radiotracers will be discussed in subsequent chapters. The structures of the tracers discussed herein are shown in Figure 1.6.

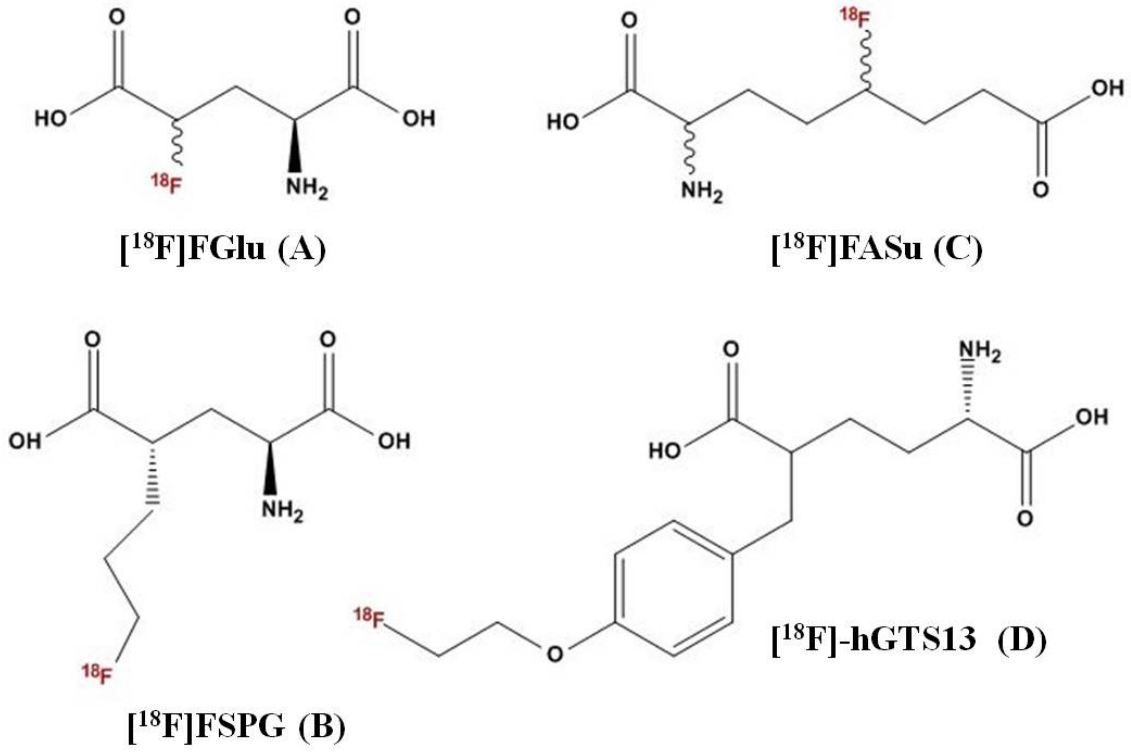

Figure 1.6 Chemical structures of A) ^{18}F-labelled 4-fluoroglutamate, B) (4S)-4-(3-fluoropropyl)-*L*-glutamate, C) 5-fluoroaminosuberic acid, and D) [^{18}F]-hGTS13.

1.4.6.1 4-[^{18}F]fluoroglutamate

4-[^{18}F]fluoroglutamate ([^{18}F]FGlu), also reported as (*2S*)-2-amino-4-[^{18}F]-fluoropentane dioic acid and BAY 85-8050) was the first reported system x_C^- specific PET tracer.[135] [^{18}F]FGlu is a derivative of glutamate which showed rapid and specific tumour cell uptake in the lung and colon cancer cells lines. Studies in healthy human volunteers demonstrated comparable dosimetry to that of [^{18}F]FDG[136] and had fast clearance from the peripheral blood and renal excretion.[137] However, [^{18}F]FGlu was not stable in humans and as early as 5 min after injection radiolabeled metabolites were detectable in plasma.[137] The reason for the instability was interpreted as a systemic metabolism in human subjects, with subsequent uptake of fluorinated metabolites and/or free fluoride in the bone.[138]

1.4.6.2 (*4S*)-4-(3-[^{18}F]fluoropropyl)-*L*-glutamate

The same group subsequently proposed another lead tracer candidate, (*4S*)-4-(3-[^{18}F]fluoropropyl)-*L*-glutamate ([^{18}F]FSPG, also reported as BAY 94-9392).[139] [^{18}F]FSPG is a glutamate derivative which was identified as the strongest uptake competitor of radiolabelled glutamate (4-[^{18}F]fluoroglutamate). The authors studied [^{18}F]FSPG in a dose-dependent manner for competition against both [^{14}C]*L*-cystine and [^{3}H]*L*-glutamate and reported IC_{50} values of 29.1 and 33.6 μmol/L, respectively. The tracer uptake was effectively blocked by system x_C^- substrates *L*-glutamate and *L*-cystine, as well as the inhibitor *p*-carboxy-phenylglycine (CPG). However, the authors also reported observing a minor competition with either *L*- or *D*-aspartate, both of which are substrates of the EAAT transporter family members 1-5 along with *L*-glutamate, thus indicating that [^{18}F]FSPG might also be a substrate of the EAAT transporters.[139] The uptake of [^{18}F]FSPG was investigated in an array of different cancer cells lines, and it ranged from 1% to 18% uptake of the applied dose per 100,000 cells in 30 min. Moreover, biodistribution analysis in rodents revealed that [^{18}F]FSPG is taken up by a variety of tumours *in vivo*, with 60 min uptake ranging from 2 to 4 percent injected dose per gram (%ID/g). The authors reported rapid blood clearance of [^{18}F]FSPG *via* the kidneys and low background activity (including the brain) providing high contrast for tumour imaging. Excellent visualisation on [^{18}F]FSPG-PET images of subcutaneous lung cancer xenograft and orthotopic glioblastoma

xenografts was achieved in animal models.[139,140] In the study with NCI-H460 (lung cancer) xenografts mice, [^{18}F]FSPG uptake reached 3.2 ± 0.4 %ID/g at 1 h post-injection (p.i.), and tumour-to-blood and tumour-to-muscle ratios of 14 and 27, respectively, at 1 h p.i.[139] In the preclinical study with orthotopic GS9L glioblastoma-bearing rats, [^{18}F]FSPG was compared to both [^{18}F]FDG and *O*-(2-[^{18}F]fluoroethyl) tyrosine ([^{18}F]FET). Even though the absolute tumour uptake values were comparable among the three tracers (~1.6 %ID/g for [^{18}F]FSPG and [^{18}F]FDG) and ~0.6 %ID/g for [^{18}F]FET), [^{18}F]FSPG had the highest tumour-to-brain ratio of 32.7, compared to 1.7 in the case of [^{18}F]FDG and 2.8 in the case of [^{18}F]FET.[140]

In contrast to its predecessor [^{18}F]FGlu, [^{18}F]FSPG was stable in humans; no fluorinated metabolites were present in plasma during examination up to 240 min after intravenous (i.v.) injection.[138] Pilot clinical studies on healthy volunteers, verified the preclinical biodistribution results: [^{18}F]FSPG accumulated in the kidneys, bladder, and pancreas, whereas no significant levels of accumulation in the brain, lungs, breasts, liver, spleen, and intestines were identified in healthy human subjects.[136] Rapid tracer clearance from the blood pool was apparent in all volunteers, and their laboratory blood tests were normal and unchanged during and after the administration of [^{18}F]FSPG. The estimated dose of [^{18}F]FSPG to the patient in this study was calculated to be 9.5 ± 1.0 mSv, which is comparable to the estimated dose of [^{18}F]FDG (5.7 mSv).[141] Exploratory clinical studies examining dosimetry and biodistribution and tumour detection in patients with breast, hepatocellular and non-small cell lung cancer showed promising results.[142,143] Furthermore, in a separate study, [^{18}F]FSPG-PET was able to identify small lung cancer metastases (1.3 and 1.7 cm) in the brains of two patients which were not evident on the [^{18}F]FDG-PET scan.[140] More recently, a clinical study from Taiwan reported successful identification of liver metastases with [^{18}F]FSPG–PET in 6/7 patients with stage III pancreatic ductal adenocarcinoma (PDAC), whereas the metastases were identified with [^{18}F]FDG-PET in only 5/7 patients.[144] This study also reported, however, that even though all primary PDAC lesions were [^{18}F]FDG-avid, they showed variable uptake on [^{18}F]FSPG–PET. Of particular interest to the research community is the potential to use [^{18}F]FSPG for imaging of intracranial malignancies, given that increased system x_C^- activity leads to accumulation of glutamate in the extracellular space causing a loss of glutamate homeostasis, tumour-associated seizures and neuronal death.[140] This promotes enhanced growth, survival, migration and invasion

of gliomas. A recent report demonstrated an association between *SLC7A11* expression in the brain and seizures and poor survival in patients with malignant glioma.[145]

1.4.6.3 [^{18}F]5-Fluoroaminosuberic acid

[^{18}F]5-Fluoroaminosuberic acid ([^{18}F]FASu) was first reported in 2014 by Webster and colleagues[102] as the most specific system x_C^- substrate out of a series of anionic amino acids of varying carbon chain lengths. This 8-atom carbon backbone "cystine – like" structure was evaluated further for preclinical evaluation of tumour xenografts. [^{18}F]FASu was reported to have system x_C^- specific uptake *in vitro,* as evidenced by uptake inhibition in the presence of the transporter's natural substrates *L*-glutamate and *L*-cystine, as well as the inhibitor sulfasalazine (SSZ). Webster *et al.* reported rapid *in vivo* clearance of the tracer and uptake by lymphoma and ovarian cancer xenografts with tumour-to-blood ratios of >12 and tumour-to-muscle ratios of >28. In a side-by-side comparison to [^{18}F]FDG in mice bearing ovarian cancer xenografts, [^{18}F]FASu showed a 5.2-fold greater tumour uptake and a 4.6-fold greater tumour-to-blood ratio.[102] Uptake of [^{18}F]FASu was much lower than that of [^{18}F]FDG in the muscle, heart, and brain. Three years later, the same group[103] tested the specificity of tracer uptake in the presence of a wide array of amino acid transporter (AAT) inhibitors and substrates, demonstrating through inhibition and *SLC7A11* knockdown studies that cells take up [^{18}F]FASu primarily *via* system x_C^-. The authors furthermore observed increased tracer uptake for *in vitro* and *in vivo* when the light chain subunit of the tracer, xCT, is overexpressed. The tracer was also shown to be taken up by three different breast cancer xenografts. The authors proposed that [^{18}F]FASu could have a use in monitoring system x_C^-activity *in vivo.*

[^{18}F]FASu uptake characterisation and significance is the major theme of this thesis, particularly of the Chapters 2, 3, 4 and 5.

1.4.6.4 [^{18}F]-hGTS13

The most recently reported system x_C^- - targeting tracer, [^{18}F]-hGTS13 is a racemic derivative of glutamate. *In vitro* evaluation of [^{18}F]-hGTS13 demonstrated positive correlation between the tracer uptake fluctuations to fluctuations in *SLC7A11* levels.[146] However, their

specificity assays indicated possible involvement of systems L and $B^{+,0}$ in the uptake of [^{18}F]-hGTS13. Preliminary preclinical studies with [^{18}F]-hGTS13-isomer2 (Figure 1.6D) report excellent H460 lung xenograft visualisation (6.3 ± 1.1 %ID/g) at 1 h p.i., higher than that of [^{18}F]FSPG (4.6 ± 0.7 %ID/g, p = 0.01). Despite the reported favourable increase in tumour uptake, [^{18}F]-hGTS13 also exhibits high liver uptake (4.6 ± 0.8 %ID/g at 1 h p.i., compared to 0.7 ± 0.01 %ID/g in the case of [^{18}F]FSPG), potentially limiting this tracer's application in hepatocellular carcinoma, where [^{18}F]FSPG has shown utility.[146,147]

1.5 Breast cancer

Breast cancer is the third most common cancer in Canada, accounting for 13% of all cancers and 25% of cancers among females.[38] Breast cancer is the second leading cause of cancer deaths of Canadian women[38] and first worldwide,[148] accounting for 13.1% and 14.7% of cancer deaths among women in Canada and globally, respectively. Canadian women are more likely to develop breast cancer than any other cancer, with 1 in 8 females expected to develop cancer in their lifetime.[38]

Breast cancer arises from abnormal increase in the growth of the epithelial cells in the ducts and lobules of the breast.[149] It is referred to as ductal carcinoma *in situ* as long as it resides in its normal place in the ducts and lobules and does not invade other tissues. This localized carcinoma can be treated with surgical resection with excellent prognosis.[149] Once the cancerous cells have broken through the basal lamina, they are considered invasive and may have a more aggressive, potentially lethal phenotype.[150] Based on the disease type, stage, level of differentiation and molecular markers breast cancers can be treated with targeted therapy, surgery, chemotherapy, hormone therapy, radiation therapy and immunotherapy.[151]

Breast cancer is a heterogenous complex of diseases which can be classified based on biological characteristics, histological grade and molecular profile.[152] With the advances in molecular biology and development of gene expression profiling (GEP), breast cancers can be classified into distinct classes based on their molecular characteristics,[152] which are not evident in or representative of certain histological features, hence enabling physicians to develop patient-tailored treatment strategies. The four molecular subtypes are: Luminal A, Luminal B, human epidermal growth factor 2 (HER2)-enriched and Basal-like[152,153] (Table 1.4). As GEP is not

readily available to all patients, traditional histological biomarkers such as progesterone receptor (PR), oestrogen receptor (ER) and HER2 are often used to stratify patients.[152,153] In addition, Ki67, or proliferating nuclear antigen,[154] is also used in further disease stratification, as it is a proliferative and prognostic marker in breast cancer patients and it has been linked to poor patient prognosis, particularly in patients with triple-negative breast cancer (TNBC)[155] or breast cancer negative for the following histological markers on immunohistochemical (IHC) staining: ER-/PR-/HER2-.

Table 1.4 Breast cancer subtypes and clinicopathological biomarkers.[152]

Molecular subtype	Incidence	Histological grade	IHC markers	Treatment
Luminal A	50-60%	low	ER+ and/or PR+ HER2- low Ki67	hormonal therapy
Luminal B	15-20%	high	high Ki67 ER+/HER2- ER+/HER2+ ER-/HER2- (6%)	chemotherapy
HER2 -enriched	15-20%	high	HER2++ PR- ER- or ER+ (low levels) high Ki67	chemotherapy, trastuzumab
Basal-like	8-37%	high	ER-/PR-/HER2- high Ki67	radiation, chemotherapy

1.5.1 Triple-negative breast cancer

Basal-like breast cancers are associated with high histological and nuclear grade, poor tubule formation, the presence of central necrotic or fibrotic zones, and have exceptionally high mitotic and proliferative indices.[152] These cancers are known to rapidly metastasize to brain and lungs and have meagre prognosis.[156] Most basal-like breast cancers are negative for ER, PR and HER2 receptors and thus “basal-like” and “triple negative” designations were previously used interchangeably. It is important to note that these terms are not synonymous and that there is

about 20 – 30% discordance across studies.[152] The "basal-like" subtype is defined *via* GEP in the research setting, whereas the term "triple-negative breast cancer" (TNBC) refers to the IHC staining of breast tumours lacking the expression of ER, PR and HER2, and remains a classification used in the clinical setting.[152]

TNBCs account for approximately 15% of all breast cancers.[157] . They are most common in African-American women, younger women and *BRCA1* mutation carriers.[157] TNBC is a very aggressive subtype of breast cancer, with very short time (7–12 months) from diagnosis to metastasis compared to other breast cancers.[158] Furthermore, the rate of recurrence of TNBC is significantly higher than that of hormone receptor-positive breast cancer,[157] and relapse-free survival and overall survival rates of patients with TNBC are lower than that of patients with non-triple negative breast cancer.[159] Given a lack of targeted therapy such as adjuvant hormonal therapy and HER-2 targeted agents, chemotherapy remains the standard of care for most TNBC patients. It is uncertain whether the reason for the poor prognosis for TNBC is due to its aggressiveness or because of lack of targeted therapy.[159] Nevertheless, the research community remains persistent in search for different biomarkers that could become useful targets for more effective TNBC therapy and/or indicators for earlier disease diagnosis.

1.5.1.1 PET imaging of TNBC

Molecular imaging with PET can detect biochemical changes within the tumour, even when they are not apparent morphologically e.g., when tumour size does not change. Perceiving such changes early on during the treatment course, can potentially help physicians assess early treatment response.[160] [^{18}F]FDG-PET has shown to be of great value in early assessment of breast cancer therapy, particularly in the case of HER2^{+} breast cancer patients treated with neoadjuvant HER2-directed therapy when given chemotherapy.[160,161] For these patients, early metabolic response on [^{18}F]FDG-PET was shown to be indicative of higher likelihood of pathologic complete response.[161]

Given the propensity of TNBC for early metastasis, accurate disease staging and prognosis can be of great help to clinicians when deciding the course (surgery, radiation, or chemotherapy) or purpose (curative or palliative) of treatment. Based on The 2016 National Comprehensive Cancer Network guidelines, systemic staging with [^{18}F]FDG-PET is

recommended, in addition to standard staging, for patients with newly diagnosed stage III non-operable breast cancer.[162] However, a retrospective study demonstrated that patients with the aggressive TNBC benefit from [^{18}F]FDG-PET/CT staging at least as early as stage IIB.[163] A substantial percentage (15%) of patients with initial stage IIB TNBC were upstaged to stage IV by [^{18}F]FDG-PET/CT.[163] These patients had lower survival rates compared to the rest of the patients from the originally determined IIB group, which is consistent with the increased burden of stage IV disease.[163] The value of this finding is in treatment repurposing – switching to palliative chemotherapy without surgery; which in future should prevent unnecessary breast surgeries as well as toxicities from intensive, curative-intent neoadjuvant and adjuvant chemotherapy.[163] Another study with [^{18}F]FDG-PET reported higher sensitivity in detecting TNBC, as compared to non-TNBC.[164] In addition, the authors demonstrated correlation between [^{18}F]FDG uptake in TNBC and proliferation index (Ki67), and thus higher histological grade and worse prognosis.

1.5.2 System x_C^- in breast cancer

System x_C^- has emerged as a compelling therapeutic target for TNBCs. Timmerman *et al.* were the first to report increased *SLC7A11* expression in TNBCs, along with increased cystine/glutamate exchange activity and deleterious effects of xCT inhibition on cancer cell growth.[128] A prior study of patient samples indicated that the aggressive triple-negative disease phenotype was associated with high oxidative stress levels.[165] These findings support the notion that the molecular signature of breast tumours is associated with its capacity on generating oxidative stress at the systemic level, which may in turn explain the ability of TNBCs to rapidly acquire resistance to standard chemotherapeutics which act in an anti-neoplastic manner by exerting profound redox changes by generating high levels of oxidative stress.[166]

With this in mind, the main hypothesis is that the system x_C^- – specific PET tracer, [^{18}F]FASu, can be a useful tool for TNBC imaging, and that it will be an indicator of intracellular redox changes that take place in response to therapy. Additionally, we hypothesize that [^{18}F]FASu-PET will provide useful information about the redox state of the lesion, which may serve as an indicator of patient prognosis, and may complement findings from [^{18}F]FDG-PET scans.

1.6 Amino acid transporters as targets for molecular imaging of cancer

Amino acid transport across the plasma membrane is mediated *via* specific membrane associated carrier proteins known as amino acid transporters (AATs). AATs are encoded by the solute carrier (*SLC*) gene family which is subdivided into smaller families.[167,168] More than 20 different AATs have been identified, and they can be classified based on their substrate specificity, transport kinetics, pH sensitivity, Na^+ dependency, H^+ dependency, tissue expression patterns and sensitivity to different inhibitors.[167,169] A number of these transporter proteins such as systems L, A and ASC are ubiquitously expressed,[169] as their substrates are crucial for normal functioning of cells, however aberrant overexpression of these and other classes of AATs (including system x_C^-) has been well documented in several cancer types.[126,128,129,167,170] The increased demand for amino acids by tumour cells as compared to normal cells makes AATs compelling drug targets for therapy and molecular imaging of cancer.

1.6.1 Amino acid radiopharmaceuticals

There is compelling evidence that amino acid availability regulates cellular physiology by modulating gene expression as well as signal transduction pathways in cancer cells.[129] Thus, it is not surprising that radiolabelled amino acids have become highly sought as imaging agents.[167]

Amino acids are excellent imaging probes. Their small size enables efficient tumour penetration, they have minimal side effects, no immunogenicity, and due to their zwitterionic structure they are soluble in aqueous solution at pH compatible with blood pH, which is ideal for injection formulation.[15] Due to the fast clearance of amino acids from non-target organs and rapid excretion *via* the renal system, the dose deposited in the patient's body is low which makes them very attractive imaging agents.[15] However, the limitation common to using most of the naturally occurring amino acids as radiopharmaceuticals is their susceptibility to *in vivo* metabolism which can decrease tumour specificity and complicate kinetic analysis.[169] Despite these complications, it is believed that tumour uptake and imaging properties primarily reflect the rate and mechanism of amino acid transport in most instances.[167] These shortcomings can be overcome with non-natural amino acids.[169]

Not only do radiolabelled amino acids have utility in cancer imaging, they are also used in imaging neurodegenerative diseases. For example, a fluorinated analogue of naturally-

occurring neurotransmitter *L*-DOPA, 3,4-dihydroxy-6-[^{18}F]fluoro-*L*-phenylanine ([^{18}F]DOPA) has been used extensively for dopaminergic imaging, and it is a well-established Parkinson's imaging agent.[171] A substrate of AAT system L, [^{18}F]DOPA also shows high uptake in primary brain tumours and has shown promise in carcinoid tumour imaging.[169] Moreover, [^{11}C]-methionine ([^{11}C]MET) has demonstrated utility in identifying hyperfunctining parathyroid glands in human patients.[172]

1.6.1.1 Amino acid radiopharmaceuticals for cancer imaging

Some of the most extensively used and evaluated amino acid–based PET tracers for tumour imaging are: [^{11}C]MET, which is the most well established amino acid based tracer for imaging brain and extracranial malignancies;[169] [^{18}F]FET, which is a synthetic system L substrate that showed utility in detecting recurrent and residual gliomas, potential to distinguish neoplasms from inflammatory lesions, had comparable brain tumour uptake and similar tumour-to-brain ratios as [^{11}C]MET.[173] However, it is also taken up by non-neoplastic lesions in the brain including brain abscesses and demyelienating lesions.[174] Another non-natural system L substrate, *anti*-1-amino-3-[^{18}F]fluorocyclobutane-1-carboxilic acid (*anti*-[^{18}F]FACBC) has shown superiority to [^{18}F]FDG in imaging intracranial malignancies in human subjects. Moreover, this tracer has shown potential in detecting primary, metastatic and recurrent prostate cancer in humans, and has recently been approved by the Federal Drug Agency (FDA) for recurrent prostate cancer imaging.[169,175]

1.6.2 Amino acid radiolabelling

Amino acids have fast pharmacokinetics and can be labelled with shorter-lived radionuclides to minimize patient exposure. The primary radionuclides used for labelling amino acids for tumour PET imaging are ^{11}C and ^{18}F.[169] ^{11}C is an excellent isotope for labelling amino acids as it is not chemically different from ^{12}C and its half-life of only 20.3 min coincides with the peak time of amino acid uptake by the tumour, which is typically achieved 15 – 20 min after i.v. injection.[169] Despite its short half-life, which demands an efficient radiolabelling process, diverse chemical transformations have been applied for the development of ^{11}C-labeled amino

acids.[176] The disadvantage remains in the fact that radiolabelling has to be completed rapidly, and their use is limited to centres with on-site cyclotrons, since distribution of the ^{11}C-labeled tracers is not possible due to its short half-life. Nonetheless, ^{11}C is commonly used for labelling natural amino acids for the purposes of cancer imaging. Examples of ^{11}C-labeled amino acids include: *L*-[^{11}C]leucine, *L*-[^{11}C]methionine and *L*-[^{11}C]tyrosine.

The use of longer-lived ^{18}F ($t_{1/2}$ = 109.77 min) circumvents the issue of regional distribution and makes batch production more feasible, however, as ^{18}F is not naturally present in amino acids, in some cases it can alter the biological properties of the molecule substantially.[167] Despite this, ^{18}F is the radionuclide most often used for routine diagnosis with PET,[176] as a variety of efficient labelling methods have been developed over the years, particularly for non-natural amino acid structures that are close analogues of the natural amino acids. These non-natural amino acid analogues can have improved stability *in vivo*, which avoids potentially confounding accumulation of activity in nontarget tissues due to the distribution of radioactive metabolites and simplifies kinetic analysis.[167]

1.6.2.1 Radiofluorination (^{18}F)

^{18}F is a radionuclide with excellent properties for PET imaging, with 97% positron emission and relatively low β^+ energy (0.64 MeV),[177] resulting in short positron linear range in tissue (~2.3 mm maximum range in water),[178] enabling high image resolution. Its half-life of 109.77 min allows for syntheses, distribution and imaging procedures to be extended over hours, while with limited amount of radiation doses for the patient.[176] ^{18}F is readily available from both particle accelerators and nuclear reactors, using a number of nuclear reactions, but most commonly it is produced in a cyclotron by bombardment of enriched ^{18}O-water target with high energy protons (the ^{18}O(p,n)^{18}F reaction).[177] ^{18}F is recovered as F^- ion from ^{18}O-water, while the ^{18}O-water can be recycled and reused. Specific activity (SA) of the produced [^{18}F]-fluoride *via* this no-carrier-added approach can be as high as 5500 GBq/μmol,[179] which is substantially higher than the SA of [^{18}F]F_2 gas (1 GBq/mmol),[179] which is obtained in a nuclear reaction of ^{18}O(p,n)^{18}F through the addition of F_2 carrier gas to an irradiated enriched [^{18}O]O_2 gas target.[177,179] This latter production method is used when ^{18}F needs to be used for electrophilic labelling reactions.

^{18}F chemistry has been well developed with a variety of synthetic strategies to incorporate the radionuclide onto the target molecule. Broadly, these radiofluorination strategies can be divided into two main categories: direct and indirect labelling, depending on whether the radionuclide is added directly onto the molecule of interest or whether it is introduced through the use of ^{18}F prosthetic groups, which usually entails a multi-step approach.[176] Mechanistically, the ^{18}F incorporation strategies are either nucleophilic (for [^{18}F]F$^-$) or electrophilic (for [^{18}]F_2 gas), and they allow access to complementary sets of molecules.[180]

Nucleophilic fluorination reactions can be direct: when ^{18}F is incorporated into the target molecule *via* either S_N2 or S_NAr (nucleophilic aromatic substitution) mechanism, or indirect – when prosthetic groups such as ^{18}F-labelled aryl fluorides or fluoroalkyl halides or sulfonates are used. In either case, [^{18}F]fluoride anion ([^{18}F]F$^-$) attacks the target molecule at an atom, normally carbon, that bears a suitable leaving group, which is replaced by the ^{18}F atom.[181] [^{18}F]F$^-$ in aqueous form surrounded by a close shell of water dipoles that effectively hinders nucleophilic action in most cases.[176,177,181] Thus, manipulations are required in order to make [^{18}F]F$^-$ into a reactive nucleophilic agent. This is usually accomplished by trapping the ^{18}F$^-$ on an ion exchange column, followed by elution using K_2CO_3 in water/acetonitrile solution.[176] Again, water removal is required in order to increase nucleophilicity of the radioactive fluoride, and this is achieved by addition of a phase-transfer reagent, typically kryptofix-222 (K_{222}), which forms a strong complex with K^+ thus leaving highly nucleophilic ^{18}F$^-$ exposed in polar aprotic solvent.[176] The main advantages of nucleophilic fluorination reactions are that the stereospecific compounds can be made in high radiochemical yield (RCY) and with high SA.[177]

Electrophilic fluorination reactions are highly exothermic and must be controlled either at low temperature, by using very dilute solutions in an inert solvent, or by converting the fluorine into a less reactive form using electrophilic fluorinating agents such as [^{18}F]fluoro-N-sulphonamides, [^{18}F]fluoropyridonesacetyl hypofluorite and others.[176,177,182] These reactions result in low to moderate SA (due to the low SA of [^{18}F]F_2 gas) of the product which may not be regiospecific, but rather present as a mixture of [^{18}F]fluorinated products.[177] Another major caveat of electrophilic fluorination reactions is that the maximum achievable RCY cannot exceed 50%.[177] SA can be improved by converting no-carrier-added [^{18}F]F$^-$ into an electrophilic form for aromatic radiofluorination.[181] This can be accomplished in a number of ways, including [^{18}F]F$^-$

capture by palladium(IV) complex to form [^{18}F]-aryl fluorides.[180] Regioselectivity can be improved with the use of organometallic intermediates such as trialkyl tin group, mercury halide, silicon or germanium.[177]

1.7 System L targeting in oncological PET imaging

Another AAT with high significance in PET radiopharmaceutical development is system L transporter. System L is a Na^+-independent amino acid transporter protein,[183] with preference for branched chain (leucine, isoleucine, valine) and bulky amino acids (phenylanaline, methionine, tyrosine *etc.*). A total of four different subtypes of system L transporters have been reported, LAT1, LAT2, LAT3 and LAT4, two of which, LAT1 and LAT2, belong to the *SLC7* gene family and are associated with the 4F2hc (CD98) heavy chain subunit, while the remaining two, LAT3 and LAT4, are members of *SLC43* gene family and function without the heavy chain subunit.[183,184] The different subtypes have preference for specific neutral amino acids, all of which are listed in Table 1.5. LAT1 and LAT2 function as concentration-driven antiporters, while LAT3 and LAT4 are facilitated diffusers of neutral amino acids.[184] System L is such an appealing therapeutic and PET target because it is ubiquitously expressed, but is upregulated in neoplasms. Most notably, the LAT1 isoform is highly upregulated in several cancers (e.g., prostate, breast and brain)[183] and at metastatic sites, making this transporter a particularly appealing target for PET radiotracer development.

Table 1.5 System L transporter subtypes and their respective substrates. Adapted from Bröer and Bröer.[184]

Transporter	Light chain	Heavy chain	Transport mechanism	Substrates
System L	LAT1 (*SLC7A5*)	4F2hc (*SLC3A3*)	antiporter	Phe, Met, Trp, Ile, Val, Leu, Tyr, His
	LAT2 (*SLC7A8*)	4F2hc (*SLC3A3*)	antiporter	Phe, Met, Trp, Ile, Val, Leu, Ala, Cys, Asn, Gln, Thr, Tyr, His
	LAT3 (*SLC43A1*)	none	uniporter	Phe, Met, Ile, Val, Leu
	LAT4 (*SLC43A2*)	none	uniporter	Phe, Met, Ile, Val, Leu

Among the wide range of amino acids transported by LAT1, leucine plays a uniquely important role in cancer biology as large cellular concentrations of leucine are required to trigger mammalian target of rapamycin complex 1 (mTORC1) activation and support accelerated protein synthesis.[185,186] Not surprisingly then, *L*-1-[^{11}C]leucine represents a promising PET imaging agent. The main issue associated with this radiotracer is the short half-life of ^{11}C, which restricts the use of the tracer to facilities with an on-site cyclotron.[187] The longer lived ^{18}F is incorporated in the tyrosine mimic [^{18}F]FET and the leucine mimic *anti*-[^{18}F]FACBC, which have found their use in recurrent and residual glioma[173] and recurrent prostate cancer imaging,[175] respectively. [^{18}F]FET-PET has been shown to have a prognostic value in patients with glioblastomas at an early stage after radiochemotherapy.[188] Piroth and colleagues, reported that early [^{18}F]FET-PET responders had significantly longer median overall (‘‘not reached’’ *vs.* 9.3 months; $p < 0.001$) and disease-free (10.3 *vs.* 5.8 months; $p < 0.01$) survival as compared to non-responders.[188] A recent review by McConathy[189] highlighted the potential to use *anti*-[^{18}F]FACBC for breast cancer imaging. Several preliminary clinical studies with *anti*-[^{18}F]FACBC reported that this tracer had higher uptake and better imaging properties than [^{18}F]FDG in more aggressive *vs.* benign breast tumour phenotype, thus highlighting its potential utility in identifying distant metastasis.[190,191] Moreover, a strong correlation was found between changes in *anti*-[^{18}F]FACBC-PET avidity of the lesions and tumour response on pathology.[190]

1.7.1 LAT1 as a cancer biomarker

LAT1 is widely expressed in non-epithelial cells such as brain, spleen, thymus, testis, liver, placenta, skeletal muscle and stomach.[168] It functions as a heterodimeric exchanger paired up with 4F2hc,[126,168] which recruits it to the plasma membrane.[168] LAT1 is the most commonly upregulated system L protein exchanger in multiple cancers,[183] examples of which include brain, colon, lung, liver and skin cancers and in cancer metastases.[126] The activity and expression of LAT1/4F4hc correlate with cell proliferation, angiogenesis and disease stage.[170] LAT1 has been used as a biomarker for malignant cancer[183] and was reported to be a negative prognostic marker with patients with pancreatic ductal adenocarcinoma.[192]

LAT1 plays a key role in cancer-associated reprogrammed metabolic networks by supplying growing tumour cells with essential amino acids that are used as nutrients to build

biomass and signalling molecules to enhance proliferation by activating pro-growth pathways such as the mammalian target of rapamycin (mTOR) pathway.[186] mTOR is a serine/threonine kinase in the PI3K-related (PIKK) family that forms catalytic subunit of two distinct protein complexes, known as mTORC1 and mTORC2,[193] whose downstream signalling is crucial for cell survival and proliferation (Figure 1.7A). mTORC1 plays a crucial role in controlling the balance between intracellular anabolic (synthesis of biomolecules) and catabolic (autophagy) pathways in response to environmental conditions and growth factor signalling.[193] LAT1 is the major source of intracellular leucine,[194] which has the power to activate mTORC1 signalling cascade by binding to Sestrin2, which acts upstream of mTORC1[185,193] (Figure 1.7B). Other than leucine, cytosolic arginine can also act as an mTORC1 pathway activator, by binding to CASTOR1, another upstream inhibitor of mTORC1.[193] Even though the signalling protein cascade upstream of mTOR has been determined (Figure 1.7B), the exact mechanisms through which sestrin2 and CASTOR1 regulate mTORC1 activity remain unknown.[193]

Gene expression and protein content of LAT1 are positively associated with mTORC1 activity; however, increases in LAT1 expression are abolished by the administration of rapamycin, suggesting that mTORC1 may also regulate LAT1 activity.[194]

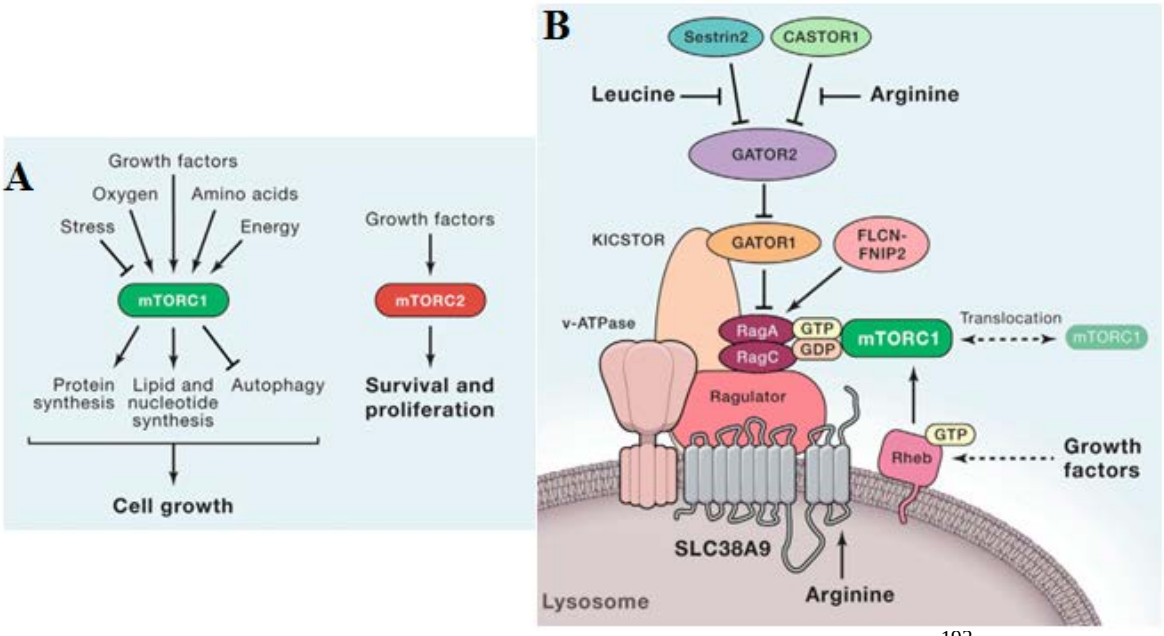

Figure 1.7 mTOR signalling regulation. Adapted from Saxton and Sabatini[193] with permission.

1.8 Thesis theme and rationale

Amino acid transporter (AAT) proteins play key roles in cells, particularly cancer cells, providing them with substrates and signalling molecules for different pathways, many of which are crucial for cancer survival and progression. Hence, these proteins are valuable targets for disease treatment but also for PET tracer development. Targeting AATs with PET for cancer diagnosis enables cancer detection *via* alternative, complementary mechanisms to that of FDG. Both x_C^- and L transporter systems are reported to be upregulated in different cancers, the former is overexpressed under oxidative stress, and thus is the main gateway for GSH precursor supply; and the latter supports accelerated protein synthesis through activation of mTORC1 signalling pathway. The work presented herein is focused on characterisation and development of PET tracers specific for either of the following molecular targets: system x_C^- and system L transporters. Both of these proteins play crucial roles in cancer survival and progression, and the overarching hypothesis of this work is the following:

Radiofluorinated amino acids are useful PET tracers for oncological imaging, and can provide functional and anatomical information which might be used for diagnostic, staging, therapy monitoring and/or planning purposes.

1.8.1 Hypotheses

For this thesis, we propose the following hypotheses, each of which will be tested in the following project chapters:

I) [^{18}F]FASu can be used as a gauge to monitor system x_C^- activity in response to oxidative stress fluctuations in breast cancer. (Chapter 2)

II) A boramino acid analogue of FASu, [^{18}F]ASu-BF_3 can be synthesized and used as system x_C^- PET tracer. (Chapter 3)

III) Chirality at the 5-position does not affect the overall biodistribution and tumour uptake of [^{18}F]FASu. (Chapter 4)

IV) [^{18}F]FASu will show improved tumour-to-nontarget ratios and pharmacokinetics over already established system x_C^- - targeting PET tracer, [^{18}F]FSPG, as well as [^{18}F]FDG. (Chapter 5)

V) Radiofluorinated leucine derivatives targeting system L can be used for cancer PET imaging. (Chapter 6)

Chapter 2: ^{18}F-labelled cystine analog, [^{18}F]5-fluoroaminosuberic acid ([^{18}F]FASu), for oxidative stress imaging with positron emission tomography

2.1 Introduction

The vital role system x_C^- plays in ROS modulation makes it an appealing target for cancer therapy and PET tracer development. The activity of system x_C^- exclusively depends on its light chain subunit, xCT.[93] xCT is expressed in one third of all TNBC *in vivo*[128] and therefore may pose a useful diagnostic target for cancer imaging.[103,159] In the absence of druggable molecular targets, there is a lack of targeted therapies for TNBC, and thus chemo- and radiation- therapy remain as the only treatment options; however, they have had limited success when compared to non-TNBC subtypes.[159] With this in mind, we have previously reported the synthesis of a PET radiotracer targeting specifically system x_C^-, [^{18}F]5-fluoroaminosuberic acid ([^{18}F]FASu).[102,103] We have demonstrated that TNBC xenografts have higher tracer uptake *in vivo* as compared to non-TNBC xenografts.[103] We believe that targeting system x_C^- transporter for tracer development will enable access to functional information regarding the cellular response to OS. The goal of this study is to evaluate whether [^{18}F]FASu can be used as indicator of xCT expression and if so, whether it can be used as a biomarker of OS *in vitro* and *in vivo*. The work reported herein links xCT mRNA, protein expression and [^{18}F]FASu uptake to the key biomarkers GSH and ROS; and examines their dynamic responses when redox homeostasis is challenged by chemicals or radiation.

Adapted by permission from: Non-invasive use of positron emission tomography to monitor chemo- and radiation-induced changes in system x_C^- expression in breast cancer. Mol Imaging Biol. (2019) Mar 5. doi: 10.1007/s11307-019-01331-8. Copyright © 2019, Springer Nature

Čolović M, [1,2] Yang H, [1] Merkens H, [2] Colpo N, [2] Benard F, [2] and Schaffer P.[1,3]

[1] Life Sciences Division, TRIUMF, Vancouver, British Columbia (BC), Canada
[2] Department of Molecular Oncology, BC Cancer Research Centre, BC Cancer, Vancouver, BC, Canada
[3] Department of Chemistry, Simon Fraser University, Burnaby, BC, Canada

MČ, PS and FB designed the study. **MČ** performed all experiments and data analysis presented in this Chapter with the exception of tracer radiolabelling (HY), Western blotting (HM) and PET/CT image acquisition (NC). **MČ** wrote the manuscript.

2.2 Materials & methods

2.2.1 General

All chemicals obtained commercially were used without further modifications unless otherwise indicated. [^{18}F]FASu was prepared as previously reported.[102,103] Quality control of the radiosynthesis was performed by HPLC (Agilent 1200 series instrument equipped with a diode array detector and Raytest GABI Star scintillation detector). Cell irradiation was performed using XRAD 320 X-ray machine (Precision X-ray Inc.). Localized tumour radiation treatment was performed on Small Animal Radiation Research Platform (SARRP, Xstrahl Limited). PET imaging experiments were conducted using a Siemens Inveon μPET/CT scanner. Radioactivity of samples was measured by a calibrated Perkin Elmer Wizard 2480 gamma counter.

2.2.2 Radiosynthesis of [^{18}F]-fluoroaminosuberic acid ([^{18}F]FASu)

[^{18}F]FASu was synthesized at TRIUMF on a TRACERlab FXFN module (GE Healthcare) in a lead-shielded hot cell using our previously reported method.[102,195] Briefly, $^{18}F^-$ /$H_2{}^{18}O$ was azeotropically dried with t-butyl ammonium bicarbonate. The precursor (di-tert-butyl 2-((bis-tert-butoxycarbonyl)amino)-5-(tosyloxy)octanedioate (**1**, Figure 2.1) was added and kept at 95°C for 15 min. After which di-tert-butyl 2-((bis-tert-butoxycarbonyl)amino)-5-fluorooctanedioate (**2**, Figure 2.1) was purified by C18 SepPak. Acetonitrile was removed under vacuum. Then TFA was added and kept at 95°C for 7 min. The final product was purified by another C18 column and taken up in PBS buffer. Decay corrected radiochemical yield (d.c. RCY) 18 ± 6% (n=6), radiochemical purity (RCP) > 98%, specific activity (SA) 17.5 ± 7 GBq/mmol (n=6). Quality control of the radiosynthesis was performed by ultraviolet and radio-HPLC.

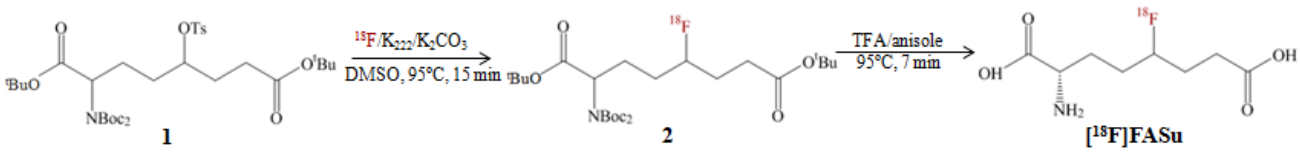

Figure 2.1 Radiosynthesis of [^{18}F]FASu. K_{222} = kryptofix[2.2.2], DMSO = dimethylsulfoxide, TFA = trifluoroacetic acid.

2.2.3 Cell culture and *in vitro* [^{18}F]FASu uptake experiments

All cell lines used in this study have been authenticated by DCC medical. The MDA-MB-231 cell line was obtained as a gift from Dr. Connie Eaves (BC Cancer), and MCF-7 from Dr. C. Kent Osborne (Baylor College of Medicine). ZR-75-1 cells were purchased from ATCC. Cell lines were maintained in their respective complete (10% fetal bovine serum (FBS) + 1% penicillin/streptomycin) media: Dulbecco Modified Eagle Medium (DMEM), DMEM + 1% Gibco MEM Non-Essential Amino Acids Solution, and RPMI 1640, for MDA-MB-231, MCF-7 and ZR-75-1 cells, respectively. Cells were maintained in a humidified incubator at 37°C with 5% CO_2 and routinely subcultured at approximately 80% confluency.

For uptake studies, MDA-MB-231, MCF-7 and ZR-75-1 cells were seeded in 24-well plates at 25,000 cells/cm^2, 20,000 cells/cm^2, and 30,000 cells/cm^2, respectively, such that they reached ~85% confluency the day before the experiment. Overnight incubation times are indicated in the specific figures, but vary from 14-18 h. At predetermined time points, cells were treated with 0.1 mM diethylmaleate (DEM) or irradiated with 2 Gy on an XRAD 320 machine. On the day of the experiment, cells were washed twice with HEPES Basal Salt Solution (HBSS), then 148 kBq of [^{18}F]FASu activity was added in 400 µL HBSS (±1 mM sulfasalazine (SSZ) as blocking agent). The cells were incubated for 1 h at 37°C with orbital shaking. After 1 h incubation, the supernatant was removed, the cells washed with HBSS once, and then lysed with 1 M NaOH solution. After 10 min, the lysate was collected and the wells were washed with another 400 µL HBSS to ensure that no radioactivity remained in the plates. Radioactivity of the supernatant, both washes and the lysates was measured on the γ-counter and normalized to protein concentration.

2.2.3.1 siRNA knockdown experiments

MDA-MB-231 cells were seeded at 50,000 cells/well in a 24-well plate 24 h before the experiment and transfected at 80% confluency. The transfection mixture contained 25 nM siRNA (Santa Cruz Biotechnology, xCT siRNA (h) cat.# sc-76933, control siRNA-A cat.# sc-37007), 1.5 mL of TransitIT siQuest transfection reagent (Mirus, cat.# MIR 2114), and Opti-MEM reduced serum medium (Life Technologies) prepared and added according to the manufacturers' directions. The cells were then incubated at 37°C with 5% CO_2 for 24 h; followed by addition of 0.1 mM DEM and further 24 h incubation. Subsequent tracer uptake or qPCR experiments were performed using the methods described herein.

2.2.3.2 qPCR

Transcriptional expression of *SLC7A11* was determined in MDA-MB-231, MCF-7 and ZR-75-1 cell lines and tumour xenografts harvested from Rag2M mice post-mortem. Tumours were preserved in RNA*later* stabilisation solution (Life Technologies) until experimental day. Total RNA was extracted from cell and tumour samples using a commercially available kit (GenElute Mammalian Total RNA Miniprep Kit, Sigma), treated with amplification grade DNase I (Sigma), and measured using a NanoDrop spectrophotometer. Total RNA (50 ng) from each sample was reverse transcribed in a 20 μL reaction using SuperScript VILO cDNA synthesis kit (Invitrogen). qPCR was set up in 384-well plates, in a total volume of 10 μL; each reaction containing 1 μL template cDNA, 500 μM forward and reverse primers, 250 μM probe, and 1X SsoAdvanced universal probes supermix (BioRad). Each reaction was performed in triplicates and repeated at least 3 times. Predefined primers (forward and reverse) and probes were purchased as PrimeTime Std qPCR Assays from IDT: Hs.PT.58.38930943 and Hs.PT.58v.45621572 for target (*SLC7A11*) and normalizer (HPRT1) genes, respectively. The data were analyzed on QuantStudio Real-Time PCR Software by standard curve method using 10-fold dilution standard curves of either *SLC7A11* or *HRPT1*. Each standard curve was assayed in triplicates and repeated 3 times. The *SLC7A11* and *HPRT1* standard curves were prepared from reverse-transcribed total RNA from MDA-MB-231 cells or tumours, and desired sequences were amplified using Q5 High-Fidelity DNA polymerase (New England BioLabs) as per manufacturer's instructions, using the same IDT primers as in the qPCR reactions. PCR products

were separated on a 2% agarose gel, target bands were excised and purified using the Monarch DNA gel extraction kit (New England BioLabs). DNA quantitation was performed using the Qubit dsDNA HS assay kit (Thermo Fisher). Information on both PCR and qPCR cycling conditions, and standard curves can be found in Appendix A (Figure A1, Tables A1and A2).

2.2.4 Western blotting

Tumour tissue of euthanized Rag2M mice was dissected, snap-frozen, minced, homogenized in RIPA buffer supplemented with protease inhibitors (Roche complete mini tablets). For *in vitro* assays, the cells were harvested when confluency exceeded 80%, washed with cold 1 × Phosphate Buffer Saline (PBS) and lysed in supplemented RIPA buffer (1 mL per 10^7 cells). The lysates were centrifuged (16,000 × g, 20 min, 4°C). Supernatant was collected and protein concentration was determined using Pierce BCA Protein Assay Kit (Thermofisher Scientific). Next, 5 or 10 µg of total protein per sample was electrophoresed on an 8% SDS-PAGE gel. Proteins were transferred onto a nitrocellulose membrane (Amersham) using a semi-dry transfer apparatus (BioRad, 10 V for 25 min). After transfer the membrane was blocked for 1 h with 1 × TBS-tween (TBS-T) with 5% skim milk powder, and probed overnight at 4°C with anti-human xCT/*SCL7A11* rabbit monoclonal antibody (Cell Signaling Technologies (CST), cat.#12691), at 1:500 dilution in 1 × TBS-T 1% skim milk powder). After the primary antibody, the membrane was washed 3 × with TBS-T. Next, the membrane was incubated with goat anti-rabbit IgG-HRP from CST (cat.#7074) at 1:1000 dilution in 1 × TBS-T 1% skim milk powder for 1 h at room temperature. After this incubation, the blot was washed for 5-10 min nine times with 1 × TBS-T. The blot was developed using ECL Select Western Blotting Detection Reagent (GE Healthcare – Amersham), according to manufacturer's instructions, and visualized with ImageQuant LAS 4000 (GE Healthcare).

2.2.5 Glutatione level measurements

Glutathione (GSH) quantification was achieved using a commercially available fluorescence-based kit, Thiol Detection Assay Kit (Cayman Chemicals), as per manufacturer's instructions. GSH content of the cell lysates was estimated from the standard curve that was

prepared for each experiment, and normalized to protein content. Fluorescence was measured on a FlexStation 3 spectrophotometer (Molecular Devices) and corrected for autofluorescence. Each experiment was run in triplicates, and repeated at least three separate times.

2.2.6 ROS detection

Commercially available ROS-reactive dye, chloromethyl-2,7-dichlorofluorescein diacetate (CM-H_2DCFDA, Invitrogen) was used for estimating intracellular ROS load. For these experiments, cells were seeded in 24-well plates in densities as outlined in section 2.2.3. Treatment with DEM and SSZ was initiated in fresh media either the evening before experimentation or at the same time as addition of 5 μM CM-H_2DCFDA. After 1 h co-incubation with the dye, the cells were washed with HBSS twice, trypsinized, collected, centrifuged (1100 RPM, 5 min, at 4°C) and resuspended in HBSS buffer. The cells were then analyzed on a FACSCalibur-Tangerine flow cytometry instrument. Dead cells were excluded from analysis based on size distribution. Control cells from all conditions, without CM-H_2DCFDA treatment, were used as the background autofluorescence signal.

2.2.7 Animal studies

All animal studies were conducted in accordance with the guidelines established by the Canadian Council on Animal Care and approved by the Animal Ethics Committee of the University of British Columbia.

2.2.7.1 *Ex vivo* biodistribution of [^{18}F]FASu

For biodistribution experiments, female NRG (NOD-*Rag1*^{null} *IL2rg*^{null}) MDA-MB-231 xenograft-bearing mice were injected with 1.5 – 2.5 MBq of [^{18}F]FASu in 100 μL of saline *via* the caudal vein. Radioactivity of the syringe was measured before and after injection to determine the exact injected dose. Mice were sacrificed by 2% isoflurane anaesthesia followed by CO_2 asphyxiation at 1 h post-injection and their blood was harvested by cardiac puncture. Organs of interest were collected in a subsequent necropsy, washed with PBS, blotted dry,

weighed and their activity was counted on the gamma counter and normalized to the injected dose.

2.2.7.2 Small animal PET/CT imaging and radiation therapy

PET/CT imaging was done 24 h before and after localized radiation therapy to the tumour. Anesthetised MDA-MB-231 tumour-bearing NRG mice were injected with 4 – 6 MBq of [^{18}F]FASu though the caudal vein. The mice were allowed to wake up and roam freely until the imaging time, when they were again anesthetised with 2% isoflurane inhalation. A CT scan was acquired before the PET static image, which was acquired over a 10 min time interval. The mice were allowed to recover, returned to their cage and were closely monitored for the signs of distress and discomfort.

On the following day the mice were anaesthetized and one group received 10 Gy dose to the tumour by using the Small Animal Radiation Research Platform (SARRP) machine (Xstrahl Limited), while the control group received mock treatment. The mice recovered from isoflurane anesthesia showing no signs of distress or discomfort. Another 24 h later, approximately 48 h after the initial PET/CT imaging, both groups of mice were injected with [^{18}F]FASu, and were sacrificed for the biodistribution study or immediately after the follow-up scan. The mice were euthanized by 2% isoflurane anaesthesia followed by CO_2 asphyxiation and their organs were collected and counted as described above.

2.2.8 Statistical analysis

All data are expressed as mean +/- SD. Statistical analysis was performed using GraphPad (7.0h) software. Outliers were removed using the ROUT method with Q = 2%. Two-way ANOVA analysis was performed for all *in vitro* and biodistribution studies, and multiple comparisons were corrected using the Šidak method. The difference was considered statistically significant when *P* value was less than 0.05.

2.3 Results

2.3.1 [^{18}F]FASu uptake, *SLC7A11* and xCT expression vary in response to prolonged DEM treatment

To confirm [^{18}F]FASu uptake is correlated to system x_C^- activity and to investigate the response to induced OS, we used siRNA to knockdown xCT mRNA (*SLC7A11*) expression and examined both *SLC7A11* and xCT expression levels and FASu uptake in MDA-MB-231, a TNBC cell line, in the presence and absence of the OS inducer diethylmaleate (DEM).

Figure 2.2A shows that siRNA knockdown induced an 8.7-fold decrease in the expression of the gene of interest, *SLC7A11*. When the same samples were treated with DEM, *SLC7A11* levels increased with control ("scramble" siRNA), xCT siRNA and when no siRNA was added compared to non-DEM treated samples, indicating the positive correlation between OS inducer DEM and *SLC7A11* expression (Figure 2.2A). Western blot analysis on these MDA-MB-231 cell lysates confirmed that translational xCT expression directly reflected changes in the transcriptional expression of *SLC7A11* (Figure 2.2C), while the expression of actin did not fluctuate under the same conditions. Furthermore, DEM induced xCT expression across board, in accordance to the qPCR results, showing that mRNA and protein expression both increase as a consequence of OS induction.

Cellular uptake of FASu was reduced by 50% in cultures treated with xCT siRNA, when compared to controls (Figure 2.2B). In the presence of DEM, [^{18}F]FASu uptake increased significantly as compared to the untreated sample, with the effect being the greatest in the case when no siRNA was added (**** $p < 0.0001$ for no siRNA and control siRNA samples, and ** $p = 0.0013$ for xCT siRNA treated sample). The system x_C^- inhibitor, sulfasalazine (SSZ), completely blocked [^{18}F]FASu uptake by MDA-MB-231 cells (Figure 2.2B). These results indicate that [^{18}F]FASu uptake is increased by DEM induction of system x_C^-.

2.3.2 System x_C^- activity changes with DEM incubation in a time-dependent manner

We performed a time-dependent study, with the stressor DEM at concentration of 0.1 mM, for which we have previously observed an effect on system x_C^- activity and xCT mRNA levels. This resulted in no change in tracer uptake in MDA-MB-231 cells within the first 1.5 h of treatment (Figure 2.3; p = 0.89 for 1.5 h time point and p = 0.97 for 45 min time point). However, at the 3 h time point, tracer uptake increased by 39.9 ± 14.2% as compared to the untreated control ($p < 0.0001$), and continued to increase over time. At the final measured time point of 15 h, [^{18}F]FASu uptake by this TNBC cell line was 137.9 ± 26.4% higher than that of the untreated sample ($p < 0.0001$). The results suggest that system x_C^- activity continuously increases in the presence of DEM, leaving the question of how other cellular biomarkers, ROS and GSH levels, change when the cells react to OS induction.

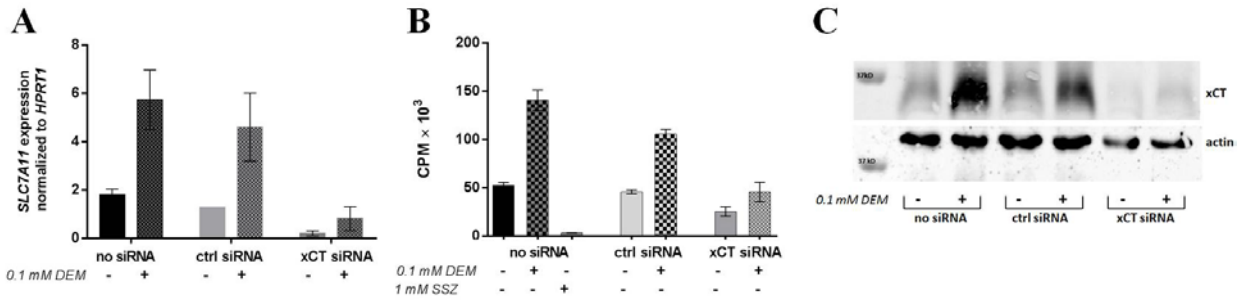

Figure 2.2 [^{18}F]FASu uptake and xCT expression with siRNA knockdown or OS-inducer treatment. A) Absolute qPCR quantitation of *SLC7A11* expression after 48 h siRNA knockdown in MDA-MB-231 cells. 24 h treatment with OS-inducer diethyl maleate (DEM, 0.1 mM) caused upregulation of *SLC7A11* expression. **B)** *In vitro* 1 h uptake of [^{18}F]FASu in MDA-MB-231 cells increased after 24 h exposure to DEM and xCT siRNA knockdown resulted in lowered tracer uptake. **C)** Western blot analysis of siRNA-treated MDA-MB-231 cell lysates showed knockdown of xCT expression in xCT siRNA–treated sample and overexpression of xCT in DEM – treated samples. The actin blot was used as loading control. *Copyright © 2019, Springer Nature*

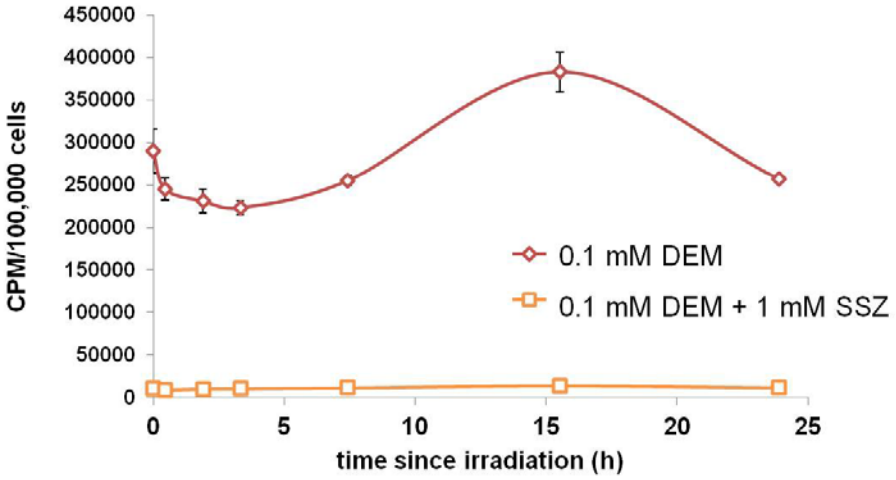

Figure 2.3 [^{18}F]FASu uptake over time with DEM treatment. One hour *in vitro* [^{18}F]FASu uptake (◊) by MDA-MB-231 cells after varying duration of treatment with DEM (0.1 mM). The uptake was blocked by xCT inhibitor SSZ (1 mM) (□). *Copyright © 2019, Springer Nature*

2.3.3 System x_C^- response to short (1 h) *vs.* long (overnight) DEM treatment in MDA-MB-231 cells

After 1 h treatment with DEM, *SLC7A11* expression, [^{18}F]FASu uptake and intracellular glutathione (GSH) content (Figure 2.4A-C, respectively) did not vary significantly from untreated controls. However, the mean fluorescence intensity, as measured using CM-H_2DCFDA dye as an indicator, increased substantially, indicating an increased ROS burden in treated MDA-MB-231 cells (Figure 2.4D). Conversely, prolonged treatment with DEM resulted in transcriptional upregulation of *SLC7A11* ($p < 0.0001$), increased [^{18}F]FASu uptake by 56.3 ± 26.1% ($p < 0.001$), and GSH content by 40.5 ± 25.8% ($p < 0.05$, Figure 2.4A-C). However, ROS levels were noted to return to baseline, with no difference between treated and untreated cells (Figure 2.4D). Evidently, shorter exposure to the stressor DEM was not sufficient to result in changes in *SLC7A11* mRNA expression, system x_C^- activity or GSH production. On the other hand, prolonged exposure to DEM caused the cells under study to respond by increasing their GSH production and upregulating *SLC7A11* expression. From these results, we hypothesize that with the enhancement of x_C^- transporter activity, ROS levels returned to normal.

2.3.4 Determination of GSH content and [^{18}F]FASu uptake in additional, ER+/PR+, breast cancer cell lines after 1 h and overnight treatment with DEM

With preliminary mRNA expression, [^{18}F]FASu uptake, GSH and ROS response data in hand, we then expanded our cohort of cell lines to include measurements of GSH content and [^{18}F]FASu uptake in two different ER^+/PR^+ cell lines, MCF-7 and ZR-75-1. As shown in Figure 2.5A, overnight treatment with DEM resulted in overexpression of xCT in all three breast cancer cell lines, independent of the molecular signature of the cells. Moreover, our results indicate that 1 h incubation with DEM, SSZ or the two in combination, caused no significant differences in GSH content (Figure 2.5C). Similarly, [^{18}F]FASu uptake did not change significantly when compared to the untreated controls (Figure 2.5B). When cells were treated with DEM overnight, GSH levels increased in all three cell lines (Figure 2.5C, **** $p < 0.0001$), as did [^{18}F]FASu uptake (Figure 2.5B, * $p< 0.05$ in the case of MDA-MB-231, ** $p < 0.01$ for the hormone receptor positive cells). SSZ was shown to block [^{18}F]FASu uptake in all cases indicating specific uptake *via* system x_C^-. GSH levels decreased when xCT was blocked by SSZ incubation overnight, and they decreased even further when both OS inducer DEM and xCT inhibitor SSZ were present together in the media overnight (Figure 2.5C).

In comparing MCF-7 to MDA-MB-231, both cell lines demonstrated increased ROS burden after 1 h incubation with DEM, whereas ZR-75-1 cells showed no corresponding fluorescent peak shift under the same conditions (Figure 2.6). In the presence of SSZ, a substantial shift in FL-1 peak occurred in all three cell lines studied, regardless of treatment duration (1 hr and overnight). After prolonged DEM incubation, none of three cells lines demonstrated fluorescent peak shift, which could be explained by increased GSH production (Figure 2.5C). Therefore, with time, we hypothesize cells adjust to the presence of the OS inducer in their media, and maintain increased antioxidant capacity in order to balance the ROS increase.

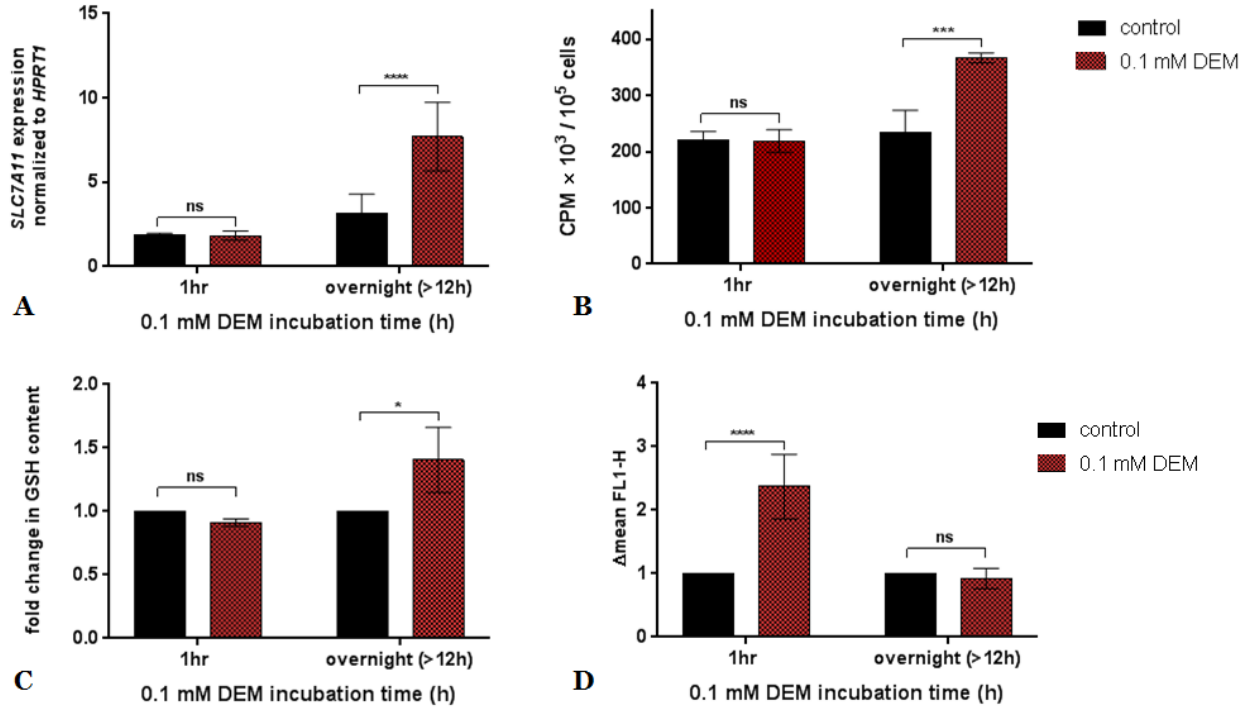

Figure 2.4 *SLC7A11* expression, [^{18}F]FASu uptake, GSH levels and ROS levels in MDA-MB-231 cells after 1 h or overnight DEM treatment. A) *HPRT1*-normalized *SLC7A11* expression with and without 1 h or overnight incubation with DEM. **B)** 1 h *in vitro* uptake of [^{18}F]FASu with and without 1h or overnight incubation with DEM. **C)** Intracellular GSH levels increased after overnight treatment with DEM (* $p < 0.05$). **D)** ROS levels measured as mean CM-H_2DCFDA fluorescence increased significantly (**** $p < 0.0001$) after 1 h co-incubation with DEM but returned to the same level as the untreated control sample in the case of overnight incubation. *Copyright © 2019, Springer Nature*

2.3.5 *Ex vivo* qPCR and Western blot experiments

qPCR studies on harvested breast cancer xenografts show the same pattern of *SLC7A11* expression as the three cell lines, with MDA-MB-231 tumour and cell line having the highest xCT mRNA expression, as compared to MCF-7 and ZR-75-1 (Figure 2.7A–B). In order to investigate whether the transcriptional expression levels are correlated with protein expression levels, we performed Western blots on cell lines and tumour lysates. Comparing two commercially available anti-xCT antibodies (Abcam and Cell Signaling Technologies (CST)), we found that the most consistent results were obtained when using the antibody sourced from CST. While both Abcam and CST anti-xCT antibodies recognize the recombinant human xCT

protein (see Appendix A, Figure A2), the anti-xCT antibody from Abcam recognizes a 55 kDa band that showed no change in response to any treatment. The anti-xCT antibody from CST, on the other hand, recognizes xCT as a 35 kDa band with changes in levels of protein expression consistent with treatment (±DEM or xCT siRNA). The Western blot comparing the three breast cancer cell and tumour lysates indicates the highest xCT expression in TNBC, MDA-MB-231 (Figure 2.5A), which is consistent with the transcriptional *SLC7A11* levels determined in our qPCR experiments (Figure 2.7). Overnight treatment with DEM increased expression of xCT in all three cell lines (Figure 2.5A).

2.3.6 *In vivo* radiotherapy and [^{18}F]FASu-PET/CT imaging

In vivo uptake of [^{18}F]FASu uptake in MDA-MB-231 tumours was examined before and after localized radiation therapy in NRG mice at 1 h post-injection, and 24 h post-treatment (Figure 2.8). While the overall tracer biodistribution did not change significantly as a consequence of localized radiotherapy (Figure 2.8A, Table 2.1), tumour uptake did increase from 3.72 ± 0.75 %ID/g to 4.60 ± 0.91 %ID/g, in non-treated *versus* treated group, respectively. This difference is not statistically significant (p = 0.078); however, tumour-to-background tissue ratios did increase sufficiently and improved image contrast (Figure 2.8B-C, Table 2.1). Tumour-to-blood and tumour-to-muscle ratios continued increasing throughout the duration of the dynamic scan. The ratios were higher after treatment in the imaged mouse.

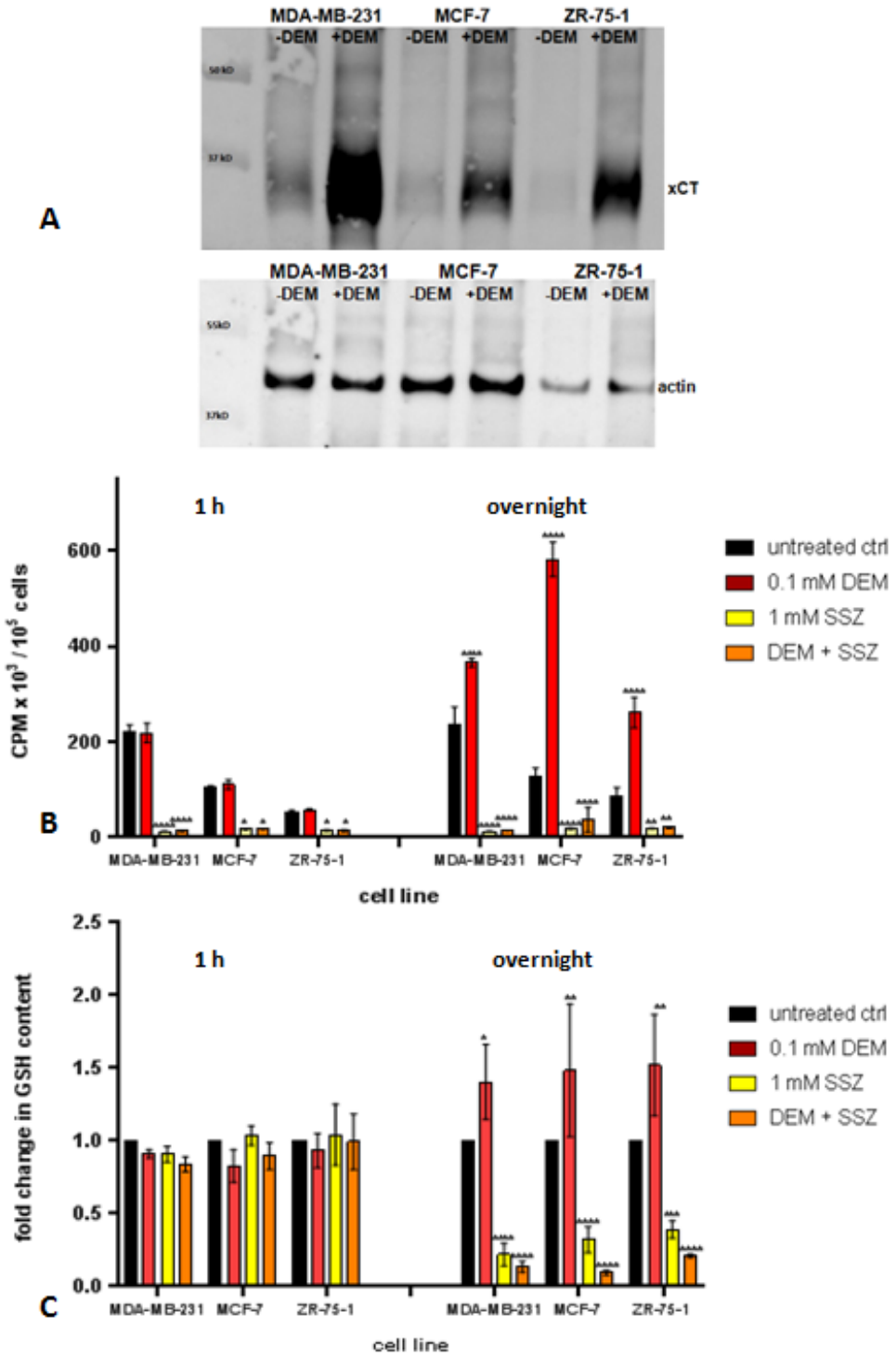

Figure 2.5 [^{18}F]FASu *in vitro* uptake is positively correlated to xCT expression and intracellular GSH levels in three breast cancer cell lines. A) Western blot showing xCT and actin expression in all three cell lines after overnight incubation with DEM. **B)** [^{18}F]FASu uptake did not change after 1 h incubation with DEM, while it was blocked by SSZ regardless of

whether DEM was present (**** $p < 0.0001$, * $p < 0.05$). Overnight treatment with DEM resulted in increased [^{18}F]FASu uptake (**** $p < 0.0001$). The tracer uptake was blocked in the presence of SSZ (**** $p < 0.0001$, ** $p < 0.01$). **C)** GSH levels remained constant in all three breast cancer cell lines after 1 h treatment with OS-inducer DEM, in the presence and absence of SSZ. One hour treatment with SSZ alone did not change intracellular GSH levels as compared with untreated control samples ($p > 0.05$). Overnight treatment with DEM, SSZ or DEM and SSZ, influenced GSH levels significantly in all three breast cancer cell lines. DEM seemed to promote GSH synthesis, while the presence of SSZ in the samples caused GSH depletion in all cells. *Copyright © 2019, Springer Nature*

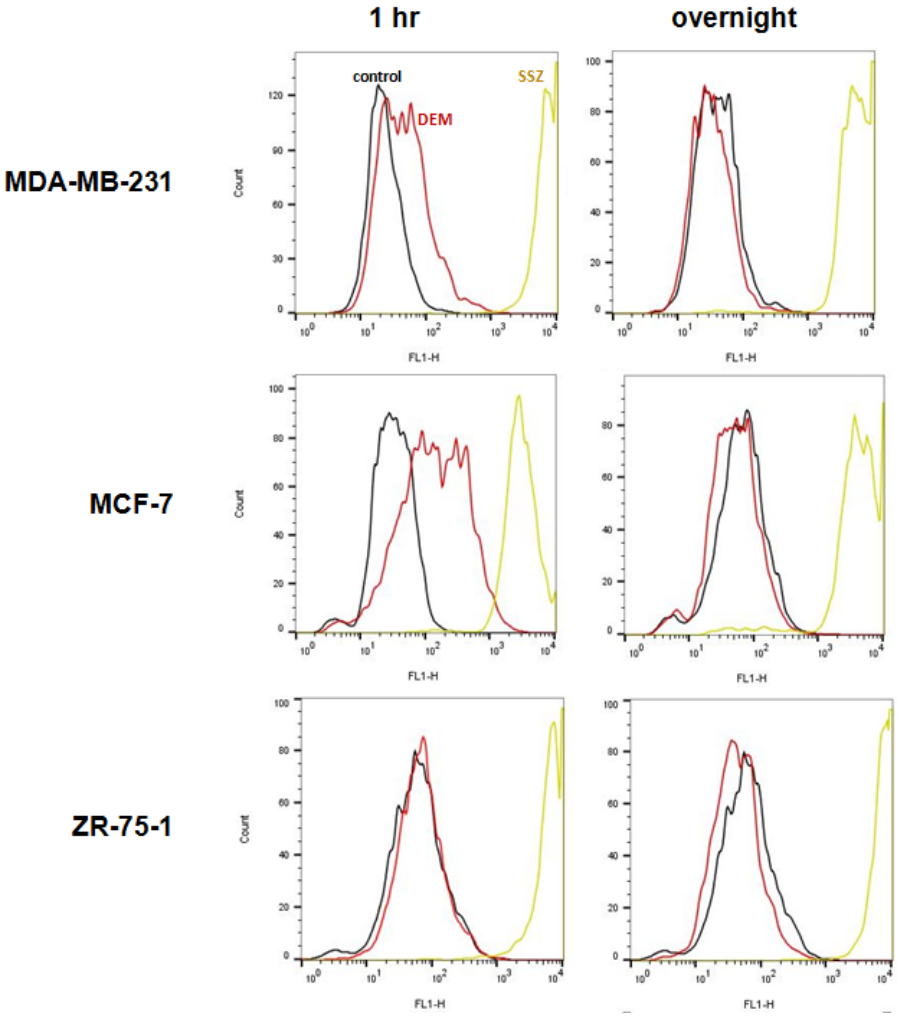

Figure 2.6 Flow cytometry CM-H_2DCFDA staining showed a partial shift in fluorescence peak after 1 h treatment with DEM (red) in MDA-MB-231 and MCF-7, but not in ZR-75-1 cells. Blocking system x_C^- with SSZ results in a 2-fold peak shift in all cell lines (yellow), regardless of the incubation duration. Control cells are presented as black lines. *Copyright © 2019, Springer Nature*

Table 2.1 Biodistribution data of [^{18}F]FASu at 1 h post-injection collected at 24 h post-radiation therapy of MDA-MB-231 xenografts in NRG mice. *Copyright © 2019, Springer Nature*

	Control, n =6		**Irradiated, n = 9**	
organs (tissues)	**% ID/g**	**± SD**	**% ID/g**	**± SD**
blood	0.63	0.11	0.65	0.20
fat	0.04	0.02	0.05	0.01
ovaries	2.97	0.75	3.32	1.41
uterus	4.36	1.87	4.20	1.80
small intestine	1.47	0.46	1.50	0.42
stomach	1.92	0.51	2.02	0.91
pancreas	26.03	1.28	27.42	3.52
spleen	1.92	0.65	2.27	1.28
liver	0.97	0.21	0.78	0.23
adrenal glands	0.71	0.23	0.74	0.25
kidneys	20.51	3.61	23.21	9.99
heart	0.26	0.05	0.27	0.08
lungs	1.84	0.23	2.17	0.39
MDA-MB-231 tumour	3.70	0.74	4.56	0.92
muscle	0.22	0.06	0.21	0.06
bone	1.03	0.17	0.88	0.24
brain	0.08	0.01	0.10	0.01
	ratio	**± SD**	**ratio**	**± SD**
Tumour/blood	5.92	0.82	7.33	1.42
Tumour/fat	93.16	26.39	102.05	23.87
Tumour/muscle	17.15	3.77	22.82	4.46
Tumour/brain	44.49	8.66	47.53	5.22

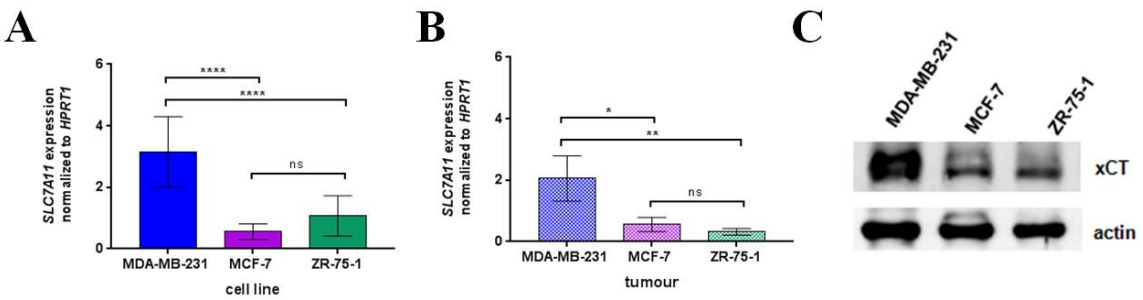

Figure 2.7 The TNBC line, MDA-MB-231, shows significantly higher *SLC7A11* and xCT expression levels, both *in vitro* and *ex vivo*. A) MDA-MB-231 cells (blue bar) expressed *SLC7A11* mRNA at significantly higher levels *in vitro* than MCF-7 and ZR-75-1 cell lines (purple and green bars, respectively, **** $p < 0.0001$). **B)** *SLC7A11* expression in harvested MDA-MB-231 tumours (blue bar) is higher than in the other two tumours (MCF-7 in purple and

ZR-75-1 in green, * $p < 0.05$, ** $p < 0.01$). There was no statistically significant difference between *SLC7A11* mRNA levels between MCF-7 and ZR-75-1 ($p > 0.05$). **C)** Western blot of MDA-MB-231, MCF-7 and ZR-75-1 tumour lysates indicated that MDA-MB-231 tumours had higher xCT expression than the two hormone receptor-positive tumours. *Copyright © 2019, Springer Nature*

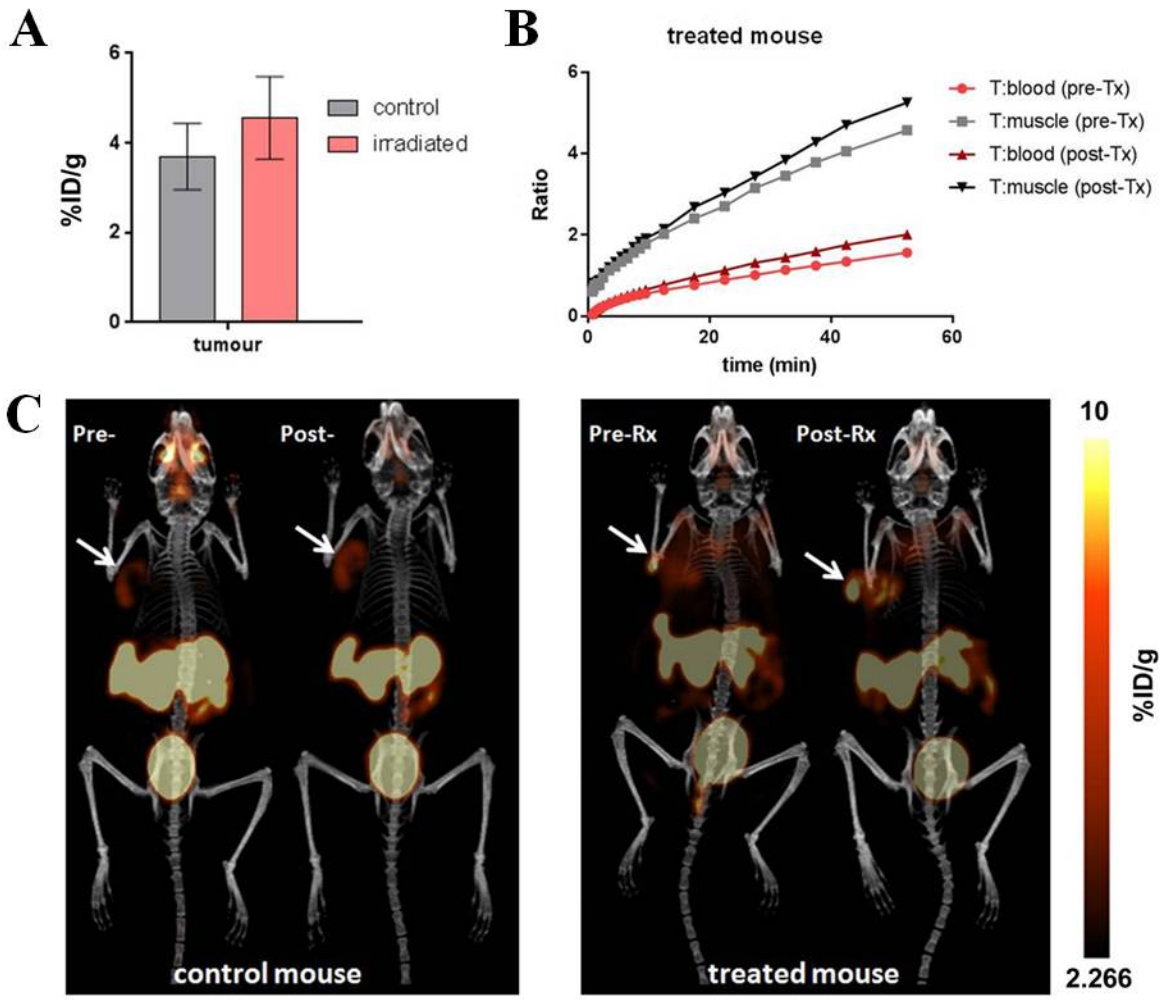

Figure 2.8 Biodistribution data and maximal intensity projections of PET/CT images with [^{18}F]FASu at 1 h post-injection taken 24 h before and post-radiation therapy of MDA-MB-231 xenografts in NRG mice. A) Biodistribution data indicate no statistically significant differences between control (n = 6) and treated (n = 9) groups. **B)** Time-activity curve (TAC) of tumour-to-nontarget ratios in a mouse that underwent localized radiation treatment. **C)** MDA-MB-231 tumours (white arrows) are clearly visualized with [^{18}F]FASu-PET 55 min post-injection. Acquisition time was 10 min. The same animal is depicted twice, for both the control and the treated mouse, with the images being the pre- and post-therapy. *Copyright © 2019, Springer Nature*

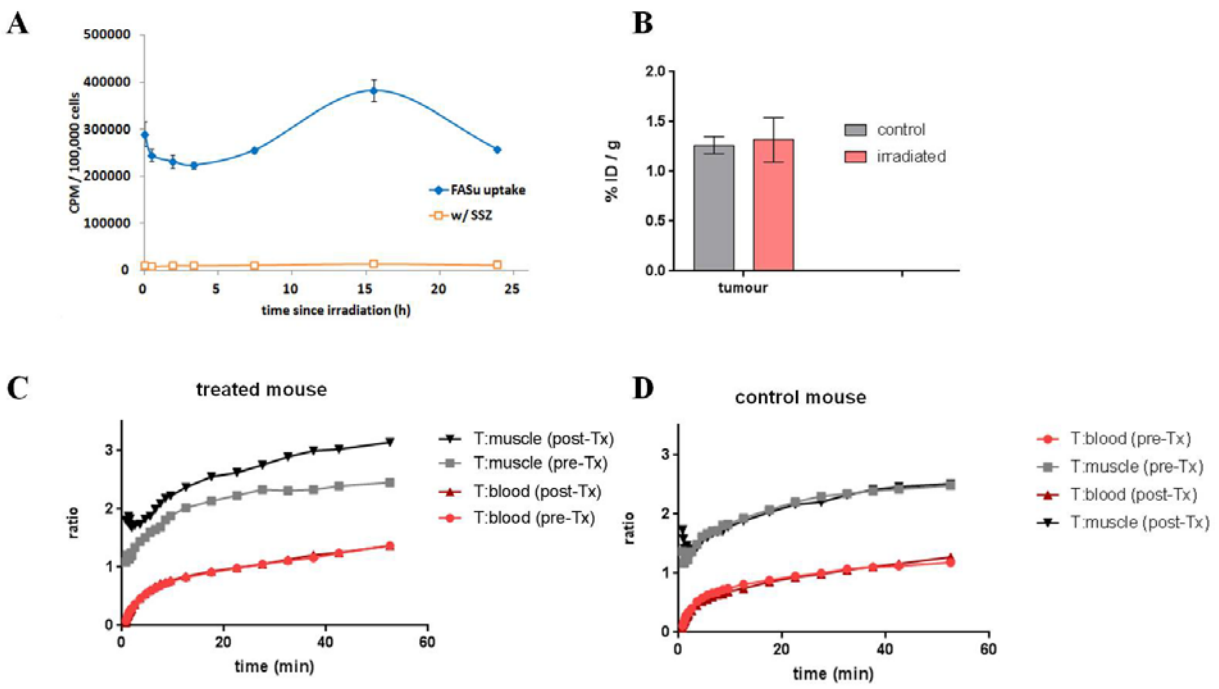

Figure 2.9 [^{18}F]FASu uptake post-radiation treatment. A) *In vitro* [^{18}F]FASu uptake (●) peaked at 16 h time point following 2 Gy irradiation of MDA-MB-231 cells. Sulfasalazine (SSZ, 1 mM) treatment was used as a negative control for each time point (□). **B)** Biodistribution data indicated no statistically significant differences between MDA-MB-231 tumour uptake in control (n = 6) and treated (n = 10) groups. **C)** TAC of tumour-to-nontarget ratios in a mouse that underwent localized radiation treatment. **D)** TAC of tumour-to-nontarget ratios in the mouse that underwent mock treatment. *Copyright © 2019, Springer Nature*

2.3.7 [^{18}F]FASu as a gauge for oxidative stress level monitoring in TNBC

To understand how [^{18}F]FASu uptake changes over time after radiation exposure, we irradiated cells with a sublethal dose of X-ray radiation (LD_{50} = 2 Gy, previously established in our lab) and measured tracer uptake at different time points following cell irradiation. We found that [^{18}F]FASu uptake did not change substantially immediately following radiation exposure (Figure 2.9A) and that it generally decreased as compared to non-irradiated cells. After more than 5 h following radiation, a gradual increase in tracer uptake was observed, which peaked at 16 h time point where it was 32.0 ± 14.4% higher than that of the control cells ($p < 0.0001$). At the final time point of 24 h post-irradiation, the tracer uptake returned to the level of the control (non-irradiated) cells.

2.3.8 *In vivo* radiotherapy and [^{18}F]FASu-PET/CT imaging – Part 2

We examined *in vivo* [^{18}F]FASu uptake 16 h after localized radiation therapy to the tumour. Once again, the overall MDA-MB-231 tumour uptake did not differ significantly between treated and control groups (Figure 2.9B, Table 2.2). Tumour-to-nontarget ratios were higher following radiation treatment as compared to the baseline levels (Figure 2.9C). Moreover, the increase in tumour-to-muscle ratios over time was not observed in the mouse that received mock treatment (Figure 2.9D).

Table 2.2 Biodistribution data of [^{18}F]FASu at 1 h post-injection collected at 16 h post-radiation therapy of MDA-MB-231 xenografts in NRG mice. *Copyright © 2019, Springer Nature*

	Control, n =6		**Irradiated, n = 10**	
organs (tissues)	**% ID/g**	**± SD**	**% ID/g**	**± SD**
blood	0.45	0.09	0.54	0.12
fat	0.06	0.02	0.05	0.02
ovaries	2.32	1.91	2.01	1.07
uterus	3.05	1.16	2.84	0.97
small intestine	1.35	0.26	1.19	0.31
stomach	1.40	0.49	1.57	0.73
pancreas	23.53	2.76	28.77	8.25
spleen	1.78	0.48	1.32	0.41
liver	0.73	0.19	0.69	0.17
adrenal glands	0.35	0.14	0.97	1.06
kidneys	16.42	4.89	20.52	6.46
heart	0.19	0.04	0.29	0.11
lungs	1.74	0.22	2.21	0.77
MDA-MB-231 tumour	1.27	0.09	1.32	0.22
muscle	0.20	0.04	0.24	0.12
bone	0.79	0.30	0.56	0.21
brain	0.09	0.02	0.11	0.04
	ratio	**± SD**	**ratio**	**± SD**
Tumour/blood	2.88	0.42	2.48	0.44
Tumour/fat	23.39	7.20	26.97	7.06
Tumour/muscle	6.43	0.95	6.44	2.50
Tumour/brain	15.16	2.05	12.40	3.46

Table 2.3 Tumour weight and [^{18}F]FASu uptake data at 1 h post-injection from the two biodistribution studies collected at 24 h and 16 h post-radiation (post-Rx) therapy of MDA-MB-231 xenografts in NRG mice. The control tumours were harvested from the animals that received mock treatment. *Copyright © 2019, Springer Nature*

	24 h post-Rx		**16 h post-Rx**	
	all tumours, n=15		**all tumours, n=16**	
	mean	**± SD**	**mean**	**± SD**
tumour weight (g) **** *p value < 0.0001*	0.5620	0.1996	0.2345	0.0892
	control tumours, n=6		**control tumours, n=6**	
	mean	**± SD**	**mean**	**± SD**
tumour weight (g) * *p value = 0.0215*	0.4362	0.0764	0.2032	0.0566
tumour uptake (%ID/g) **** *p value < 0.0001*	3.70	0.74	1.27	0.09

2.4 Discussion

Radiolabelled glucose analog, 2-deoxy-2-[^{18}F]fluoro-*D*-glucose ([^{18}F]FDG) is the most widely used PET tracer in the clinical management of several cancer types.[196] Increased demand for glucose has been recognized as one of the hallmark features of cancer,[49] and as such has been exploited by [^{18}F]FDG-PET which found its use in cancer detection, staging, and monitoring of therapy response.[31,49,197,198] However, the lack of specificity of [^{18}F]FDG-PET limits its utility as the background uptake can be high in highly metabolically active organs; slow growing and low-grade tumours may not be [^{18}F]FDG-PET avid, and poor signal-to-noise ratio PET images can be difficult to interpret.[199–201] For these reasons, we hypothesize that utilizing system x_C^-, a cystine/glutamate antiporter, with a very narrow natural substrate binding profile, yet sufficient upregulation in disease to be a useful target for PET imaging[102,103] may be a complementary methodology to [^{18}F]FDG-PET. System x_C^- has been shown to be upregulated under OS, a process common in many diseases, which plays an important role in cancer differentiation and proliferation.[74,75] A specific radiotracer driven by OS may have value in detection, staging, and therapy response monitoring. It has been reported previously that TNBC has higher xCT expression and cystine consumption, which supports the potential utility of [^{18}F]FASu-PET in clinical breast cancer management.[103,128] The purpose of this study was to evaluate whether

[^{18}F]FASu can be used as an OS level biomarker and as such, whether variations in tracer uptake could provide us with useful information on radiation therapy monitoring.

In an attempt to address the question of [^{18}F]FASu uptake specificity, we have previously reported higher [^{18}F]FASu uptake both *in vitro* and *in vivo* in HEK293::xCT cells and tumours as compared to the wild-type HEK293 cells.[103] However, we were unable to prove the direct correlation to xCT protein expression levels, due to the lack of a reliable and specific anti-xCT antibody.[202] Western blot experimentation combined with siRNA knockdown and qPCR studies convinced us that the 35 kDa band recognized by the antibody from CST is the true functional human xCT protein. This finding contradicts a previously drawn conclusion that the 50-55 kDa band is the functional xCT,[104] but is in concordance with more recently published findings with in-house made antibodies by multiple groups.[202–206] Our specificity study in Figure 2.2 showed direct correlation of tracer uptake and *SCL7A11* and xCT levels in MDA-MB-231 cells. With this study we have thus established a link between transcriptional and translational levels of xCT and the transport activity of system x_C^-, which is reflected in [^{18}F]FASu uptake.

It was previously demonstrated that [^{18}F]FASu uptake and GSH levels increase with DEM treatment,[103] presumably due to increased ROS which resulted in system x_C^- upregulation. To understand the changes reflected upon these biomarkers when OS is artificially induced by DEM, and also to understand the timeframe for those changes to occur, we investigated GSH, ROS, *SLC7A11* and [^{18}F]FASu uptake at various time points after DEM treatment. First, we performed an uptake study in which the incubation time with 0.1 mM DEM was varied. In Figure 2.3 (p.48) we observed that system x_C^- activity continuously increased in the presence of DEM, as reflected by increase in cellular uptake of [^{18}F]FASu. There was upregulation in system x_C^- expression or activity in cells for incubation duration superior to 3 h.

Utilizing the TNBC cell line, MDA-MB-231, we wanted to compare cellular markers of OS, GSH and ROS levels, in relation to xCT mRNA expression and [^{18}F]FASu uptake, at 1 and 16 h. Not surprisingly, a 1 h treatment with DEM did not result in increased tracer uptake or *SLC7A11* expression in the TNBC cell line, MDA-MB-231. In fact, a rapid increase in crude ROS levels was observed *via* fluorescence assay, with little to no effect on GSH levels. On the contrary, at the longer time point, *SLC7A11* expression, [^{18}F]FASu uptake and GSH all increased substantially, whereas ROS levels were not observed to be different from untreated controls. We

suspect ROS returned to basal levels due to an increase in antioxidant (glutathione) production following xCT gene (*SLC7A11*) and x_C^- protein upregulation.

When we expanded the cohort to compare three breast cancer cell lines and assessed antioxidant load and [^{18}F]FASu uptake, we found that, similarly to MDA-MB-231 cells, the ER^+/PR^+ cell lines showed the same positive correlation between system x_C^- activity and GSH levels. Regardless of the molecular signature of the breast cancer cells, it seems that increase in GSH production is enabled due to system x_C^- upregulation (Figure 2.5). Correspondingly, no fluorescent peak shift was observed after prolonged incubation of the cells with DEM (Figure 2.6). We hypothesize that cells adjust to the presence of the OS inducer in their media, and maintain increased antioxidant capacity in order to balance the ROS increase. Blocking system x_C^- with xCT inhibitor SSZ had the smallest impact on ZR-75-1 cells (Figure 2.5B-C), as reflected in lower percentage of [^{18}F]FASu uptake blocking (78% uptake inhibition compared to 86% and 94% in MCF-7 and MDA-MB-231 cells, respectively) and lesser decrease in amount of GSH (60% compared to 68% and 78% in MCF-7 and MDA-MB-231 cells, respectively), suggesting some alternative, unknown, mode of cystine uptake that ZR-75-1 cells rely on to a greater extent. Similarly, flow cytometry results with ZR-75-1 differed from those with MCF-7 and MDA-MB-231 cells (Figure 2.6). No fluorescent peak shift was observed after 1 h treatment with DEM, indicating no detectable increase in ROS burden in ZR-75-1 cells. Evidently, OS compensation is taking place at a different rate in this cell line, but under a mechanism that remains unclear.

When we compared *in vitro SLC7A11* mRNA abundance to the one extracted from harvested tumours, we found that the TNBC has the highest *SLC7A11* expression both *in vitro* and *ex vivo* (Figure 2.7), consistent with MDA-MB-231 cells having higher [^{18}F]FASu uptake than MCF-7 and ZR-75-1 (Figure 2.5). Additionally, we have also previously demonstrated that MDA-MB-231 tumours have the highest [^{18}F]FASu uptake *in* vivo, as compared to MCF-7 and ZR-75-1.[103] Western blot analysis demonstrated that xCT protein expression levels are the greatest in the triple-negative cells and tumours, MDA-MB-231 (Figures 2.5A and 2.7C, respectively).

Having established a correlation between [^{18}F]FASu and biomarkers associated with OS, we wanted to determine the potential for [^{18}F]FASu to serve as a non-invasive gauge of OS via

PET. In order to test this hypothesis, *in vitro* experiments were performed in which tracer uptake was determined in irradiated MDA-MB-231 cells at multiple time points. These studies (Figure 2.9A) indicated that [^{18}F]FASu uptake was maximal at 16 h post-irradiation, and decreased back to base levels by the 24 h time-point. With cell data in support of our hypothesis, we then measured [^{18}F]FASu uptake in MDA-MB-231 tumour-bearing NRG mice before and after localized radiation therapy. We imaged MDA-MB-231 tumour-bearing NRG mice at 16 h after localized radiotherapy, but observed no significant differences between [^{18}F]FASu uptake of treated *versus* control mice (Figure 2.9B, 1.32 ± 0.22 and 1.27 ± 0.09 %ID/g, $p = 0.590$). An analysis of tumour uptake at 24 h post irradiation also did not demonstrate statistically significant difference in tracer uptake between treated and untreated animals (4.56 ± 0.92 and 3.70 ± 0.74 %ID/g, $p = 0.078$). Despite this, time-activity curves from the dynamic scans, revealed an increase in tumour-to-muscle ratios after radiation therapy, while this phenomenon was not observed in the control tumour (Figure 2.9C and D). Tumour-to-blood ratios remained unchanged on baseline and follow-up scans, for both treated and control tumours. It should be noted that there were significant differences in baseline [^{18}F]FASu uptake in the MDA-MB-231 tumour between the two imaging studies, and we are examining extenuating factors that may contribute to these differences, including but not limited to differences in tumour mass between subjects (Table 2.3, $p < 0.0001$), and cell treatment methods, particularly in the case of such an aggressive cell line as MDA-MB-231.

2.5 Conclusion

In summary, we found that intracellular GSH levels directly reflect changes in the system x_C^- activity and support our hypothesis that [^{18}F]FASu could be used as a tool to monitor the cystine transporter activity which is a reflection of intracellular OS burden. Work is currently underway to better understand the interplay of these factors *in vivo*. Preliminary animal PET/CT studies with [^{18}F]FASu indicate potential to use [^{18}F]FASu-PET to monitor tumour response to radiation therapy, however additional studies must be done in order to determine the ideal follow-up time point. It will be important to determine how this specific response to OS contributes to our ability to use PET to better understand the role of system x_C^- in cancer and other OS-related diseases.

Chapter 3: Synthesis and evaluation of an ^{18}F-labelled boramino acid analogue of aminosuberic acid for PET imaging of the antiporter system x_C^-

3.1 Introduction

Currently, reported system x_C^--targeting PET imaging probes are derivatives of the natural substrates (glutamate and cystine) of this transporter (Figure 3.1). (4S)-4-(3-[^{18}F]Fluoropropyl)-*L*-glutamate ([^{18}F]FSPG, also called ^{18}F-BAY 94-9392), a glutamate analog developed by Bayer,[139] is currently used in clinical trials for lung, liver and breast cancer imaging.[142,143] 5-[^{18}F]Fluoroaminosuberic acid (([^{18}F]FASu), developed by Webster *et al.*,[102] is structurally similar to cystine and has been successfully used in pre-clinical imaging of lymphoma, breast, and ovarian cancer xenografts.[102,103] The synthesis of enantiomerically pure [^{18}F]FASu was recently reported by our group using optically pure precursors and milder radiolabeling conditions to prevent racemisation.[195]

Recently, boramino acids generated by replacing the α-carboxylate group of amino acids with a trifluoroborate motif were showed to mimic their amino acid counterparts.[207] Liu *et al.* reported the synthesis of ^{18}F-labeled Phe-BF_3, Leu-BF_3, Ala-BF_3 and Pro-BF_3 (Figure 3.2).[207] Among them, [^{18}F]Phe-BF_3 was further evaluated *in vivo*, and showed significant accumulation (7.31 %ID/g at 2 h post-injection) in U-87 glioma xenografts presumably *via* the action of the system L amino acid transporter (LAT). The *in vivo* evaluation of [^{18}F]Ala-BF_3 was recently reported by Liu *et al.*[208] As a substrate of the system ASC amino acid transporter, [^{18}F]Ala-BF_3

Adapted with permission from: Synthesis and evaluation of an ^{18}F-labeled boramino acid analog of aminosuberic acid for PET imaging of the antiporter system x_C^-. Bioorganic & Medicinal Chemistry Letters 28 (2018) 3579–3584.

Čolović M,[1,2] Rousseau É,[1] Zhang Z,[1] Lau J,[1] Zhang CC,[1] Kuo HT,[1] Yang H,[2] Schaffer P,[2,3] Bénard F,[1,3,4] Lin KS[1,3,4]

[1] Department of Molecular Oncology, BC Cancer Agency, Vancouver, BC, V5Z 1L3, Canada
[2] Life Sciences, TRIUMF, Vancouver, BC, V6T 2A3, Canada
[3] Department of Radiology, University of British Columbia, Vancouver, BC, V5Z 1M9, Canada
[4] Department of Functional Imaging, BC Cancer Agency, Vancouver, BC, V5Z 4E6, Canada

MČ performed the *in vitro* uptake studies and PC-3 tumour-bearing animal imaging and biodistribution studies. ÉR and JL performed animal studies with probenecid treatment and HPLC analyses of mouse urine. Precursor and tracer syntheses were performed by ZZ and HTK, and plasma stability assays by CCZ. The authors thank Nadine Colpo and Navjit Hundal-Jabal for their help with μPET/CT imaging studies.

was used to successfully visualize BGC-823 stomach cancer xenografts (5.49 %ID/g at 45 min post-injection) in PET images. The synthesis and evaluation of [^{18}F]Met-BF_3, a boramino acid derivative of the clinical LAT PET tracer ^{11}C-labeled methionine ([^{11}C]MET), was reported by Yang *et al.*[209] [^{18}F]Met-BF_3 showed good uptake (>2 %ID/g at 60 min post-injection) in orthotopic C6 and U-87 glioma xenografts. Due to the low uptake of [^{18}F]Met-BF_3 in normal brain, these orthotopic tumor xenografts were clearly visualized in PET images with good contrast.

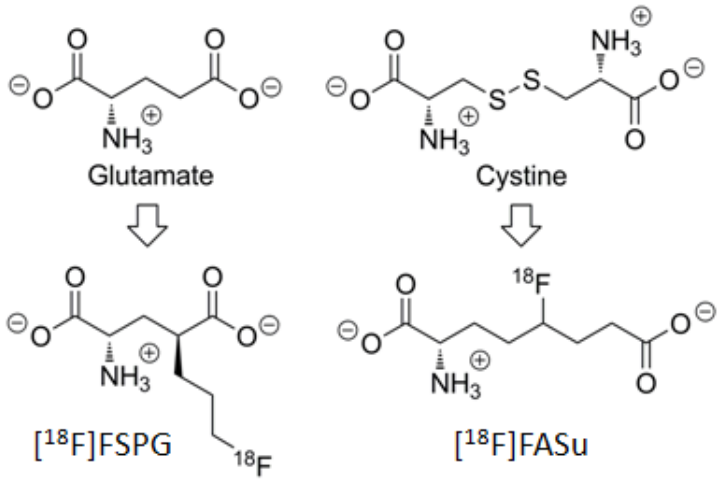

Figure 3.1 Chemical structures of glutamate and cystine, and their respective derivatives ^{18}F-FSPG and ^{18}F-FASu for imaging the system x_C^- transporter with positron emission tomography.

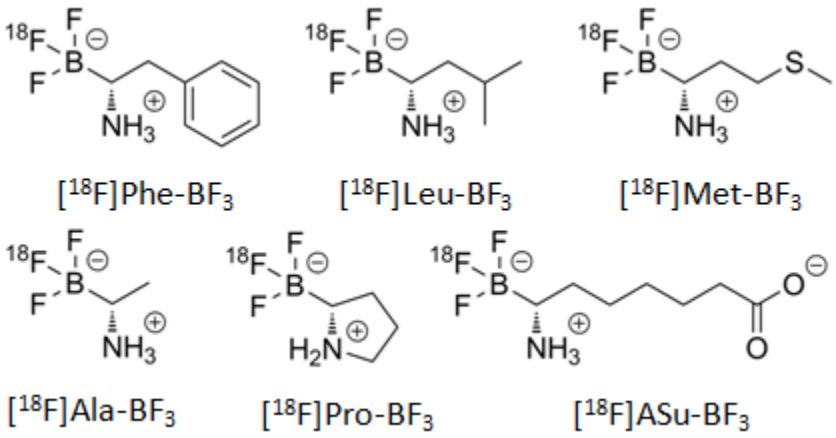

Figure 3.2 Chemical structures of ^{18}F-labeled boramino acid derivatives of Phe, Leu, Met, Ala, Pro and ASu.

The preparation of previously reported ^{18}F-labeled amino acids generally requires multiple reaction steps (^{18}F-nucleophilic or electrophilic substitution, and deprotection). On the other hand, preparation of the reported ^{18}F-labeled boramino acids involves only one reaction step: the ^{18}F-^{19}F isotope exchange on the trifluoroborate motif and no protection is required for the α-amino group. Such ease-of-synthesis prompted us to design the boramino acid derivative of aminosuberic acid (ASu), ASu-BF_3, and evaluate if [^{18}F]ASu-BF_3 could mimic ASu and be taken up into cells by the system x_C^- transporter overexpressed in cancers for PET imaging.

3.2 Materials & methods

3.2.1 Chemicals and instrumentation

Methyl 7-oxoheptanoate (**1**, Figure 3.3) was prepared according to literature procedures.[210] All other chemicals and solvents were obtained from commercial sources, and used without further purification. Purification and quality control of [^{18}F]ASu-BF_3 were performed on Agilent HPLC systems equipped with a model 1200 quaternary pump, a model 1200 UV absorbance detector (set at 220 nm), and a Bioscan (Washington, DC, USA) NaI scintillation detector. The operation of Agilent HPLC systems was controlled using the Agilent ChemStation software. The HPLC columns used were a Phenomenex (Torrance, CA, USA) semi-preparative column (Luna C18, 5 µ, 250 × 10 mm) and a Phenomenex analytical column (Luna C18, 5 µ, 150 × 4.6 mm). NMR spectra were obtained using a Bruker (Billerica, MA, USA) Avance 300 Spectrometer, and were reported in parts per million. Mass analyses were performed using an AB SCIEX (Framingham, MA, USA) 4000 QTRAP mass spectrometer system with an ESI ion source. ^{18}F-Fluoride Trap & Release columns were purchased from ORTG Inc. (Orkdale, TN, USA). ^{18}F-Fluoride was produced *via* the ^{18}O(p, n)^{18}F reaction using an Advanced Cyclotron Systems Inc. (Richmond, BC, Canada) TR19 cyclotron. Radioactivity of ^{18}F-ASu-BF_3 was measured using a Capintec (Ramsey, NJ, USA) CRC®-25R/W dose calibrator, and the radioactivity of mouse tissues collected from biodistribution studies were counted using a Perkin Elmer (Waltham, MA, USA) Wizard2 2480 automatic gamma counter.

3.2.2 Chemical syntheses

3.2.2.1 Synthesis of methyl 7-[(*R*)-2-methyl-propane-2-sulfinylimino]heptanoate (2)

To a solution of compound **1** (0.80 g, 5.0 mmol) and (*R*)-(+)-2-methyl-2-propanesulfinamide (0.73 g, 6.0 mmol) in THF (20 mL) was added $Ti(OEt)_4$ (2.1 mL, 10 mmol). The reaction mixture was stirred at room temperature overnight. Subsequently, water (30 mL) and ethyl acetate (20 mL) was added and the resultant mixture was stirred for another 5 min. The mixture was filtered through celite and the filtrate was separated in a separation funnel. The aqueous phase was washed with ethyl acetate (25 mL × 2). The combined organic phase was washed with brine (100 mL) and then dried over $MgSO_4$. The solid was removed by filtration and the volatile solvent was removed on a rotary evaporator. The residue was purified by flash chromatography (silica gel, ethyl acetate/hexanes 1:4) to provide compound **2** as a colorless oil (0.72 g, yield 55%). ^{1}H NMR (300 MHz, $CDCl_3$) δ 8.06 (t, *J* = 4.6 Hz, 1H, NC*H*), 3.67 (s, 3H, OCH_3), 2.53 (td, *J* = 7.4, 4.7 Hz, 2H, NCHCH_2), 2.32 (t, *J* = 7.4 Hz, 2H, COCH_2), 1.70 – 1.63 (m, 4H, CH_2), 1.50 – 1.32 (m, 2H, CH_2), 1.20 (s, 9H, ^{t}*Bu*). MS (ESI): $[M]^+$ calculated for $C_{12}H_{23}NO_3S$ 261.1, found $[M+H]^+$ 262.2.

3.2.2.2 Synthesis of methyl (*S*)-[7-(4,4,5,5-tetramethyl-1,3,2-dioxaborolan-2-yl)-7-((*R*)-2-methyl-propane-2-sulfinylamino)]heptanoate

$PCy_3 \cdot HBF_4$ (13.2 mg, 0.04 mmol), $CuSO_4$ (5.7 mg, 0.04 mmol), water (1.2 mL), toluene (0.6 mL) and benzylamine (16.2 μL, 0.15 mmol) were mixed and stirred at room temperature for 10 min. Compound **2** (0.72 g, 2.7 mmol) in toluene (5.0 mL) was added followed by bis(pinacolato)diboron (1.52 g, 6.0 mmol). The resultant mixture was stirred at room temperature overnight. 50 mL of ethyl acetate was added the reaction mixture and the suspension was passed through a short pad of silica gel. The silica gel was washed with ethyl acetate (20 mL × 3). The combined filtrate was evaporated and the residue was purified by flash chromatography (silica gel, ethyl acetate/CH_2Cl_2 1:4) to provide compound **3** as a colorless oil (0.47 g, yield 45%). ^{1}H NMR (300 MHz, $CDCl_3$) δ 3.66 (s, 3H, OCH_3), 3.23 (d, *J* = 6.9 Hz, 1H, N*H*), 3.01 (q, *J* = 7.0 Hz, 1H, NHC*H*), 2.30 (t, *J* = 7.5 Hz, 2H, COCH_2), 1.80 – 1.61 (m, 6H, CH_2), 1.38 – 1.34 (m, 2H, CH_2), 1.27 (s, 12H, CCH_3), 1.19 (s, 9H, ^{t}*Bu*). MS (ESI): $[M]^+$ calculated for $C_{18}H_{36}BN_5OS$ 389.2, found $[M+H]^+$ 390.3.

3.2.2.3 Synthesis of (*S*)-(7-trifluoroboryl-7-ammonio)heptanoic acid (ASu-BF_3)

To a solution of **3** (50.0 mg, 0.51 mmol) in 0.8 mL of acetonitrile, KHF_2 (0.86 mL, 3 M, 2.6 mmol) was added followed by HCl (0.77 mL, 4 M, 3.1 mmol). The reaction mixture was stirred at 45°C for 2 h. After incubation, volatile solvents were removed under reduced pressure. Acetonitrile (6 mL) was added and the suspension was filtered. The solid was washed with acetonitrile (3 mL × 3). The combined filtrate was evaporated to dryness. The crude product was purified by HPLC (Luna C18 semi-prep column, 4.5 mL/min, 8% acetonitrile (0.1% TFA) and 92% water (0.1% TFA), retention time 13.2 min) to provide ASu-BF_3 as a white powder (21.6 mg, yield 79%). ^{1}H NMR (300 MHz, Acetone) δ 10.55 (s, 1H, COO*H*), 7.09 – 6.32 (m, 3H, N*H*$_3$), 2.28 (t, *J* = 7.4 Hz, 2H, COC*H*$_2$), 2.22 (s, 1H, BC*H*), 1.77 – 1.54 (m, 4H, C*H*$_2$), 1.53 – 1.41 (m, 2H, C*H*$_2$), 1.41 – 1.26 (m, 2H, C*H*$_2$). ^{19}F NMR (282 MHz, Acetone) δ -75.45 (TFA), -151.26 (B*F*$_3$). MS (ESI): $[M]^+$ calculated for $C_7H_{15}BF_3NO_2$ 213.1, found $[M+H]^+$ 214.2.

3.2.3 Radiosynthesis of [^{18}F]ASu-BF_3

^{18}F-Fluoride (51.8 – 70.3 GBq) was trapped on an ^{18}F Trap & Release cartridge. Pyridazine-HCl buffer (1M, pH 2.0, 0.1 mL) was passed through the cartridge to elute ^{18}F-fluoride into a 6-mL falcon tube preloaded with ASu-BF_3 (100 nmol) and KHF_2 (0.08 μL, 0.127 M, 10 nmol) in DMF (15 μL). The reaction mixture was incubated at 80°C for 5 min and then for additional 15 min under vacuum. At the end of the incubation, the reaction mixture was diluted with 1.5 mL water. The resultant mixture was directly purified by semi-prep HPLC using 0.5% EtOH in 20 mM ammonium acetate (pH 5.0) with a flow rate at 4.5 mL/min. The retention time of ^{18}F-ASu-BF_3 was 35.0 min. The collected [^{18}F]ASu-BF_3 was further diluted with PBS to appropriate concentration for animal studies. QC was performed on the analytical column using 0.5% EtOH in 20 mM ammonium acetate (pH 5.0) with flow rate at 2 mL/min. The retention time of ^{18}F-ASu-BF_3 was 12.0 min.

3.2.4 *In vivo* stability in mouse plasma

The in vitro stability of [^{18}F]ASu-BF_3 was measured following literature procedures.[211,212] Briefly, aliquots of [^{18}F]ASu-BF_3 (100 μL, ~ 300 μCi) were mixed with 400

µL of BALB/c mouse plasma (Innovative Research, Novi, MI, USA) and then incubated at 37 °C for pre-determined time points (5, 15, 30 and 60 min). At the end of each incubation period, 0.5 mL of acetonitrile was added to each sample to precipitate the proteins in plasma. The samples were centrifuged and the supernatants were passed through a 0.22 micron filter to further remove particulates. The filtrates were loaded onto the semi-preparative HPLC to check the percentage of intact [^{18}F]ASu-BF$_3$ using 8% acetonitrile (0.1% TFA) and 92% water (0.1% TFA) with a flow rate at 2 mL/min. The retention time of [^{18}F]ASu-BF$_3$ was 12.5 min.

3.2.5 Cell uptake assays

A cell based uptake study was performed following literature procedures.[102,103,139] PC-3 cells were seeded in 24-well plates at 60,000 cells/well 24 h before the experiment. On the day of the experiment, the cells were washed twice with HEPES Basal Salt Solution and incubated with [^{18}F]ASu-BF$_3$ (~148 kBq) in HEPES solution (400 µL) in the absence or presence of 1 mM of the system x_C^- inhibitor (SSZ or ASu) for 60 min at 37 °C. Afterwards, the supernatant was collected, and cells were washed with cold HEPES buffer and lysed with 1 M NaOH. The wells were washed one last time, to collect any residual activity. The radioactivity of the lysates, washes and supernatant samples were counted on a gamma counter. The assay was performed in triplicates and uptake values were normalized to cell number.

3.2.6 Biodistribution and PET/CT imaging studies in PC-3 tumour-bearing mice

Animal studies were conducted in accordance with the guidelines established by the Canadian Council on Animal Care and approved by the Animal Ethics Committee of the University of British Columbia. Biodistribution and PET/CT imaging studies were conducted following previously published procedures.[213] Male NOD.*Cg-Prkdc^{scid}Il2rg^{tm1Wjl}*/SzJ (NSG) immunocompromised mice were purchased from in-house colonies at the Animal Research Centre, BC Cancer, Vancouver, Canada. Following isoflurane anesthesia (2% isoflurane in oxygen), mice were subcutaneously injected with 5×10^6 PC-3 cells (in 100 µL PBS and matrigel at 1:1 ratio) under the left dorsal flank. PET/CT imaging and biodistribution studies were conducted three weeks after tumor inoculation.

For biodistribution study, mice were anesthetized by inhalation of 2% isoflurane in oxygen and injected with ~3.2 – 4.8 MBq of [^{18}F]ASu-BF_3. After 1 h, the mice were euthanized by CO_2 asphyxiation after isoflurane inhalation. Blood was promptly drawn via cardiac puncture, and organs/tissues were harvested, rinsed with PBS, blotted dry and weighted. The radioactivity of the collected samples was counted on the gamma counter and normalized to injected dose and organ weight. The presented values are expressed in %ID/g (percentage of injected dose per gram of tissue).

PET/CT imaging experiments were conducted using a Siemens (Knoxville, TN, USA) Inveon μPET/CT scanner. Mice bearing PC-3 tumors as described above were used. For dynamic imaging study, the mice were sedated with 2% isoflurane in oxygen inhalation and positioned in the scanner. A baseline CT scan was obtained for localization and attenuation correction before radiotracer injection, using 60 kV X-rays at 500 mA, three sequential bed position with 33% overlap, and 220 degree continuous rotation. The mice were kept warm by a heating pad during acquisition. The dynamic acquisition of 60 min was started at the time of intravenous injection with 5.6 – 8.3 MBq of [^{18}F]BF_3-ASu. The list mode data were rebinned into time intervals (12 × 10 sec, 6 × 30 sec, 5 × 60 sec, 6 × 300 sec, and 2 × 600 sec) to obtain tissue time-activity curves. Images were reconstructed using the 3-dimensional ordered-subsets expectation maximization (OSEM3D, 2 iterations) followed by a fast maximum a priori algorithm (FastMAP: 18 iterations). The mice were euthanized at the end of imaging section, and their tissues were not used in the biodistribution study.

For the static imaging study, mice were briefly sedated for intravenous injection of the radiotracer (7.1 – 9.3 MBq), and then allowed to recover and roam freely in their cages. Just before imaging, the mice were sedated with 2% isoflurane in oxygen inhalation and placed on the scanner. An attenuation correction CT scan was obtained as described above, followed by a single static emission scan that was acquired for 13 min at ~1 h post-injection. Images were reconstructed in one frame using the reconstruction parameters described above. The mice were euthanized and the organs/tissues were harvested for biodistribution as described above.

3.2.7 Biodistribution studies of [^{18}F]ASu-BF$_3$ in mice with/without probenecid treatment

Probenecid (12.5 mg) was reconstituted in a 1 M NaOH solution (65 µL), adjusted to pH ~7 by addition of HCl (1 M), and then diluted in PBS to a final concentration of 12.6 mg/mL. NSG mice were divided in two groups: the control group received only [^{18}F]ASu-BF$_3$ (1.35 ± 0.60 MBq), and the probenecid group received 50 mg/kg i.v. of the probenecid solution 10 min before [^{18}F]ASu-BF$_3$ (1.49 ± 0.58 MBq) administration. The procedures for injection and biodistribution are the same as stated above with biodistribution time points at 10, 20, and 30 min post tracer injection except that no anesthesia was used for i.v. injections. Analysis was performed with R 3.4.0 (R Foundation for Statistical Computing, Vienna, Austria) and GraphPad Prism version 7.0a (GraphPad Software, La Jolla, California, USA). Both groups were compared at each time-point using Wilcoxon's rank sum test.

3.2.8 Quantification of metabolites of [^{18}F]ASu-BF$_3$ in mouse urine

NSG mice (n = 3) were injected with [^{18}F]ASu-BF$_3$ (5.34 ± 0.12 MBq) *via* tail vein injection without anesthesia as described above. At 30 min post-injection, the mice were sacrificed and urine samples were collected. The urine samples were analyzed by HPLC using the analytical column. The solvent conditions were 0.5% EtOH in 20 mM ammonium acetate (pH 5.0) with flow rate at 2 mL/min. The retention time of [^{18}F]ASu-BF$_3$ was 11.6 min.

3.3 Results & discussion

Synthesis of ASu-BF$_3$ was modified from the strategy developed by Beenen *et al.*[214] *via* the asymmetric copper-catalyzed synthesis of α-amino boronate esters from *N*-*tert*-butanesulfinyl aldimines. As depicted in Scheme 3.1A, reaction of methyl 7-oxoheptanoate **1** [210] with (*R*)-(+)-2-methyl-2-propanesulfinamide in the presence of titanium(IV) ethoxide afforded the sulfinamide **2** in 55% yield. Subsequent reaction of **2** with bis(pinacolato)diboron in a mixture of water/toluene in the presence of tricyclohexylphosphine tetrafluoroborate, copper(II) sulfate, and benzylamine led to the boronic acid pinacol ester **3** in 45% yield. Treating compound **3** with hydrochloric acid in the presence of excess potassium hydrogen difluoride converted boronate

ester into trifluoroborate with concomitant hydrolysis of the methyl ester and sulfinamide groups. The desired ASu-BF_3 was obtained in 79% yield.

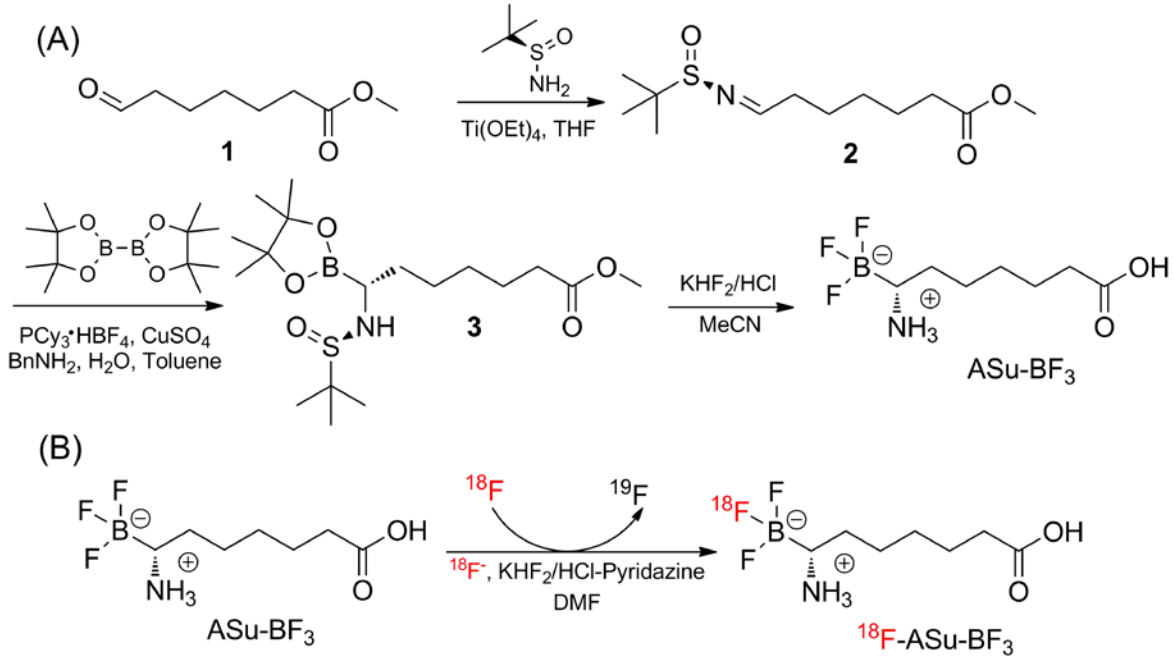

Figure 3.3 Synthesis of (A) nonradioactive and (B) ^{18}F-labeled ASu-BF_3.

The radiolabeling of ASu-BF_3 with ^{18}F was conducted *via* ^{18}F-^{19}F isotope exchange reaction (Figure 3.3B) following similar reaction conditions reported previously.[215–219] After incubating ASu-BF_3 (100 nmol), KHF_2 (10 nmol) and ^{18}F-fluoride (51.8 – 70.3 GBq) in pyridazine-HCl buffer (pH 2) at 80 ^{o}C for 20 min, the reaction mixture was purified by HPLC. The desired ^{18}F-labeled ASu-BF_3 was obtained in 25.5 ± 9.7% (n = 5) decay-corrected radiochemical yield with > 96% radiochemical purity. The stability of [^{18}F]ASu-BF_3 was first assessed in mouse plasma and monitored by HPLC over time. As shown in Figure 3.4, no observable metabolites of [^{18}F]ASu-BF_3 were formed after incubation in mouse plasma at 37°C for up to 60 min.

Cell uptake assays for ASu-BF_3 were conducted using PC-3 prostate cancer cells as the model. The PC-3 cell line was selected as it has been shown that OS is inherent in prostate cancer cells and is required for their aggressive phenotype.[220] The comparison of different prostate cancer cell lines indicated that PC-3 cells produced significantly higher amounts of ROS including hydrogen peroxide and superoxide than LNCaP and DU145 cells.[220] Furthermore, as

reported by Koglin *et al*. the uptake of the system x_C^- PET tracer [^{18}F]FSPG was higher in PC-3 tumour xenografts than those derived from other cell lines including melanoma (SKMEL3 and A375), lung (H460 and A549), prostate (LNCaP and DU145), breast (MCF-7) and ovarian (SKOV3) cancers.[139]

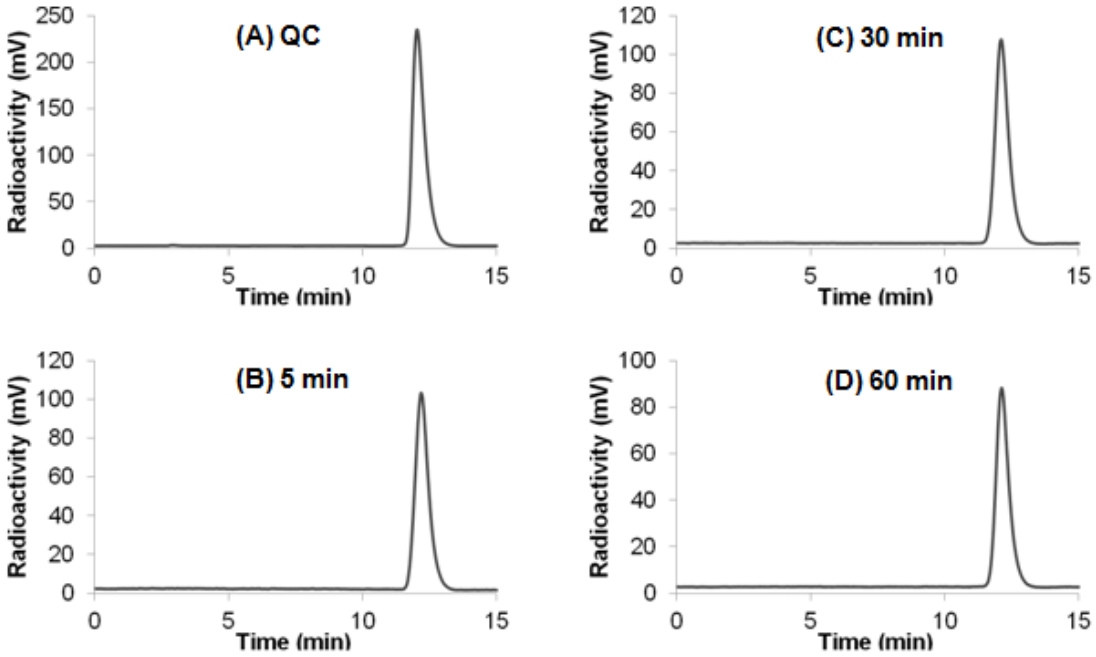

Figure 3.4 HPLC chromatograms of (A) [^{18}F]ASu-BF_3 QC sample , and [^{18}F]ASu-BF_3 samples after being incubated in mouse plasma for (B) 5 min; (C) 30 min and (D) 60 min.

As shown in Figure 3.5A, the uptake of [^{18}F]ASu-BF_3 into PC-3 cells increased steeply in the first 15 min, after which it remained relatively constant at ~0.45% uptake per 100,000 cells throughout the study (up to 60 min). Therefore, the 60 min time point was selected as the incubation time for the subsequent inhibition assays. The inhibition assays were conducted under the same conditions in the presence of HEPES buffer (control) or 1 mM of a system x_C^- inhibitor (sulfasalazine (SSZ) or ASu). As shown in Figure 3.5B, the presence of SSZ or ASu reduced ~45% and 58% uptake of [^{18}F]ASu-BF_3 into PC-3 cells, respectively, when compared to those in the control group, confirming that [^{18}F]ASu-BF_3 is a substrate of the system x_C^- transporter.

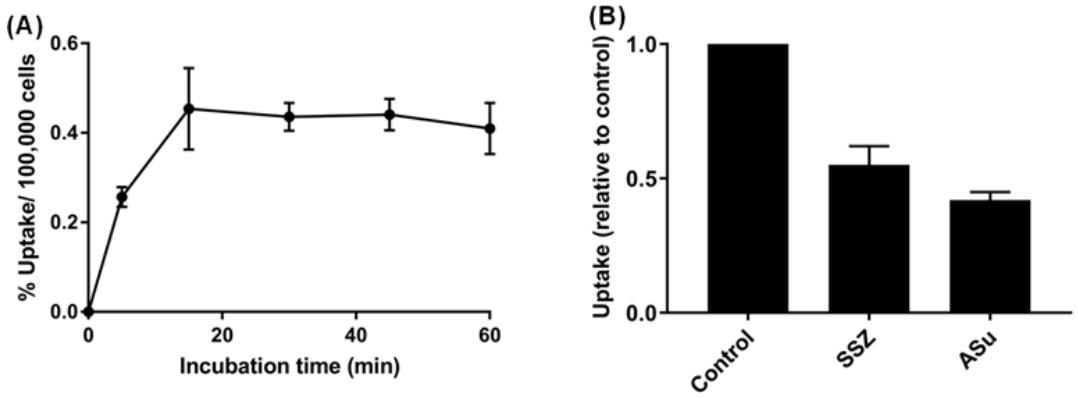

Figure 3.5 *In vitro* evaluation of [^{18}F]ASu-BF$_3$. (A) Cell uptake of [^{18}F]ASu-BF$_3$ into PC-3 cells over time. Uptake values are expressed as percentage of the total added radioactivity per 100,000 cells (mean ± SD, n = 3). (B) Uptake inhibition of [^{18}F]ASu-BF$_3$ into PC-3 cells induced by 1 mM of SSZ and ASu. The uptake values (mean ± SD, n = 3) are normalized to the uptake of ^{18}F-ASu-BF$_3$ in the control group without the addition of inhibitor.

PET imaging and biodistribution studies were conducted in mice bearing PC-3 tumour xenografts. As shown in Figure 3.6A, the PC-3 tumour xenograft was visualized in dynamic PET images along with high background radioactivity level especially in the kidneys. As the time-activity curves show in Figure 3.6B, the uptake in kidneys increased quickly in the first 4 min and reached its peak value at 30.5%ID/g. The kidney uptake decreased gradually from 5 – 15 min to ~20 %ID/g, and then remained roughly at the same level until the end of dynamic imaging study. The uptake values for heart, liver, and brain reached their highest at ~ 1.5 min (to 22.7, 8.72, and 1.63 %ID/g, respectively), dropped quickly in the next 5 min (2 – 7 min), and then reduced very slowly afterwards. The uptake values of tumour, muscle and bone peaked at 3.55, 1.67 and 1.19 %ID/g, respectively, at ~ 5 min post-injection and decreased slowly afterwards. The clear visualization of the PC-3 tumour xenografts was achieved due to the sustained higher uptake of [^{18}F]ASu-BF$_3$ into tumour than the surrounding tissues (muscle).

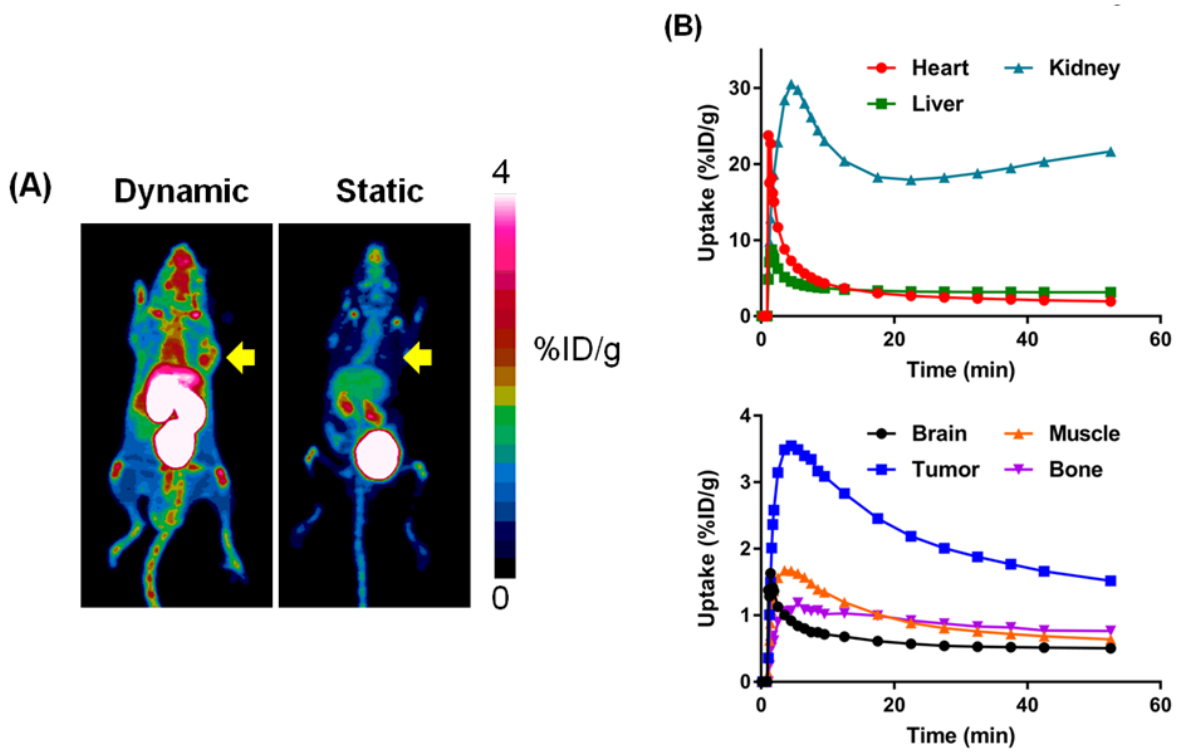

Figure 3.6 *In vivo* evaluation of [^{18}F]ASu-BF$_3$.(A) Representative dynamic (left) and static (right) maximum-intensity-projection PET images of [^{18}F]ASu-BF$_3$ in PC3-tumor-bearing mice taken at 60 min post-injection. (B) Time-activity curves of [^{18}F]ASu-BF$_3$ in major organs and PC3 tumor based on ROIs drawn from dynamic imaging data.

Unlike the clear tumour visualization and high background radioactivity level observed in dynamic PET images, static images of [^{18}F]ASu-BF$_3$ taken at 1 h post-injection revealed no tumor visualization along with very low and clean background (Figure 3.6A). Biodistribution study at 1 h post-injection confirmed the observations from static images, and the results are shown in Figure 3.7 and Table 3.1. The uptake of [^{18}F]ASu-BF$_3$ in the PC-3 tumour was only 0.58 ± 0.20 %ID/g, and was not different from muscle uptake (0.54 ± 0.37 %ID/g), leading to no tumour visualization in the static images. The biodistribution data also reveals very rapid excretion of [^{18}F]ASu-BF$_3$ by the renal pathway, as indicated by high radioactivity collected in the urine (up to ~90% ID, data not shown) at 60 min post-injection. Not much radioactivity remained in the collected organs/tissues at 60 min post-injection except in kidneys (2.82 ± 1.17 %ID/g), liver (2.18 ± 0.82 %ID/g) and bone (2.43 ± 0.66 %ID/g).

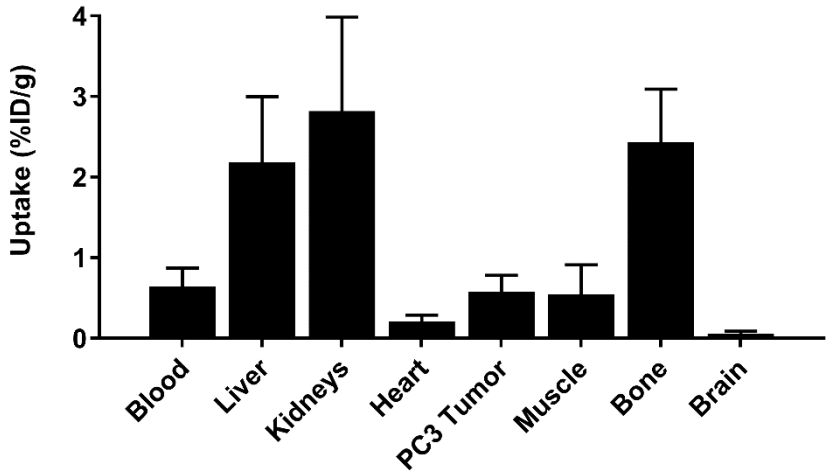

Figure 3.7: Biodistribution data of [^{18}F]ASu-BF_3 in selected organs for PC3 tumour-bearing mice at 1 h post-injection.

Table 3.1 Biodistribution data of [^{18}F]ASu-BF_3 in PC-3 tumour-bearing mice at 1 h post-injection.

Organ/tissue	**Uptake (mean ± SD %ID/g, n = 5)**
blood	0.64 ± 0.23
fat	0.11 ± 0.04
small intestine	0.84 ± 0.25
stomach	0.09 ± 0.03
pancreas	0.20 ± 0.09
spleen	0.23 ± 0.12
liver	2.18 ± 0.82
adrenal glands	0.21 ± 0.12
kidneys	2.82 ± 1.17
heart	0.21 ± 0.08
lungs	0.35 ± 0.13
PC-3 tumour	**0.58 ± 0.20**
muscle	0.54 ± 0.37
bone	2.43 ± 0.66
brain	0.06 ± 0.03

Our data suggest that the discrepancy on tumour visualization between dynamic and static imaging was due to the extremely fast excretion of [^{18}F]ASu-BF_3 in mice used in the static imaging study. This phenomenon was not observed previously using the system x_C^- tracer [^{18}F]FASu.[102,103] The prolonged anaesthesia with isoflurane used for the dynamic imaging study slowed down the excretion of [^{18}F]ASu-BF_3, leading to tumour visualization and also high retention in major organs/tissues especially in the kidneys. We hypothesized that the excretion of [^{18}F]ASu-BF_3 in mice without prolonged anaesthesia could be facilitated by the action of the organic anion transporter that is involved in the excretion of the renal imaging tracer [^{99m}Tc]MAG3.[221]

To verify our hypothesis, additional biodistribution studies were conducted in mice with/without pretreatment with the organic anion transporter inhibitor probenecid (50 mg/kg IV, 10 min before tracer injection). Because of postulated interference of isoflurane anesthesia on excretion, these mice were injected with the inhibitor and/or [^{18}F]ASu-BF_3 without the application of anaesthesia. As shown in Figure 3.8 and Table 3.2, the probenecid pretreatment reduced renal uptake of [^{18}F]ASu-BF_3, and increased its retention in other tissues/organs at evaluated time points (10, 20 and 30 min). To verify the chemical identity of the excreted radioactivity, additional mice were injected with [^{18}F]ASu-BF_3, and urine samples were collected at 30 min post-injection and analyzed by HPLC. As shown by the radio-HPLC chromatograms provided in the Figure 3.9, > 90% of the radioactivity excreted into urine was the intact [^{18}F]ASu-BF_3. The remaining ^{18}F-labeled compounds were ^{18}F-fluoride (3.0 – 4.5%) and an unidentified metabolite (4.9 – 5.1%) eluted with the retention time at 2.5 min. Taken together, our data indicate that [^{18}F]ASu-BF_3 is stable *in vivo* and its extremely fast renal excretion is at least in part mediated by the organic anion transporter.

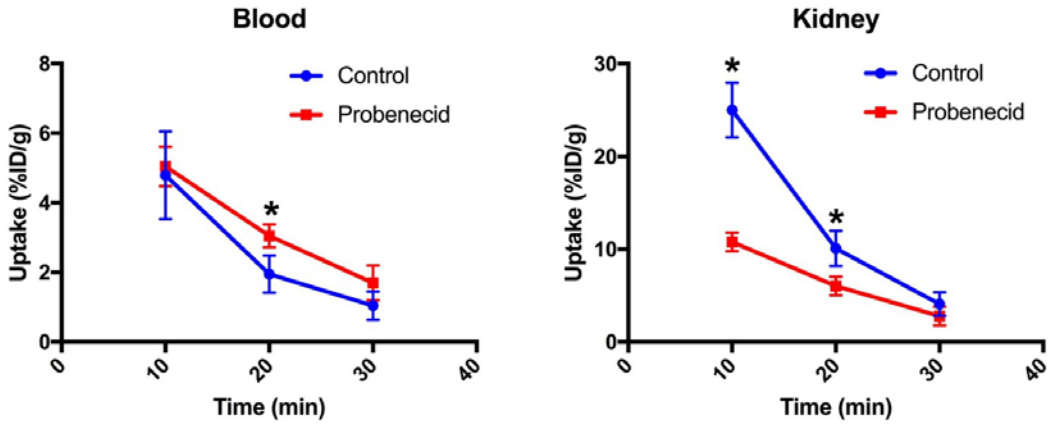

Figure 3.8 Uptake values of [^{18}F]ASu-BF_3 in blood and kidneys with/without probenecid treatment (* $p < 0.05$).

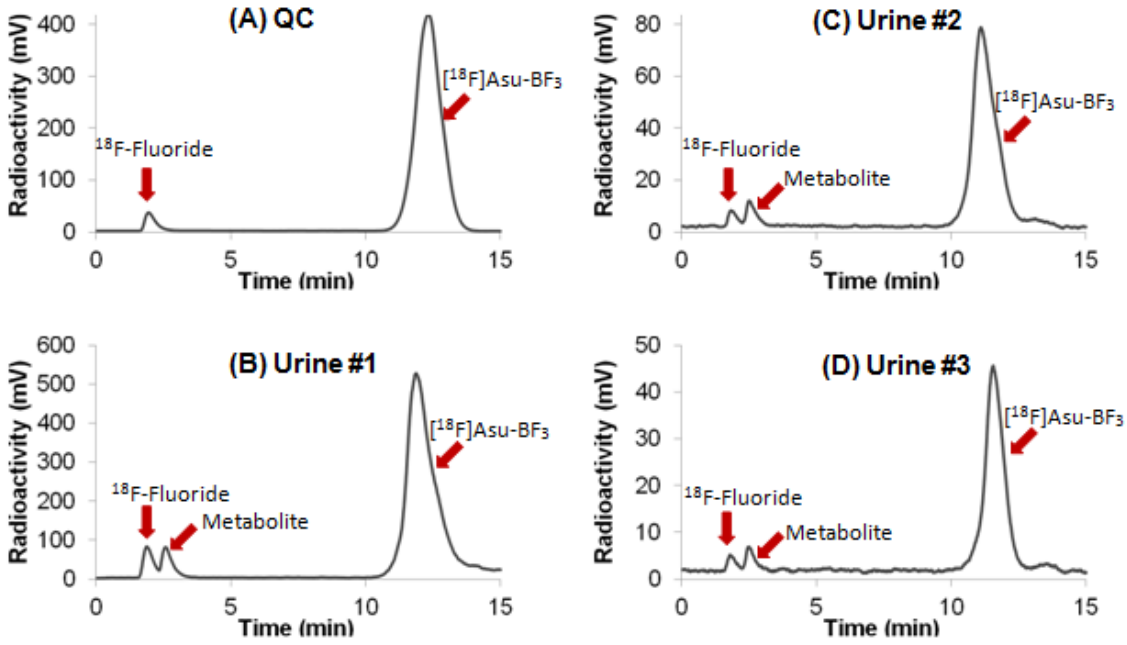

Figure 3.9: HPLC chromatograms of (A) [^{18}F]ASu-BF_3 QC sample, and urine samples collecetd from three separate mice (B-D) at 30 min post-injection.

Table 3.2 Biodistribution data (mean ± SD %ID/g, n = 4) of [^{18}F]ASu-BF_3 in mice without (control) or with probenecid treatment (50 mg/kg) 10 min before the tracer injection.

Organ/Tissue	10 min		20 min		30 min	
	Control	Probenecid	Control	Probenecid	Control	Probenecid
Blood	4.79 ± 1.26	5.04 ± 0.57	1.95 ± 0.53	3.05 ± 0.33	1.04 ± 0.41	1.70 ± 0.50
Fat	0.28 ± 0.04	0.40 ± 0.07	0.13 ± 0.04	0.22 ± 0.04	0.09 ± 0.04	0.15 ± 0.08
Intestines	1.33 ± 0.32	1.66 ± 0.28	0.68 ± 0.20	1.08 ± 0.09	0.45 ± 0.15	0.79 ± 0.23
Stomach	0.55 ± 0.17	0.80 ± 0.21	0.25 ± 0.14	0.35 ± 0.09	0.12 ± 0.06	0.21 ± 0.10
Spleen	1.57 ± 0.64	1.64 ± 0.64	0.74 ± 0.30	1.02 ± 0.22	0.42 ± 0.28	0.61 ± 0.31
Liver	2.20 ± 0.35	2.93 ± 0.43	1.03 ± 0.29	1.91 ± 0.29	0.60 ± 0.20	1.19 ± 0.20
Pancreas	1.26 ± 0.32	1.15 ± 0.23	0.64 ± 0.22	0.75 ± 0.07	0.30 ± 0.11	0.43 ± 0.08
Adrenal	0.81 ± 0.24	0.95 ± 0.28	0.40 ± 0.11	0.61 ± 0.08	0.26 ± 0.16	0.41 ± 0.14
Kidneys	25.0 ± 2.97	10.8 ± 0.83	10.1 ± 1.89	6.05 ± 1.14	4.08 ± 1.29	2.80 ± 0.67
Lungs	3.05 ± 0.47	3.81 ± 0.89	1.37 ± 0.40	2.22 ± 0.24	0.61 ± 0.21	1.25 ± 0.30
Heart	1.28 ± 0.11	1.44 ± 0.09	0.60 ± 0.11	0.90 ± 0.09	0.26 ± 0.08	0.52 ± 0.08
Muscle	0.91 ± 0.14	1.27 ± 0.60	0.38 ± 0.07	0.55 ± 0.01	0.39 ± 0.34	0.37 ± 0.15
Bone	1.59 ± 0.34	1.51 ± 0.35	1.04 ± 0.35	1.23 ± 0.18	0.92 ± 0.46	0.91 ± 0.20
Brain	0.11 ± 0.03	0.11 ± 0.02	0.06 ± 0.02	0.08 ± 0.01	0.05 ± 0.02	0.07 ± 0.03

3.4 Conclusion

In summary, we successfully synthesized [^{18}F]ASu-BF_3, a close boramino acid analogue of [^{18}F]FASu, *via* a facile one-step ^{18}F-^{19}F isotope exchange reaction. [^{18}F]ASu-BF_3 was stable in mouse plasma and, similar to [^{18}F]FASu, can be taken up into cells via the system x_C^- amino acid transporter. A dynamic imaging study showed that the continuous use of isoflurane for anaesthesia slowed down the pharmacokinetics of [^{18}F]ASu-BF_3, leading to visualization of PC-3 tumour xenografted in mice. In contrast, the mice under brief anaesthesia during tracer injection and static imaging at 60 min post-injection had much faster renal excretion of [^{18}F]ASu-BF_3, resulting in no tumour visualization in static PET images. Biodistribution studies with/without probenecid treatment confirmed that the renal excretion of [^{18}F]ASu-BF_3 can be mediated by the organic anion transporter. The extremely fast renal excretion of [^{18}F]ASu-BF_3 was not observed using the previously reported [^{18}F]FASu, indicating the discrepancy of pharmacokinetics between [^{18}F]FASu and its close boramino acid analogue [^{18}F]ASu-BF_3. Therefore, care should be taken when using the boramino acid strategy to design and prepare ^{18}F-labeled tracers for imaging amino acid transporters/receptors with PET.

Chapter 4: The effect of chirality on the application of [^{18}F]5-fluoro-aminosuberic acid ([^{18}F]FASu) for oncological PET imaging

4.1 Introduction

There is compelling evidence that amino acid availability regulates cellular physiology by modulating gene expression as well as signal transduction pathways in cancer cells.[129] Recent literature reports that (over)expression of amino acid transporters carries prognostic,[126,128,129,170,183,222] as well as potentially therapeutic[188,192] significance in cancer patients. Thus, it is not surprising that radiolabelled amino acids have been identified as promising positron emission tomography (PET) imaging agents.[169]

A variety of ^{18}F-labelled amino acid radiopharmaceuticals have been developed, particularly non-natural amino acid structures that are close analogues of the natural amino acids. Non-natural amino acids have increased stability *in vivo*, avoiding potentially confounding accumulation of activity in non-target tissues due to the distribution of radioactive metabolites, and simplifying kinetic analysis.[167] Radiofluorinated amino acids, like their natural counterparts, may also have chiral centres which result in formation of multiple stereoisomers, the biodistribution and tumour uptake of which might differ between congeners. For instance, four stereospecific ^{18}F-labelled 4-fluoro-glutamine (4-FGln) isomers have been synthesized and evaluated in brain tumour models, and it was found that *in vitro* uptake is highly specific for only two of the *L*-glutamine analogues, (2*S*,4*R*)-[^{18}F]FGln and (2*S*,4*S*)-[^{18}F]FGln.[223] Between them,

---

Adapted by permission from: The Effect of Chirality on the Application of [^{18}F]5-Fluoroaminosuberic Acid for Oxidative Stress Imaging. Mol Imaging Biol. (2019). https://doi.org/10.1007/s11307-019-01450-2. [E-pub ahead of print]. Copyright (2019) Springer Nature.

M Čolović,[1,2] H Yang,[1] H Merkens,[2] N Colpo,[2] F Benard,[2,3] P Schaffer.[1,3,4]

[1] Life Sciences Division, TRIUMF, Vancouver, British Columbia, Canada
[2] Department of Molecular Oncology, BC Cancer Research Centre, BC Cancer, Vancouver, BC, Canada
[3] Department of Radiology, Faculty of Medicine, University of British Columbia, Vancouver, BC, Canada
[4] Department of Chemistry, Faculty of Science, Simon Fraser University, Burnaby, BC, Canada

MČ and HY designed the study and were involved in experimentation together with HM and NC. **MČ** wrote the manuscript.

(2*S*,4*R*)-[^{18}F]FGln was selected as the leading probe for further biological evaluation[223] and it has shown promise in a recent clinical study with breast cancer patients.[224] In contrast, the *D*-isomer of an artificial neutral amino acid *O*-[^{18}F]fluoromethyltyrosine (*D*-[^{18}F]FMT) was found to provide better tumour-to-background contrast, as compared to the counterpart, due to different susceptibility to physiological concentrations of extracellular amino acids and excretion rates of these two FMT isomers from various organs.[225]

We have developed an optically active amino acid radiotracer, [^{18}F]-5-fluoroaminosuberic acid ([^{18}F]FASu), which exhibits uptake specific to the cystine/glutamate antiporter system x_C^-.[102,103,226] [^{18}F]FASu has two chiral centers, at the 2- and 5- positions, yielding a total of four stereoisomers on synthesis (Figure 4.1). We have recently demonstrated the synthesis of optically pure 2*S*-[^{18}F]FASu from chiral precursors and initial studies uncovered that the uptake of the 2*S*- isomers was preferred over the 2*R*- isomers.[195] The objectives of the present work, therefore, are to separate and radiolabel the 5- position isomers (2*S*,5*R*-[^{18}F]FASu and 2*S*,5*S*-[^{18}F]FASu) of 2*S*-[^{18}F]FASu and evaluate the potential value of the optically pure 5-position diastereomers in comparison with the racemate (2*S*,5*R/S*-[^{18}F]FASu) in xenograft-bearing mice.

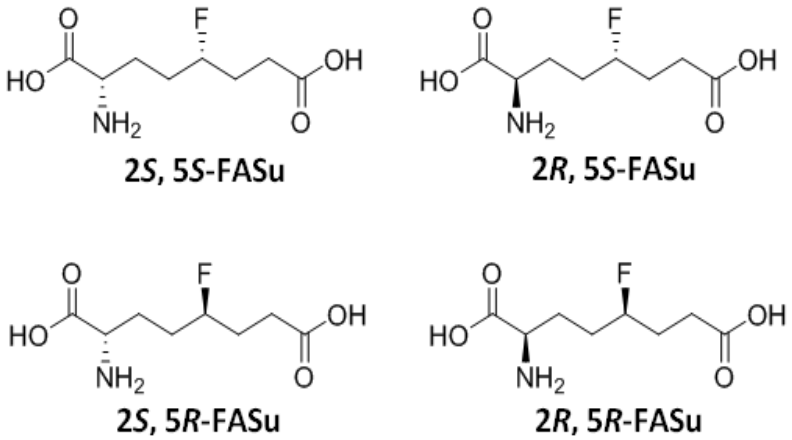

Figure 4.1 Chemical structures of 5-fluoro-aminosuberic acid (FASu) isomers in four stereoisomeric configurations. *Copyright © 2019, Springer Nature*

4.2 Materials & methods

4.2.1 Tracer synthesis and purification

The synthesis of pure 2*S*,5*R/S*-[^{18}F]FASu was previously reported.[195] Briefly, a protected 2*S*-5-tosylate precursor (5-OTs) was first synthesized and resolved by chiral HPLC. The 5-position isomers of 5-OTs were subsequently separated using a Phenomenex amylase-1 column into two single 5-position enantiomers. Each enantiomer was then radiolabeled using K2.2.2/K_2CO_3 method. The optimal radiolabeling conditions involved using TBA-HCO_3, DMSO and labeling for 15 min at 95°C, which maximized yield and optical purity.[195] The 5-position diastereomers were confirmed by HPLC using a cellulose-1 column (MeCN:H_2O = 45:55 isocratic, 1 ml/min) and their configurations were resolved by applying Mosher's method combined with 2D NMR. Quality control data from each production are shown in Table 4.1.

Table 4.1 Summary of quality control data for each [^{18}F]FASu production run. *Copyright © 2019, Springer Nature*

Radiotracer	Tumor	% Decay-corrected radiochemical yield[£]	% Radiochemical purity	Molar Activity (MBq/μmol)
2*S*,5*S*-[^{18}F]FASu	MDA-MB-231	9.3	97	74
2*S*,5*R*-[^{18}F]FASu	MDA-MB-231	11.8	99	84
2*S*,5*R/S*-[^{18}F]FASu	PC-3	6.7	97	62
2*S*,5*S*-[^{18}F]FASu	PC-3	8.0	98	71
2*S*,5*R*-[^{18}F]FASu	PC-3	5.8	98	53
2*S*,5*R/S*-[^{18}F]FASu	U-87	4.9	99	40
2*S*,5*S*-[^{18}F]FASu	U-87	2.8	97	54
2*S*,5*R*-[^{18}F]FASu	U-87	3.4	96	56

[£]yield calculated as purified final product over F-18 obtained from target, decay corrected.

4.2.2 Cell culture

All cell lines used in this study were authenticated by DCC Medical. MDA-MB-231 triple-negative breast cancer cells were obtained as a gift from Dr. Connie Eaves (BC Cancer, Vancouver, Canada). Glioblastoma U-87 cell line and prostate cancer PC-3 cells were obtained from ATCC. The cells were cultured in their respective media supplemented with 10% fetal

bovine serum and 100 U/mL penicillin-streptomycin. MDA-MB-231 cells were maintained in Dulbecco's Modified Eagle's Medium (DMEM); U-87 cells in Roswell Park Memorial Institute (RPMI) 1640 Medium; and PC-3 cells in F12K Medium.

In vitro uptake studies were performed according to previously reported procedures.[102,103,227] Briefly, the cells were seeded in 24-well plates and were cultured until reaching ~85% confluency. Cells were then washed twice with HEPES Basal Salt Solution and incubated with [^{18}F]FASu (~148 kBq) in HEPES solution (400 µl) in the absence or presence of 1 mM of the system x_C^- inhibitor sulfasalazine (SSZ) for 60 min at 37°C. The supernatant was collected, and cells were washed with cold HEPES buffer and lysed with 1 M NaOH solution. The wells were washed with cold HEPES one last time, to collect any residual activity. The radioactivity of the lysates, washes and supernatant samples were recorded using a Perkin Elmer Wizard 2480 gamma counter. The assay was performed in triplicates and uptake values were normalized to protein concentration as determined using Pierce BCA Protein Assay Kit (Thermofisher Scientific).

4.2.3 Western blotting

MDA-MB-231, U-87 and PC-3 cells were routinely sub-cultured in Petri-dishes and were collected upon reaching ~85% confluency. The cells were disrupted with cold RIPA buffer supplemented with protease inhibitors and the lysates were collected after centrifugation at 16,000 RPM, 20 min at 4°C. Protein quantification was performed using Pierce BCA Protein Assay Kit (Thermofisher Scientific). Samples were prepared in SDS sample buffer with dithiothreitol (DTT) and were heated for 5 min at 95°C. Next, 10 µg of total protein was separated on 8% SDS-PAGE gel and transferred onto a nitrocellulose membrane (Amersham) using a semi-dry transfer apparatus (BioRad, 10 V for 25 min). The resulting blots were incubated overnight at 4°C with anti-human xCT/*SCL7A11* rabbit monoclonal antibody (Cell Signaling Technologies (CST), cat.#12691S), at 1:250 dilution in 1 × TBS-T 1% skim milk), and subsequently incubated for 2 h at room temperature with goat anti-rabbit IgG-HRP from CST (cat.#7074S) at 1:500 dilution in 1 × TBS-T 1% BSA. An anti-β-actin antibody (Abcam, cat.#ab119716, at 1:500 dilution) was used monitor β-actin as a loading control. Finally, the blots were developed using ECL Select Western Blotting Detection Reagent (GE Healthcare –

Amersham), according to manufacturer's instructions, and visualized with ImageQuant LAS 4000 (GE Healthcare).

4.2.4 Animal studies

All *in vivo* experiments were conducted in accordance with the guidelines established by the Canadian Council on Animal Care and were approved by the Animal Ethics Committee of the University of British Columbia. Immunodeficient 129S6/SvEvTac-*Rag2tm1Fwa* (Rag2M) mice bred in-house at the Animal Research Centre, British Columbia Cancer Research Centre (BCCRC), Vancouver, Canada were used in this study.

4.2.4.1 Tumour inoculation

The mice were sedated briefly with 2.5% isoflurane in 2.0 l/min of oxygen during cell implantation. 5×10^6 MDA-MB-231, U-87 or PC-3 cells (in 100 µl of 1 × PBS and BD Matrigel Matrix at 1:1 ratio) were injected subcutaneously on the dorsal flank of mice. Biodistribution studies and PET/CT imaging were performed when tumours reached 7-9 mm in diameter.

4.2.4.2 Preclinical PET/CT imaging

PET imaging studies were conducted using a Siemens Inveon µPET/CT scanner. Mice sedated with 2.5% isoflurane in 2.0 l/min oxygen were injected with 3.83 – 5.92 MBq of 2*S*,5*R/S*-, 2*S*,5R- or 2*S*,5*S*-[^{18}F]FASu *via* the caudal vein. For blocking experiments, mice were intravenously co-injected with 100 mg/kg of the non-radioactive standard, aminosuberic acid (ASu) (100-200 µl saline, i.v.). At 1 h post-injection (p.i.), a 10 min PET acquisition was performed. For dynamic scans, the PET acquisition was started immediately after tracer injection and lasted 60 min. For anatomical localisation, a 10 min CT scan was performed prior to each PET acquisition. PET data were acquired in list mode and the images were reconstructed using the 3D-Ordered Subset-Expectation Maximization (3D OSEM) – Maximum A Priori (MAP) algorithm with CT-based attenuation correction. The Inveon Research Workplace (IRW) software was used for image analysis and drawing 3D regions of interest (ROI) to determine the

%ID/g of tissue for selected organs. After the scan, the mice were euthanized by CO_2 asphyxiation followed by cardiac puncture.

4.2.4.3 Biodistribution studies

The tumour-bearing mice were anesthesized briefly with isoflurane inhalation and injected with 1.1 – 3.5 MBq of 2*S*,5*R/S*-, 2*S*,5R- or 2*S*,5*S*-[^{18}F]FASu (100 – 200 µl in saline or the cold standard (ASu, i.v.). The mice were allowed to roam freely in their cages for an hour and were then sacrificed by CO_2 asphyxiation. Their blood was promptly collected by cardiac puncture. Organs/tissues of interest were harvested in a subsequent necropsy, washed with PBS, blotted dry and weighed. Their activity was counted on the gamma counter, normalized to the injection time and expressed as the percentage of the injected dose per gram of tissue (%ID/g).

4.2.5 Statistical analysis

All data are expressed as mean ± SD. Statistical analysis was performed using GraphPad (7.0 h) software. Outliers were removed using the ROUT method with Q = 2%. P values for the difference of tracer uptake in mouse tissues between unblocked and blocked groups were calculated using a t-test adjusted for multiple comparisons using the Šidak method. Two-way ANOVA was performed for *2S,5R/S- v. 2S,5R- v. 2S,5S-* isomer comparison. The difference was considered statistically significant when *p* value was less than 0.05.

4.3 Results

Cellular uptake of the 2*S*,5*R/S*-[^{18}F]FASu isomer was measured in three cancer cell lines: MDA-MB-231 (breast), U-87 (glioblastoma) and PC-3 (prostate). The uptake increased over time and was reduced more than 80% in all cases by the 40 min time point when the system x_C^- inhibitor sulfasalazine (SSZ) was added (Figure 4.2A). 2*S*,5*R/S*-[^{18}F]FASu was taken up to the greatest extent by the PC-3 cells, at 2.79 ± 0.09% of the total radioactivity in each well per µg protein (%/µg) after 1h (n=4), whereas the glioblastoma cell line uptake was at 2.46 ± 0.19 %/µg protein (n=4). MDA-MB-231 cells had the lowest uptake overall, at 1.81 ± 0.06 %/µg protein at the 1 h time point (n=4). Two-way ANOVA/Dunnett's multiple comparisons test yielded

adjusted *p* values of < 0.0001 and 0.0026 for the comparison of 60 min uptake between PC-3 cells and U-87 and MDA-MB-231 cells, respectively. The uptake trended similarly to xCT expression levels in these cell lines, with PC-3 cell lysates showing the highest xCT band intensity and MDA-MB-231 the lowest, on a Western blot (Figure 4.2B).

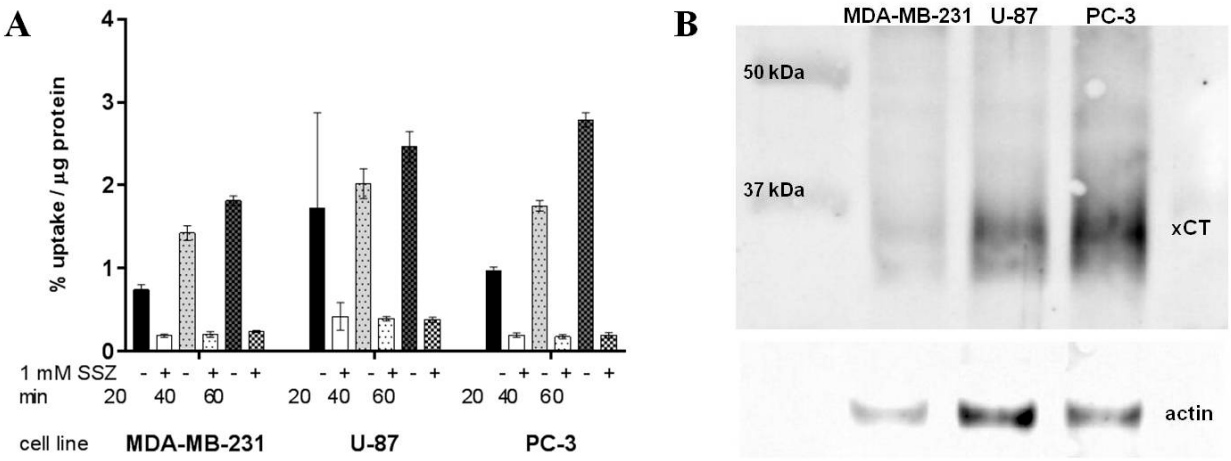

Figure 4.2 *In vitro* experimentation. A) *In vitro* 1 h uptake of 2*S*,5*R/S*-[^{18}F]FASu in MDA-MB-231, U-87 and PC-3 cells (n=4). Sulfasalazine (SSZ) was used as blocking agent. **B)** Western blot of MDA-MB-231, U-87 and PC-3 cell lysates. *Copyright © 2019, Springer Nature*

Representative decay-corrected PET images of U-87 and PC-3 xenograft-bearing mice shown in Figure 4.3 indicate system x_C^- - specific tumour uptake of 2*S*,5*R/S*-[^{18}F]FASu. Tumour uptake at 1 h p.i. was 7.09 ± 3.64 percent injected dose per gram (%ID/g) in glioblastoma and 9.19 ± 1.14 %ID/g in prostate cancer xenografts (Figure 4.3A), and was blocked by co-injection of ASu to 1.79 ± 0.72 %ID/g (p = 0.0128) and 3.81 ± 0.52 %ID/g (p < 0.0001) respectively, suggesting specific tracer uptake. 2*S*,5*R/S*-[^{18}F]FASu displayed high image contrast in both cases, with tumour-to-muscle and tumour-to-brain ratios exceeding 20 (Figure 4.3B). In addition to tumour, uptake was observed in excretory organs such as kidneys and bladder, as well as the pancreas (Figure 4.3C). Co-injection of ASu also reduced the pancreatic uptake (from 34.64 ± 3.65 to 5.52 ± 0.70 %ID/g in PC-3 bearing mice (p < 0.0001) and from 34.36 ± 14.46 to 3.47 ± 1.26 in U-87 tumour bearing mice (p = 0.0014, Table 4.2).

Biodistribution data with the 5-position diastereomers revealed system x_C^- - specific [^{18}F]FASu accumulation in all tumour xenografts (Figure 4.4). MDA-MB-231 tumours exhibited the lowest uptake, totalling 1.13 ± 0.12 %ID/g for 2*S*,5*S*-[^{18}F]FASu and 1.25 ± 0.67 %ID/g for

2*S*,5*R*-[^{18}F]FASu, at 2 h p.i. Two-way ANOVA/Šidak's multiple comparisons test for 2*S*,5*S*-[^{18}F]FASu biodistribution in MDA-MB-231 xenograft-bearing mice resulted in *p* values of < 0.0001 and 0.0306 for the comparison with PC-3 and U-87 tumour uptake, respectively, and 0.0229 and 0.9984 in the case of 2*S*,5*R*-[^{18}F]FASu. There were no statistically significant differences in the uptake of 2*S*,5*S*- and 2*S*,5*R*- diastereomers in MDA-MB-231 tumour bearing mice (Table 4.3).

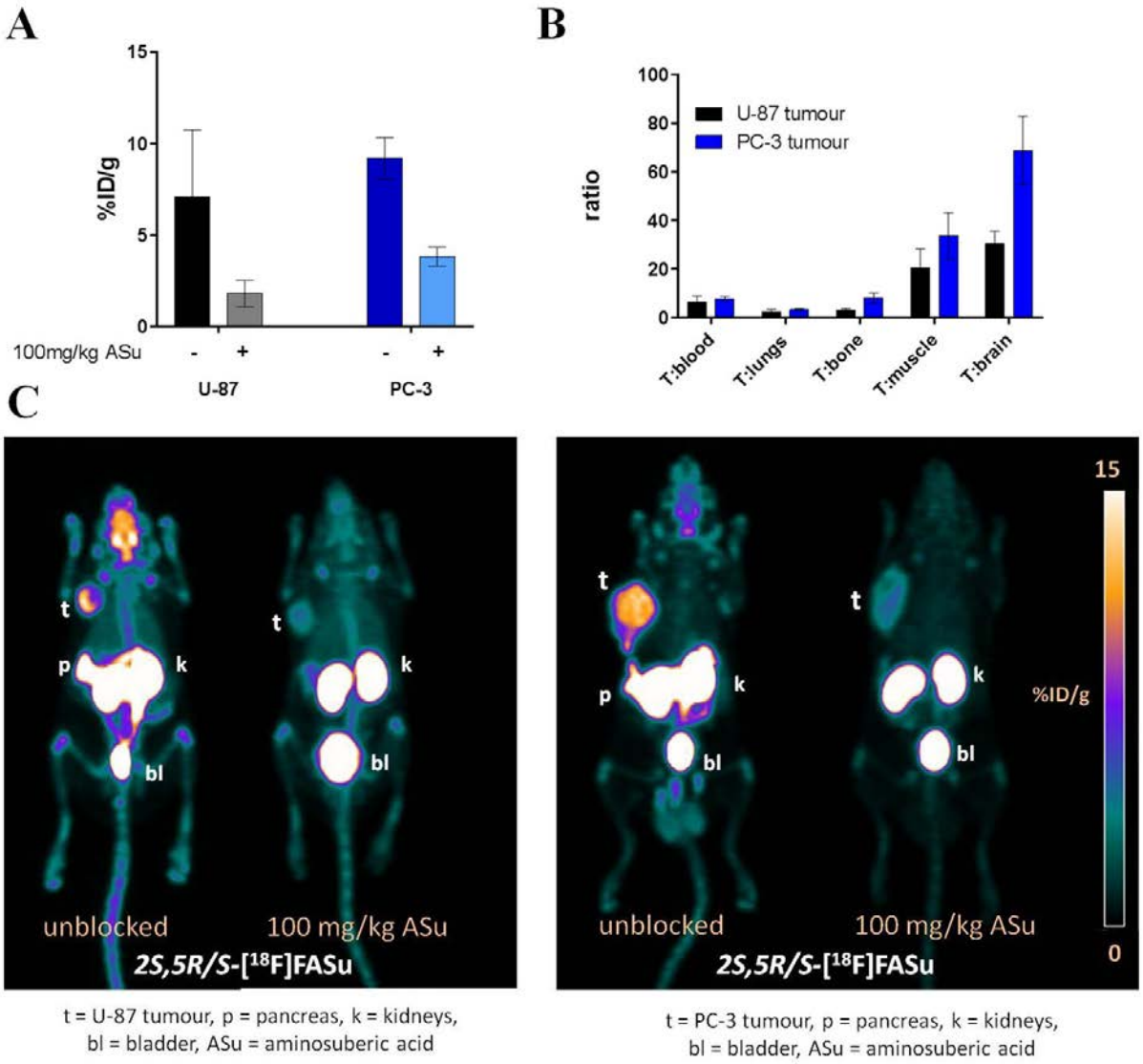

Figure 4.3: ***In vivo*** **evaluation of the 5-position racemate. A)** Tumour uptake in mice bearing U-87 and PC-3 tumours at 1 h after injection with (+) and without (-) co-injection with aminosuberic acid (ASu). n = 5 mice per group; Complete biodistribution data table is shown in Table 4.2. **B)** Tumour-to-nontarget tissue ratios in U-87 and PC-3 tumour-bearing mice at 1 h p.i. **C)** U-87 (images on the left) and PC-3 (images on the right) tumours were visualized with

2*S*,5*R*/*S*-[^{18}F]FASu-PET 60 min post-injection. The acquisition time was 10 min. 100 mg/kg of ASu was co-injected with the tracer for blocking studies. 5.15 MBq and 5.73 MBq of [^{18}F]FASu were injected into the U-87 tumour-bearing mice for unblocked and blocked scan, respectively, and 3.83 MBq and 4.79 MBq of [^{18}F]FASu were injected into PC-3 tumour-bearing unblocked and blocked mouse, respectively. t tumour, p pancreas, k kidneys, bl bladder. *Copyright © 2019, Springer Nature*

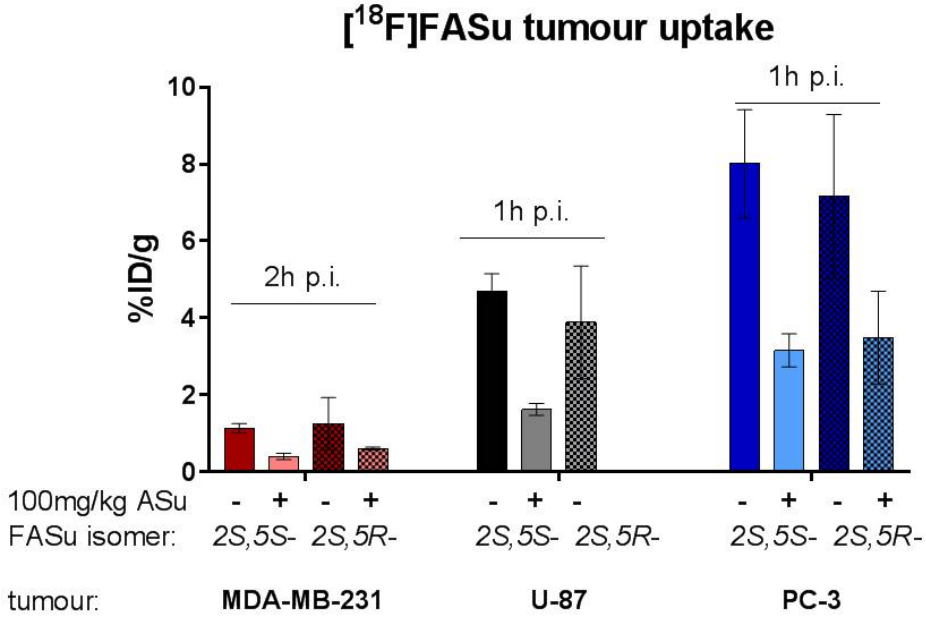

Figure 4.4 Tumour uptake of [^{18}F]FASu 5-position diastereomers, 2*S*,5*S*-[^{18}F]FASu and 2*S*,5*R*-[^{18}F]FASu. MDA-MB-231 tumours (red bars) had the lowest tracer uptake, whereas PC-3 tumours (blue bars) had the highest tracer uptake. Tumour uptake was blocked by co-injection of the cold standard, ASu. *Copyright © 2019, Springer Nature*

Table 4.2 Biodistribution data of 2*S*,5*R/S*-[^{18}F]FASu at 2h post-injection (p.i.) in breast cancer (MDA-MB-231) and at 1h p.i. glioblastoma (U-87) and prostate cancer (PC-3) xenograft-bearing Rag2M mice. *Copyright © 2019, Springer Nature*

	MDA-MB-231 tumour-bearing mice[£]	**U-87 tumour-bearing mice**		**PC-3 tumour-bearing mice**	
	unblocked, n=9	unblocked, n=5	blocked, n=5	unblocked, n=5	blocked, n=5
tissue	%ID/g ± SD	%ID/g ± SD	%ID/g ± SD	%ID/g ± SD	%ID/g ± SD
blood	0.19 ± 0.12	0.79 ± 0.12	0.63 ± 0.49	1.20 ± 0.08	1.26 ± 0.31
fat	0.03 ± 0.02	0.09 ± 0.07	0.06 ± 0.05	0.05 ± 0.01	0.04 ± 0.01
uterus	2.34 ± 1.24	11.17 ± 4.20	0.90 ± 0.45***	1.39 ± 0.17	0.50 ± 0.11****
ovaries	2.36 ± 1.85	5.63 ± 3.42	0.90 ± 0.30	2.85 ± 0.24	0.53 ± 0.10****
small intestine	1.34 ± 0.70	2.62 ± 0.23	0.54 ± 0.29****	4.04 ± 1.80	0.80 ± 0.19****
stomach	0.58 ± 0.36	3.21 ± 2.35	0.41 ± 0.37	1.25 ± 0.64	0.34 ± 0.20
pancreas	13.55 ± 7.90	34.36 ± 14.46	3.47 ± 1.26**	34.64 ± 3.65	5.52 ± 0.70****
spleen	2.33 ± 1.08	7.26 ± 4.36	0.68 ± 0.48	5.91 ± 0.90	1.20 ± 0.36****
adrenal glands	0.40 ± 0.20	0.87 ± 0.14	0.35 ± 0.09***	1.04 ± 0.35	0.63 ± 0.23
kidneys	2.83 ± 0.75	21.5 ± 3.47	19.4 ± 15.6	86.5 ± 11.7	45.0± 9.21****
liver	0.40 ± 0.19	0.93 ± 0.12	0.67 ± 0.08	1.23 ± 0.29	0.98 ± 0.20
heart	0.12 ± 0.03	0.34 ± 0.05	0.32 ± 0.26	0.47 ± 0.06	0.43 ± 0.09
lungs	1.96 ± 0.70	3.43 ± 2.55	1.94 ± 0.32	2.85 ± 0.25	2.40 ± 0.52
tumour	1.38 ± 0.27	7.09 ± 3.64	1.79 ± 0.72	9.19 ± 1.14	3.81 ± 0.52****
muscle	0.17 ± 0.10	0.26 ± 0.04	0.13 ± 0.04	0.29 ± 0.10	0.21 ± 0.02
bone	0.51 ± 0.18	2.51 ± 1.42	1.37 ± 0.47	1.18 ± 0.30	0.76 ± 0.11
brain	0.08 ± 0.02	0.25 ± 0.16	0.09 ± 0.05	0.14 ± 0.03	0.08 ± 0.02
T:blood	6.36 ± 1.38	7.13 ± 2.04	3.53 ± 1.23	7.67 ± 0.99	3.12 ± 0.68
T:fat	41.7 ± 16.7	94.2 ± 40.5	48.3 ± 31.7	192 ± 44.8	91.8 ± 29.9
T:bone	3.03 ± 1.14	2.95 ± 0.77	1.31 ± 0.24	8.15 ± 2.02	5.08 ± 0.91
T:muscle	10.5 ± 5.3	22.1 ± 7.9	11.9 ± 1.9	33.7 ± 9.52	18.0 ± 3.46
T:brain	16.8 ± 3.59	30.4 ± 5.07	20.5 ± 4.08	68.8 ± 14.1	46.0 ± 6.05

[£]This data has been previously published in J Nucl Med 2017; 58:367–373. as a bar graph[103] but shown here in table form to aid comparison to U-87 and PC-3 datasets.

Table 4.3 Biodistribution data of 2*S*,5*S*-[^{18}F]FASu and 2*S*,5*R*-[^{18}F]FASu at 2h p.i. in triple-negative breast cancer (MDA-MB-231) xenograft-bearing Rag2M mice. *Copyright © 2019, Springer Nature*

	2S,5S-[^{18}F]FASu biodistribution		**2S,5R-[^{18}F]FASu biodistribution**	
	unblocked, n=4	blocked, n=4	unblocked, n=5	blocked, n=4
tissue	mean %ID/g ±SD	mean %ID/g ±SD	mean %ID/g ±SD	mean %ID/g ±SD
blood	0.31 ± 0.24	0.12 ± 0.02	0.23 ± 0.12	0.21 ± 0.14
fat	0.03 ± 0.02	0.01 ± 0.01	0.02 ± 0.01	0.02 ± 0.01
uterus	2.16 ± 1.51	0.29 ± 0.06	0.97 ± 0.84	0.28 ± 0.12
ovaries	1.88 ± 1.36	0.38 ± 0.09	2.02 ± 1.70	0.23 ± 0.10
small intestine	0.71 ± 0.27	0.20 ± 0.04	1.00 ± 0.55	0.20 ± 0.04
pancreas	12.9 ± 2.00	1.98 ± 0.11****	11.6 ± 4.52	2.36 ± 0.20
spleen	2.67 ± 0.74	0.38 ± 0.06***	2.16 ± 0.95	0.48 ± 0.03
stomach	0.32 ± 0.23	0.83 ± 1.40	0.54 ± 0.33	0.12 ± 0.06
liver	0.33 ± 0.03	0.29 ± 0.04	0.38 ± 0.17	0.32 ± 0.03
adrenal glands	0.40 ± 0.21	0.18 ± 0.08	0.23 ± 0.09	0.14 ± 0.08
kidneys	2.98 ± 0.68	1.03 ± 0.25**	4.39 ± 3.96	1.78 ± 0.52
heart	0.12 ± 0.01	0.08 ± 0.01	0.13 ± 0.07	0.11 ± 0.01
lungs	1.11 ± 0.20	1.85 ± 1.25	1.06 ± 0.32	1.35 ± 0.65
MDA-MB-231	1.13 ± 0.12	0.39 ± 0.08****	1.25 ± 0.67	0.60 ± 0.04
bone	1.30 ± 0.40	0.93 ± 0.22	1.28 ± 0.73	1.00 ± 0.04
muscle	0.37 ± 0.33	0.06 ± 0.03	0.27 ± 0.28	0.10 ± 0.02
brain	0.10 ± 0.01	0.04 ± 0.00****	0.09 ± 0.02	0.05 ± 0.00
T:blood	3.63 ± 2.43	3.32 ± 0.77	5.50 ± 0.82	3.60 ± 1.48
T:fat	41.8 ± 28.3	29.9 ± 10.5	69.7 ± 12.3	38.9 ± 18.2
T:bone	0.87 ± 0.32	0.43 ± 0.11	1.04 ± 0.37	0.60 ± 0.02
T:muscle	3.08 ± 7.44	6.37 ± 2.31	7.74 ± 3.88	6.31 ± 0.96
T:brain	11.3 ± 0.8	9.15 ± 1.53	13.6 ± 4.1	11.5 ± 1.3

Injected activity of 2*S*,5*R*- isomer varies 2.94-4.25 MBq, and of 2*S*,5*S*- from 2.05-3.49 MBq.

Extrapolated U-87 tumour uptake from the ROI analysis of a dynamic scan revealed that 4.8 ± 1.6 %ID/g of 2*S*,5*R*-[^{18}F]FASu accumulated in the tumour at the last scanning frame (55 min p.i., Figure 4.5A). The time-activity curve (TAC) shown in Figure 4.5A indicates that the tumour uptake peaked at ~2 min p.i. after which it decreased slightly reaching a constant level of 4.8 ± 1.6 %ID/g. This observation is in accordance with the biodistribution data indicating tumour uptake of 3.88 ± 1.47 %ID/g at 1 h p.i. (Figure 4.5C, Table 4.4). 2*S*,5*R*-[^{18}F]FASu uptake of non-target tissues such as muscle and brain remained low throughout the scan,

resulting in high image contrast. Calculated tumour-to-muscle and tumour-to-brain ratios from the biodistribution data were 18.0 ± 6.8 and 30.6 ± 10.0, respectively. The static images corroborated the findings from the biodistribution analysis. Figure 4.5B is showing the 2*S*,5*R*- and 2*S*,5*S*-[^{18}F]FASu PET scans at 60 min p.i. The diastereomers showed excellent tumour visualisation and high image contrast. Aside from the U-87 tumour, tracer uptake was also present in the pancreas, kidneys and bladder. A blocking study with ASu confirmed the uptake specificity of 2*S*,5*S*-[^{18}F]FASu for system x_C^-. The biodistribution data showed that this blocking of U-87 tumour uptake was statistically significant (4.70 ± 0.46 %ID/g *v.* 1.62 ± 0.16 %ID/g for unblocked and blocked mice, respectively; $p<0.0001$, Table 4.4).

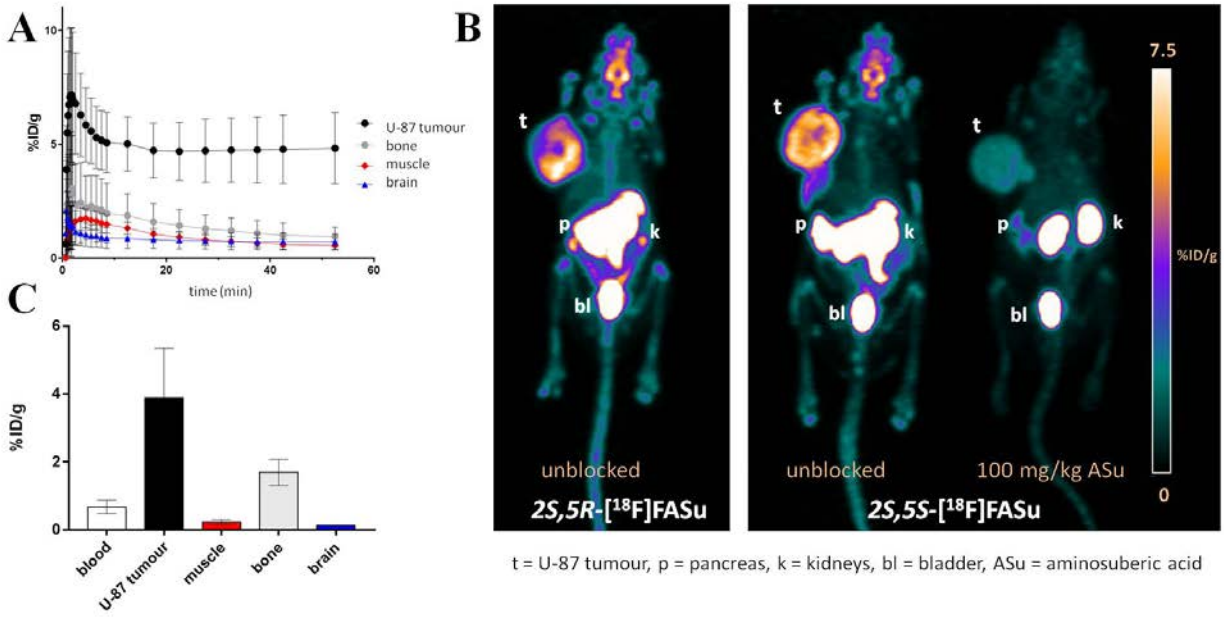

Figure 4.5 Studies with glioblastoma xenograft-bearing mice. A) Time-activity curve of 2*S*,5*R*-[^{18}F]FASu tumour-to-nontarget ratios in a glioblastoma (U-87) xenograft-bearing mouse. **B)** U-87 tumours were clearly visualized with 2*S*,5*R*-[^{18}F]FASu and 2*S*,5*S*-[^{18}F]FASu-PET 60 min post-injection; t tumour, p pancreas, k kidneys, bl bladder; **C)** 2*S*,5*R*-[^{18}F]FASu biodistribution data showing the mean uptake in the U-87 tumour and select organs. *Copyright © 2019, Springer Nature*

Table 4.4 Biodistribution data of 2*S*,5*R*-[^{18}F]FASu and 2*S*,5*S*-[^{18}F]FASu at 1h p.i. in glioblastoma (U-87) xenograft-bearing Rag2M mice. *Copyright © 2019, Springer Nature*

	2S,5R-[^{18}F]FASu	**2S,5S-[^{18}F]FASu biodistribution**	
	unblocked, n=5	unblocked, n=5	blocked, n=4
tissue	mean %ID/g ± SD	mean %ID/g ± SD	mean %ID/g ± SD
blood	0.67 ± 0.20	0.49 ± 0.03	0.55 ± 0.16
fat	0.04 ± 0.02	0.03 ± 0.01	0.03 ± 0.01
ovaries	5.34 ± 4.43	2.21 ± 0.37	0.76 ± 0.17
uterus	6.93 ± 2.39	4.28 ± 0.71	0.55 ± 0.08****
small intestine	2.56 ± 0.86	2.30 ± 0.59	0.54 ± 0.08
stomach	1.41 ± 0.71	1.16 ± 0.53	0.30 ± 0.07
pancreas	27.0 ± 6.56	26.1 ± 1.15	3.80 ± 0.23****
spleen	3.98 ± 0.79	3.12 ± 0.43	0.77 ± 0.04**
liver	0.95 ± 0.27	0.68 ± 0.35	0.52 ± 0.21
adrenal glands	1.01 ± 0.35	14.42 ± 2.21	13.96 ± 4.50
kidneys	16.60 ± 2.17	0.74 ± 0.11	0.65 ± 0.04
heart	0.30 ± 0.06	0.23 ± 0.04	0.22 ± 0.07
lungs	2.69 ± 0.37	1.62 ± 0.21	1.61 ± 0.40
U-87 tumour	3.88 ± 1.47	4.70 ± 0.46	1.62 ± 0.16****
muscle	0.23 ± 0.07	0.15 ± 0.02	0.17 ± 0.04
bone	1.69 ± 0.38	0.96 ± 0.11	0.58 ± 0.13
brain	0.13 ± 0.02	0.11 ± 0.02	0.06 ± 0.01
T:blood	6.31 ± 2.99	9.81 ± 0.55	3.11 ± 1.00
T:fat	105 ± 40.6	167± 36.0	51.9 ± 14.9
T:muscle	18.0 ± 6.82	32.1 ± 2.83	10.3 ± 3.59
T:bone	2.27 ± 0.61	4.91 ± 0.40	2.87 ± 0.56
T:brain	30.6 ± 10.0	42.7 ± 7.22	25.7 ± 3.82

Injected activity of 2*S*,5*R*- isomer varies 1.22-3.42 MBq, and of 2*S*,5*S*- from 1.40-2.31 MBq.

Similarly to the findings with glioblastoma xenograft-bearing mice, studies with PC-3 tumour-bearing mice showed the specificity of 2*S*,5*R*- and 2*S*,5*S*-[^{18}F]FASu uptake by the tumour for system x_C^- (Figure 4.6). Both diastereomers provided good tumour visualisation at high contrast, as reflected in the tumour-to-nontarget tissue ratios (Table 4.5). The biodistribution data showed that 2*S*,5*S*-[^{18}F]FASu uptake by the PC-3 tumour was 8.00 ± 1.41

%ID/g at 1 h p.i., decreasing to 3.15 ± 0.43 %ID/g due to ASu co-injection (p<0.001). PC-3 uptake of the 2*S*,5*S*-[^{18}F]FASu isomer was 7.16 ± 2.13 %ID/g, as compared to 3.49 ± 1.20 %ID/g in the blocked group (p = 0.171). The two-way ANOVA analyses of the three isomers showed no statistically significant differences in tumour uptake between the three isomers of [^{18}F]FASu, both in PC-3 and U-87 tumour-bearing mice (Tables 4.2, 4.4 and 4.5). Adjusted p values for 2*S*,5*R/S*- *v.* 2*S*,5*S*-, 2*S*,5*R/S*- *v.* 2*S*,5*R*- and 2*S*,5*R* - *v.* 2*S*,5*S*- isomer comparisons for PC-3 tumours were 0.8141, 0.5459 and 0.8992, respectively, and for the comparisons for U-87 tumours the p values were 0.3515, 0.1553 and 0.8857.

All three isomers of [^{18}F]FASu provided excellent PC-3 tumour visualisation and good image contrast at 1 h p.i (Figure 4.7A). ROI analysis of the dynamic scans of PC-3 tumour-bearing mice with the three isomers, 2*S*,5*R/S*-, 2*S*,5*R*-, and 2*S*,5*S*-[^{18}F]FASu, showed a steady increase of the tracer uptake by tumours and a clear separation from the activity in background organs, as evident on the TACs (Figure 4.7B).

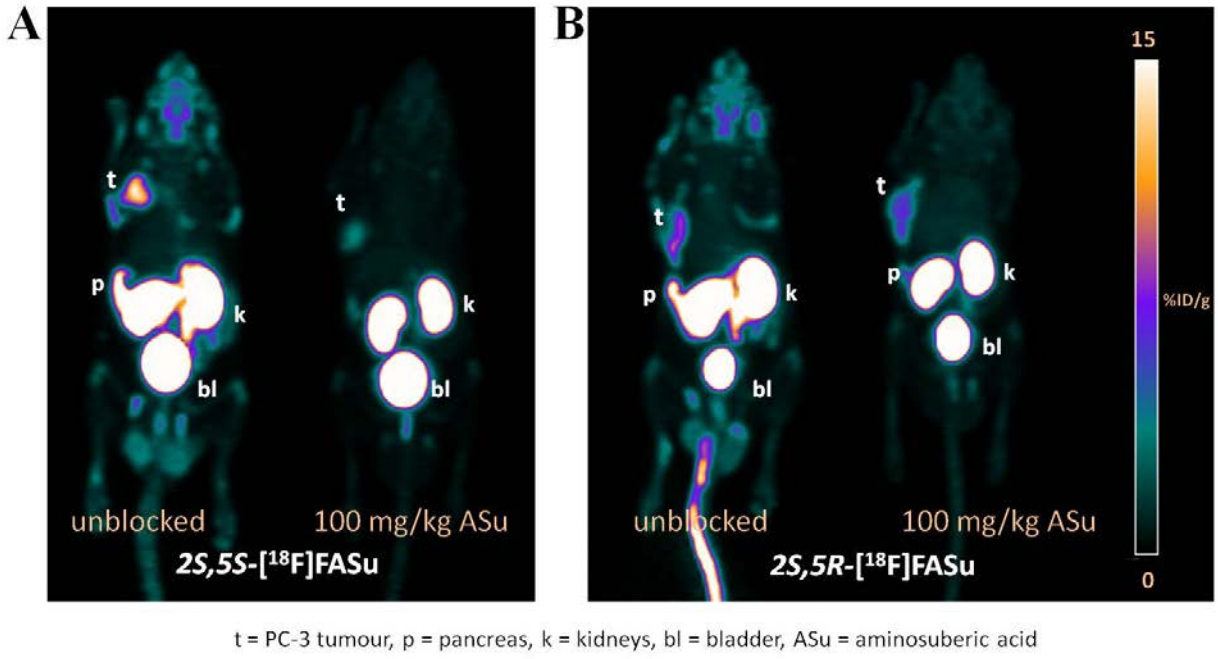

Figure 4.6 Studies with PC-3 xenograft-bearing mice. A) 2*S*,5*S*-[^{18}F]FASu-PET images of PC-3 xenograft-bearing mice at 60 min post-injection. Co-injection of ASu reduced tumour uptake. The kidneys and bladder were also visible on each image, while the pancreas was visible only in the unblocked condition. **B)** 2*S*,5*R*-[^{18}F]FASu-PET images of PC-3 xenograft-bearing mice at 60 min post-injection. t tumour, p pancreas, k kidneys, bl bladder. *Copyright © 2019, Springer Nature*

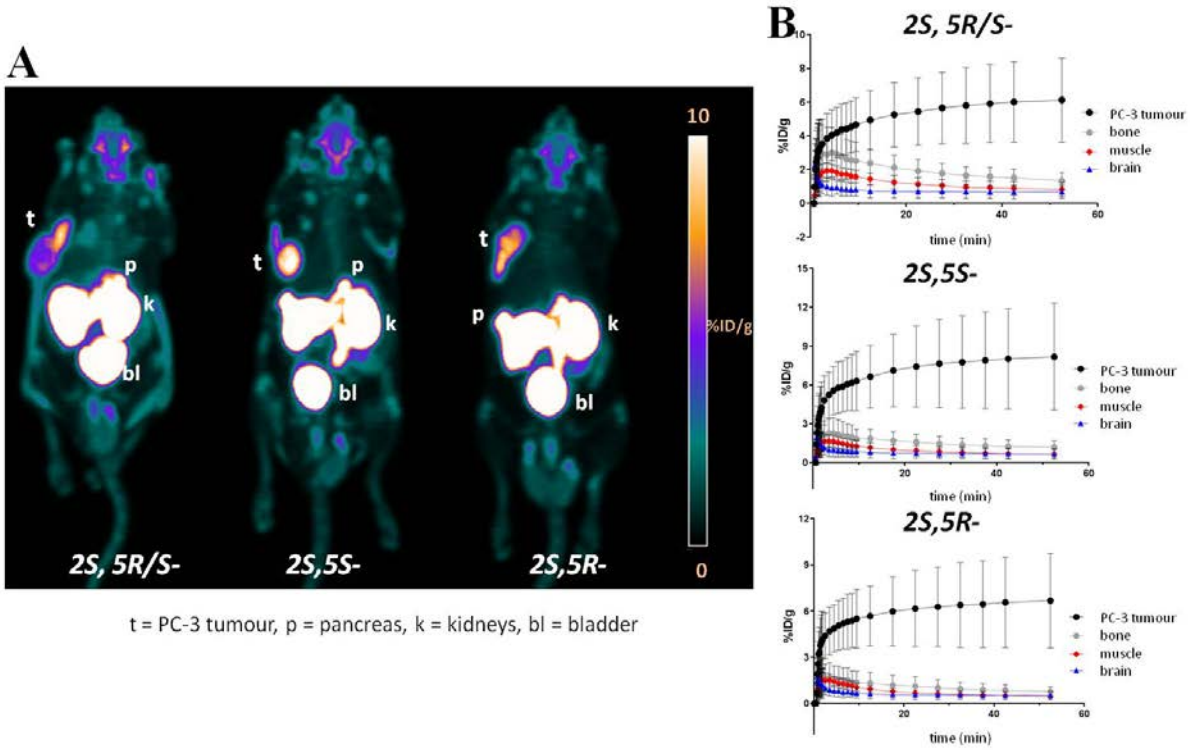

Figure 4.7 Dynamic images of PC-3 tumour-bearing mice with all three 5-position tracer configurations. A) PET MIP images at 55 min post injection, left: 2*S*,5*R/S*-[^{18}F]FASu, middle: 2*S*,5*S*-[^{18}F]FASu, right: 2*S*,5*R*-[^{18}F]FASu; the PC-3 xenograft, pancreas, kidneys and bladder were visible on each image. **B)** Time-activity curves of tumour-to-nontarget ratios in each of the three mice. *Copyright © 2019, Springer Nature*

Table 4.5 Biodistribution data of 2*S*,5*R*-[^{18}F]FASu and 2*S*,5*S*-[^{18}F]FASu at 1h p.i. in prostate cancer (PC-3) xenograft-bearing Rag2M mice. *Copyright © 2019, Springer Nature*

	2S,5R-[^{18}F]FASu biodistribution		**2S,5S-[^{18}F]FASu biodistribution**	
	unblocked, n=5 mean %ID/g ± SD	blocked, n=5 mean %ID/g ± SD	unblocked, n=5 mean %ID/g ± SD	blocked, n=5 mean %ID/g ± SD
blood	1.21 ± 0.19	1.03 ± 0.20	0.98 ± 0.19	0.76 ± 0.11
fat	0.10 ± 0.07	0.06 ± 0.02	0.04 ± 0.01	0.07 ± 0.06
testes	2.97 ± 0.78	0.54 ± 0.06***	3.09 ± 0.45	0.40 ± 0.09****
seminal	2.02 ± 0.51	1.11 ± 0.58	0.86 ± 0.07	4.65 ± 4.23
small intestine	2.57 ± 0.63	0.58 ± 0.16***	3.04 ± 0.61	0.64 ± 0.12***
stomach	0.97 ± 0.27	0.21 ± 0.06***	1.22 ± 0.52	0.18 ± 0.03
pancreas	31.1 ± 6.00	5.12 ± 1.86****	32.6 ± 3.19	4.04 ± 0.83****
spleen	7.03 ± 2.24	1.14 ± 0.17**	5.09 ± 1.05	0.91 ± 0.13***
liver	1.01 ± 0.17	0.90 ± 0.15	0.82 ± 0.06	0.72 ± 0.04
adrenal glands	1.70 ± 1.01	0.75 ± 0.40	0.97 ± 0.57	0.67 ± 0.27
kidneys	81.8 ± 13.9	47.4 ± 3.48**	72.4 ± 9.11	38.0 ± 4.01***
heart	0.56 ± 0.13	0.48 ± 0.09	0.37 ± 0.06	0.33 ± 0.05
lungs	2.55 ± 0.37	2.33 ± 0.61	1.90 ± 0.26	2.07 ± 0.60
PC-3 tumour	7.16 ± 2.13	3.49 ± 1.20	8.00 ± 1.41	3.15 ± 0.43***
muscle	0.28 ± 0.07	0.19 ± 0.02	0.26 ± 0.04	0.16 ± 0.03
bone	0.81 ± 0.20	0.46 ± 0.08	0.98 ± 0.10	0.54 ± 0.11***
brain	0.16 ± 0.03	0.07 ± 0.01**	0.12 ± 0.03	0.06 ± 0.01
T:blood	5.98 ± 1.77	3.29 ± 0.64	8.29 ± 1.23	4.18 ± 0.74
T:fat	96.8 ± 50.1	62.6 ± 28.6	188 ± 30.8	62.5 ± 31.3
T:muscle	25.3 ± 4.97	18.5 ± 5.64	31.4 ± 4.54	20.4 ± 2.67
T:bone	9.04 ± 2.79	7.58 ± 2.49	8.19 ± 1.22	5.94 ± 0.39
T:brain	46.9 ± 15.7	46.2 ± 10.4	69.9 ± 23.8	51.6 ± 8.44

Injected activity of 2*S*,5*R*- isomer varies 1.40-1.92 MBq, and of 2*S*,5*S*- from 1.70-3.21 MBq.

4.4 Discussion

Chirality plays an important role in tracer biodistribution and tumour uptake.[223–225,228–234] We observed this with 2-position diastereomers of [^{18}F]FASu where we found that the uptake of the 2*S*- (or *L*-) isomer is preferred compared to the 2*R*- congener.[195] This finding motivated us to evaluate the impact of the 5-position stereocenter. Other than the additional step of tosylate precursor purification, the radiolabeling procedure itself was unaffected. We aimed to address in this study whether it is necessary to resolve the 5-position configuration of [^{18}F]FASu for optimal tumor visualization by PET imaging.

Two-way ANOVA analysis uncovered no significant differences in the uptake of 2*S*,5*R*-[^{18}F]FASu, 2*S*,5*S*-[^{18}F]FASu and 2*S*,5*S/R*-[^{18}F]FASu in glioblastoma (U-87) and prostate cancer (PC-3) xenograft-bearing mice. Similarly, the overall biodistribution of 2*S*,5*R*-[^{18}F]FASu in MDA-MB-231 tumor-bearing mice did not differ significantly from that of 2*S*,5*S*-[^{18}F]FASu, indicating that the optical orientation at the 5-position of [^{18}F]FASu did not affect tracer biodistribution. PET images with all formulations, 2*S*,5*R/S*-, 2*S*,5*R*-, and 2*S*,5*S*-[^{18}F]FASu, provided excellent tumor visualisation in mice bearing U-87 and PC-3 tumors, with minimal activity accumulation in normal tissues, except for the pancreas, kidneys and bladder (Figures 4.3 and 4.5-7).

In vitro uptake of 2*S*,5*R/S*-[^{18}F]FASu was comparable between the three cell lines, ranging from 1.81 ± 0.06 %uptake/µg protein in MDA-MB-231 cells to 2.79 ± 0.09 %uptake/µg protein in PC-3 cells (Figure 4.2A). Western blot analysis indicated that xCT expression was the highest in PC-3 cells, followed by the glioblastoma (U-87) cell line, and finally the breast cancer (MDA-MB-231) cells (Figure 4.2B), corresponding to *in vitro* uptake trends of the [^{18}F]FASu racemate. This is in accordance with our previous findings, where we found a positive correlation between xCT expression and [^{18}F]FASu uptake.[103,226] In an *in vivo* setting, however, we found that there was several fold higher uptake in U-87 and PC-3 xenografts, compared to the breast cancer xenografts. Average U-87 and PC-3 tumor uptake of the 2*S*,5*R/S*-[^{18}F]FASu at 1 h p.i. was 7.09 ± 3.64 %ID/g and 9.19 ± 1.14 %ID/g, respectively, compared to the previously reported uptake by the MDA-MB-231 tumor of 1.38 ± 0.27 % ID/g at 2 h p.i.[103] The underlying reason for the difference in uptake of 2*S*-[^{18}F]FASu between MDA-MB-231 and the other two tumor models is likely complex and cannot be explained solely based on the current data. We

hypothesize that the upregulation of x_C^- in PC-3 and U-87 xenografts *in vivo* could be due to a number of tumor-related factors including perfusion, interstitial pressure, differences in the number of cells per volume of tissue, differences in signaling that affect xCT expression *in vivo*, or metabolic reprogramming.

This work shows potential utility of [^{18}F]FASu for the detection of two additional cancer types, glioblastoma and prostate cancer. Moreover, we demonstrated that using optically pure amino acid tracer, 2*S*,5*R*- or 2*S*,5*S*-[^{18}F]FASu in this case, makes no practical difference in terms of their utility for PET imaging. Therefore, the 5-position racemic mixture, 2*S*,5*R/S*-[^{18}F]FASu, can be used with comparable image contrast and background uptake to the pure 5-position enantiomers.

4.5 Conclusion

Herein, we demonstrated that in the case of [^{18}F]FASu, chirality at the 5-position does not significantly affect tracer biodistribution or tumour uptake in the three tumour models studied, allowing for continued studies of this tracer without the need for chiral resolution of the product at this position.

Chapter 5: Comparison of two xCT-targetting imaging agents, [^{18}F]5-fluoroaminosuberic acid ([^{18}F]FASu) and (4S)-4-(3-[^{18}F]fluoropropyl)-L-glutamate ([^{18}F]FSPG)

5.1 Introduction

The most widely used oncological PET imaging agent is 2-deoxy-2-[^{18}F]-fluoro-*D*-glucose ([^{18}F]FDG),[196] despite its lack of uptake specificity and difficulties in visualising slow growing tumours.[32,34] Oxidative stress has been implied as one of the key factors in cancer progression,[74] (see Chapter 1 [1.3]), and thus we believe that monitoring activity of system x_C^- will provide us with useful and complementary information about the lesion identity, in addition to [^{18}F]FDG-PET. To do this, a specific tracer is required.

In Chapter 5, we report comparative evaluation of two xCT-imaging agents, [^{18}F]5-fluoroaminosuberic acid ([^{18}F]FASu) and (4S)-4-(3-[^{18}F]fluoropropyl)-L-glutamate ([^{18}F]FSPG). The comparison study was performed in non-small cell lung cancer (A549) and glioblastoma (U-87) cell lines and tumour–bearing mice. Additionally, we report *in vivo* comparison of these two tracers to [^{18}F]FDG. [^{18}F]FASu and [^{18}F]FSPG are two main compounds that have been reported to specifically target xCT. [^{18}F]FSPG, a glutamate analogue that demonstrated specific tumour uptake, is currently under evaluation in multiple multi-center clinical trials to determine its efficacy in detection and staging of various types of cancer including but not limited to non-small cell lung cancer, ovarian, brain and renal cell cancer; triple-negative, estrogen receptor negative, and HER2/Neu negative breast cancer, and mesothelioma (ClinicalTrials.gov).

The work presented in this chapter is not published. [^{18}F]FASu and [^{18}F]FSPG radiosyntheses were performed by Dr. Hua Yang and Lily Southcott (TRIUMF). All *in vitro* and *in vivo* experiments were performed by MČ with Helen Merkens' assistance with biodistribution studies and Nadine Colpo's assistance with the μPET/CT imaging. Western blots were performed by HM. *In vitro* uptake, biodistribution data and image analyses were performed by MČ.

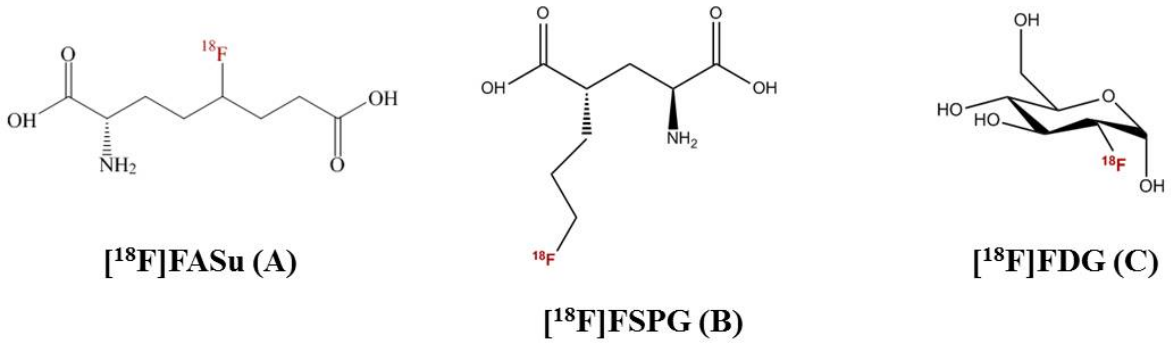

Figure 5.1 Chemical structures of ^{18}F-labelled (2S)-5-fluoroaminosuberic acid **(A)**, (4S)-4-(3-fluoropropyl)-*L*-glutamate **(B)** and 2-deoxy-2-fluoro-*D*-glucose **(C)**.

5.2 Materials & methods

5.2.1 Chemicals and instrumentation

[^{18}F]FDG was obtained from BC Cancer. [^{18}F]FASu and [^{18}F]FSPG were synthesized at TRIUMF according to previously published procedures on a GE tracerlab FXFN automated synthesis module.[102,139] All other chemicals and solvents were obtained from commercial sources, and used without further purification. The quantity of injected radiofluorinated tracers was measured using a Capintec (Ramsey, NJ, USA) CRC®-25R/W dose calibrator, and the radioactivity of mouse tissues collected from biodistribution studies were counted using a Perkin Elmer Wizard 2480 gamma counter. PET imaging experiments were conducted using a Siemens Inveon μPET/CT scanner.

5.2.2 Syntheses of radiotracers

5.2.2.1 [^{18}F]-fluoroaminosuberic acid ([^{18}F]FASu)

[^{18}F]FASu was synthesized as reported.[195] Briefly, $^{18}F^-/H_2{}^{18}O$ was azeotropically dried with t-butyl ammonium bicarbonate. The precursor (di-tert-butyl 2-((bis-tert-butoxycarbonyl)amino)-5-(tosyloxy)octanedioate was added and kept at 95°C for 15 min. After which di-tert-butyl 2-((bis-tert-butoxycarbonyl)amino)-5-fluorooctanedioate was purified by C18 SepPak. Acetonitrile was removed under vacuum. Then TFA was added and kept at 95°C for 7 min. The final product was purified by another C18 column and taken up in PBS buffer. Decay

corrected radiochemical yield (d.c. RCY) 18 ± 6% (n=6), radiochemical purity (RCP) > 98%, specific activity (SA) 17.5 ± 7 GBq/mmol (n=6).

5.2.2.2 (4S)-4-(3-[^{18}F]fluoropropyl)-*L*-glutamate ([^{18}F]FSPG)

[^{18}F]FSPG was synthesized as reported.[139] Briefly, $^{18}F^-/H_2{}^{18}O$ was azeotropically dried with Kryptofix 2.2.2./K_2CO_3. The precursor di-tert-butyl (2S,4S)-2-tert-butoxycarbonylamino-4-nitrophenylsulfonyloxy-propyl)-pentanedioate was added and kept at 70°C for 5 min and fluorinated product was purified by C18 SepPak and eluted in 2 mL acetonitrile. Then HCl (2 M, 2 mL) was added and kept at 100°C for 8 min. The final product was purified by SCX cation exchange column and taken up in PBS buffer. d.c. RCY 28 ± 7% (n=4), RCP > 98%, SA 15 ± 5 GBq/mmol (n=4).

5.2.3 *In vitro* uptake specificity studies

All cell lines used in this study have been authenticated by DCC medical. MDA-MB-231 triple negative breast cancer cells were obtained as a gift from Dr. Connie Eaves (BC Cancer, Vancouver, Canada). Glioblastoma U-87 cell line and prostate cancer PC-3 cells were obtained from ATCC. HT-29 human colorectal cancer cells were obtained as a gift from Dr. Donald Yapp (BC Cancer, Vancouver, Canada). SKOV3 ovarian cancer cells and A549 non-small cell lung cancer cell line were obtained as a gift from Dr. Poul Sorensen (BC Cancer, Vancouver, Canada).

Cells were cultured in their respective media supplemented with 10% fetal bovine serum and 100 U/mL penicillin-streptomycin. MDA-MB-231 cells were maintained in Dulbecco's Modified Eagle's Medium; SKOV3 and HT-29 cells in McCoy`s 5A Medium; U-87 cells in Roswell Park Memorial Institute 1640 Medium; A549 and PC-3 cells in F12K Medium.

For tracer uptake and competition studies, the tumour cells were seeded in 24-well plates at appropriate concentrations. The cell number used for seeding was adjusted for every tumor cell line to yield approximately 200,000 cells per well at the day of uptake study. Cells were usually grown for 2 to 3 days under standard conditions (37 °C, 5% CO_2) until subconfluency. The cell number at the day of the uptake assay was determined by detaching cells in 3

representative wells and cell counting using MOXI Z Mini Automated Cell counter Kit. Uptake data were normalized to 100,000 cells or per protein content in representative wells.

Prior to the radioactive uptake assay, the cell culture medium was removed and the cells were washed twice with HEPES Basal Salt Solution (HBSS buffer). Radiotracers were added to the assay buffer by using 148 kBq/well. For competition experiments, the cells were co-incubated with competitors either in excess at 1 mmol/L or in a dose dependent manner (0.001 – 1 mmol/L). Tracer uptake was stopped by removal of the assay buffer at the time points indicated. Cells were quickly washed twice with ice cold HBSS buffer and lysed by the addition of 1 M NaOH. The cell lysate was removed from the plates. Radioactivity of ^{18}F samples was determined using a Perkin Elmer Wizard gamma counter.

5.2.4 Western blotting

Tumour tissue of euthanized Rag2M mice was dissected, snap-frozen, minced, homogenized in RIPA buffer supplemented with protease inhibitors (Roche complete mini tablets). The lysates were centrifuged (16,000 × g, 20 min, 4°C). Supernatant was collected and protein concentration determination was determined using Pierce BCA Protein Assay Kit (Thermofisher Scientific). Next, 10 µg of total protein per sample was electrophoresed onto an 8% SDS-PAGE gel. Proteins were transferred onto a nitrocellulose membrane (Amersham) using a semi-dry transfer apparatus (BioRad, 10 V for 25 min). After transfer the membrane was blocked for 1 h with 1 × TBS-tween (TBS-T) with 5% skim milk powder, and probed overnight at 4 °C with anti-human xCT/*SCL7A11* rabbit monoclonal antibody (Cell Signaling Technologies (CST), cat.#12691), at 1:500 dilution in 1 × TBS-T 1% skim milk powder). After the primary antibody, the membrane was washed 3 × with TBS-T. Next, the membrane was incubated with goat anti-rabbit IgG-HRP from CST (cat.#7074) at 1:1000 dilution in 1 × TBS-T 1% skim milk powder for 1 h at room temperature. After this incubation, the blot was washed for 5-10 min nine times with 1 × TBS-T. The blot was developed using ECL Select Western Blotting Detection Reagent (GE Healthcare – Amersham), according to manufacturer's instructions, and visualized with ImageQuant LAS 4000 (GE Healthcare).

5.2.5 Animal studies

Immunodeficient 129S6/SvEvTac-*Rag2*^{tm1Fwa} (Rag2M) and NOD.Cg-*Prkdc*^{scid}*Il2rg*^{tm1Wjl}/SzJ (NSG) mice bred in-house at the Animal Research Centre, British Columbia Cancer Research Centre (BCCRC), Vancouver, Canada were used in this study. All *in vivo* experiments were conducted in accordance with the guidelines established by the Canadian Council on Animal Care and approved by the Animal Ethics Committee of the University of British Columbia.

5.2.5.1 Tumour inoculation

Mice were anesthetized briefly with 2.5% isoflurane in 2.0 L/min of oxygen during cell implantation. After shaving the upper back area below the left shoulder, the injection site was wiped with an alcohol prep pad, and a 28½ - gauge needle was used to inject 5×10^6 U-87 cells or 2×10^6 A549 cells (in 100 μL of 1 × PBS and BD Matrigel Matrix at 1:1 ratio) subcutaneously. Biodistribution studies and PET/CT imaging were performed when tumours reached 5-7 mm in diameter.

5.2.5.2 Biodistribution studies

The NSG mice were subjected to fasting for 12-14 h prior to tracer injection. Water was provided *ad libitum* during this period. Tumour-bearing mice were anesthesized briefly with isoflurane inhalation and injected with 0.9 – 2.5 MBq of [^{18}F]FASu, [^{18}F]FSPG or [^{18}F]FDG (100 – 200 μL in saline, i.v.). Mice were let to roam freely in their cages for an hour and were then sacrificed by CO_2 asphyxiation. Their blood was promptly harvested by cardiac puncture. Organs/tissues of interest were collected in a subsequent necropsy, washed with PBS, blotted dry, weighed and their activity was counted, normalized to the injected dose and expressed as the percentage of the injected dose per gram of tissue (%ID/g).

5.2.5.3 PET imaging and data analysis

Anesthetized mice were injected with 3.94 – 5.22 MBq *via* caudal vein. A 10 min CT scan was performed followed by a 10 – 60 min PET acquisition. PET data were acquired in list

mode. At 1 h p.i., mice were euthanized by CO_2 asphyxiation followed by cardiac puncture. The tissues of interest were harvested, weighed, and counted as described in Section 3.2.5.2. The PET data were reconstructed using the 3D-Ordered Subset-Expectation Maximization (3D OSEM) – Maximum A Priori (MAP) algorithm with CT-based attenuation correction. Inveon Research Workplace (IRW) software was used for image analysis and drawing 3D regions of interest (ROI) to determine the %ID/g of tissue for selected organs.

5.2.6 Statistical analysis

All data are expressed as mean ± SD. Statistical analysis was performed using GraphPad (7.0h) software. Outliers were removed using the ROUT method with Q = 2%. Two-way ANOVA analysis was performed for all *in vitro* and biodistribution studies and multiple comparisons were corrected using the Šidak method. The difference was considered statistically significant when *P* value was less than 0.05.

5.3 Results & discussion

In this study, we compared the *in vitro* uptake and *in vivo* biodistribution of two xCT - targeting radiotracers, [^{18}F]FASu and [^{18}F]FSPG. In addition, *in vivo* imaging and biodistribution of these amino acid–based tracers were evaluated in comparison to [^{18}F]FDG in two different tumour models. Both compounds have been reported to show system x_C^- – specific uptake *in vitro* and *in vivo*.[102,103,139]

In vitro uptake studies indicate system x_C^- - specific uptake of both [^{18}F]FASu and [^{18}F]FSPG. Uptake of the two tracers was measured in five different cancer cell lines: MDA-MB-231 (breast), U-87 (glioblastoma), HT-29 (colorectal), A549 (non-small cell lung cancer) and SKOV3 (ovarian). The uptake generally increased over time and was blocked by the system x_C^- inhibitor sulfasalazine (SSZ) in all cases (Figures 5.2 and 5.3). [^{18}F]FSPG had higher uptake overall, with the cell line on the lower end of the spectrum, U-87, taking up 5.8 ± 0.5 % activity per μg protein at 60 min time point, and the uptake of those cell lines on the higher end of the spectrum (A549 and SKOV3) exceeding 29.6 ± 2.4% uptake/μg protein (Figure 5.2). [^{18}F]FASu uptake, on the other hand, was also system x_C^- specific across all cell lines studied (Figure 5.3),

however the activity taken up by the cells ranged from 1.8 ± 0.1% uptake/μg protein to 12.2 ± 1.0% uptake/μg protein in the case of the cell line with the highest uptake at 60 min, A549. Interestingly, when the uptake values of only the blocked wells are plotted on the same graph (Figure 5.4), we observed that the overall uptake (CPM/μg protein) for the two tracers no longer differed several fold, in all cell lines except SKOV3. Furthermore, we observed that the uptake of [^{18}F]FASu in the presence of 1 mM SSZ does not change with increasing incubation time, except in A549 cells where it increased significantly from 47.0 ± 6.4 CPM/μg protein at 40 min to 68.0 ± 16.5 CPM/μg protein at 60 min, whilst [^{18}F]FSPG uptake under the same conditions keeps increasing with prolonged incubation in all cell lines, the exception being U-87 cells in which we observed no significant changes in blocked [^{18}F]FSPG uptake over time.

Wanting to explore these differences further, particularly the intriguing disparate uptake pattern in A549 and U-87 cells, we focused our *in vivo* studies on these two models. U-87 cells were on the lower end of the uptake spectra of both tracers, and no increase in blocked uptake of either tracer was evident *in vitro*. The non-small cell lung cancer cells, A549, on the other hand, demonstrated high *in vitro* uptake of both radiotracers and increasing uptake over time despite oversaturation with SSZ, a system x_C^- inhibitor.

Even though the original [^{18}F]FASu formulation used was trifluoroacetic acid (TFA), in this study, we used the tracer formulated in HCl in order to have as few variables as possible when comparing our tracer with [^{18}F]FSPG. Our validation biodistribution studies indicated no statistically significant differences in biodistribution of [^{18}F]FASu based on the formulation used (Figure 5.5). Complete biodistribution data are shown in Appendix B, Table B1 (p.177).

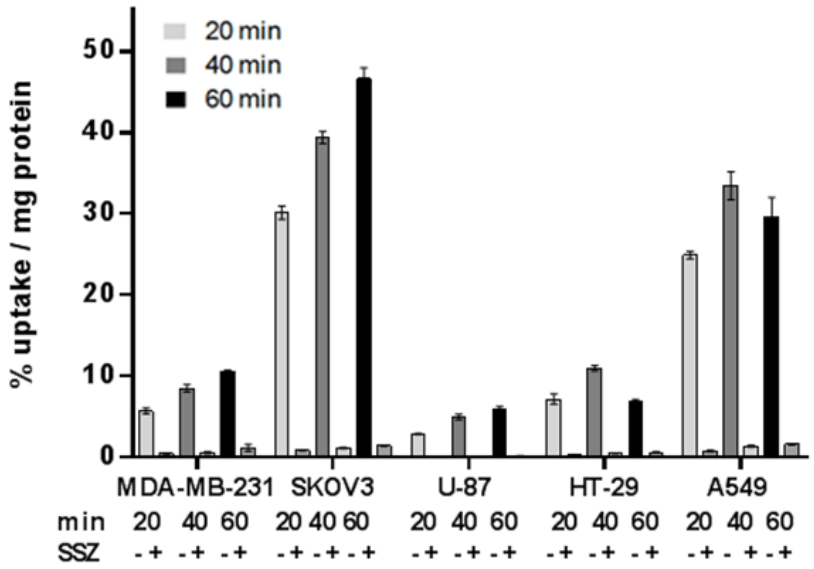

Figure 5.2 [^{18}F]FSPG *in vitro* uptake at 20, 40 and 60 min in the absence and presence of xCT inhibitor sulfasalazine (SSZ). All uptake values are normalized to protein concentration and presented in percent uptake per minute per microgram of protein (%/µg protein).

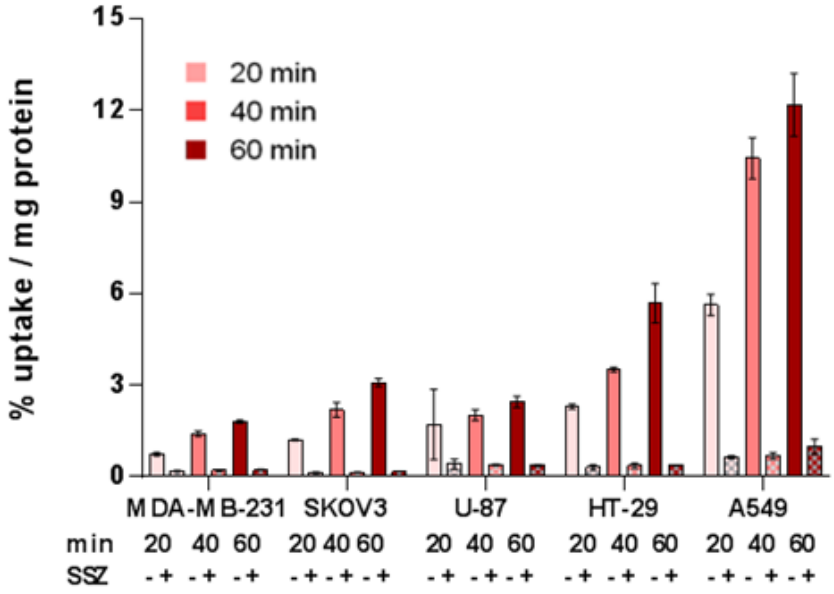

Figure 5.3 [^{18}F]FASu *in vitro* uptake at 20, 40 and 60 min in the absence and presence of xCT inhibitor sulfasalazine (SSZ). All uptake values are normalized to protein concentration and presented in percent uptake per minute per microgram of protein (%/µg protein).

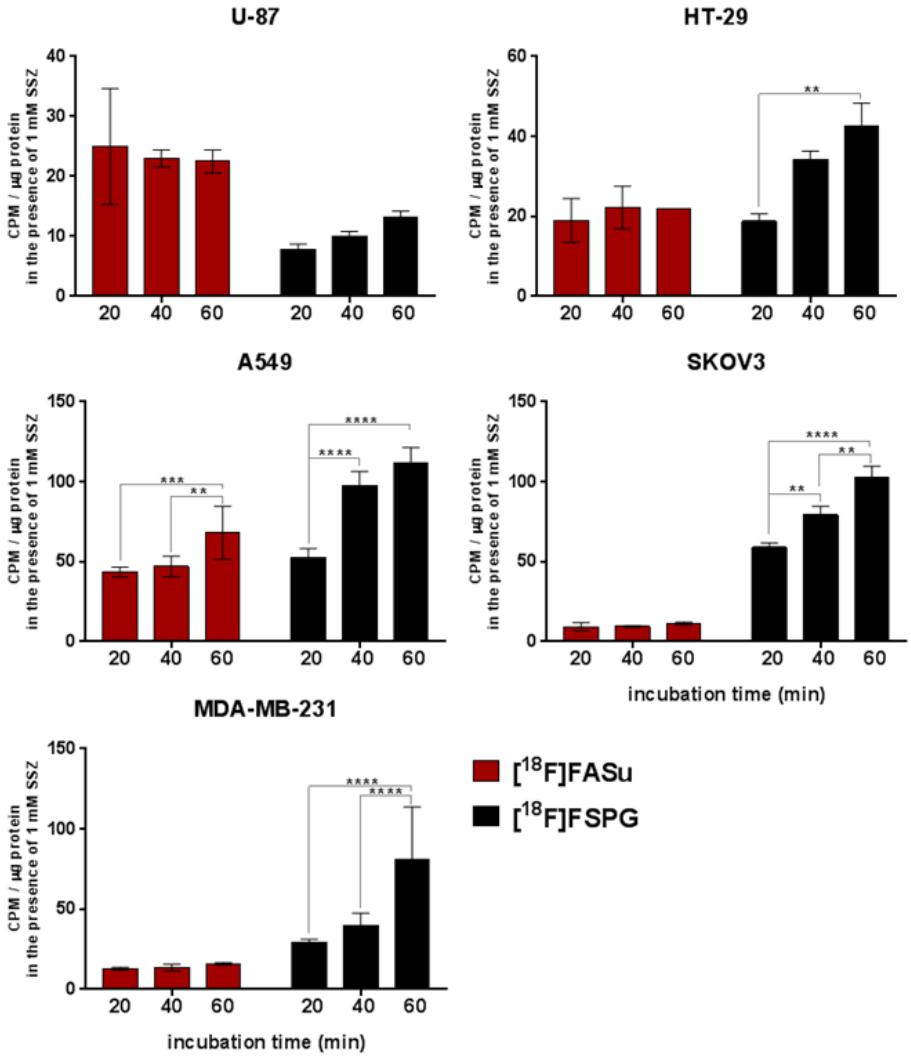

Figure 5.4 [^{18}F]FASu and [^{18}F]FSPG *in vitro* uptake blocked with SSZ. SSZ, a system x_C^- inhibitor, was used as blocking agent at 1 mM concentration. Cells were incubated with the tracer (red bars for [^{18}F]FASu, black for [^{18}F]FSPG) for 20, 40 or 60 min. SSZ was co-added with the tracer.

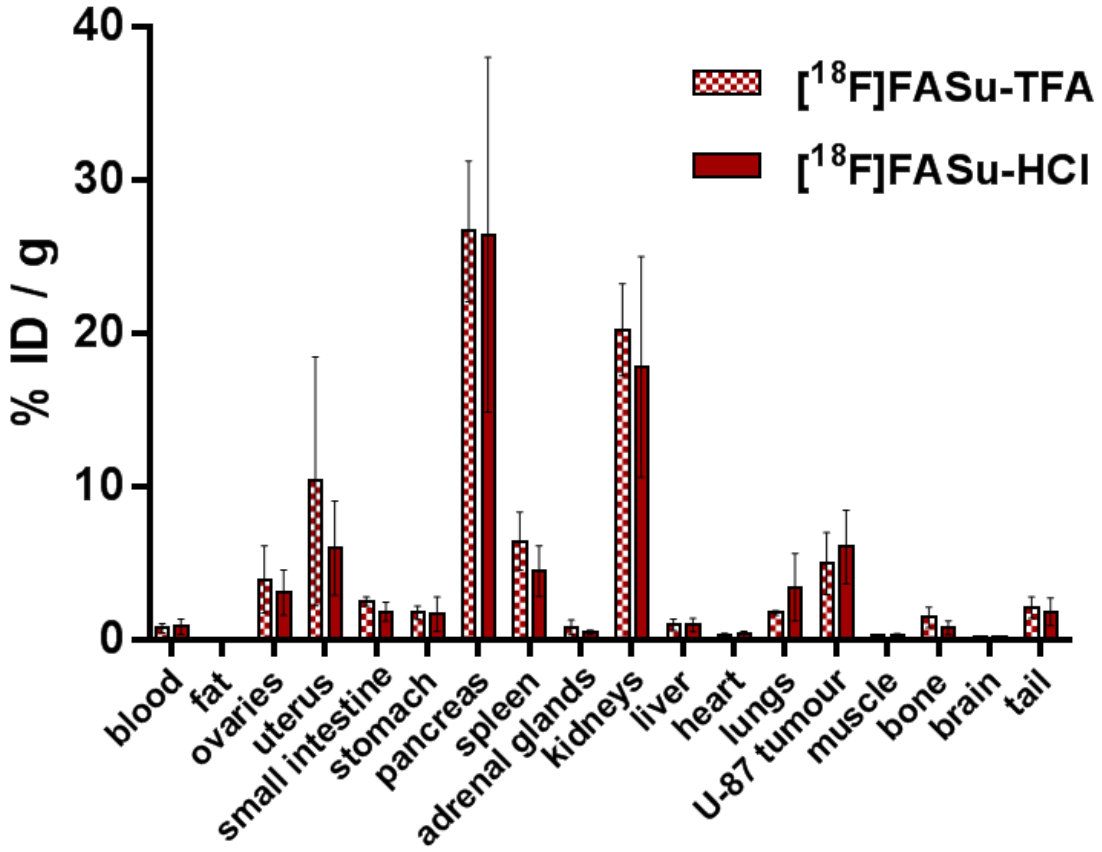

Figure 5.5 Validation study: biodistribution of [^{18}F]FASu in two different formulations. Statistical analysis revealed no significant differences in the uptake of two tracer formulations ($n \geq 3$).

We have confirmed the expression of xCT in A549 and U-87 tumours with Western blot analysis (Figure 5.6), which revealed higher abundance of xCT in A549 tumour lysate. Representative decay–corrected PET images and biodistribution data table of A549 tumour-bearing Rag2M mice are shown in Figure 5.7 and Table 5.1. [^{18}F]FASu and [^{18}F]FSPG gave PET images with low background uptake, high image contrast and clear tumour visualization. Renal clearance was evident from both biodistribution data and images. [^{18}F]FASu and [^{18}F]FSPG both had high pancreatic uptake, 24.93 ± 2.92 and 17.71 ± 3.63 %ID/g, respectively. Both A549 tumour and pancreatic uptake were blocked with co-injection of the cold standard, aminosuberic acid (ASu, 100 mg/kg, intravenous), indicating uptake specificity of [^{18}F]FASu and [^{18}F]FSPG to system x_C^- (Table 5.1). Tumour uptake of [^{18}F]FDG, [^{18}F]FASu and [^{18}F]FSPG was 2.33 ± 0.63, 5.00 ± 0.83 and 6.27 ± 1.32 %ID/g, respectively, though it was not statistically significantly

different from one another (Figure 5.8). [^{18}F]FASu and [^{18}F]FSPG had significantly higher tumour-to-muscle and tumour-to-brain ratios than [^{18}F]FDG, and significantly lower brain uptake (**** $p < 0.0001$, Figure 5.8). [^{18}F]FSPG had significantly higher tumour-to-brain ratio than [^{18}F]FASu (* $p < 0.05$), but otherwise there were no significant differences in the biodistribution of these two tracers.

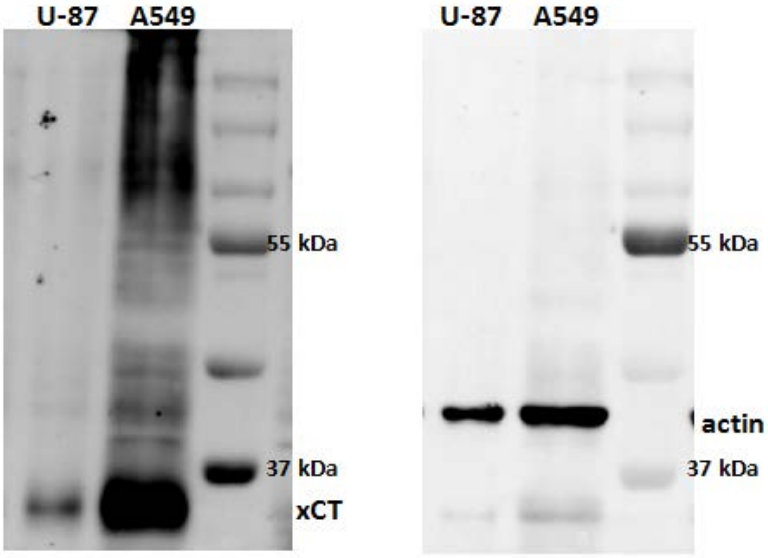

Figure 5.6 Western blot image of tumour lysates indicating 35 kDa xCT protein expression in U-87 and A549 tumour lysates. Corresponding actin blot is shown on the right. 10 μg of protein was loaded per lane.

In the case of U-87 tumour-bearing Rag2M mice, the images (Figure 5.9) and biodistribution data (Table 5.2) much resemble those of A549 tumour-bearing animals. Radiofluorinated amino acids [^{18}F]FASu and [^{18}F]FSPG generated good contrast PET images in the xCT-expressing glioblastoma xenografts. Both of these tracers indicated similar biodistribution pattern in the organs and tissues studied (Table 5.2). In addition to tumour, uptake was observed in excretory organs like the kidneys ([^{18}F]FASu, [^{18}F]FSPG) and bladder ([^{18}F]FDG, [^{18}F]FASu and [^{18}F]FSPG), indicating renal excretion pathway (Figure 5.9). Blood clearance was rapid, with 0.66 ± 0.23, 0.84 ± 0.50 and 0.59 ± 0.08 %ID/g of [^{18}F]FDG, [^{18}F]FASu and [^{18}F]FSPG present at 1 h post-injection, respectively. [^{18}F]FASu and [^{18}F]FSPG both had high pancreatic uptake, 26.42 ± 11.59 and 16.81 ± 1.38 %ID/g, respectively, due to high xCT expression in this organ.[113] U-87 tumour uptake of [^{18}F]FDG, [^{18}F]FASu and [^{18}F]FSPG at 1 h p.i. was 3.75 ± 1.15, 6.05 ± 2.40 and 11.18 ± 4.12 %ID/g, respectively.

Table 5.1 Biodistribution and tumour-to-non-target ratios of [^{18}F]FDG, [^{18}F]FASu and [^{18}F]FSPG in A549 xenograft-bearing Rag2M mice.

	[^{18}F]FDG	**[^{18}F]FASu**		**[^{18}F]FSPG**	
organ	**(n ≥ 7)**	**unblocked (n ≥ 5)**	**100 mg/kg ASu[a]**	**unblocked (n ≥ 6)**	**100 mg/kg ASu[a]**
blood	0.75 ± 0.15	0.78 ± 0.44	0.64 ± 0.11	0.51 ± 0.08	0.55 ± 0.16
fat	0.29 ± 0.11	0.04 ± 0.01	0.04 ± 0.01	0.03 ± 0.01	0.02 ± 0.00
ovaries	2.71 ± 0.73	2.91 ± 0.50	0.91 ± 0.21[b]	9.13 ± 2.77	1.14 ± 0.20[b]
uterus	3.41 ± 1.97	7.96 ± 2.88	0.59 ± 0.11[b]	6.29 ± 2.99	0.91 ± 0.34
small intestine	2.48 ± 0.51	2.53 ± 0.21	0.87 ± 0.61[b]	2.51 ± 0.37	0.46 ± 0.13[b]
stomach	0.90 ± 0.25	0.66 ± 0.12	0.61 ± 0.42	0.85 ± 0.29	0.33 ± 0.18
pancreas	2.79 ± 0.57	24.93 ± 2.92	3.96 ± 1.18[b]	17.71 ± 3.63	3.99 ± 0.70[b]
spleen	3.58 ± 0.74	3.89 ± 2.01	1.04 ± 0.26	6.14 ± 0.84	1.02 ± 0.20[b]
adrenal glands	3.58 ± 0.67	0.65 ± 0.15	0.51 ± 0.24	0.53 ± 0.05	0.59 ± 0.16
kidneys	3.76 ± 0.73	13.29 ± 1.60	22.19 ± 5.85	17.49 ± 2.11	21.07 ± 10.60
liver	1.29 ± 0.33	0.74 ± 0.08	0.75 ± 0.17	0.63 ± 0.13	0.60 ± 0.32
heart	56.31 ± 20.70	0.24 ± 0.06	0.26 ± 0.05	0.16 ± 0.03	0.17 ± 0.08
lungs	3.89 ± 0.68	1.92 ± 0.46	2.66 ± 0.28	1.36 ± 0.07	1.00 ± 0.37
muscle	2.97 ± 0.90	0.15 ± 0.02	0.16 ± 0.03	0.17 ± 0.05	0.10 ± 0.03
bone	0.96 ± 0.21	0.56 ± 0.08	0.33 ± 0.07[b]	0.14 ± 0.04	0.20 ± 0.07
brain	9.23 ± 2.74	0.13 ± 0.02	0.09 ± 0.01	0.64 ± 0.21	0.09 ± 0.04
tail	1.40 ± 0.28	1.25 ± 0.20	0.75 ± 0.29	0.21 ± 0.01	0.44 ± 0.20[b]
A549 tumour	**2.33 ± 0.63**	**5.00 ± 0.83**	**2.04 ± 0.36[b]**	**6.27 ± 1.32**	**3.53 ± 0.69**
Tumour / blood	3.11 ± 0.46	7.61 ± 3.58	3.22 ± 0.58	12.36 ± 2.52	6.67 ± 1.81
Tumour / muscle	0.78 ± 0.53	33.18 ± 4.39	13.72 ± 4.40	37.92 ± 9.55	39.15 ± 11.34
Tumour / lungs	0.60 ± 0.18	2.70 ± 0.65	0.78 ± 0.20	4.59 ± 0.92	3.77 ± 1.17
Tumour / brain	0.25 ± 0.08	39.79 ± 6.67	23.40 ± 6.53	52.95 ± 10.29	45.58 ± 17.86

Biodistributions and ratios are at 1 h p.i. Values (%ID/g) are presented as mean ± standard deviation.

[a]Blocked with co-injection of the cold standard, aminosuberic acid (ASu).

[b]Co-injection significantly reduced uptake of the same organ for the tracer ($p < 0.05$).

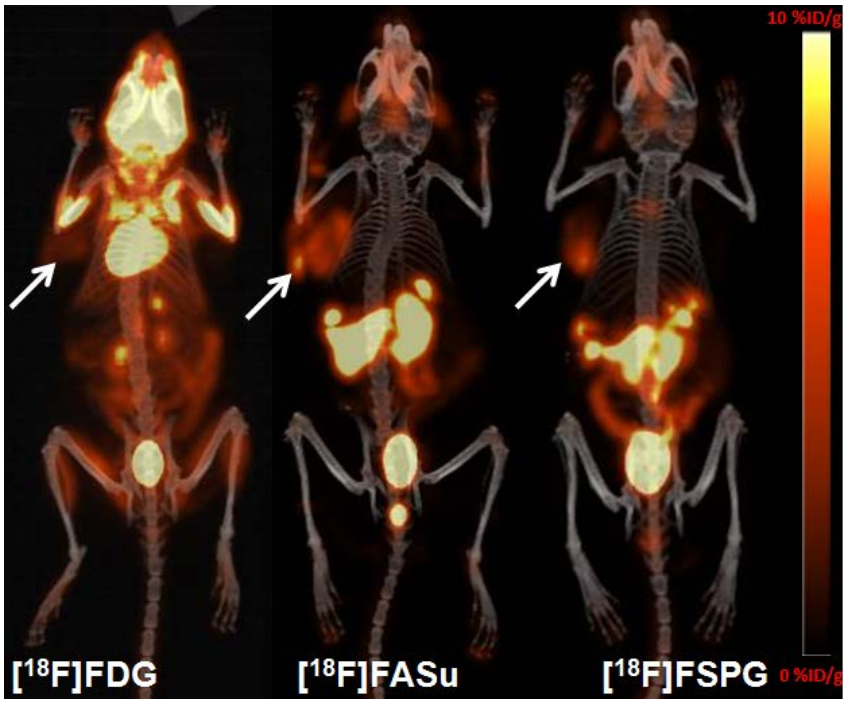

Figure 5.7 Comparative study: uptake of [^{18}F]FDG, [^{18}F]FASu and [^{18}F]FSPG in A549 tumour-bearing mice at 1 h post – injection. White arrows are pointing at A549 tumours.

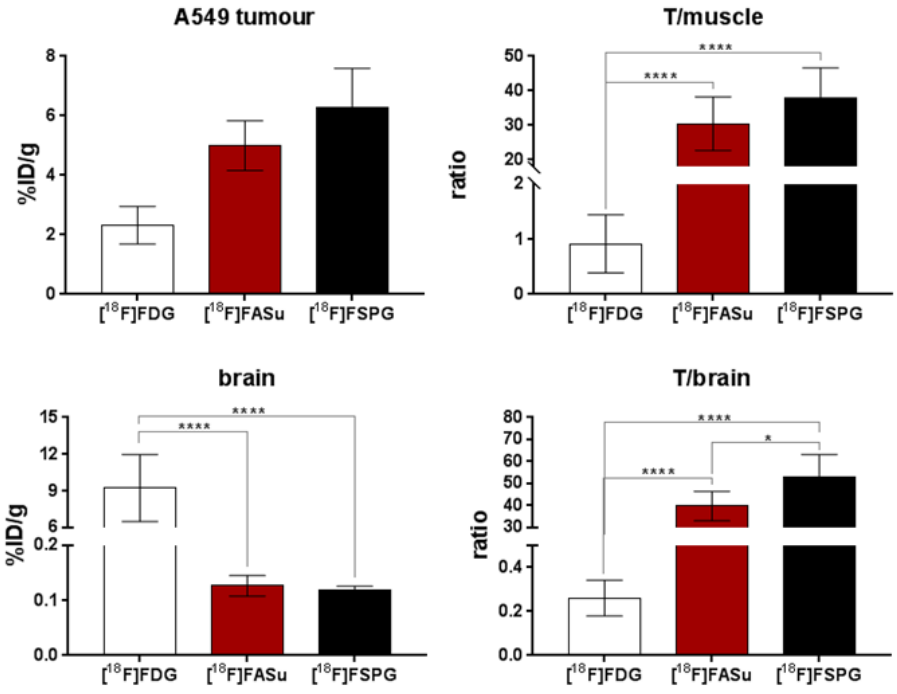

Figure 5.8 Two-way ANOVA analysis of tumour-to-muscle and tumour-to-brain ratios, tumour and brain uptake for [^{18}F]FDG, [^{18}F]FASu and [^{18}F]FSPG in A549 tumour-bearing mice at 1 h post – injection. * $p < 0.05$, **** $p < 0.0001$.

[^{18}F]FSPG tumour uptake was statistically significantly higher than that of [^{18}F]FDG (*** $p < 0.001$) and [^{18}F]FASu (* $p < 0.05$), as were tumour-to-muscle and tumour-to-brain uptake ratios (**** $p < 0.0001$, Figure 5.10). There was no significant difference in tumour uptake or tumour-to-muscle ratios of [^{18}F]FASu as compared to [^{18}F]FDG ($p = 0.071$, Figure 5.10). [^{18}F]FDG brain uptake, however, was statistically significantly higher than the uptake of [^{18}F]FASu and [^{18}F]FSPG (** $p < 0.01$). This difference is particularly apparent on the PET images (Figure 5.11). The reason for elevated background tissue uptake, particularly that of the muscle, of [^{18}F]FDG which contributed to poorer image contrast could be the fact that the mice were not fasted prior to the imaging experiments, nor were they kept anaesthetized between the injection time and imaging/biodistribution time.

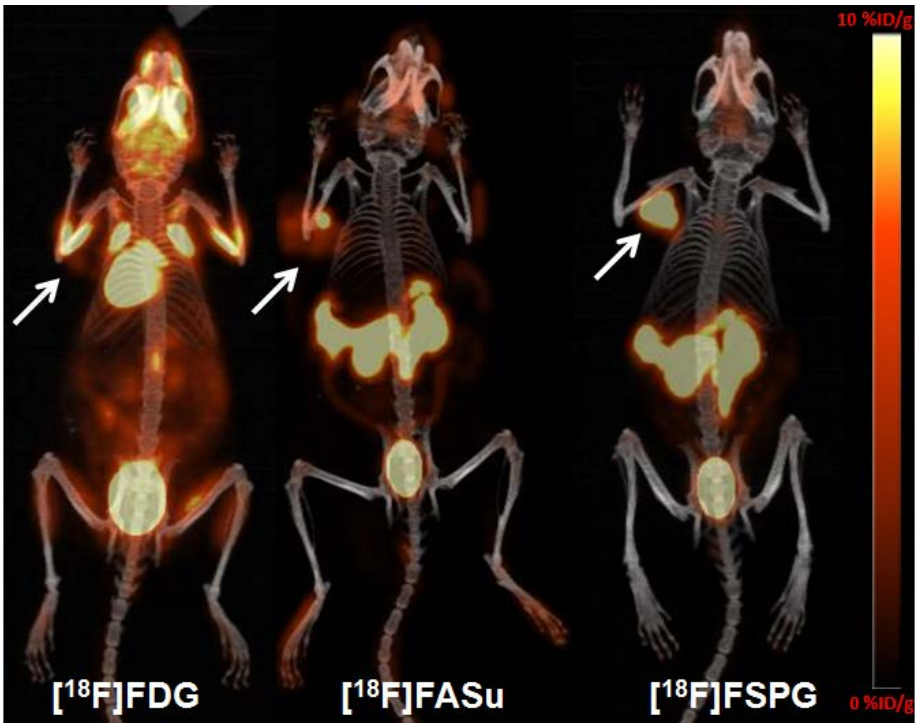

Figure 5.9 Comparative study: uptake of [^{18}F] FDG, [^{18}F]FASu and [^{18}F]FSPG in U-87 tumour-bearing mice at 1 h post – injection. White arrows are pointing at U-87 tumours.

Literature reports indicate that fasting animals the night before [^{18}F]FDG imaging contributes to significant changes in myocardial and brain standardized uptake values (SUVs), but does not significantly affect SUVs of the skeletal muscle.[235] Another report found that depending on study conditions, [^{18}F]FDG uptake by normal tissues varied several fold for skeletal muscle, brown adipose tissue and myocardium.[236] The authors found that depending on

whether the animals are anaesthetized or not, [^{18}F]FDG uptake significantly changed both in normal tissues and in xenografted tumours. In our study, isoflurane anaesthesia was only used briefly prior to and during radiotracer injection and during imaging. The only effect that was observed was the difference between static (Figure 5.9) and the dynamic FDG image (Figure 5.11) in non-fasted animals. In contrast to Fueger's findings,[236] we observed considerably higher tumour uptake on the dynamic *versus* static [^{18}F]FDG image, which was attributed to prolonged isoflurane anaesthesia of the animal that underwent dynamic imaging. The tumour uptake of the mouse that had undergone static imaging is within the range of the tumour uptake from biodistribution data. The workflow was constant between [^{18}F]FDG and non-[^{18}F]FDG experiments, the dynamically scanned mice were not included in the biodistribution data, and thus we do not think the anaesthesia conditions could have affected our results substantially. Rather, we suspect that fasting animals would improve [^{18}F]FDG biodistribution profile, and particularly increase tumour-to-background organ ratios, which is why we repeated the study and imaged mice that were subjected to overnight fasting with either [^{18}F]FDG or [^{18}F]FASu, in order to investigate if/to what extent fasting affects uptake of these tracers.

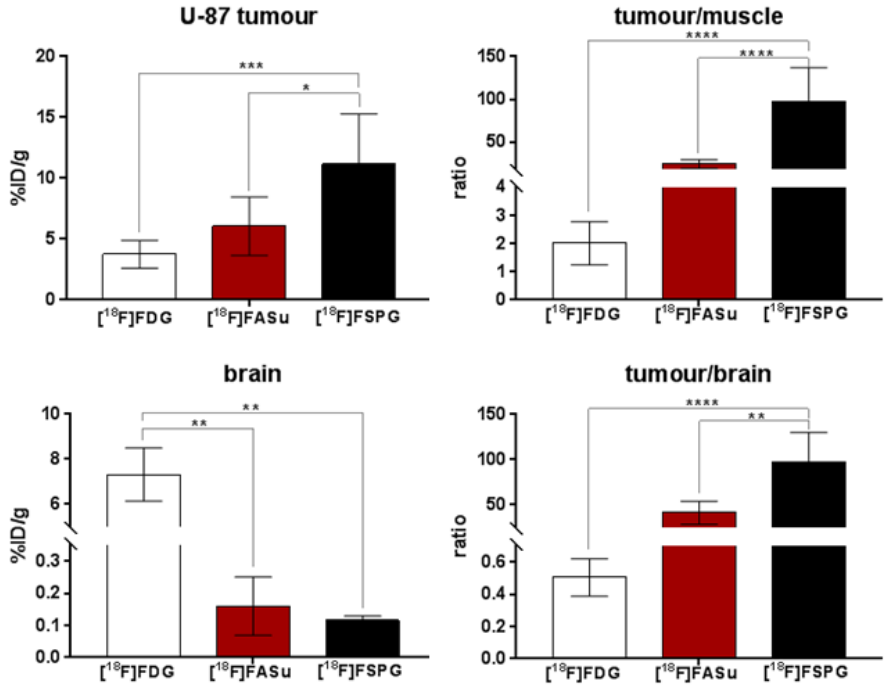

Figure 5.10 Two-way ANOVA analyses of tumour-to-muscle and tumour-to brain ratios, tumour and brain uptake for [^{18}F]FDG, [^{18}F]FASu and [^{18}F]FSPG in U-87 tumour-bearing mice at 1 h post – injection. * $p < 0.05$, ** $p < 0.01$, *** $p < 0.001$ and **** $p < 0.0001$.

Table 5.2 Biodistribution and tumour-to-non-target ratios of [^{18}F]FDG, [^{18}F]FASu and [^{18}F]FSPG in U-87 xenograft-bearing Rag2M mice.

	[^{18}F]FDG	**[^{18}F]FASu**	**[^{18}F]FSPG**
organ	**unblocked (n ≥ 5)**	**unblocked (n ≥ 4)**	**unblocked (n ≥ 4)**
blood	0.66 ± 0.23	0.84 ± 0.50	0.59 ± 0.08
fat	0.23 ± 0.07	0.04 ± 0.02	0.02 ± 0.00
ovaries	2.50 ± 0.61	3.07 ± 1.48	5.62 ± 4.09
uterus	3.32 ± 1.40	5.97 ± 3.08	5.07 ± 0.73
small intestine	2.62 ± 0.89	1.83 ± 0.64	2.18 ± 0.40
stomach	1.00 ± 0.27	1.66 ± 1.13	1.08 ± 0.73
pancreas	2.12 ± 0.74	26.42 ± 11.59	16.81 ± 1.38
spleen	3.62 ± 0.89	4.47 ± 1.65	6.58 ± 1.58
adrenal glands	2.59 ± 0.49	0.46 ± 0.15	0.55 ± 0.05
kidneys	3.03 ± 0.79	17.79 ± 7.20	17.92 ± 2.49
liver	1.24 ± 0.28	0.95 ± 0.44	0.59 ± 0.14
heart	32.8 ± 17.70	0.36 ± 0.21	0.17 ± 0.01
lungs	3.80 ± 1.12	3.41 ± 2.20	1.39 ± 0.16
muscle	1.94 ± 0.57	0.26 ± 0.11	0.12 ± 0.02
bone	0.99 ± 0.37	0.76 ± 0.46	0.76 ± 0.17
brain	7.32 ± 1.18	0.16 ± 0.09	0.12 ± 0.01
tail	1.45 ± 0.08	1.82 ± 0.90	1.26 ± 0.24
U-87 tumour	**3.75 ± 1.15**	**6.05 ± 2.40**	**11.18 ± 4.12**
Tumour / blood	5.62 ± 0.96	7.96 ± 2.81	18.67 ± 6.30
Tumour / muscle	2.02 ± 0.77	24.08 ± 5.20	97.86 ± 38.99
Tumour / lungs	0.99 ± 0.19	1.96 ± 0.51	8.04 ± 2.60
Tumour / brain	0.50 ± 0.11	41.30 ± 12.73	97.22 ± 33.15

Biodistributions and ratios are at 1 h p.i. Values (%ID/g) are presented as mean ± standard deviation.
[a]Blocked with co-injection of the cold standard, aminosuberic acid (ASu).

To our surprise and contrary to the findings of Fueger & colleagues,[236] we observed a slight decrease in tumour-to-muscle ratio for [^{18}F]FDG biodistribution in fasted mice (Table 5.3, Figure 5.12A), as compared to the non-fasted study. Tumour-to-muscle and tumour-to-brain ratios were substantially higher for [^{18}F]FASu, as compared to [^{18}F]FDG, 14.74 ± 2.55 and 1.83 ± 1.47 were tumour-to-muscle, and 28.45 ± 6.34 and 0.41 ± 0.11 were tumour-to-brain ratios for [^{18}F]FASu and [^{18}F]FDG, respectively. Brain uptake of [^{18}F]FDG remained high after fasting and the average of biodistribution data totalled 11.17 ± 4.87 %ID/g. U-87 tumour uptake of [^{18}F]FDG (4.35 ± 1.40 %ID/g) did increase compared to the uptake in non-fasted animals, resulting in excellent tumour visualisation on the dynamic scan (Figure 5.12A), however it remained statistically no different from that of [^{18}F]FASu based on the biodistribution data (p =

0.995, Figures 5.13 and 5.14). More importantly, tumour-to-brain ratio of [^{18}F]FASu remained high, despite lowered tumour %ID/g (Figure 5.14), giving it potential for, and advantage over [^{18}F]FDG in intracranial malignancy imaging. Clearance of both tracers from most organs was rapid, with the exception of heart and brain activity in the case of [^{18}F]FDG (Figure 5.12B). [^{18}F]FDG activity in the heart kept increasing over time, and the activity in the brain and U-87 xenograft levelled off within the first five minutes of the scan and remained constant throughout the scan duration, with the tumour uptake (ROI: 6.59 %ID/g) being lower than that of the brain (ROI: 7.10 %ID/g). [^{18}F]FASu, on the other hand, demonstrated rapid clearance from all background tissues within the first five minutes of the scan (Figure 5.12B), accumulating in the tumour (ROI activity was 3.48 %ID/g for the imaged mouse). Average U-87 tumour uptake of [^{18}F]FASu was 2.51 ± 0.52 %ID/g, which is lower than the uptake we observed in non-fasted animals (6.05 ± 2.40 %ID/g), however there is a small region of high uptake within the U-87 tumour on both [^{18}F]FASu PET images (Figures 5.9 and 5.12A), which may be attributed to the intra-tumoural heterogeneity. We hypothesize that these regions would align with regions of high xCT expression within the tumour, and also likely with high expression of hypoxia markers, as the link between xCT expression and hypoxia has been confirmed in several studies.[237–240]

Irrespective of the tumour inoculated (U-87 or A549), as shown in Tables 5.1 and 5.2, [^{18}F]FASu and [^{18}F]FSPG have very similar biodistribution profiles and excretion pathways. This is not at all surprising, given the structural similarity of the two tracers and both targeting the same transporter.[103,139] Compared to [^{18}F]FASu, [^{18}F]FSPG had higher *in vivo* tumour uptake in both cases: statistically significantly higher uptake in the U-87 tumour (Figure 5.10, * $p < 0.05$), and not statistically significantly higher in A549 ($p = 0.79$), despite higher xCT expression in these tumours, (Figure 5.6). This may be an indication of [^{18}F]FASu uptake being more reliant on system x_C^- than [^{18}F]FSPG, since its structural analogue cystine enters the cells predominantly *via* system x_C^-, whereas glutamate, the structural analogue of [^{18}F]FSPG, gets transported into the cells by the action of the excitatory amino acid transporter proteins (EAATs), or system x_{AG}^-, in addition to system x_C^-.[241] Moreover, an early paper on [^{18}F]FSPG's specificity by Koglin and colleagues[139] demonstrated that while [^{18}F]FSPG does predominantly use system x_C^- to enter cells, both *L*-cystine and *L*-glutamate achieved higher levels of tracer uptake inhibition than a very potent system x_C^- inhibitor, *p*-carboxy-phenylglycine (CPG) – indicating that other AATs

whose substrates are *L*-glutamate and/or *L*-cystine such as EAATs (EAAT1/2/4/5 for *L*-Glu, and EAAT3 for both),[184] might be taking up [^{18}F]FSPG to a certain extent. The authors also reported observing a minor competition with either *L*- or *D*- aspartate which are both substrates along with *L*-glutamate for the EAAT family members 1-5.[184] Webster and colleagues[102] performed a similar *in vitro* uptake inhibition uptake assay with [^{18}F]FASu, and in their study SSZ was more effective in blocking tracer uptake than *L*-glutamate, signifying a preference of [^{18}F]FASu for system x_C^-. The authors reported observing very little effect of *D*-aspartate on [^{3}H]ASu, [^{3}H]Glu and [^{3}H]Leu uptake.

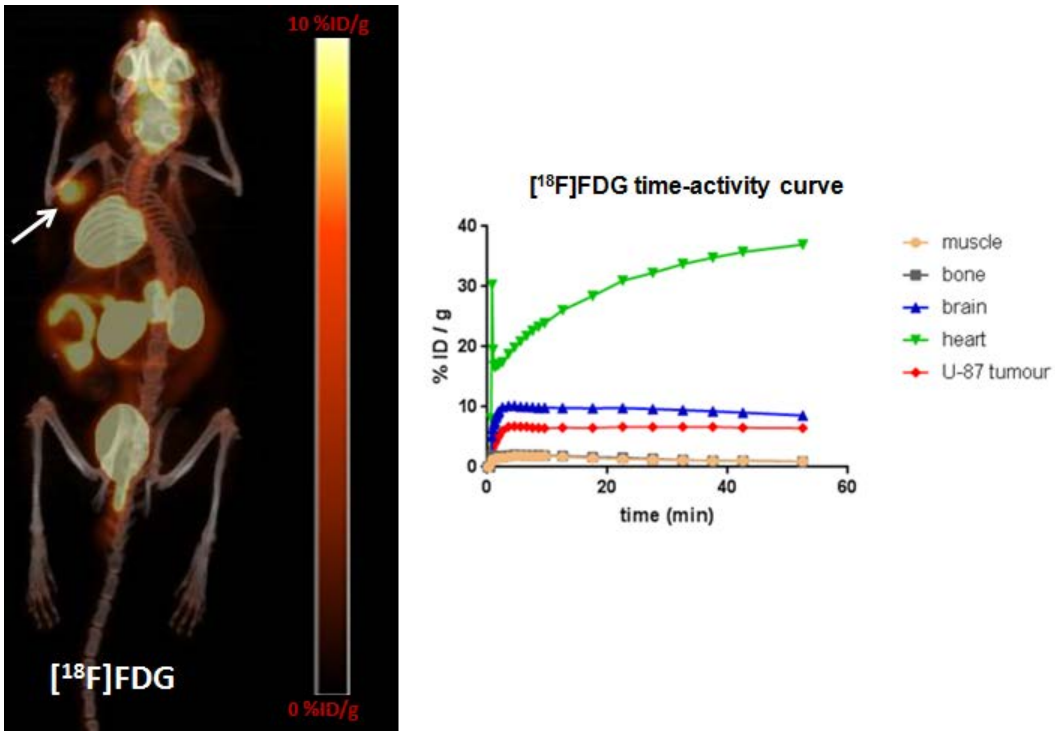

Figure 5.11 Dynamic PET maximum intensity projection of [^{18}F]FDG uptake 45-60 min after injection in U-87 tumour-bearing Rag2M mouse. White arrow is pointing at the U-87 tumour. **Right panel:** Time-activity curve of selected ROIs 0 – 55 min after injection.

Table 5.3 Biodistribution and tumour-to-non-target ratios of [^{18}F]FDG and [^{18}F]FASu in U-87 xenograft-bearing NSG mice that had been subjected to fasting for 12-14 h.

FASTED mice	**[^{18}F]FDG**	**[^{18}F]FASu**
	unblocked (n = 4)	**unblocked (n = 5)**
blood	0.80 ± 0.19	0.58 ± 0.11
fat	0.30 ± 0.09	0.05 ± 0.01
ovaries	2.31 ± 0.55	3.36 ± 1.90
uterus	3.26 ± 0.61	2.84 ± 0.56
small intestine	3.69 ± 0.89	1.22 ± 0.15
stomach	1.08 ± 0.53	1.64 ± 0.30
pancreas	2.09 ± 0.55	21.28 ± 2.82
spleen	3.98 ± 1.65	1.92 ± 0.58
adrenal glands	1.79 ± 0.56	0.45 ± 0.09
kidneys	2.64 ± 0.59	15.93 ± 2.37
liver	1.11 ± 0.15	0.89 ± 0.12
heart	24.42 ± 11.91	0.23 ± 0.03
lungs	4.16 ± 0.53	2.02 ± 0.39
muscle	3.16 ± 1.40	0.17 ± 0.02
bone	1.64 ± 0.70	1.26 ± 0.18
brain	11.17 ± 4.87	0.09 ± 0.01
tail	11.96 ± 6.43	1.77 ± 0.41
U-87 tumour	**4.35 ± 1.40**	**2.51 ± 0.53**
Tumour / blood	5.34 ± 0.50	4.30 ± 0.37
Tumour / muscle	1.83 ± 1.47	14.74 ± 2.55
Tumour / lungs	1.04 ± 0.27	1.27 ± 0.30
Tumour / brain	0.41 ± 0.11	28.45 ± 6.34

The first aim of this study was to compare performance of the two tracers *in vitro* and *in vivo*, in a variety of cancer cell lines and tumours. We found that [^{18}F]FSPG is taken up more readily *in vitro* by all cell lines tested, and that *in vivo* it showed higher uptake than [^{18}F]FASu in glioblastoma and non-small cell lung cancer xenografts. We also discovered that overnight fasting did not substantially affect biodistribution of [^{18}F]FDG. Since the two studies (non-fasted *vs.* fasted) were done in two different strains of mice, we cannot make direct comparisons and draw conclusions, however, fasting did cause tumour uptake of [^{18}F]FASu to drop from 6.05 ± 2.40 %ID/g to 2.51 ± 0.53 %ID/g on average and thus worsen the tumour visualisation on the

static PET scan (Figure 5.13). Further studies are required to understand the impact of imaging conditions (food, anaesthesia *etc.*) on the biodistribution of amino acid tracers.

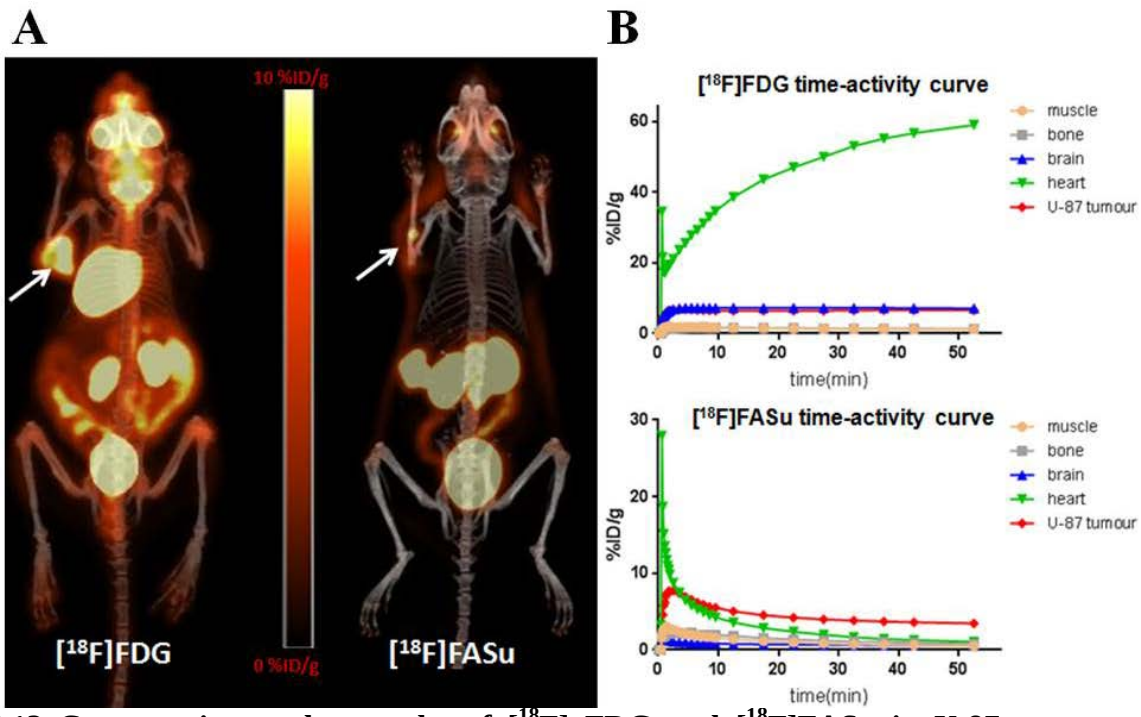

Figure 5.12 Comparative study: uptake of [^{18}F] FDG and [^{18}F]FASu in U-87 tumour-bearing mice at 1 h post – injection. A) Maximum-intensity projection PET/CT images of [^{18}F]FDG and [^{18}F]FASu at 45 – 60 min after injection. White arrows are pointing at U-87 tumours. **B)** Time-activity curves of selected ROIs for [^{18}F]FDG and [^{18}F]FASu from 0 – 55 min after injection.

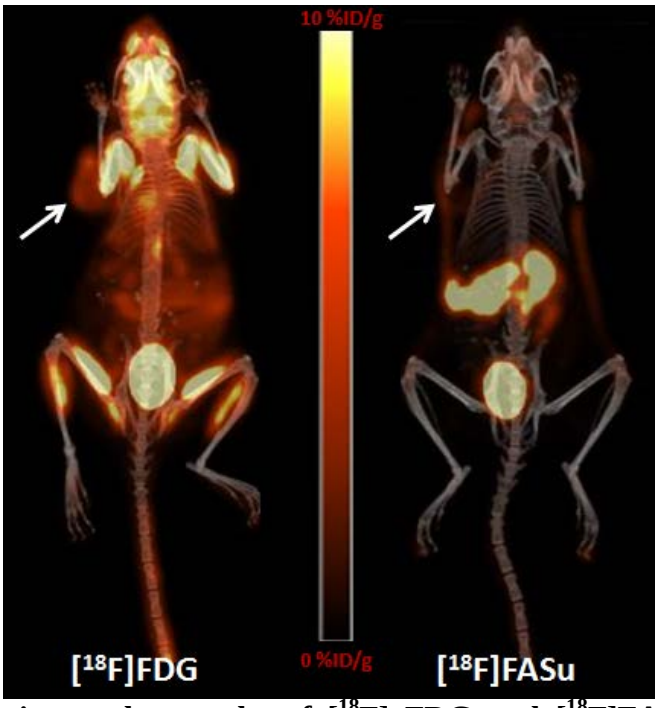

Figure 5.13 Comparative study: uptake of [^{18}F] FDG and [^{18}F]FASu in U-87 tumour-bearing mice at 1 h post – injection. White arrows are pointing at U-87 tumours. The mice were subjected to overnight fasting.

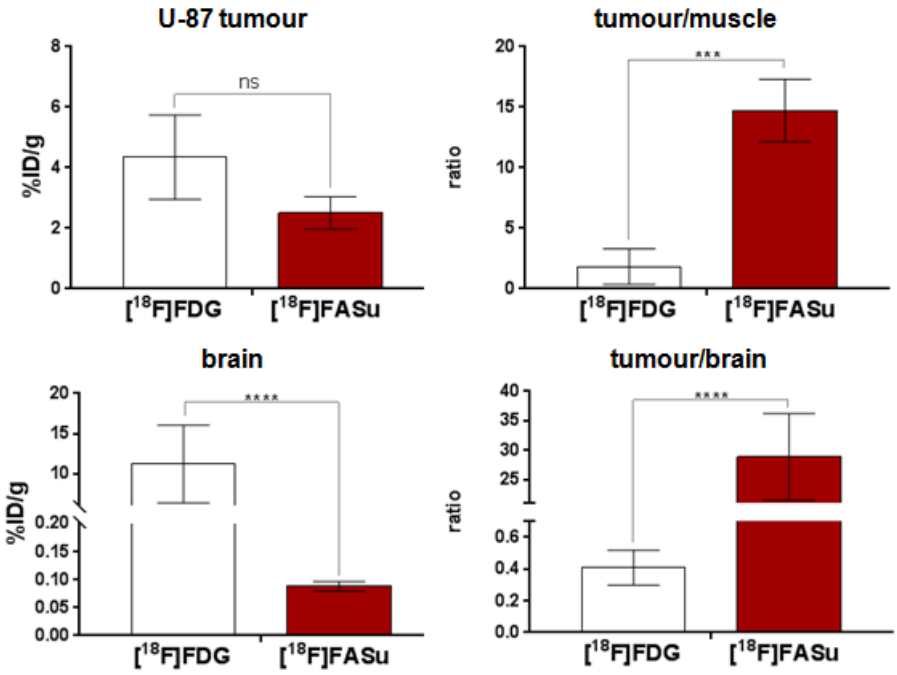

Figure 5.14 Two-way ANOVA analysis of tumour-to-muscle and tumour-to-brain ratios, tumour and brain uptake for [^{18}F]FDG and [^{18}F]FASu in U-87 tumour-bearing fasted NSG mice at 1 h post – injection. *** $p < 0.001$, **** $p < 0.0001$.

An answer to the question on the specificity of [^{18}F]FASu and [^{18}F]FSPG toward system x_C^- cannot be derived without a comprehensive, carefully designed study. We have, therefore, set this as an additional aim of this project. Our approach to answer this question involved a series of *in vitro* assays, including specificity assays with both tracers as well as competition assays against increasing concentrations of the two natural system x_C^- substrates, *L*-cystine and *L*-glutamate.

In vitro specificity assays were done in A549, U-87 and MDA-MB-231 cell lines using system x_C^- inhibitor sulfasalazine (SSZ), as well as inhibitors of vesicular glutamate transporters (VGLUTs - Rose Bengal),[242] of the EAAT family of transporters, (*L-trans*-pyrrolidine-2,4-dicarboxylic acid or PDC),[243] and of system L transporter (2-aminobicyclo-(2,2,1)-heptane-2-carboxylic acid or BCH)),[168,244,245] in addition to *L*-serine, which is a known substrate of transporter systems A, ASC, B^0 and asc.[184] Once again, SSZ inhibited uptake of both [^{18}F]FASu and [^{18}F]FSPG significantly across board (*p* value varied for each comparison but was in all cases < 0.05, n=3, Figure 5.15). [^{18}F]FASu uptake was not lowered substantially in the excess of PDC, *L*-serine or BCH. On the other hand, [^{18}F]FSPG uptake was decreased significantly in excess of PDC in A549 and MDA-MB-231 cells ($p = 0.0006$ and $p < 0.0002$, respectively), but not in U-87 cell line ($p = 0.457$), indicating reliance on EAATs in these cell lines. This finding is consistent with the report of Koglin and colleagues who also reported competition of [^{18}F]FSPG uptake with both aspartate and glutamate, the natural substrates of the EAATs.[139,184] An unexpected finding was that the most potent VGLUT inhibitor Rose Bengal[246] inhibited the uptake of both [^{18}F]FASu and [^{18}F]FSPG ($p < 0.01$) and that it had better blocking efficacy than SSZ in the case of both tracers, and across all cell lines (Figure 5.15).

The selectivity of [^{18}F]FASu and [^{18}F]FSPG to system x_C^- transporter was further studied in a dose dependent manner in competition assays against the natural substrates of system x_C^-, *L*-cystine and *L*-glutamate. IC_{50} values of 3.92 ± 0.60 µM and 3.23 ± 1.01 µM were determined for *L*-cystine in competition with [^{18}F]FASu and [^{18}F]FSPG, respectively, in A549 cells (Figure 5.16). These values are lower than the values determined in the competition with *L*-glutamate: 10.93 ± 1.00 µM for [^{18}F]FASu and 5.20 ± 1.18 µM for [^{18}F]FSPG. While the difference in IC_{50} values for *L*-cystine was not substantial ($p = 0.6503$), the *L*-glutamate IC_{50} values differed

significantly (p = 0.0002), once again indicating higher reliance of [^{18}F]FSPG on alternative modes of glutamate transport.

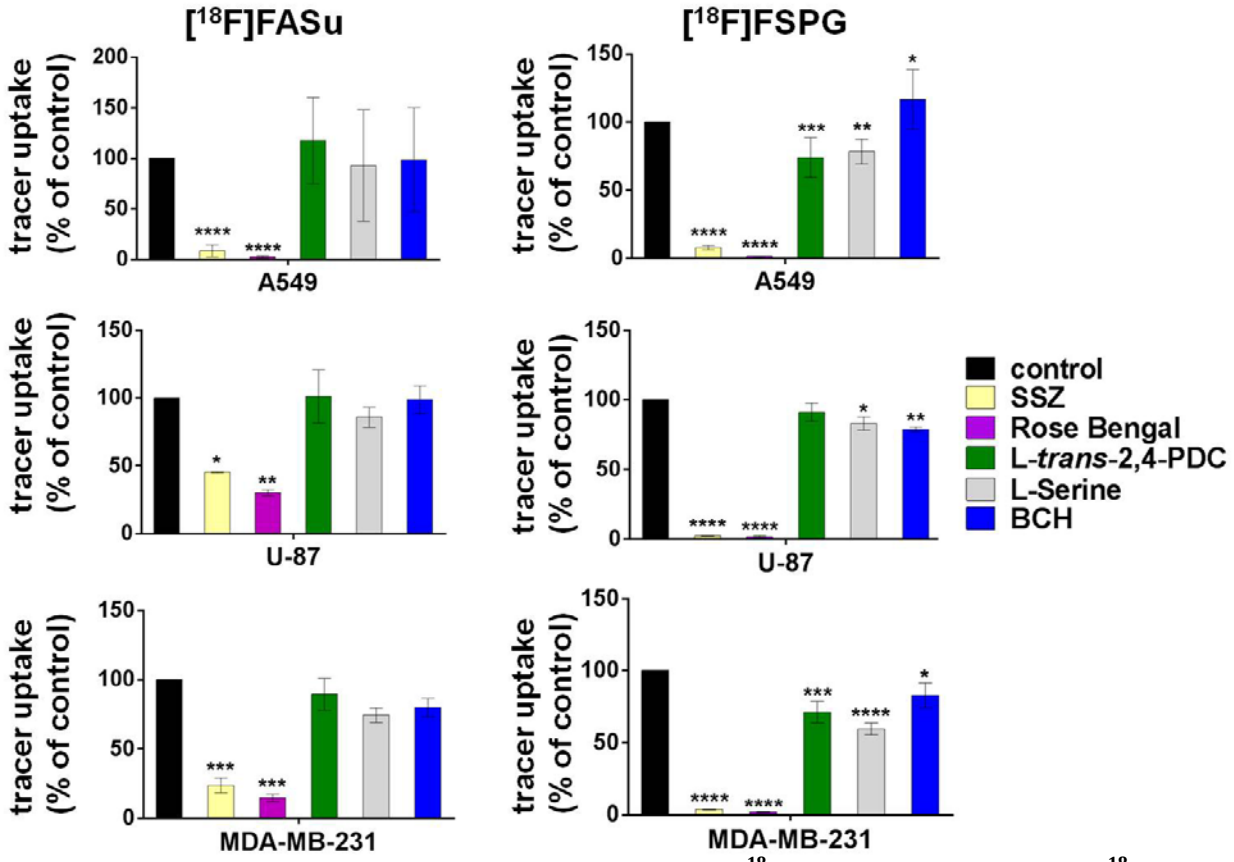

Figure 5.15 Two-way ANOVA analysis of 1h uptake of [^{18}F]FASu (left panel) and [^{18}F]FSPG (right panel) in A549, U-87 and MDA-MB-231 cells, expressed as percent of control sample uptake. * $p < 0.05$, ** $p < 0.01$, *** $p < 0.001$, **** $p < 0.0001$.

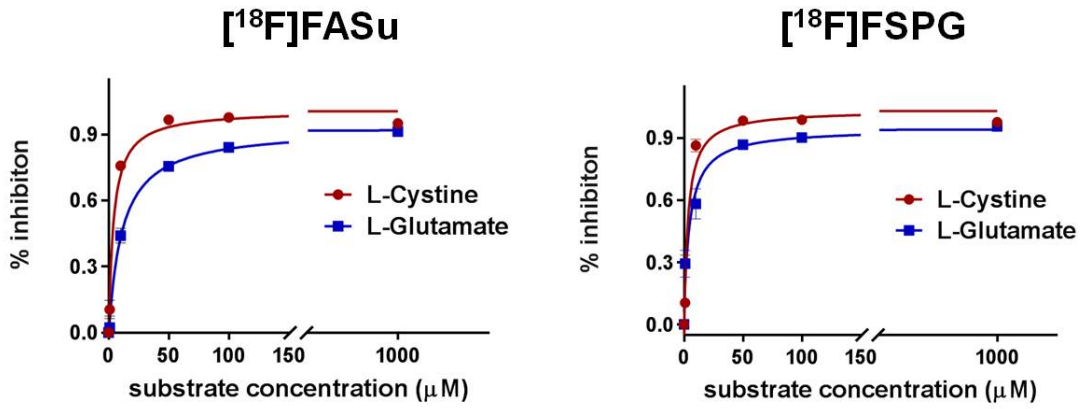

Figure 5.16 Dose-dependent competition cell uptake assays were carried out in A549 cell line using 148 kBq/well of either [^{18}F]FASu (left) and [^{18}F]FSPG (right) and increasing concentration of L-cystine or L-glutamate.

5.4 Conclusion

We synthesized the ^{18}F-labelled cystine analog, [^{18}F]FASu, and evaluated its potential as a cancer imaging agent in comparison to the previously characterized glutamate analogue, [^{18}F]FSPG. [^{18}F]FSPG had higher *in vitro* uptake than [^{18}F]FASu in all tested cell lines, however our results did indicate that [^{18}F]FSPG relies not only on system x_C^- to enter the cells, but also EAATs, and likely other glutamate transporters. An incidental finding in this study was the ability of Rose Bengal, a known VGLUT inhibitor, to block amino acid transport *via* system x_C^-. *In vivo* studies showed equally good ability to image glioblastoma (U-87) and non-small lung cancer (A549) xenografts, with [^{18}F]FSPG having notably higher contrast. Both tracers exhibited low background uptake and moderate to high tumour-to-blood, tumour-to-brain, and tumour-to-muscle ratios. Additionally, [^{18}F]FASu and [^{18}F]FSPG were compared to [^{18}F]FDG in studies done on non-fasted mice. The fluorinated system x_C^--targeting tracers were superior to [^{18}F]FDG in tumour visualization, image contrast, and perhaps most importantly, exhibited low brain uptake, which demonstrated promising potential for imaging of intracranial malignancies. Under fasting conditions, however, [^{18}F]FDG showed slightly increased, though not significantly different, U-87 tumour uptake as compared to [^{18}F]FASu. We found that the duration of isoflurane anaesthesia greatly affected tumour uptake of [^{18}F]FDG regardless of the fasting state, and that higher tumour-to-background contrast was achieved when then the mice were anaesthetized longer. Nevertheless, our results showed that the amino-acid based tracers do provide us with useful complementary information to [^{18}F]FDG-PET, particularly regarding heterogeneity of the tumour.

Chapter 6: ^{18}F-labelled system L substrates for imaging with positron emission tomography

6.1 Introduction

The selective imaging of cancers with PET often exploits radiotracers that target aberrant cellular metabolism or increased protein expression.[31] For example, the widely used cancer diagnostic 2-deoxy-2-[^{18}F]fluoro-*D*-glucose[4,31] (Figure 6.1, [^{18}F]FDG (**1**)) takes advantage of the increased glucose uptake and glycolysis in many tumours. Increased amino acid uptake through overexpression of AATs is also a signature feature of cancers, and radiolabelled amino acids (e.g., Figure 4.1, **2**[173] and **3**[223]) are highly sought imaging agents.[12,167] The uptake of amino acids by *L*-type AATs (LATs)[183] is a particularly appealing target for PET radiotracers. Most notably, the LAT1 isoform transports branched and aromatic amino acids, and is highly upregulated in several cancers (e.g., prostate, breast and brain) and at metastatic sites.[183]

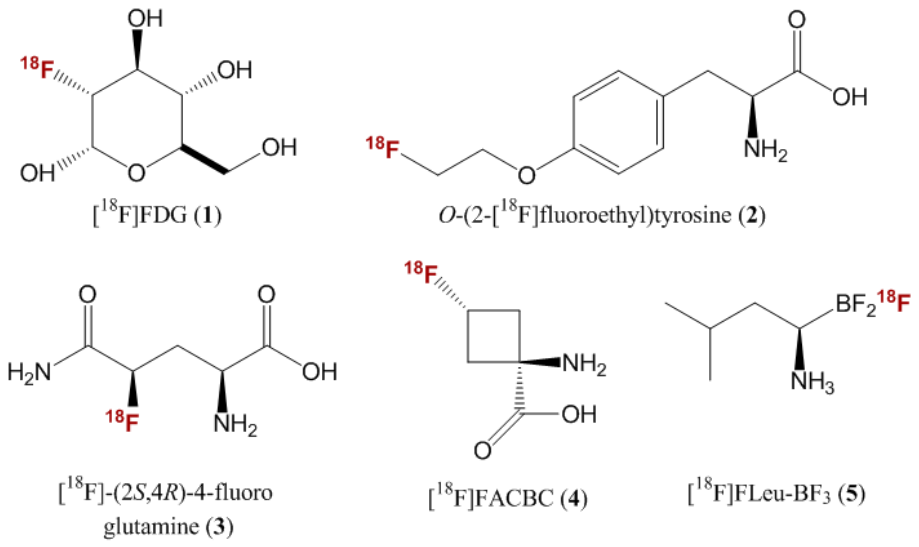

Figure 6.1. Radiotracers for PET imaging in oncology and ^{18}F-labelled analogues of leucine. Reprinted with permission from Nodwell, Yang, Čolović, *et al.*(2017). ^{18}F-Fluorination of Unactivated C-H Bonds in Branched Aliphatic Amino Acids: Direct Synthesis of Oncological Positron Emission Tomography Imaging Agents. *JACS*, 2017; 139(10):3595-3598. © Copyright (2017) American Chemical Society.

Among the wide range of amino acids transported by LAT1, leucine plays a uniquely important role in cancer biology as large cellular concentrations of leucine are required to trigger mTORC1 activation and support accelerated protein synthesis.[185] Not surprisingly then, *L*-1-[^{11}C]leucine has been developed, and represents a promising PET imaging agent.[247] Unfortunately, its widespread use is limited by a reliance on the fast decaying radionuclide ^{11}C ($t_{1/2}$ = 20.4 min), which restricts use to PET clinics with on-site cyclotron facilities. The longer lived radionuclide ^{18}F ($t_{1/2}$ = 109.8 min) is incorporated in the leucine mimic anti-1-amino-3-[^{18}F]fluorocyclobutane-1-carboxylic acid (Figure 6.1, [^{18}F]FACBC (**4**)), which was recently approved by the U.S. FDA for recurrent prostate cancer imaging.[248] Recently, the boramino acid [^{18}F]Leu-BF_3 (**5**) was also reported,[207] adding to the repertoire of radiolabeled leucine mimics. Notwithstanding these and other advances,[167] there is no general synthetic strategy to effect selective ^{18}F-labeling of amino acids such as leucine without significantly altering the parent structure or relying on prosthetic groups. Here, the direct radiofluorination[249] of unprotected, branched aliphatic amino acids is described. The PET imaging of mice bearing subcutaneous PC-3 or U-87 xenografts using a new ^{18}F-labeled analogue of leucine highlights the potential for this convenient reaction to rapidly access amino acid-derived imaging agents for cancer. Additionally, we report the biological evaluation of five new LAT1-targetting tracers (Figure 6.10), all of which have been synthesized using our novel direct radiofluorination method.

The Britton laboratory at Simon Fraser University has recently reported the decatungstate-catalyzed fluorination of unactivated C−H bonds[250] and has applied this strategy to the selective fluorination of aliphatic[250,251] and benzylic[252] C-H bonds. This reaction involves hydrogen atom abstraction by a photoactivated decatungstate catalyst,[253] followed by fluorine atom transfer[254] from N-fluorobenzenesulfonimide (NFSI) to the resultant carbon radical (e.g., **8**, Figure 6.2). Considering the high degree of selectivity observed for C−H fluorination at the branched position in esters of leucine[251] and valine,[250] we contemplated development of the photocatalytic C-H ^{18}F-fluorination reaction depicted in Figure 6.2 using [^{18}F]NFSI,[255] a reagent that has been developed by Gouverneur and Luthra.[255–258] This unique process would provide

direct access to 4-[^{18}F]FL (**7**)[259] or other radiolabeled amino acid substrates for LAT1 from readily available or natural amino acids (e.g., **6**, Figure 6.2).

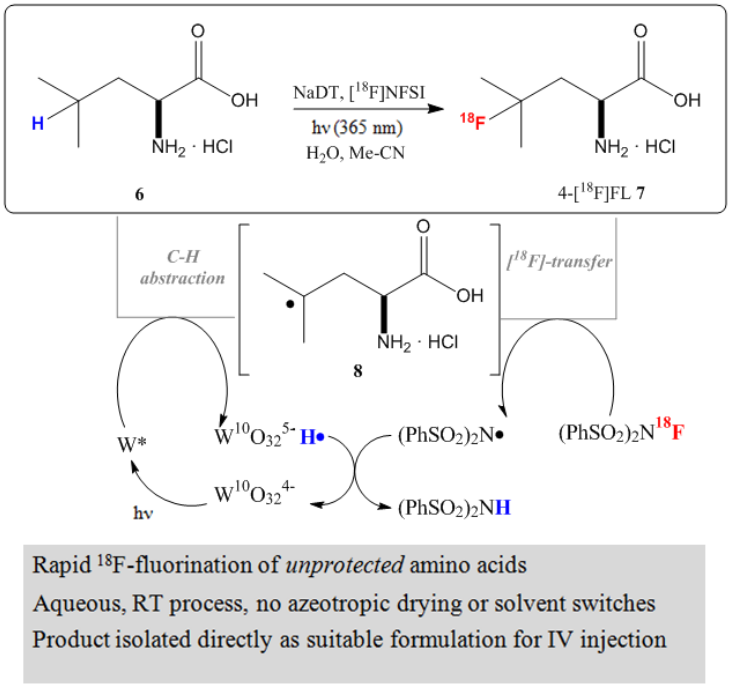

Figure 6.2 Decatungstate-catalyzed C-H fluorination applied to the production of 4-[^{18}F]fluoroleucine (4-[^{18}F]FL (7)). Copyright © 2017, American Chemical Society.

In this work, we applied this novel radiofluorination method to label several new branched aliphatic amino acids, evaluated these novel tracers as LAT1 substrates and as PET cancer imaging agents.

Adapted with permission from: ^{18}F-Fluorination of Unactivated C-H Bonds in Branched Aliphatic Amino Acids: Direct Synthesis of Oncological Positron Emission Tomography Imaging Agents. *J Am. Chem. Soc.*, 2017; 139(10):3595-3598. Copyright (2017) American Chemical Society.

Matthew B. Nodwell, Hua Yang, **Milena Čolović**, Zheliang Yuan, Helen Merkens, Rainer E. Martin, Francois Benard, Paul Schaffer, and Robert Britton

And: ^{18}F-branched chain amino acids: structure-activity relationships and PET imaging potential. *J Nuc Med*, Published online January 25, 2019. Doi: 10.2967/jnumed.118.220483

Matthew B. Nodwell, Hua Yang, Helen Merkens, Noeen Malik, **Milena Čolović**, Bjoern Wagner, Rainer E. Martin, Francois Benard, Paul Schaffer, and Robert Britton

RB, PS, FB, REM, MBN and HY designed the study. MBN and HY performed tracer radiosyntheses. MBN and ZY performed the non-radioactive synthesis. **MČ** and HM performed biological studies. MBN, HY and **MČ** were involved in acquisition of data and interpretation of the findings. All authors wrote the manuscripts.

6.2 Materials & methods

6.2.1 Reagents and instrumentation

All reactions were carried out with commercial solvents and reagents that were used without further modification. Radioactivity of ^{18}F-labeled tracers were measured using a Capintec (Ramsey, NJ) CRC®-25R/W dose calibrator. A PerkinElmer Wizard 2480 gamma counter was used for measuring radioactivity of samples from cell uptake and biodistribution studies.

The detailed reaction protocols can be found in detail in our publications.[260,261] They are not included here because they are beyond the scope of this thesis, which encompasses biological evaluation of the tracers in *in vitro* and *in vivo* studies.

6.2.2 Photo-catalyzed fluorination: radiochemistry

6.2.2.1 Synthesis of 4-[^{18}F]FL, 5-[^{18}F]FHL, 5-[^{18}F]FBAHL, 3-[^{18}F]FV and α-Me-[^{18}F]FL

Radiofluorinated amino acids were produced at TRIUMF, as described elsewhere.[255] Briefly, the [^{18}F]N-fluorodibenzenesulfonamide ([^{18}F]NFSI) solution was added to a slurry of the substrate (*L*-leucine.HCl =10 mg (55 μmol), β-aminohomoleucine · TFA = 13 mg (50 μmol), homoleucine · TFA = 12 mg (46 μmol) and valine · TFA = 12mg (52 μmol) and sodium decatungstate (NaDT, 5 mg, 2.0 μmol) in 200-400 μL H_2O and mixed briefly. The solution was then loaded onto the photoreactor (15 W F15T8/BLB lamp and vial used in the fluorination) and irradiated for 40 min. After this time the solution was removed and the photoreactor was washed with CH_3CN (5 mL). The resulting solution was loaded onto a preconditioned strong cation exchange cartridge (Silicycle, 500 mg resin) and the cartridge was washed with CH_3CN (10 mL) followed by H_2O (10 mL). 4-[^{18}F]FL, 5-[^{18}F]FBAHL, 5-[^{18}F]FHL, 3-[^{18}F]FV or α-Me-[^{18}F]FL were then eluted from the cartridge with 1 mL aliquots of 150 mM $NaHCO_3$, yielding a mixture of fluorinated product and starting material. The bulk of the activity was typically eluted in the 4th and 5th 1 mL aliquot. Analytical HPLC was carried out on Phenomenex Monolithic C_{18} analytical column (4.6 × 100 mm column, 1 mL/min) using a gradient of 2% solvent A (0.1% TFA in H2O) and 98% solvent B (0.1% TFA in CH_3CN) to 100% solvent B over 30 min or on a

Phenomenex Luna C_{18} (4.6 x 100 mm, 1 mL/min) using a gradient of 100% solvent A (0.1% TFA in H2O) to 100% solvent B (0.1% TFA in CH_3CN) over 15 min. RadioTLC analysis was carried out in BuOH:H_2O:HOAc (12:5:3), followed by ninhydrin staining and radioTLC detection. To determine the enantiopurity of 4-[^{18}F]FL, the above reaction was carried out simultaneously with both *D/L*-leucine and *L*-leucine and the final products were analyzed by Chiral HPLC eluting on a Phenomenex D-Penicillamine 4.6 × 100 mm column, 1 mL/min, isocratic, 20% EtOH and 80% 1 mM aq. $CuSO_4$.

The radiochemical yield (RCY) is reported as a percentage and represents the total activity present in the purified ^{18}F-labeled amino acid divided by the total activity present in the purified [^{18}F]NFSI × 100.

6.2.2.2 Determination of specific activity

To determine the specific activity (SA) of 4-[^{18}F]FL, 5-[^{18}F]FBAHL, 5-[^{18}F]FHL, 3-[^{18}F]VL and α-Me-[^{18}F]FL the purified product mixtures were eluted from the ion exchange column in 1 mL fractions. Each fraction was counted, then the whole sample was allowed to decay at –20 °C. After ~100 h, the fractions were then lyophilized to dryness. Each entire dried fraction was then taken up in D_2O and *N*,*N*-dimethylformamide (5 µl, 65 µmol) was added as an internal standard. After thorough mixing the ^{1}H and ^{19}F NMR spectra were recorded. Amounts of 4-FL, 5-FBAHL, 5-FHL 3-[^{18}F]VL and α-Me-[^{18}F]FL were determined by analysis of the ^{1}H NMR spectra (not shown here). SA was then determined by correlating the amount of fluorinated product in each fraction to its activity. SA measurements were determined *via* at least three independent experiments. As the radiofluorination process described in this report does not remove any unreacted amino acid, we have also calculated the effective SA – a number which takes into account the amounts of fluorinated amino acid as well as amounts of parent amino acid. These values are presented in Table 6.1.

Table 6.1 ^{18}F-fluorination of unprotected branched aliphatic amino acids. All radiosynthesis times including purification were less than 60 min and the radiochemical purity of each tracer was > 97%.

^{18}F-labelled amino acid	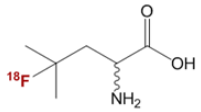 4-[^{18}F]FL (**7**)	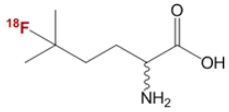 5-[^{18}F]FHL (**8**)	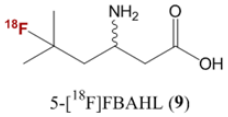 5-[^{18}F]FBAHL (**9**)	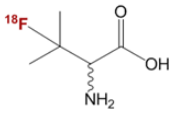 3-[^{18}F]FV (**10**)	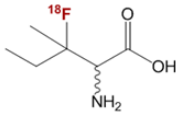 3-[^{18}F]FI (**11**)
Radiochemical yield (%)[a,b]	23.3 ± 3.3%	27.9 ± 3.3%	29.8 ± 0.7%	6.4 ± 0.4%	< 5%[d]
Specific activity (MBq μmol^{-1})	7.1 ± 1.9	6.3 ± 0.9	2.6 ± 0.6	3.4 ± 1.6	ND
Effective SA (MBq μmol^{-1})[c]	3.82 ± 0.91	4.92 ± 1.47	2.2 ± 0.50	0.43 ± 0.40	ND
Bone uptake (%ID/g)[a]	11.9 ± 1.6	1.6 ± 0.1	1.2 ± 0.4	ND	ND

Copyright © 2017, American Chemical Society

[a] All experiments were repeated ≥ 3 times. [b] RCYs determined from [^{18}F]NFSI are decay corrected. [c] Effective SA values take into account amounts of both fluorinated amino acid as well as parent, unreacted amino acid present in the purified product. [d] Produced as an inseparable 1.2:1 mixture of 3-[^{18}F]FI:4-[^{18}F]FI.

6.2.3 *In vitro* experiments

6.2.3.1 Tissue culture

The LNCaP, PC-3 and U-87 cell lines were obtained from ATCC. MCF-7 cells were obtained as a gift from Dr. C.K. Osborne (Houston, TX). All cell lines were authenticated by short tandem repeat (STR) profiling.

6.2.3.2 *In vitro* uptake studies

The cells were seeded in 24-well plates until approximately 90% confluence, and a fixed amount (74 kBq) of radioactive tracer (4-[^{18}F]FL or 5-[^{18}F]FHL) was added to each well in a fixed volume (400 μL). The cells were incubated with the radiotracer at 37 °C for 20, 40 and 60 minutes with gentle agitation. Blocking experiments were performed using 10 mM 2-amino-2-

norbornanecarboxylic (BCH), an inhibitor of *L*-amino acid transport. Following incubation, each well was washed with ice-cold HEPES buffer. Replicate wells were used for cell counting. The cells were lysed with 1 M NaOH. The activity in supernatant, washes and cell lysates was measured using a PerkinElmer Wizard 2480 gamma counter.

For competition assays, the PC-3 cell line was obtained from ATCC. All cell lines were authenticated by short tandem repeat (STR) profiling. The cells were seeded in 24-well plates until approximately 90% confluence, and a fixed amount (74 kBq) of radioactive tracer was added to each well. Blocking experiments were performed using 10 mM of competitive substrate. Following a 60 min incubation, each well was washed with ice-cold HEPES buffer. Replicate wells were used for cell counting. The cells were lysed with 1 M NaOH. The activity in supernatant, washes and cell lysates was measured using the gamma counter. The activity is reported as the percentage of incubated activity, and cellular uptake was normalized to cell number.

6.2.4 Animal studies

All animal experiments were conducted in accordance with the guidelines established by the Canadian Council on Animal Care and approved by the Animal Care Committee of the University of British Columbia.

6.2.4.1 Biodistribution studies

In vivo biodistribution studies were performed in healthy mice (C57BL/6J, n=4 each) to evaluate normal organ uptake of 4-[^{18}F]FL, 5-[^{18}F]FHL and 5-[^{18}F]FBAHL. Biodistribution studies were also obtained in immunocompromized mice (NOD.Cg-Rag1tm1Mom Il2rgtm1Wjl/SzJ) bearing human glioma (U-87) or prostate cancer cell xenografts (PC-3) to evaluate tumor accumulation of 5-[^{18}F]FHL. For tumor bearing mice, 5×10^6 cells were injected subcutaneously in the dorsal flank of the mice. The tumors were grown to a diameter of approximately 5-7 mm prior to the biodistribution study. The animals were lightly sedated with isoflurane, and 1-2 MBq of ^{18}F-labeled radiotracer was administered intravenously via the caudal lateral tail vein. The radioactivity in the syringe was measured before and after injection to

ensure accurate determination of the amount injected. The animals quickly recovered from sedation and were allowed to roam free in the cage during the uptake period. At 15 (U-87 tumors, n=3) and 60 minutes (U-87, n=4 and PC-3, n=5), the animals were sedated with isoflurane, sacrificed by CO_2 asphyxiation and their blood was collected by cardiac puncture. The organs were harvested, rinsed with saline, blotted dry, and weighed. Radioactivity in each organ was measured using the gamma counter, calibrated using a standard curve of ^{18}F. Organ uptake data is reported as the percentage of injected dose per gram of tissue (%ID/g).

6.2.4.2 PET/CT imaging

Dynamic PET/CT acquisitions were performed in a distinct set of mice to obtain representative images and follow the kinetics of uptake in normal organs (4[^{18}F]FL) as well as normal organs and u (5-[^{18}F]FHL). The mice were sedated with isoflurane inhalation, a catheter was placed in the caudal lateral tail vein, and the mice were placed in a preclinical PET/CT scanner (Siemens Inveon). A low-dose CT scan was performed using 40 kV X-rays at 500 μA. Following CT imaging, the list-mode dynamic acquisition was started, and the radiotracer was injected (3.2 – 3.4 MBq). Dynamic scanning was continued for 60 minutes. In addition to dynamic images, static images were reconstructed at 50-60 minutes using an iterative reconstruction algorithm (3D-OSEM/MAP).

6.2.5 Statistical analysis

Data analyses were performed using GraphPad Prism 7 software. All data are expressed as mean ± SD. Two-way ANOVA analysis was performed for all *in vitro* data and multiple comparisons were corrected using the Šidak method. The difference was considered statistically significant when p value was < 0.05.

6.3 Results & discussion

We started exploring the fluorination of L-leucine·HCl by using conditions previously reported by the Britton group for the large scale non-radioactive synthesis of 4-fluoroleucine methyl ester.[251] We were able to implement direct fluorination of the unprotected amino acid,

and 4-FL was initially produced in modest yield (~20%) after 1 h. Several reactor configurations (batch and flow) were evaluated and ultimately, a narrow-bore PTFE tube wrapped around a BLB lamp proved optimal, with ~60% conversion to 4-FL observed after only 40 min. Although separable by HPLC, the removal of leucine from 4-FL was ultimately deemed unnecessary as plasma concentrations of leucine range from 100 to 150 μM,[262] making it unlikely that residual leucine would interfere with the pharmacokinetic performance of the tracer. It was eventually found that a strong cation exchange resin retained the 4FL/leucine mixture and not NFSI, NHSI or other reaction byproducts, and that the purified AA mixture could then be rapidly eluted using aqueous base (without requirement for HPLC).

The synthesis process (Figure 6.2) proved to be optimal for radiofluorination of tertiary carbons on a wide variety of structures. The main advantages of this reaction are its rapidness and ability to start from a deprotected, commercially available precursor. The reaction does not cause racemisation of the chiral centre. It is done in aqueous solution, at room temperature; the synthesis is rapid (1 h 20 min from start to finish), and the final product does not require HPLC purification. Interestingly, a recently published manuscript by Chin *et al.* reported synthesis and evaluation of 5-[^{18}F]fluoroleucine (5-[^{18}F]FL).[263] While their final RCY of 30.0 ± 14.3%[263] was slightly higher than ours (23.3 ± 3.3% for 4-[^{18}F]FL,[187] Table 6.1), Chin and colleagues' strategy involved a 9-step synthesis of 5-FL and its mesylate precursor, followed by an additional three step synthesis of 5-[^{18}F]FL from the mesylate precursor. Aside from this strategy being more complex and time-consuming, it also involves the use of protecting groups, which need to be removed in the final steps of the synthesis process, and HPLC purification of the final product.

We next examined the uptake of 4-[^{18}F]FL in prostate (LNCaP and PC-3) and breast (MCF-7) cancer cell lines (Figure 6.3). Notably, there was significant uptake in MCF-7 cells, lower uptake in PC-3 cells and almost no uptake in LNCaP cells (Figure 6.3), which mirrors the expected LAT1 mRNA expression levels (RMA log 2) in these cell lines of 13.05 (MCF-7), 10.40 (PC-3) and 6.49 (LNCaP).[264] The uptake of 4-[^{18}F]FL in both PC-3 and MCF-7 cells was also significantly blocked by the addition of 2-amino-2-norbornanecarboxylic acid (BCH), a LAT1 inhibitor,[245] suggesting that LAT1 is largely responsible for their 4-[^{18}F]FL uptake. However, analysis of the biodistribution of 4-[^{18}F]FL in healthy mice showed high bone

accumulation (Figure 5.4, 11.92 ± 1.66 %ID/g), which is indicative of *in vivo* defluorination of the radiotracer and an obvious barrier to its further clinical development.

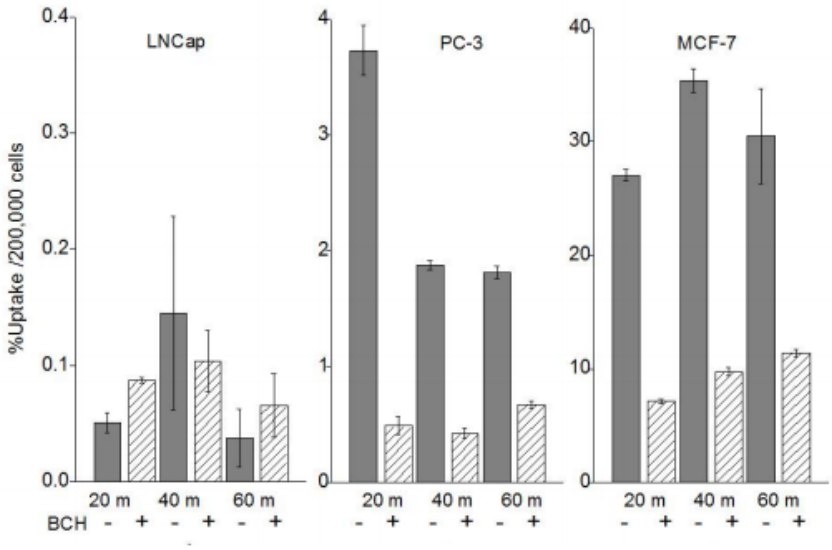

Figure 6.3 Uptake of 4-[^{18}F]FL (7) in LNCaP, PC-3 and MCF-7 cells at 20, 40 and 60 min in the presence (+) and absence (-) of the LAT1 inhibitor BCH (10 mM). 74 kBq was added to each well, and tracer uptake is normalized to cell number**.** Copyright © 2017, American Chemical Society

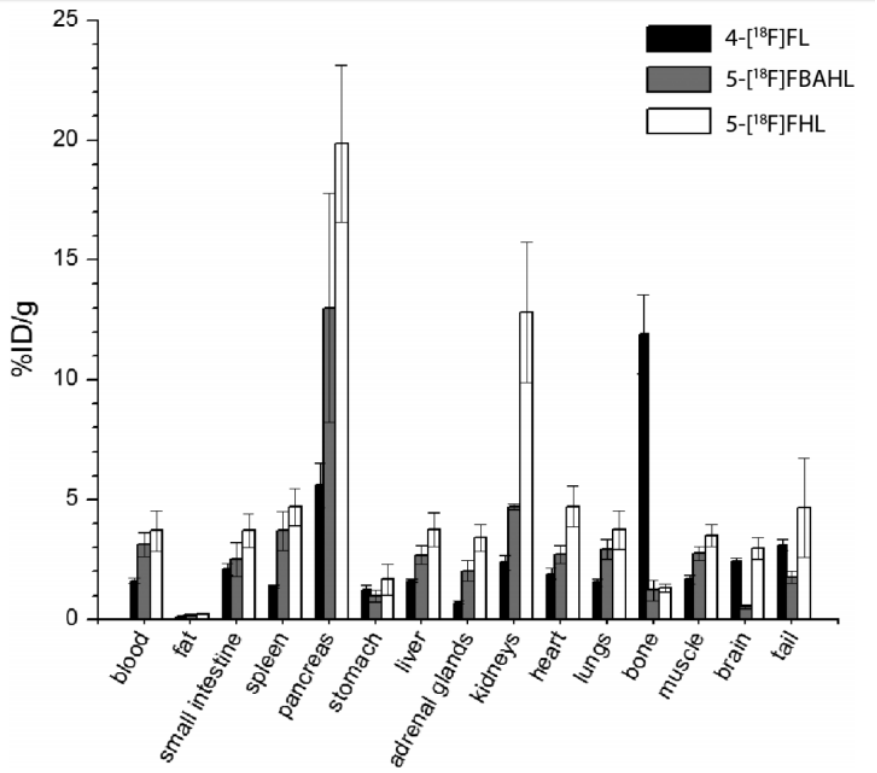

Figure 6.4 Biodistribution at 60 min p.i. of 4-[^{18}F]FL (7), 5-[^{18}F]FHL (8) and 5-[^{18}F]FBAHL (9) in healthy mice. Copyright © 2017, American Chemical Society

We suspected that cyclization followed by γ-lactone formation[265] might have been the reason for the *in vivo* defluorination of 4-[^{18}F]FL. It this is the case, analogues with longer chains may have slower defluorination rates, as the rate of lactone formation is strongly influenced by ring size.[266] Therefore, we contemplated the radiosynthesis of 5-[^{18}F]fluorohomoleucine (5-[^{18}F]FHL (**8**)), 5-[^{18}F]fluoro-β-amino-homoleucine (5-[^{18}F]FBAHL (**9**)), 3-[^{18}F]fluorovaline (3-[^{18}F]FV (**10**)), and 3-[^{18}F]fluoroisoleucine (3-[^{18}F]FI (**11**)). It was expected that defluorination of these amino acids via β- or δ-lactone formation would be greatly attenuated. Moreover, in addition to transporting branched aliphatic and aromatic amino acids, a recent report by Kannai[267] highlighted the efficient transport of homoleucine and β-aminohomoleucine by LAT1 in HeLA S3 cells. As summarized in Table 6.1, 5-[^{18}F]FHL (**8**) and 5-[^{18}F]FBAHL (**9**) could be readily prepared and purified without modification to the process established for 4-[^{18}F]FL. The radiofluorination of valine and isoleucine afforded 3-[^{18}F]FV (**10**) and mixtures of 3- and 4-[^{18}F]FI (e.g., **11**) albeit in lower RCY owing to the decreased rate of these reactions, which is

consistent with our earlier findings from the fluorination of aliphatic esters.[250] The biodistribution of both **8** and **9** was examined in healthy mice (Figure 6.4), and we found that neither of these radiotracers showed any appreciable accumulation of activity in the bone at 60 min p.i. (1.32 ± 0.15 %ID/g and 1.22 ± 0.43 %ID/g for 4- [^{18}F]FHL (**8**) and 5-[^{18}F]FBAHL (**9**), respectively). The uptake of **8** was also examined in a panel of LAT1-expressing cancer cell lines that included LNCaP, PC-3, MCF-7 and U-87 (glioma) (Figure 6.5). Again, uptake in these cancer cell lines correlated well with their expected mRNA expression levels for LAT1[264] and was substantially blocked by addition of the LAT1 inhibitor BCH, suggesting that transport of this radiotracer is significantly mediated by LAT1 (Figure 6.5).

The uptake of 5-[^{18}F]FHL (**8**) in several cancer cell lines and its improved biodistribution over 4-[^{18}F]FL inspired us to undertake an imaging study using this tracer in mice bearing human glioma (U-87) or prostate cancer (PC-3) xenografts. Biodistribution studies indicated high tumour accumulation (5.9 ± 0.7 %ID/g (n = 4) for U-87, 5.6 ± 3.2 %ID/g (n = 5) for PC-3 at 60 min p.i.) of 5-[^{18}F]FHL was observed with both U-87 and PC-3 xenografts (Figures 6.8 and 6.9). Combined with low background uptake, 5-[^{18}F]FHL provided excellent tumour visualization and high tumour contrast ratios as evidenced in Figures 6.6 and 6.9. Excretion of 5- [^{18}F]FHL occurred predominantly by renal clearance, with accumulation observed in the pancreas, kidneys and bladder. Tissue time-activity curves (Figure 6.7) obtained in selected organs using dynamic images showed rapid accumulation of 5-[^{18}F]FHL in the tumours and pancreas, peaking shortly before 10 min, followed by slow efflux. Low uptake was observed in muscle and bone, further evincing the improved *in vivo* stability of 5-[^{18}F]FHL over the *L*-leucine derivative 4-[^{18}F]FL.

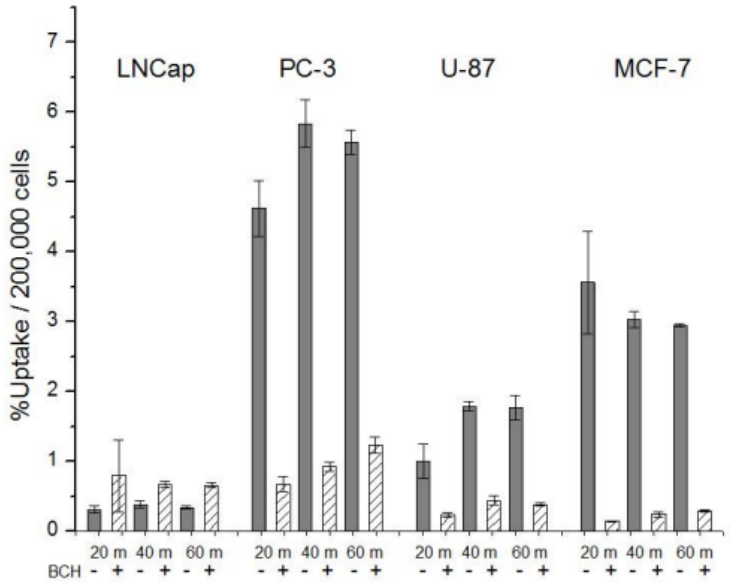

Figure 6.5 Uptake of *L*-5-[^{18}F]FHL (9) in LNCaP, PC-3, U-87 and MCF-7 cells at 20, 40 and 60 min in the presence (+) and absence (-) of the LAT1 inhibitor BCH (10 mM). 74 kBq was added to each well, and tracer uptake is normalized to cell number**.** Copyright © 2017, American Chemical Society

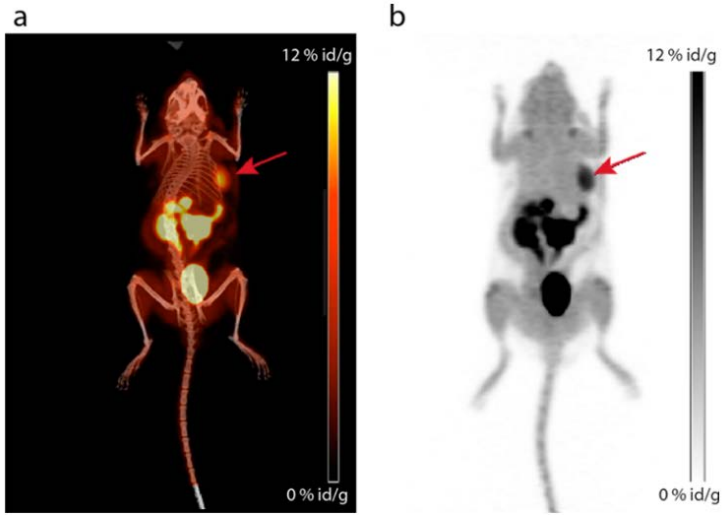

Figure 6.6 PET imaging of *L*-5-[^{18}F]FHL in mice bearing human glioma (U-87) xenografts. Maximum intensity projection images overlaid on CT (a) and standalone PET images (b) of the biodistribution of *L*-5-[^{18}F]FHL at 60 min show high accumulation of *L*-5-[^{18}F]FHL in the tumour (red arrow). Copyright © 2017, American Chemical Society

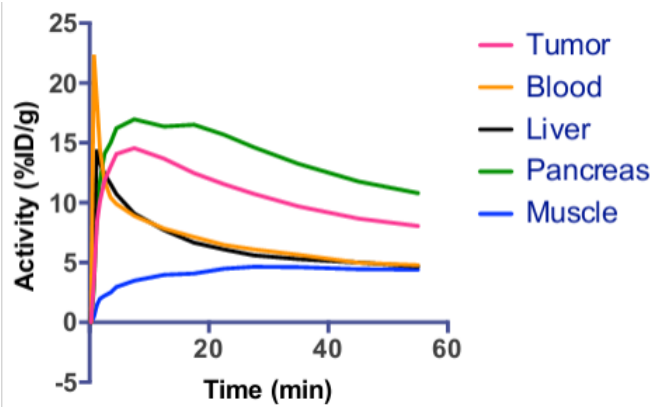

Figure 6.7 Time-activity curves of the accumulation of *L*-5-[^{18}F]FHL in selected organs. Activity accumulated rapidly in the U-87 tumour and pancreas peaking shortly before 10 minutes, followed by a slow progressive efflux of the amino acid. Copyright © 2017, American Chemical Society

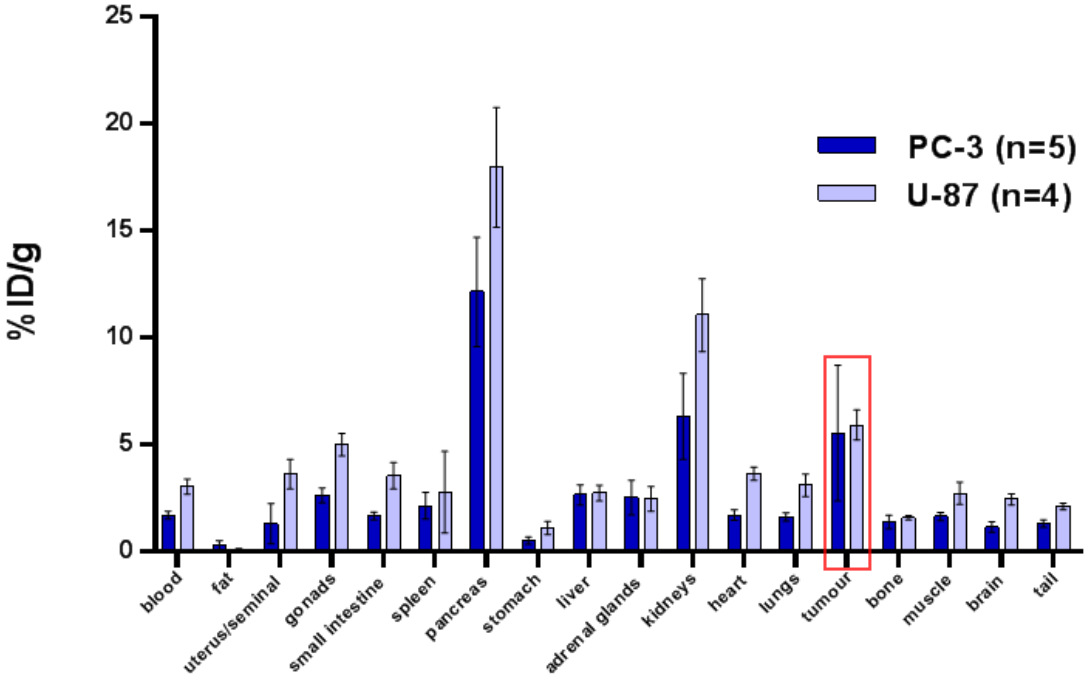

Figure 6.8 Biodistribution of *L*-5-[^{18}F]FHL in selected organs at 1 h p.i. in NSG mice bearing U-87 (light blue bars) and PC-3 (navy bars) xenograft tumours. Tumour uptake values are marked with the red rectangle. Copyright © 2017, American Chemical Society

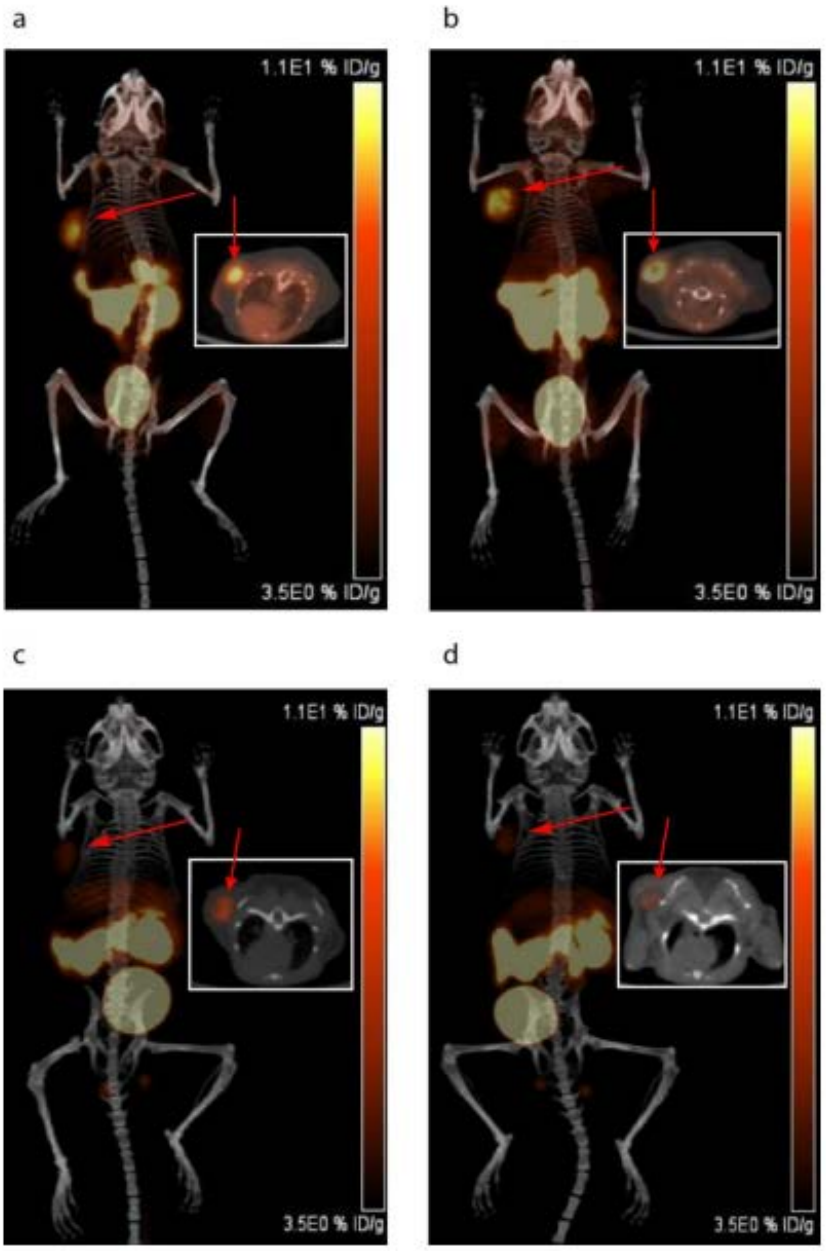

Figure 6.9 Whole-body maximum intensity projection images overlaid on CT of the biodistribution of *L*-5-[^{18}F]FHL at 50-60 minutes for the U-87 tumour xenografts (a and b) and for the PC-3 tumour xenografts (c and d). Cross sectional images are shown in the insets. Each image represents an individual mouse, and a red arrow indicates tumour position. Copyright © 2017, American Chemical Society

With such an effective ^{18}F-labeling strategy in hand, we started testing a selected panel of leucine analogues, in pursuit of the best system L-targeting candidate for clinical translation. The syntheses of these tracers were performed according to the protocol outlined above (Section 6.2.2.1). Uptake of these radiotracers was measured with or without the addition of a large excess of competitive amino acid substrates to interrogate the specificity of uptake. Here, the trend observed was that the *L*- isomers have higher uptake than their *D*- counterparts, with *L*-[^{18}F]FHL demonstrating the highest overall uptake by PC-3 cells *in vitro* (Figure 6.10). The preference for *L*- isomers is not surprising, given that the naturally occurring amino acids are in the *L*- conformation.[268] The uptake of all five tracers was blocked to a similar extent (>70% inhibition, Figure 6.11) by *L*-leucine and BCH, which are LAT specific inhibitors.[269] Another system L substrate, *L*-phenylalanine, had substantial impact on the uptake of *L*-[^{18}F]FBAHL, *D*-[^{18}F]FBAHL and *L*-α-2-methyl-4-[^{18}F]fluoroleucine (*L*-α-Me-[^{18}F]FL). *L*-Phenylalanine is also a substrate of systems $B^{0,+}$, B^0, T and PHE transporter,[184] indicating that [^{18}F]FBAHL and α-Me-[^{18}F]FL may be taken up partially due to these transporter proteins also (Figure 6.12). Not surprisingly, the uptake was not blocked by *L*-glutamate, an inhibitor for EAATs, glutamate transporters and xCT.[250] The uptake was also not affected by *L*-serine or N-methyl α-aminoisobutyric acid (MeAIB), indicating that these new tracers are not transported by system A or system ASC. This later finding is important as it clearly differentiates these radiotracers from the amino acid tracer anti-1-amino-3-[^{18}F]-fluorocyclobutane-1-carboxylic acid ([^{18}F]FACBC).[251] Notably, uptake in PC-3 cells was the highest for (*L*)-5-[^{18}F]FHL, followed by (*D*)-5-[^{18}F]FHL, (*L*)-5-[^{18}F]FBAHL, (*D*)-5-[^{18}F]FBAHL and (*L*)-4-[^{18}F]FαML.

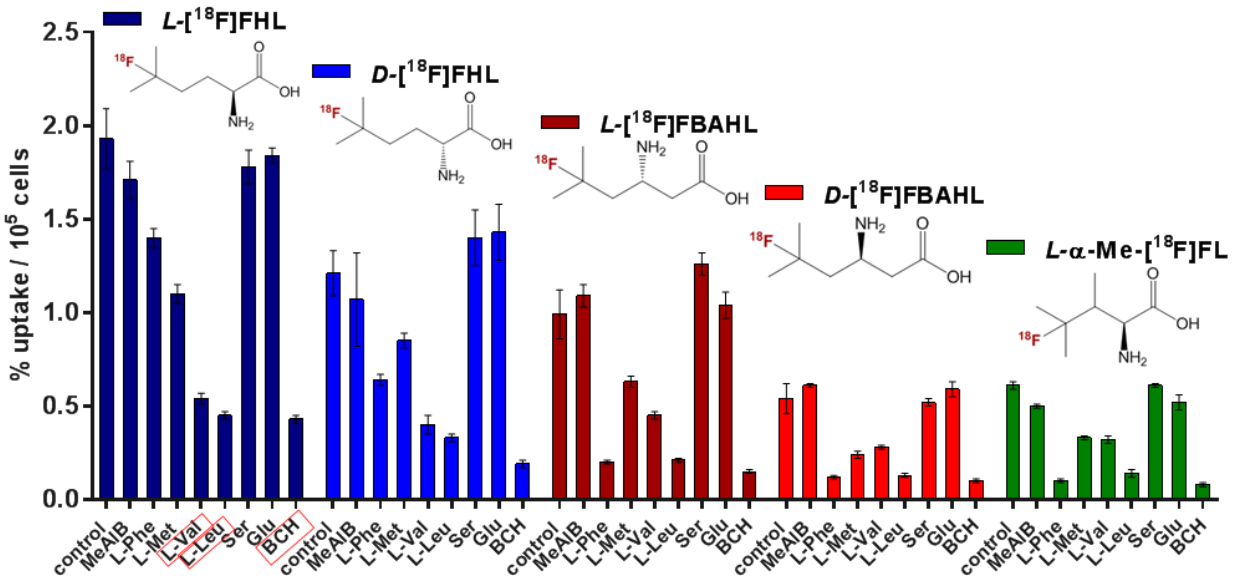

Figure 6.10 Uptake of *L*- [^{18}F]FHL, *D*- [^{18}F]FHL, *L*- [^{18}F]FBAHL, *D*- [^{18}F]FBAHL and *L*-α-Me-[^{18}F]FL in PC-3 cells at 60 min in the presence of substrates/inhibitors of a wide array of amino acid transporters. 74 kBq was added to each well, and tracer uptake is normalized to cell number. Control (no inhibitor added), MeAIB (transport A system inhibitor[270]), *L*-Phe (substrate of systems L, B^0, PHE, T and $B^{0,+}$), *L*-Met (substrate of systems L, B^0, A and y^+L), *L*-Val (substrate of systems L and B^0), Ser (substrate of systems B^0, A, asc and ASC), Glu (substrate of systems x_C^-, and x_A^-, vesicular Glu transporters (VGLUT) and Glu carriers (GC)), BCH (system L inhibitor).[184] Copyright © 2019 by the Society of Nuclear Medicine and Molecular Imaging.

% inhibition	> 80 %	70 - 79.9 %	60 - 69.9 %	40 - 59.9 %	30 - 39.9 %	20 - 29.9 %	0 - 19 %
color code							

tracer/substrate(inhibitor)	MeAIB	L-Phe	L-Met	L-Val	L-Leu	Ser	Glu	BCH
L-[^{18}F]FHL	0.11	0.28	0.43	0.72	0.77	0.07	0.04	0.78
D-[^{18}F]FHL	0.12	0.47	0.30	0.67	0.73	-0.15	-0.17	0.84
L-[^{18}F]FBAHL	-0.10	0.80	0.36	0.54	0.79	-0.27	-0.05	0.84
D-[^{18}F]FBAHL	-0.12	0.78	0.55	0.48	0.76	0.04	-0.09	0.82
L-α-Me-[^{18}F]FL	0.18	0.83	0.46	0.47	0.78	-0.01	0.15	0.87

Figure 6.11 Percent inhibition of *L*-[^{18}F]FHL, *D*-[^{18}F]FHL, *L*-[^{18}F]FBAHL, *D*-[^{18}F]FBAHL and *L*-α-Me-[^{18}F]FL uptake by PC-3 cells at 60 min. The values were calculated in comparison to the uptake of the control (untreated sample) for each individual tracer. The colour scheme was determined arbitrarily, with the scale bar describing the boundaries.

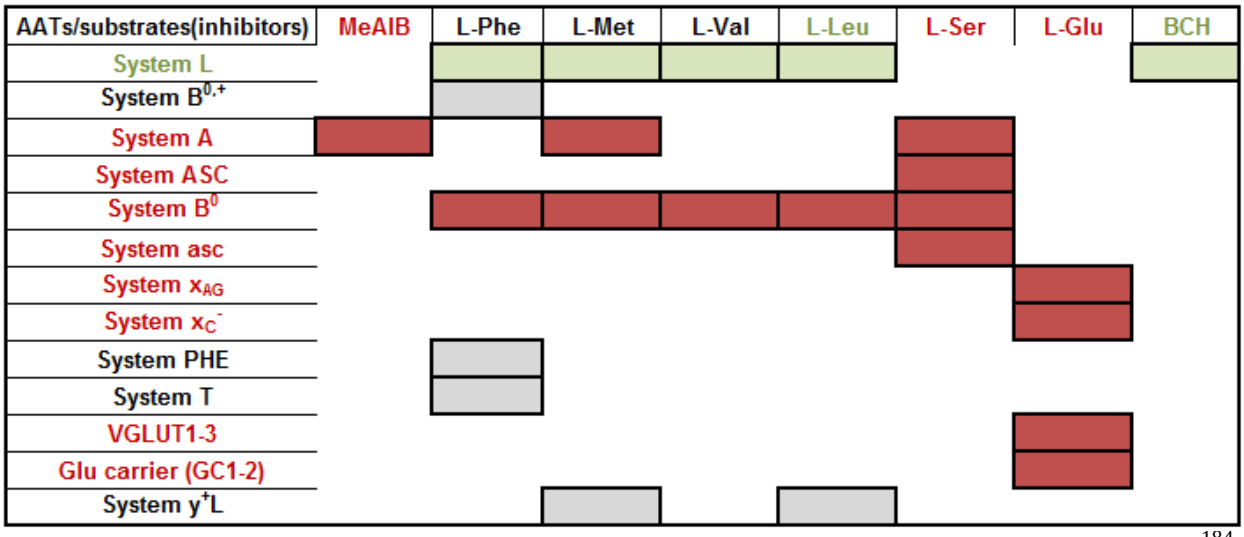

Figure 6.12 Substrates/inhibitors used in the cell study and their respective transporters[184]. Red blocks mark amino acid transporters (AATs) and substrates/inhibitors which had little to no effect on tracer uptake (<30% inhibition, Figure 6.11). Green blocks mark AATs and substrates/inhibitors which had most impact on tracer uptake (>70% inhibition). Grey marks possible partial involvement in tracer uptake (31-69% inhibition). The absence of blocks is an indicative of no known relationship between the AATs and a listed substrate/inhibitor.

We went on to perform biodistribution studies on healthy animals with *L*- and *D*- isomers of [^{18}F]FL and [^{18}F]FBAHL, and with *L*-α-Me-[^{18}F]FL. All five tracers showed similar biodistribution profile, with low overall uptake, with the exception of pancreas and kidneys, and in the case of [^{18}F]FL, bone. High pancreatic uptake of these compounds is likely due to moderate to strong LAT1 expression in this organ,[192] whilst high renal uptake is an indicator of the clearance pathway for these tracers. Both *L*- or *D*- [^{18}F]FL isomers showed significant defluorination *in vivo*, as reflected by the high bone uptake (11.92 ± 1.66 %ID/g for *L*- and 7.02 ± 0.80 %ID/g for *D*-[^{18}F]FL, Figure 6.13). Our original reasoning that this may be due to γ-lactone formation *in vivo* is challenged with these results, since the *L*- and *D*-[^{18}F]FL should have the same degree of lactone formation and defluorination. Therefore, we believe that the [^{18}F]FL tracer is unstable *in vivo* possibly due to enzymatic degradation. Neither isomer of [^{18}F]FBAHL (Figure 6.14) nor *L*-α-Me-[^{18}F]FL (Figure 6.15) had high bone uptake, which further supports that the defluorination of the [^{18}F]FL *in vivo* was not due to lactone formation. In the case of [^{18}F]FBAHL, the *L*- isomer demonstrated higher uptake both *in vitro* and *in vivo*, which is indicative of the preference of the LAT1 transporter for the *L*- substrate configuration.

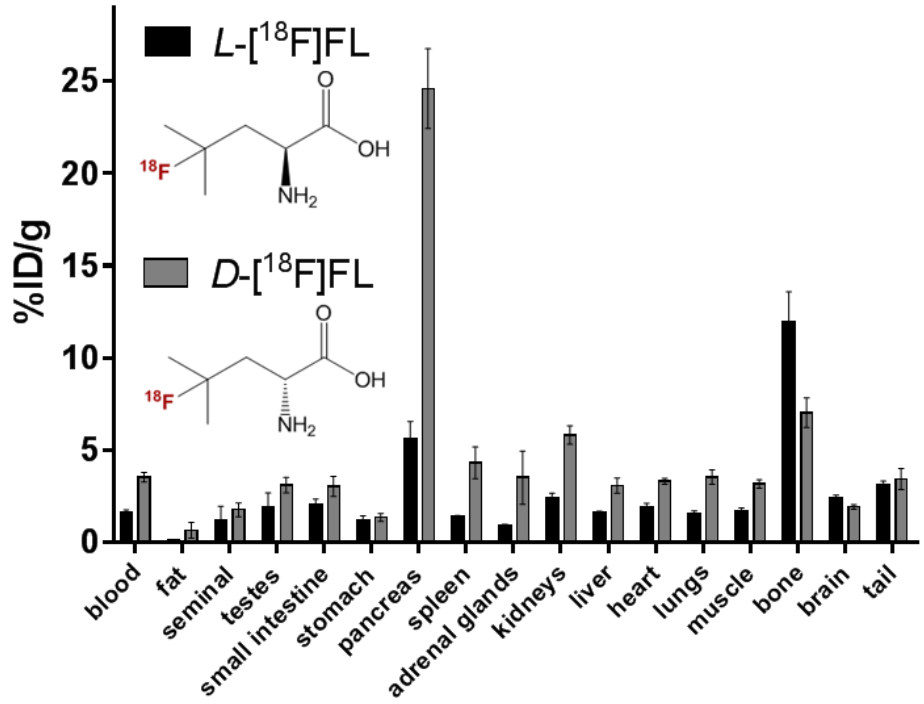

Figure 6.13 Biodistribution of *L*- and *D*- isomers of [^{18}F]FL at 1 h p.i. in healthy mice.

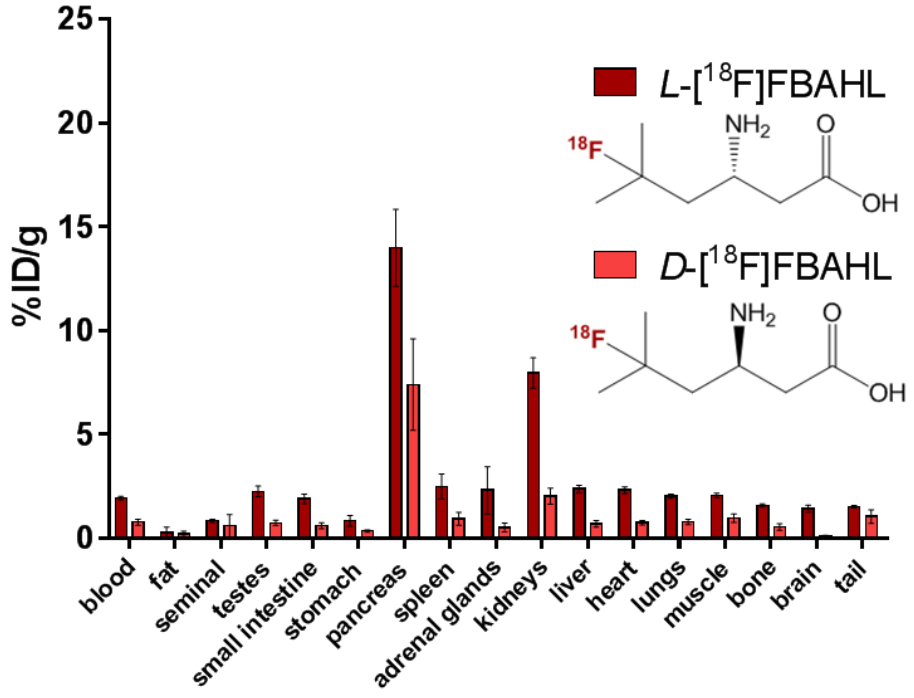

Figure 6.14 Biodistribution of *L*- and *D*- isomers of [^{18}F]FBAHL at 1 h p.i. in healthy mice.

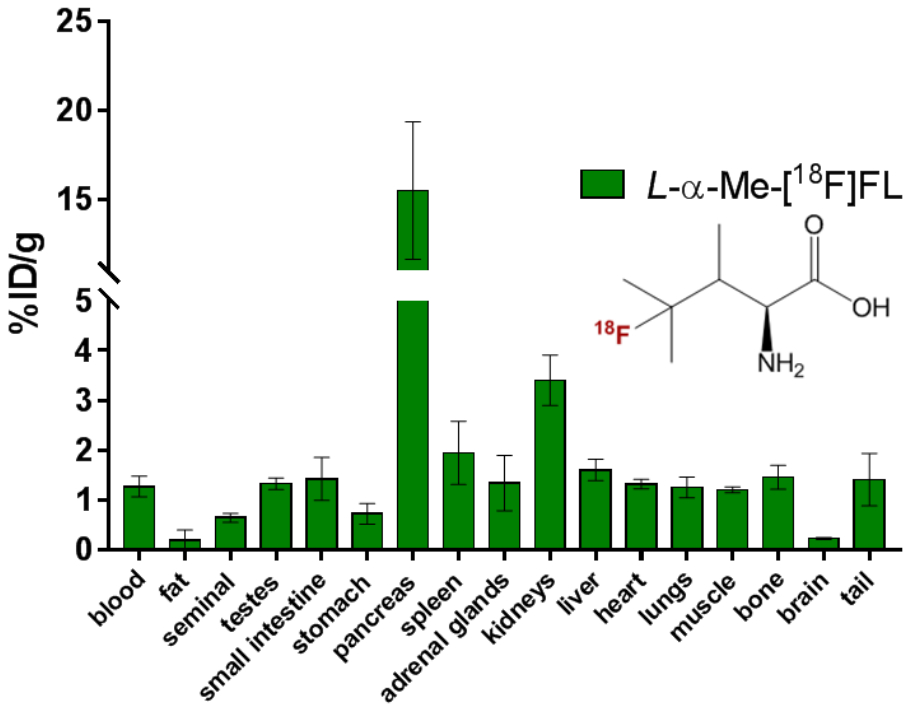

Figure 6.15 Biodistribution of *L*-α-Me-[^{18}F]FL at 1 h p.i. in healthy mice.

To ascertain if the *in vitro* specificity data translates to *in vivo* systems, we then selected three radiofluorinated leucine derivatives, each with high, moderate and low LAT uptake *in vitro* (Figure 6.10) and examined their biodistribution in mice bearing U-87 cell line xenografts predicted to overexpress LAT.[271] We found that tumour accumulation correlated well with *in vitro* findings. As predicted, (*L*)-4-[^{18}F]FαML showed lesser tumour accumulation (1.55 ± 0.32 %ID/g) at 60 min p.i. than both (*L*)-5-[^{18}F]FBAHL and (*L*)-5-[^{18}F]FHL (3.04 ± 0.22 %ID/g and 5.29 ± 0.84 %ID/g, respectively, Table 6.2). Finally, the imaging potential of (*L*)-5-[^{18}F]FHL was examined in a PET imaging study. Dynamic PET image of U-87 tumors in NSG mice at 60 min with (*L*)-5-[^{18}F]FHL was obtained and confirmed the results shown in Figure 6.16A. In particular, (*L*)-5-[^{18}F]FHL showed good tumor visualization at 60 min and rapid tumor uptake, reaching a plateau around 10 min which then remains stable until 55 min of acquisition time, as evidenced by the time-activity curve in Figure 6.16B.

Table 6.2 Biodistribution of (*L*)-5-[^{18}F]FHL, (*L*)-5-[^{18}F]FBAHL and (*L*)-4-[^{18}F]FαML in U-87 tumor bearing mice at 60 min post injection. All values are % ID/g of tissue. Copyright © 2019 by the Society of Nuclear Medicine and Molecular Imaging.

	radiotracer		
tissue	(*L*)-5-[^{18}F]FHL	(*L*)-5-[^{18}F]FBAHL	(*L*)-4-[^{18}F]FaML
blood	2.74 ± 0.36	2.54 ± 0.36	1.24 ± 0.12
fat	0.24 ± 0.07	0.22 ± 0.05	0.12 ± 0.05
uterus	3.04 ± 0.98	2.53 ± 0.43	1.54 ± 0.28
ovaries	4.89 ± 1.76	3.83 ± 0.82	2.37 ± 1.61
intestine	2.49 ± 0.29	2.31 ± 0.6	1.24 ± 0.28
spleen	3.28 ± 0.84	2.77 ± 0.35	1.68 ± 0.38
pancreas	15.59 ± 1.45	15.2 ± 5.56	13.59 ± 3.78
stomach	1.16 ± 0.27	0.95 ± 0.35	0.54 ± 0.21
liver	2.50 ± 0.37	2.25 ± 0.19	1.47 ± 0.02
adrenal glands	2.19 ± 0.86	2.06 ± 0.58	0.93 ± 0.68
kidneys	8.26 ± 1.43	4.19 ± 0.49	3.79 ± 0.53
heart	2.94 ± 0.45	2.14 ± 0.17	1.41 ± 0.12
lungs	2.69 ± 0.44	2.21 ± 0.17	1.27 ± 0.2
U-87 tumour	5.29 ± 0.84	3.04 ± 0.22	1.55 ± 0.32
bone	1.25 ± 0.35	1.40 ± 0.25	0.93 ± 0.14
muscle	2.43 ± 0.34	2.26 ± 0.18	1.11 ± 0.09
brain	1.63 ± 0.3	0.37 ± 0.02	0.37 ± 0.12
tail	2.16 ± 0.32	2.25 ± 0.77	1.33 ± 0.39

The substrate pool for this novel radiofluorination methodology is large, and the results presented herein were just the initial biological evaluation studies. From this study, we are able to identify several promising ^{18}F-labelled branched chain amino acid tracers that will be subjected to further study in models of glioma, prostate cancer and multiple myeloma. Work is underway to improve the specific activity of the synthesized tracers and plans are in motion to attempt orthotopic glioblastoma μPET/CT imaging studies.

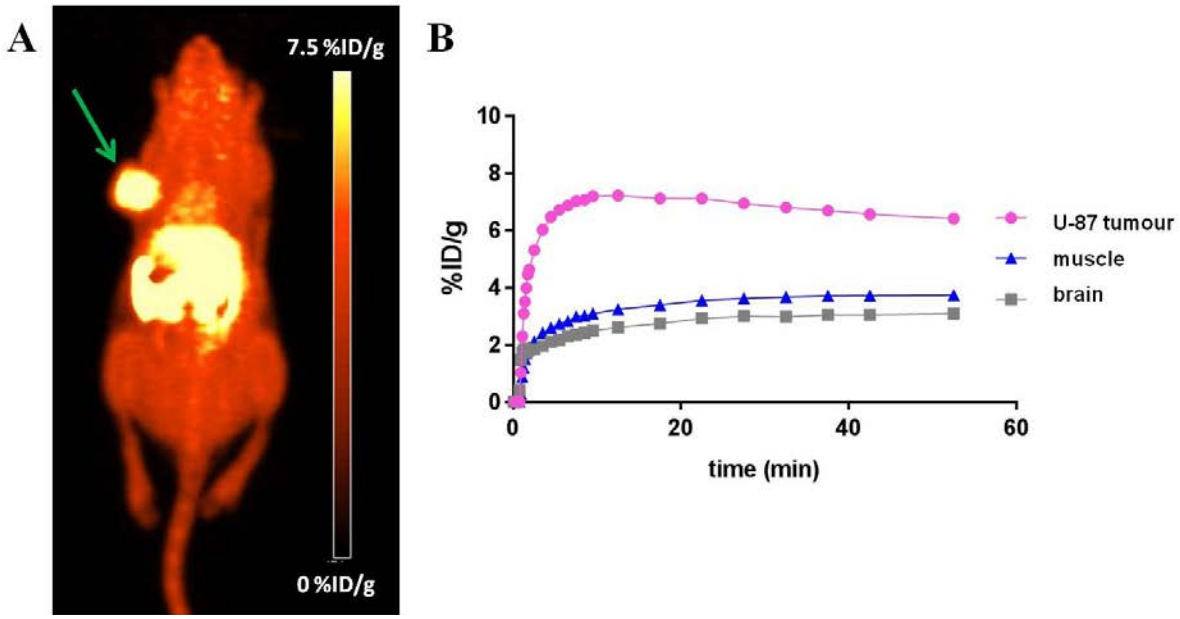

Figure 6.16 A) *In vivo* dynamic PET imaging of (*L*)-5-[^{18}F]FHL in NSG mouse bearing U-87 xenograft at 60 min post injection. **B)** Time-activity curve of (*L*)-5-[^{18}F]FHL in the U-87 tumour, brain and muscle tissues over 55 min p.i. Copyright © 2019 by the Society of Nuclear Medicine and Molecular Imaging.

6.4 Conclusion

In summary, we have developed a mild ^{18}F-labeling strategy that selectively replaces the tertiary C−H bond in branched aliphatic amino acids with a C−^{18}F bond. Importantly, this process obviates both complicated precursor synthesis and the use of prosthetic groups. Using this photocatalytic fluorination platform, we were able to rapidly access several fluorinated and radiofluorinated branched-chain amino acids. Firstly, the uptake of both 4-[^{18}F]FL and 5-[^{18}F]FHL in several cancer cell lines was investigated and found to correlate well with LAT1 expression, highlighting their potential as metabolic PET imaging agents. However, the biodistribution of these two radiotracers differed significantly, with 4-[^{18}F]FL displaying high bone uptake which is suggestive of *in vivo* defluorination. The imaging ability of 5-[^{18}F]FHL was examined in mice bearing human glioma and prostate cancer xenografts and high accumulation was found in the tumours, which provided excellent tumour visualization and no significant defluorination was observed. Notably, this convenient radiofluorination should enable

rapid proof-of-feasibility studies on a variety of related amino acids and biomolecules and support high throughput production of radiotracers. Initial work with this regard was also presented in this chapter. We evaluated uptake specificity and biodistribution of five different structures and we found that the *L*- isomers have higher *in vitro* uptake than their *D*-counterparts. We further found in our *in vitro* competition assay that these novel radiofluorinated branched chain amino acids are LAT specific substrates. The radiotracers show comparable *in vivo* biodistribution with prominent pancreatic and renal uptake values. As the high-throughput tracer radiofluorination is ongoing, following further biological characterization, the lead tracer structures may potentially be used for imaging the expression/activity of LAT1 with PET in the clinic.

Chapter 7: Conclusion

7.1 Summary of study and findings

The goal of this thesis was to examine the suitability of a number of amino acid imaging agents, including [^{18}F]FASu and [^{18}F]FSPG as indicators of system x_C^- activity, and a number of [^{18}F]FLeu derivatives as measures of system L activity in a number of different cancer types. We sought to establish [^{18}F]FASu as a reliable redox modulation gauge, and to explore its utility in cancer detection with PET. Tumours with advanced ROS defence capability, such as triple-negative breast cancers (TNBCs), which are insensitive to hormone therapies, can develop resistance to radiation and selected chemotherapies; hence, the treatment for these cancers often involves combinatorial treatments especially at the metastatic stage. Consequently, patients with TNBC have the worst outcome after chemotherapy with a very short median time to relapse and death.[272] xCT, the functional subunit of system x_C^-, represents a potential co-target in TNBC and other xCT overexpressing cancers, in synergy with other chemotherapeutics[128] such as cisplatin,[273] doxorubicin,[274] geldanamycin,[275] and gemcitabine.[276] It has been reported that xCT inhibition sensitizes cancer cells to the effects of numerous chemotherapeutic agents.[128] We believe that the establishment of a non-invasive companion diagnostic may accelerate clinical research on xCT targeted therapies.

Chapters 2, 3, 4 and 5 focus on the evaluation of three tracers targeting system x_C^-, whereas the work presented in Chapter 6 is an evaluation of five novel radiotracers for system L imaging *in vivo*. In Chapter 2, we evaluated the system x_C^- - targeting radiopharmaceutical, [^{18}F]FASu, in the context of redox regulation in breast cancer, with the focus on the triple-negative subtype. Our efforts to directly correlate the xCT expression levels with [^{18}F]FASu uptake were fruitful, with a finding that mRNA expression closely followed xCT protein expression, which in turn is an indicator of x_C^- transporter activity. In addition, we showed that fluctuations in system x_C^- activity correlated with changes in intracellular antioxidant and reactive oxygen species levels. We also demonstrated that ionising radiation induced x_C^- transporter activity *in vitro*, however our attempts to observe the same effect *in vivo* were unsuccessful. Work is underway to establish if tracer uptake in irradiated tumours still reflects xCT expression levels.

In Chapter 3, we synthesized [^{18}F]ASu-BF_3, a close boramino acid analog of [^{18}F]FASu, *via* ^{18}F-^{19}F isotope exchange reaction and evaluated its potential for imaging with PET. [^{18}F]ASu-BF_3 was stable in mouse plasma and taken up into PC-3 prostate cancer cells *via* the system x_C^- amino acid transporter. The continuous use of isoflurane for anesthesia during dynamic imaging acquisition slowed down the excretion of [^{18}F]ASu-BF_3 and enabled visualization of PC-3 tumor xenografts in mice. In contrast, no tumor visualization was observed from static images of [^{18}F]BF_3-ASu due to its rapid renal excretion mediated in part by the organic anion transporter. Our data indicate that the pharmacokinetics of amino acids could be altered after being converted into their boramino acid analogs. Therefore, care should be taken when using the boramino acid strategy to design and prepare ^{18}F-labeled tracers for imaging amino acid transporters/receptors with PET.

In Chapter 4, we evaluated the 5-position diastereomers as well as the racemic (2*S*,5*R/S*-) mixture of [^{18}F]FASu, for their biodistribution and tumour imaging potential. All three tracer conformations allowed for the visualisation of tumour xenografts at 1 h (for U-87 and PC-3 tumours) or 2 h (in the case of MDA-MB-231 xenografts) post-injection, with the racemate (2*S*,5*R/S*-) displaying similar image contrast as compared to the 5- position diastereomers and the 2*S*,5*S*-[^{18}F]FASu conformation exhibiting relatively higher contrast for imaging U-87 and PC-3 xenografts. Tumour uptake of the isomers was blocked in excess of the non-radioactive standard, aminosuberic acid (ASu), confirming target specificity. Our data suggest that 2*S*-[^{18}F]FASu can be used to noninvasively image system x_C^- in a variety of cancers, either as the racemic mixture (2*S*,5*R/S*-) or optically pure form. Furthermore, this work shows the potential utility of [^{18}F]FASu for detection of glioblastoma and prostate cancer.

In Chapter 5, we compared two system x_C^- - targeting tracers, [^{18}F]FASu and [^{18}F]FSPG, in five different cancer cell lines *in vitro*, and in two xenograft models *in vivo*. The tracers showed similar uptake trends *in vitro*, with [^{18}F]FSPG having higher uptake values overall. *In vivo,* both radiopharmaceuticals showed equally good ability to image glioblastoma and non-small cell lung cancer xenografts, with low background uptake and rapid clearance *via* the renal pathway. [^{18}F]FSPG, notably, exhibited better image contrast than [^{18}F]FASu. Moreover, we compared both tracers with [^{18}F]FDG, the current gold-standard of oncological PET, and they achieved better tumour visualisation and image contrast than [^{18}F]FDG in non-fasting conditions.

However, [^{18}F]FDG, when used under fasting conditions, had higher uptake in a glioma model compared to [^{18}F]FASu and provided better visualisation of the subcutaneous tumour xenografts than [^{18}F]FASu.

The secondary goal of this thesis was to screen different ^{18}F-labeled aliphatic branched chain amino acids that may serve as potential radiotracers for targeting system L for cancer imaging. Increased system L activity is an indication of accelerated protein synthesis, which is one of the hallmark features of cancer progression. With the approach taken, our hope is to establish a new ^{18}F-fluorination approach that will enable the rapid development of system L–targeting radiotracers, and/or leucine-containing peptides targeted toward specific tumour antigens, and overall facilitate better diagnostics and decision-making for physicians. In Chapter 6, we evaluated five novel radiofluorinated neutral amino acid structures in prostate cancer cells. We found that they were all substrates to system L transporter, and that *in vivo*, these radiotracers exhibited low background uptake and rapid clearance. We also found that the uptake of *L*-isomers was preferred to their *D*- counterparts. High *in vivo* accumulation of 5-[^{18}F]FHL was observed in both glioma and prostate cancer xenografts, with good tumour-to-background ratios.

7.2 Strengths and limitations of this study

There were a number of strengths and limitations associated with this study. Our study represents a comprehensive evaluation of the role system x_C^- plays in response to oxidative stress induction in breast cancer. Our study showed that [^{18}F]FASu can indeed be used to directly monitor x_C^- transporter activity, and that the changes in tracer uptake directly reflect fluctuations in intracellular glutathione levels in response to stimuli. Furthermore, with our Western blot and qPCR assay work, we were able to establish certainty in the relationship between xCT mRNA and protein levels – which was not well demonstrated in previous publications. Our results clearly indicate that the molecular weight of functionally active xCT is 37 kDa, and not 55 kDa – which was our initial postulation. With an effective tool in hand, we explored the *in vitro* response of cancer cells to two different stressors (chemical and radiation), thus establishing the framework for similar explorations *in vivo*. Our initial efforts to test fluctuations in system x_C^- activity *in vivo* after radiation treatment had limited success. The reasons for this may be an inadequate radiation dose or we chose an inadequate imaging time point. For this reason, further

investigations are under way. However, our results indicate clear changes in uptake in certain regions within the tumour, suggesting that certain aspects of tumour microenvironment might be affecting the uptake of [^{18}F]FASu, with bulk tumour uptake measurements (e.g., SUV or %ID/g) affording an average representation of tracer behaviour. We started investigating this further and our initial attempt at autoradiography imaging supported findings from the PET scans about heterogeneous activity distribution within the tumour (Figure 7.1A). Furthermore, we processed and analyzed control and irradiated MDA-MB-231 tumours in an absolute quantification qPCR assay and found that relative *SLC7A11* levels were elevated in the treated tumour, as compared to the control (Figure 7.1B). This could explain the presence of additional focal areas of increased activity on PET/CT images in the tumour after treatment (Chapter 2), since increased localized transporter expression could account for the observed changes in subtumoural uptake. The best way to test this hypothesis would involve overlaying the [^{18}F]FASu autoradiograph with an adjacent stained slide, when we would likely observe overlap of radioactive regions with the regions with elevated xCT expression. However, this cannot be done currently due to the lack of reliable and tested anti-xCT antibody adapted for immunohistochemical staining. We used the MDA-MB-231 human breast cancer cell line for the evaluation of [^{18}F]FASu uptake post-radiotherapy. Working with patient-derived xenografts (PDX) would probably be a better approach, given that the ultimate goal is clinical translation of the results. Using PDX models is advantageous because this is the best way to mimic the clinical situation in a pre-clinical setting. Studies to date indicate that histology and gene expression profiles of PDX are retained in addition to the fact that clinical responses to treatment can be predicted through studies with PDX models.[277] However, variable engraftments rates and long latency periods of the grafts still pose significant issues when working with PDX models.[277]

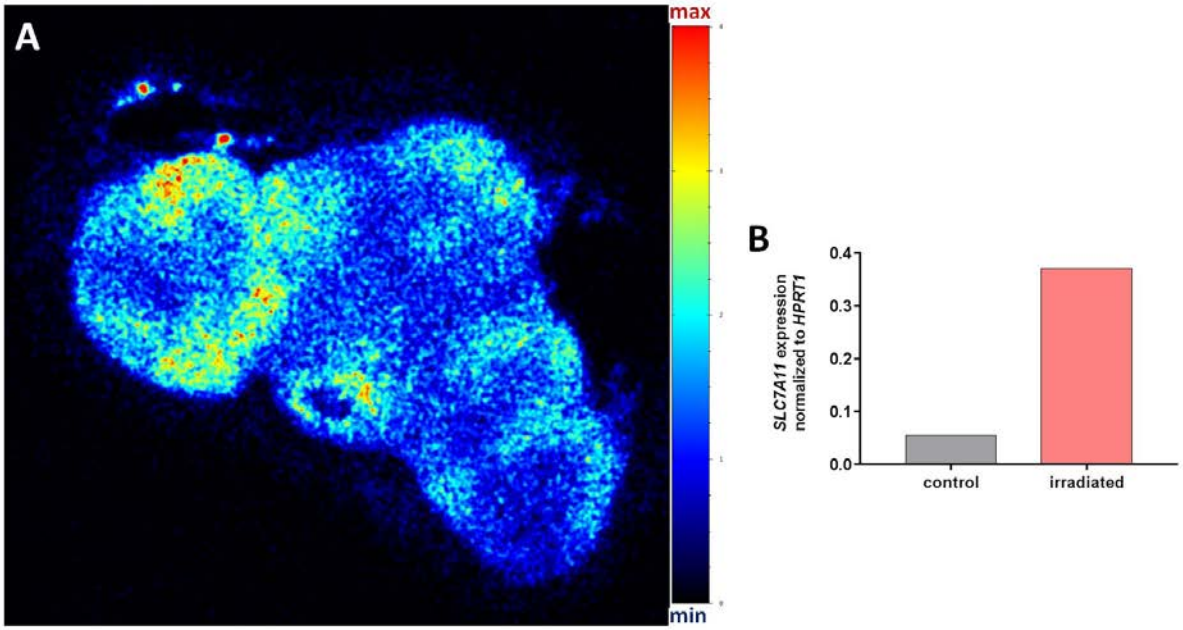

Figure 7.1 MDA-MB-231 tumour analysis data. A) An ^{18}F beta autoradiograph of MDA-MB-231 tumour. 20 MBq of [^{18}F]FASu was injected *via* the tail vein. The tumour was harvested at 1 h p.i. Autoradiograph is a courtesy of Dr. Jason Crawford. **B)** Relative expression of *SLC7A11* in MDA-MB-231 tumours *ex vivo*. The irradiated tumour was treated with 10 Gy of localized external bean radiation therapy. Both tumours were harvested 24 h post-treatment (either mock or radiotherapy, n = 1 per group).

In Chapter 3, we designed a boramino acid derivative of [^{18}F]FASu, [^{18}F]ASu-BF_3, and evaluated its biological behaviour. While the alteration of the radiolabelling strategy resulted in a simpler procedure: including an ^{18}F-^{19}F isotope exchange on the trifluoroborate motif, without required protection of the α-amino group, we discovered that the pharmacokinetic nature of the resulting modified tracer was greatly changed. [^{18}F]ASu-BF_3 was excreted extremely rapidly *via* the renal pathway, restricting its utility for tumour imaging and biodistribution studies. Our findings indicate that addition of the boramino acid moiety to the aminosuberic acid structure can significantly affect tracer pharmacokinetics and that such an approach for radiofluorinating amino acids should be taken with care. In Chapter 4, beyond the demonstration that 5-position optical configuration plays no role in [^{18}F]FASu biodistribution, the uptake of [^{18}F]FASu in prostate cancer and glioblastoma tumor models was reported here for the first time, thus broadening the spectrum of cancers for which the tracer has shown potential detection utility.

Additionally, in Chapter 5, we evaluated [^{18}F]FASu in contrast to another xCT-targeting radiopharmaceutical [^{18}F]FSPG. Our study was a direct comparison of the uptake of the two tracers, and results showed that [^{18}F]FSPG had higher uptake *in vitro* and *in vivo,* but that its uptake fluctuated inverse to the difference in xCT expression in the imaged tumours. We hypothesized that this is due to the lower specificity of this tracer to the system x_C^- transporter as compared to [^{18}F]FASu, and reliance on other transporter systems, but further validation studies are required. Finally, in Chapter 6, we evaluated five amino acid tracers as potential system L imaging agents. While promising results were obtained in the initial screening assays, the main issue with these tracers remains – and that is low specific activity of the final products, which, unless resolved, may hinder the process of translation of these radiotracers into the clinic.

7.3 Future research directions

7.3.1 Chemo- and radiation therapy monitoring *in vivo*

Reports that increased xCT expression might render some tumours more resistant to radiation and chemotherapy bring up the question of whether we can identify such tumours in advance and change the course of treatment, or use combination therapy with xCT inhibitors, to sensitize cancers to other treatments. For this purpose, imaging and biodistribution studies can be performed with [^{18}F]FASu prior to, during and/or after chemotherapy or radiation treatment to better gauge tumour response in a patient-specific manner. Mice bearing xCT-expressing tumours will be treated with localized radiation therapy or systemic chemotherapy, optimal doses of which should be determined in advance. The wellbeing of the animals and tumour size will be monitored regularly, and the tumours will be imaged on a μPET/CT scanner at multiple time points (e.g., 5, 18, 24, 72 and 120 h) to establish tracer accumulation trends and select the time point at which there is the biggest difference in the uptake as compared to the baseline scan (before treatment). Due to the rapid clearance of [^{18}F]FASu and short half-life of ^{18}F, imaging can be done repeatedly, over the course of the treatment, with the goal of observing any changes in uptake of the tumour caused by the treatment. In parallel to this biodistribution and imaging study, intratumoural GSH and ROS levels can also be monitored, along with the measurements of xCT expression. Needless to say, the same biomarker measurements and PET scans will be performed on control animals, which had not been subjected to treatment.

In the situation where fluctuations in [^{18}F]FASu tumour uptake are observed due to treatment, a further step can be taken to explore the implications of this phenomenon. Two separate cohorts of tumour-bearing animals, one bearing tumours with high expression of xCT, and the other one with low xCT expression, can be subjected to treatment which mimics normal chemotherapy regimen used for human patients. Baseline [^{18}F]FASu-PET scans should be done and the animals' response to treatment will be followed until the tumours have vanished or until humane endpoint is reached. Tumours will be scanned again several times during the course of the therapy, and the data will be analyzed retroactively. We will compare the initial and follow-up scans (and biodistribution data) of the animals from the two groups, and investigate whether their differential response to treatment could have been predicted based on the baseline [^{18}F]FASu tumour uptake. This approach might enable us to establish xCT as a prognostic marker in certain types of cancer, but more importantly it will provide oncologists with a non-invasive approach to decide which patients will benefit from certain therapies.

7.3.2 Using CRISPR as an alternative approach for the tracer specificity studies

Our tracer comparison study in Chapter 5 shed more light on the specificity of [^{18}F]FASu and [^{18}F]FSPG, giving further indication that the uptake of [^{18}F]FSPG might also be attributed to alternative modes of glutamate transport. However, it did not completely answer the question: which tracer has higher specificity to system x_C^-? The ultimate answer to this question could be obtained by creating an xCT knockout (KO) cell line with the CRISPR method, and using it to evaluate [^{18}F]FASu and [^{18}F]FSPG uptake *in vitro* and *in vivo*. Whichever tracer relies on entering the cells *via* a transporter other than system x_C^-, will still be taken up by the KO cells. In the event that intracellular uptake is observed by both tracers, whichever tracer has higher uptake in the KO cells, is by definition more reliant on other transporter systems. A necessary control would include performing the same uptake assays, in parallel, with the wild-type cell line as well as the KO cell line in which xCT was reintroduced, as a proof of concept, as tracer uptake is successfully restored.

7.4 Clinical translation of [^{18}F]FASu

The tracers presented in Chapter 6 are all novel PET radiopharmaceuticals, and their further development is pending upon improvements of the low SA issue. The main theme of Chapters 2, 4-5, on the other hand, [^{18}F]FASu, is a radiotracer whose uptake characteristics have been well-understood. [^{18}F]FASu has excellent qualities for clinical translation, with good contrast, low background uptake, excellent *in vivo* stability and rapid clearance. Most importantly, it specifically targets cancers overexpressing xCT, which enables them to maintain intracellular redox balance and thus yields these cancers more resistant to chemotherapy. In addition, [^{18}F]FASu-PET has the potential to serve as a diagnostic tool for TNBC, and it shows new therapeutic potential for these patients, as it would uncover xCT as a valuable therapeutic target, in addition to enabling sensitization of the tumours to stress-inducing chemotherapeutics.

Prior to candidacy for clinical trials, thorough pre-clinical toxicological and dosimetry studies need to be conducted with [^{18}F]FASu in order to evaluate possible toxic effects and estimate the absorbed radiation dose from the tracer. The radiotracer preparation and biodistribution studies need to be performed under good laboratory practice (GLP) conditions. The biodistribution data can be used to estimate the radiation-absorbed doses in humans (mSv/Bq) using the OLINDA/EXM software. A two week acute toxicology study is required by Health Canada for radiopharmaceuticals intended to be administered as a single dose to humans in a Phase I clinical trial.[278] Toxicity studies are performed in healthy rats by administrating 1000-fold higher dose than the dose that will be used in humans for imaging studies, based on the specific activity of [^{18}F]FASu, or an equivalent volume of saline (for the control animals). Animals will be closely observed over a period of 14 days, their weights will be monitored daily, and blood chemistry and necropsies performed on the last day of the study to see if any differences are observed between treated and control groups. GLP toxilocogy and biodistribution studies can be performed at our facility, at BC Cancer, thanks to Investigational Drug Program which was developed for this purpose.

7.5 Overall significance and implications of research findings

The main objective of this thesis was to evaluate amino acid-based tracers as potential cancer diagnostics that can provide complementary information about the nature of the lesion. Transporter systems x_C^- and L show increased expression in certain cancer types, and consequently have emerged as promising imaging and therapeutic biomarkers. It has been reported that inhibition of these biomarkers slows or completely stops tumour growth in a pre-clinical setting,[128,130] and that it also sensitizes tumours to chemotherapy.[128] Moreover, studies have indicated that xCT is associated with advanced stage and primary tumour factor in tongue cancer[222] and that LAT1 is a predictor of poor prognosis for patients with pancreatic ductal adenocarcinoma.[192] Our goal was to not only accelerate such applications but also to enable physicians to more effectively and in a non-invasive manner stratify patients that would benefit most from certain therapies and/or determine if intratumoural expression of the biomarker is sufficient enough for effective implementation of targeted or combination therapies. Furthermore, radiopharmaceuticals may be useful for assessing patients' response to treatment or optimizing therapeutic dosage. In conclusion, the development of *in vivo* imaging agents toward the x_C^- and L transporters would benefit both basic science and clinical research; providing the community with widely applicable non-invasive tools for cancer diagnosis, and potentially treatment monitoring.

Bibliography

1. Kramer-Marek, G. & Capala, J. The role of nuclear medicine in modern therapy of cancer. *Tumor Biol.* **33**, 629–640 (2012).
2. Pysz, M. A., Gambhir, S. S. & Willmann, J. K. Molecular imaging: current status and emerging strategies. *Clin. Radiol.* **65**, 500–516 (2010).
3. Chen, Z. Y. *et al.* Advance of molecular imaging technology and targeted imaging agent in imaging and therapy. *Biomed Res. Int.* **2014**, (2014).
4. Gambhir, S. S. *et al.* Molecular imaging for personalized cancer care. *Acad. Radiol.* **8**, 4–14 (2001).
5. Cherry, S. R. The 2006 Henry N. Wagner lecture: Of mice and men (and positrons) - Advances in PET imaging technology. *J. Nucl. Med.* **47**, 1735–1745 (2006).
6. Lu, F. & Yuan, Z. PET / SPECT molecular imaging in clinical neuroscience : recent advances in the investigation of CNS diseases. *Quant. Imaging Med. Surg.* **5**, 433–447 (2015).
7. Weissleder, R. & Pittet, M. J. Imaging in the era of molecular oncology. *Nature* **452**, 580–589 (2008).
8. Bénard, F. Personal communication. (2019).
9. Blankenberg, F. G. & Strauss, H. W. Nuclear medicine applications in molecular imaging: 2007 update. *Q. J. Nucl. Med. Mol. Imaging 99* **51**, 99–110 (2007).
10. Celler, A. Nuclear Medicine: SPECT and PET imaging principles. *Med. Imaging Princ. Detect. Electron.* 101–126 (2009).
11. Beer, A. J., Kessler, H. & Wester, H. J. Multimodality Imaging of Integrin α v β 3 Expression. *Theranostics* **1**, 48–57 (2011).
12. Gambhir, S. S. Molecular imaging of cancer with positron emission tomography. *Nat. Rev. Cancer* **2**, 683–693 (2002).
13. New, S. E. P. & Aikawa, E. Molecular imaging insights into early inflammatory stages of arterial and aortic valve calcification. *Circ. Res.* **108**, 1381–1391 (2011).
14. Gomes, C. M., Abrunhosa, A. J., Ramos, P. & Pauwels, E. K. J. Molecular imaging with SPECT as a tool for drug development. *Adv. Drug Deliv. Rev.* **63**, 547–554 (2011).
15. Saha, G. B. *Fundamentals of Nuclear Pharmacy*. (Springer-Verlag New York, 2010).

doi:10.1007/978-1-4419-5860-0

16. Fani, M. & Maecke, H. R. Radiopharmaceutical development of radiolabelled peptides. *Eur. J. Nucl. Med. Mol. Imaging* **39**, (2012).
17. Kircher, M. F., Hricak, H. & Larson, S. M. Molecular imaging for personalized cancer care. *Mol. Oncol.* **6**, 182–195 (2012).
18. Ametamey, S. M., Honer, M. & Schubiger, P. A. Molecular Imaging with PET. 1501–1516 (2008). doi:10.1021/CR0782426
19. Lopci, E. *et al.* Imaging with non-FDG PET tracers: outlook for current clinical applications. *Insights Imaging* **1**, 373–385 (2010).
20. Cai, W. & Chen, X. Multimodality Molecular Imaging of Tumor Angiogenesis. *J. Nucl. Med.* **49**, 113S-128S (2008).
21. Leung, K. [11C]Choline. *Molecular Imaging and Contrast Agent Database (MICAD) [Internet]* 1–5
22. Miele, E. *et al.* Positron Emission Tomography (PET) radiotracers in oncology--utility of 18F-Fluoro-deoxy-glucose (FDG)-PET in the management of patients with non-small-cell lung cancer (NSCLC). *J. Exp. Clin. Cancer Res.* **27**, 52 (2008).
23. Pacák, J., Točik, Z. & Černy, M. Synthesis of 2-deoxy-2-fluoro-D-glucose. *Chem. Commun.* 1 (1969).
24. Yu, S. Review of 18F-FDG synthesis and quality control. *Biomed. Imaging Interv. J.* **2**, (2006).
25. Fowler, J. S. & Ido, T. Initial and subsequent approach for the synthesis of18FDG. *Semin. Nucl. Med.* **32**, 6–12 (2002).
26. Reivich, M. *et al.* The [18F]Fluorodeoxyglucose Method for the Measurement of Local Cerebral Glucose Utilization in Man. *Circ. Res.* **44**, 127–137 (1979).
27. Pauwels, E. K. J., Sturm, E. J., Bombardieri, E., Cleton, F. J. & Stokkel, M. P. M. Positron-emission tomography with [18 F]¯uorodeoxyglucose. *J. Cancer Res. Clin. Oncol.* **126**, 549–559 (2000).
28. Warburg, O. the Metabolism of Tumors in the Body. *J. Gen. Physiol.* **8**, 519–530 (1927).
29. Vander Heiden, M., Cantley, L. & Thompson, C. Understanding the Warburg effect: The metabolic Requiremetns of cell proliferation. *Science (80-.).* **324**, 1029–1033 (2009).

30. Ben-Haim, S. & Ell, P. 18F-FDG PET and PET/CT in the Evaluation of Cancer Treatment Response. *J. Nucl. Med.* **50**, 88–99 (2008).
31. Zhu, A., Lee, D. & Shim, H. Metabolic positron emission tomography imaging in cancer detection and therapy response. *Semin. Oncol.* **38**, 55–69 (2011).
32. Griffeth, L. K. Use of PET/CT scanning in cancer patients: technical and practical considerations. *Proc. (Bayl. Univ. Med. Cent).* **18**, 321–30 (2005).
33. Pimlott, S. L. & Sutherland, A. Molecular tracers for the PET and SPECT imaging of disease. *Chem. Soc. Rev.* **40**, 149–162 (2011).
34. Michalski, M. H. & Chen, X. Molecular imaging in cancer treatment. *Eur. J. Nucl. Med. Mol. Imaging* **38**, 358–377 (2011).
35. Hillner, B. E. *et al.* Impact of positron emission tomography/computed tomography and positron emission tomography (PET) alone on expected management of patients with cancer: Initial results from the National Oncologic PET Registry. *J. Clin. Oncol.* **26**, 2155–2161 (2008).
36. Hillner, B. E. *et al.* The impact of positron emission tomography (PET) on expected management during cancer treatment. *Cancer* **115**, 410–418 (2009).
37. Worsley, D. F., Wilson, D. C., Powe, J. E. & Benard, F. Impact of F-18 Fluorodeoxyglucose Positron Emission Tomography-Computed Tomography on Oncologic Patient Management: First 2 Years' Experience at a Single Canadian Cancer Center. *Can. Assoc. Radiol. J.* **61**, 13–18 (2010).
38. Canadian Cancer Society's Advisory Committee on Cancer & Statistics. *Canadian Cancer Statistics 2017*. *Canadian Cancer Statistics 2017* (2017). doi:0835-2976
39. Martinuk, S. D. *The Use of Positron Emission Tomography (PET) for Cancer Care Across Canada Time for a National Strategy*. *Classic Printing Services Ltd* (2011).
40. Morrison, S. & Andra, G. Publicly Funded Uses of PET Scans in Canada Context. *Can. Agency Drugs Technol. Heal.* **8**, 1–11 (2015).
41. Hanahan, D. & Weinberg, R. A. The hallmarks of cancer. *Cell* **100**, 57–70 (2000).
42. Deutsch, G., Kirchoff DD & Faries MB. Metastasectomy for Stage IV Melanoma. *Surg. Oncol. Clin. N. Am.* **24**, 279–298 (2015).
43. Barth, A., Wanek, L. & Morton, D. Prognostic factors in 1,521 melanoma patients with

distant metastasis. *J. Am. Coll. Surg.* **181**, A193–A201 (1995).

44. Jackson, S. E. & Chester, J. D. Personalised cancer medicine. *Int. J. Cancer* **137**, 262–266 (2015).
45. Tsai, J Lee , JT Wang, W. *et al.* Discovery of a selective inhibitor of oncogenic B-Raf kinase with potent antimelanoma activity. *Proc. Natl. Acad. Sci. United States Am.* **105**, 3041–3046 (2008).
46. Chapman, P. B. *et al.* Improved Survival with Vemurafenib in Melanoma with BRAF V600E Mutation. *N. Engl. J. Med.* **364**, 2507–2516 (2011).
47. Chen, S. & Parmigiani, G. Meta-analysis of BRCA1 and BRCA2 penetrance. *J. Clin. Oncol.* **25**, 1329–1333 (2007).
48. Lostumbo, L., Carbine, N. E. & Wallace, J. Prophylactic mastectomy for the prevention of breast cancer. *Cochrane Database Syst. Rev.* CD002748 (2010). doi:10.1002/14651858.CD002748.pub3
49. Hanahan, D. & Weinberg, R. A. Hallmarks of cancer: The next generation. *Cell* **144**, 646–674 (2011).
50. Hanahan, D. & Coussens, L. M. Accessories to the Crime: Functions of Cells Recruited to the Tumor Microenvironment. *Cancer Cell* **21**, 309–322 (2012).
51. Gupta, G. P. & Massagué, J. Cancer Metastasis: Building a Framework. *Cell* **127**, 679–695 (2006).
52. Brown, L. *et al.* Vascular stroma formation in carcinoma in situ, invasive carcinoma, and matastatic carcinoma of the breast. *Clin. Cancer Res.* **5**, 1041–56 (1999).
53. Pavlova, N. N. & Thompson, C. B. The Emerging Hallmarks of Cancer Metabolism. *Cell Metab.* **23**, 27–47 (2016).
54. Liotta, L. A. & Kohn, E. C. The microenvironment of the tumour-host interface. *Nature* **411**, 375–379 (2001).
55. Vaccariello, M., Javaherian, A., Wang, Y., Fusenig, N. E. & Garlick, J. A. Cell interactions control the fate of malignant keratinocytes in an organotypic model of early neoplasia. *J. Invest. Dermatol.* **113**, 384–391 (1999).
56. Phaniendra, A., Jestadi, D. B. & Periyasamy, L. Free Radicals: Properties, Sources, Targets, and Their Implication in Various Diseases. *Indian J. Clin. Biochem.* **30**, 11–26

(2015).

57. Holmström, K. M. & Finkel, T. Cellular mechanisms and physiological consequences of redox-dependent signalling. *Nat. Rev. Mol. Cell Biol.* **15**, 411–421 (2014).
58. Sena, L. & Chandel, N. Physiological roles of mitochondrial reactive oxygen species. *Mol. Cell* **48**, 158–167 (2012).
59. Reuter, S., Gupta, S. C., Chaturvedi, M. M. & Aggarwal, B. B. Oxidative stress, inflammation, and cancer: How are they linked? *Free Radic Biol Med* **49**, 1603–1616 (2010).
60. Fransen, M., Nordgren, M., Wang, B. & Apanasets, O. Role of peroxisomes in ROS/RNS-metabolism: Implications for human disease. *Biochim. Biophys. Acta - Mol. Basis Dis.* **1822**, 1363–1373 (2012).
61. Lambeth, J. NOX enzymes and the biology of reactive oxygen. *Nat. Rev. Immunol.* **4**, 181–189 (2004).
62. Cairns, R. A., Harris, I. S. & Mak, T. W. Regulation of cancer cell metabolism. *Nat. Rev. Cancer* **11**, 85–95 (2011).
63. Trachootham, D., Alexandre, J. & Huang, P. Targeting cancer cells by ROS-mediated mechanisms: A radical therapeutic approach? *Nat. Rev. Drug Discov.* **8**, 579–591 (2009).
64. Schieber, M. & Chandel, N. ROS function in redox signaling and oxidative stress. *Curr Biol* **24**, R453-462 (2014).
65. Thannickal, V. J. & Fanburg, B. L. Reactive oxygen species in cell signaling. *Am J Physiol Lung Cell Mol Physiol* **279**, L1005-1028 (2000).
66. Denu, J. M. & Tanner, K. G. Specific and reversible inactivation of protein tyrosine phosphatases by hydrogen peroxide: Evidence for a sulfenic acid intermediate and implications for redox regulation. *Biochemistry* **37**, 5633–5642 (1998).
67. Kamata, H. *et al.* Reactive oxygen species promote TNFα-induced death and sustained JNK activation by inhibiting MAP kinase phosphatases. *Cell* **120**, 649–661 (2005).
68. Yan, S. R., and Berton, G. Regulation of Src Family Tyrosine Kinase Activities in Adherent Evidence that Reactive Oxygen Intermediates Produced by Adherent Neutrophils. *J Biol Chem* **271**,38: 23464–23471 (1996).
69. Lee, S. R. *et al.* Reversible inactivation of the tumor suppressor PTEN by H2O2. *J. Biol.*

Chem. **277**, 20336–20342 (2002).

70. Lü, J.-M., Lin, P. H., Yao, Q. & Chen, C. Chemical and molecular mechanisms of antioxidants: experimental approaches and model systems. *J. Cell. Mol. Med.* **14**, 840–860 (2010).
71. Gao, P. & et al. HIF-dependent antitumorigenic effect of antioxidants in vivo. *Cancer Cell* **12**, 230–238 (2007).
72. Garrido, C. & et al. Mechanisms of cytochrome c release from mitochondria. *Cell Death Differ* **13**, 1423–1433 (2006).
73. Trachootham, D., Ogasawara, M., Nilsa, R. & Huang, P. Redox regulation of cell survival. *Antioxid. Redox Signal.* **10**, 1343–1374 (2008).
74. Gorrini, C., Harris, I. S. & Mak, T. W. Modulation of oxidative stress as an anticancer strategy. *Nat. Rev. Drug Discov.* **12**, 931–947 (2013).
75. Diehn, M. *et al.* Association of Reactive Oxygen Species Levels and Radioresistance in Cancer Stem Cells. *Nature* **458**, 780–783 (2009).
76. Chi V. Dang. MYC on the Path to Cancer. *Cell* **149**, 22–35 (2012).
77. Miller, D. M., Thomas, S. D., Islam, A., Muench, D. & Sedoris, K. c-Myc and Cancer Metabolism. *Clin. Cancer Res.* **18**, 5546–5553 (2012).
78. Basak, P., Sadhukhan, P., Sarkar, P. & Sil, P. C. Perspectives of the Nrf-2 signaling pathway in cancer progression and therapy. *Toxicol. Reports* **4**, 306–318 (2017).
79. Kansanen, E., Kuosmanen, S. M., Leinonen, H. & Levonenn, A. L. The Keap1-Nrf2 pathway: Mechanisms of activation and dysregulation in cancer. *Redox Biol.* **1**, 45–49 (2013).
80. DeNicola, G. M. *et al.* Oncogene-induced Nrf2 transcription promotes ROS detoxification and tumorigenesis. *Nature* **475**, 106–109 (2012).
81. Gorrini, C. *et al.* Estrogen controls the survival of BRCA1-deficient cells via a PI3K-NRF2-regulated pathway. *Proc. Natl. Acad. Sci.* **111**, 4472–4477 (2014).
82. Svineng, G., Ravuri, C., Rikardsen, O., Huseby, N.-E. & Winberg, J.-O. The Role of Reactive Oxygen Species in Integrin and Matrix Metalloproteinase Expression and Function. *Connect. Tissue Res.* **49**, 197–202 (2008).
83. Wojtala, A. *et al.* Methods to monitor ROS production by fluorescence microscopy and

fluorometry. *Methods in Enzymology* **542**, (Elsevier Inc., 2014).

84. Winterbourn, C. C. The challenges of using fluorescent probes to detect and quantify specific reactive oxygen species in living cells. *Biochim. Biophys. Acta - Gen. Subj.* **1840**, 730–738 (2014).
85. Ameziane-El-Hassani, R. & Dupuy, C. Detection of Intracellular Reactive Oxygen Species (CM-H2DCFDA). *Bio-protocol* **3**, 67–68 (2013).
86. Wardman, P. Fluorescent and luminescent probes for measurement of oxidative and nitrosative species in cells and tissues: Progress, pitfalls, and prospects. *Free Radic. Biol. Med.* **43**, 995–1022 (2007).
87. Kalyanaraman, B. *et al.* Measuring reactive oxygen and nitrogen species with fluorescent probes: Challenges and limitations. *Free Radic. Biol. Med.* **52**, 1–6 (2012).
88. Gomes, A., Fernandes, E. & Lima, J. L. F. C. Fluorescence probes used for detection of reactive oxygen species. *J. Biochem. Biophys. Methods* **65**, 45–80 (2005).
89. Robinson, K. M., Janes, M. S. & Beckman, J. S. The selective detection of mitochondrial superoxide by live cell imaging. *Nat. Protoc.* **3**, 941–947 (2008).
90. Owusu-Ansah, E., Yavari, A. & Banerjee, U. A protocol for in vivo detection of reactive oxygen species. *Protoc. Exch. (Nature Publ. Group)* 1–9 (2008). doi:10.1038/nprot.2008.23
91. Wu, D. & Yotnda, P. Production and Detection of Reactive Oxygen Species (ROS) in Cancers. *J. Vis. Exp.* 2–5 (2011). doi:10.3791/3357
92. Royall, J. & Ischiropoulos, H. Evaluation of 2',7'-dichlorofluorescin and dihydrorhodamine 123 as fluorescent probes for intracellular H2O2 in cultured endothelial cells. *Arch Biochem Biophys* **302**, 348–55 (1993).
93. Conrad, M. & Sato, H. The oxidative stress-inducible cystine/glutamate antiporter, system xc-: Cystine supplier and beyond. *Amino Acids* **42**, 231–246 (2012).
94. Bannai, S. & Kitamura, E. Transport Interaction of L-Cystine and L-Glutamate in Human Diploid Fibroblasts in Culture. *J. Biol. Chem.* **265**, 2372–2376 (1980).
95. Bannai, S. Induction of cystine and glutamate transport activity in human fibroblasts by diethylmaleate and other electrophilic agents. *J. Biol. Chem.* **259**, 2435–2440 (1984).
96. Sato, H. *et al.* Redox imbalance in cystine/glutamate transporter-deficient mice. *J. Biol.*

Chem. **280**, 37423–37429 (2005).

97. Lo, M., Wang, Y. Z. & Gout, P. W. The xc- cystine/glutamate antiporter: A potential target for therapy of cancer and other diseases. *J. Cell. Physiol.* **215**, 593–602 (2008).
98. Go, Y. M. & Jones, D. P. Cysteine/cystine redox signaling in cardiovascular disease. *Free Radic. Biol. Med.* **50**, 495–509 (2011).
99. Dixon, S. J. *et al.* Ferroptosis: An iron-dependent form of nonapoptotic cell death. *Cell* **149**, 1060–1072 (2012).
100. Bridges, R. J., Natale, N. R. & Patel, S. A. System xc- cystine/glutamate antiporter: An update on molecular pharmacology and roles within the CNS. *Br. J. Pharmacol.* **165**, 20–34 (2012).
101. Sasaki, H. *et al.* Electrophile response element-mediated induction of the cystine/glutamate exchange transporter gene expression. *J. Biol. Chem.* **277**, 44765–44771 (2002).
102. Webster, J. M. *et al.* Functional Imaging of Oxidative Stress with a Novel PET Imaging Agent, ^{18}F-5-Fluoro-L-Aminosuberic Acid. *J. Nucl. Med.* **55**, 657–664 (2014).
103. Yang, H. *et al.* ^{18}F-5-Fluoroaminosuberic acid as a potential tracer to gauge oxidative stress in breast cancer models. *J. Nucl. Med.* **58**, 367–373 (2017).
104. Sato, H., Tamba, M., Ishii, T. & Bannai, S. Cloning and Expression of a Plasma Membrane Cystine / Glutamate Exchange Transporter Composed of Two Distinct Proteins *. *Biochemistry* 2–5 (1999). doi:10.1074/jbc.274.17.11455
105. Chillaron, J., Roca, R., Valencia, A., Zorzano, A. & Palacin, M. Heteromeric amino acid transporters: biochemistry, genetics, and physiology. *Am J Physiol Ren. Physiol* **281**, F995–F1018 (2001).
106. Sun, A., Liu, X. & Tang, G. Carbon-11 and Fluorine-18 Labeled Amino Acid Tracers for Positron Emission Tomography Imaging of Tumors. *Front. Chem.* **5**, 1–16 (2018).
107. Yanagida, O. *et al.* Human L-type amino acid transporter 1 (LAT1): characterization of function and expression in tumor cell lines. *Biochim. Biophys. Acta - Biomembr.* **1514**, 291–302 (2001).
108. Sato, H. *et al.* Effect of Oxygen on Induction of the Cystine Transporter by Bacterial Lipopolysaccharide in Mouse Peritoneal Macrophages. *J. Biol. Chem.* **276**, 10407–10412

(2001).

109. Jiménez-Vidal, M. *et al.* Thiol Modification of Cysteine 327 in the Eighth Transmembrane Domain of the Light Subunit xCT of the Heteromeric Cystine/Glutamate Antiporter Suggests Close Proximity to the Substrate Binding Site/Permeation Pathway. *J. Biol. Chem.* **279**, 11214–11221 (2004).
110. Torrents, D. *et al.* Identification and Characterization of a Membrane Protein (y+L Amino Acid Transporter-1) That Associates with 4F2hc to Encode the Amino Acid Transport Activity y+L. *J. Biol. Chem.* **273**, 32437–32445 (1998).
111. Bridges, C. C. *et al.* Structure, function, and regulation of human cystine/glutamate transporter in retinal pigment epithelial cells. *Invest Ophthalmol Vis Sci* **42**, 47–54 (2001).
112. Gasol, E., Jiménez-Vidal, M., Chillarón, J., Zorzano, A. & Palacín, M. Membrane topology of System xc-light subunit reveals a re-entrant loop with substrate-restricted accessibility. *J. Biol. Chem.* **279**, 31228–31236 (2004).
113. Lewerenz, J. *et al.* The Cystine/Glutamate Antiporter System x_c^- in Health and Disease: From Molecular Mechanisms to Novel Therapeutic Opportunities. *Antioxid. Redox Signal.* **18**, 522–555 (2013).
114. Sato, H. *et al.* Redox Imbalance in Cystine/Glutamate Transporter-deficient Mice. *J. Biol. Chem.* **280**, 37423–37429 (2005).
115. Dixon, S. J. *et al.* Pharmacological inhibition of cystine-glutamate exchange induces endoplasmic reticulum stress and ferroptosis. *Elife* **3**, e02523 (2014).
116. Koppula, P., Zhang, Y., Zhuang, L. & Gan, B. Amino acid transporter SLC7A11/xCT at the crossroads of regulating redox homeostasis and nutrient dependency of cancer. *Cancer Commun. (London, England)* **38**, 13 (2018).
117. Shaffer, P. L., Goehring, A., Shankaranarayanan, A. & Gouaux, E. Structure and Mechanism of a Na+-Independent Amino Acid Transporter. *Science (80-.).* **325**, 1010–1014 (2009).
118. Pearson, W. R. & Lipman, D. J. Improved tools for biological sequence comparison. *Proc. Natl. Acad. Sci.* **85**, 2444–2448 (1988).
119. Larkin, M. A. *et al.* Clustal W and Clustal X version 2.0. *Bioinformatics* **23**, 2947–2948 (2007).

120. Ishii, T. *et al.* Transcription Factor Nrf2 Coordinately Regulates a Group of Oxidative Stress-inducible Genes in Macrophages*. *J. Biol. Chem.* **275**, 16023–16029 (2000).
121. Lim, J. K. M. *et al.* Cystine/glutamate antiporter xCT (SLC7A11) facilitates oncogenic RAS transformation by preserving intracellular redox balance. *Proc. Natl. Acad. Sci. U. S. A.* **116**, 9433–9442 (2019).
122. Sato, H., Fujiwara, K., Sagara, J. & Bannai, S. Induction of cystine transport activity in mouse peritoneal macrophages by bacterial lipopolysaccharide. *Biochem. J.* **310**, 547–551 (1995).
123. Largo, C., Cuevas, P., Somjen, G. G., Martín del Río, R. & Herreras, O. The effect of depressing glial function in rat brain in situ on ion homeostasis, synaptic transmission, and neuron survival. *J. Neurosci.* **16**, 1219–29 (1996).
124. Dringen, R., Pfeiffer, B. & Hamprecht, B. Synthesis of the Antioxidant Glutathione in Neurons: Supply by Astrocytes of CysGly as Precursor for Neuronal Glutathione. *J. Neurosci.* **19**, 562–569 (1999).
125. Oka, A., Belliveau, M. J., Rosenberg, P. A. & Volpe, J. J. Vulnerability of oligodendroglia to glutamate: pharmacology, mechanisms, and prevention. *J. Neurosci.* **13**, 1441–53 (1993).
126. Ganapathy, V., Thangaraju, M. & Prasad, P. D. Nutrient transporters in cancer: Relevance to Warburg hypothesis and beyond. *Pharmacol. Ther.* **121**, 29–40 (2009).
127. Jiang, J. *et al.* Redox regulation in tumor cell epithelial–mesenchymal transition: molecular basis and therapeutic strategy. *Signal Transduct. Target. Ther.* **2**, 17036 (2017).
128. Timmerman, L. A. *et al.* Glutamine Sensitivity Analysis Identifies the xCT Antiporter as a Common Triple Negative Breast Tumor Therapeutic Target. *Cancer Cell* **24**, 450–465 (2013).
129. Nakanishi, T. & Tamai, I. Solute carrier transporters as targets for drug delivery and pharmacological intervention for chemotherapy. *J. Pharm. Sci.* **100**, 3731–3750 (2011).
130. Gout, P. W., Buckley, A. R., Simms, C. R. & Bruchovsky, N. Sulfasalazine, a potent suppressor of lymphoma growth by inhibition of the x(c)-cystine transporter: a new action for an old drug. *Leuk. Off. J. Leuk. Soc. Am. Leuk. Res. Fund, U.K* **15**, 1633–1640 (2001).
131. Ishimoto, T. *et al.* CD44 Variant Regulates Redox Status in Cancer Cells by Stabilizing

the xCT Subunit of System xc- and Thereby Promotes Tumor Growth. *Cancer Cell* **19**, 387–400 (2011).

132. Hasegawa, M. *et al.* Functional interactions of the cystine/glutamate antiporter, CD44v and MUC1-C oncoprotein in triple-negative breast cancer cells. *Oncotarget* **7**, 11756–11769 (2016).
133. Kufe, D. W. MUC1-C Oncoprotein as a Target in Breast Cancer; Activation of Signaling Pathways and Therapeutic Approaches Donald. *Oncogene* **32**, 1073–1081 (2013).
134. Alam, M., Rajabi, H., Ahmad, R., Jin, C. & Kufe, D. Targeting the MUC1-C oncoprotein inhibits self-renewal capacity of breast cancer cells. *Oncotarget* **5**, 2622–34 (2014).
135. Krasikova, R. N. *et al.* 4-[^{18}F]fluoroglutamic acid (BAY 85-8050), a new amino acid radiotracer for PET imaging of tumors: Synthesis and in vitro characterization. *J. Med. Chem.* **54**, 406–410 (2011).
136. Smolarz, K. *et al.* Biodistribution and radiation dosimetry in healthy volunteers of a novel tumour-specific probe for PET/CT imaging: BAY 85-8050. *Eur. J. Nucl. Med. Mol. Imaging* **40**, 1861–1868 (2013).
137. Krause, B., Smolarz, K., Graner, F.-P. & et al. [^{18}F]BAY 85-8050 (TIM-1): a novel tumor specific probe for PET/CT imaging: dosimetry [abstract]. *J. Nucl. Med.* **51**, 1434 (2010).
138. Smolarz, K. *et al.* (S)-4-(3-^{18}F-Fluoropropyl)-L-Glutamic Acid: An ^{18}F-Labeled Tumor-Specific Probe for PET/CT Imaging--Dosimetry. *J. Nucl. Med.* **54**, 861–866 (2013).
139. Koglin, N. *et al.* Specific PET imaging of x_C^- transporter activity using a ^{18}F-labeled glutamate derivative reveals a dominant pathway in tumor metabolism. *Clin. Cancer Res.* **17**, 6000–6011 (2011).
140. Mittra, E. S. *et al.* Pilot preclinical and clinical evaluation of (4S)-4-(3-[^{18}F]Fluoropropyl)-L-Glutamate (^{18}F-FSPG) for PET/CT imaging of intracranial malignancies. *PLoS One* **11**, 1–17 (2016).
141. Mattsson, S. *et al. Radiation Dose to Patients from Radiopharmaceuticals: A Compendium of Current Information Related to Frequently Used Substances*. *International Commission on Radiological Protection (RCRP)* **44**, (2014).
142. Baek, S. *et al.* Exploratory clinical trial of (4S)-4-(3-[^{18}F]fluoropropyl)-L- glutamate for imaging x_C^- transporter using positron emission tomography in patients with non-small

cell lung or breast cancer. *Clin. Cancer Res.* **18**, 5427–5437 (2012).

143. Baek, S. *et al.* (4S)-4-(3-^{18}F-Fluoropropyl)-L-Glutamate for Imaging of x_C^- Transporter Activity in Hepatocellular Carcinoma Using PET: Preclinical and Exploratory Clinical Studies. *J. Nucl. Med.* **54**, 117–123 (2013).
144. Cheng, M. F. *et al.* Prospective comparison of (4S)-4-(3-^{18}F-fluoropropyl)-l-glutamate versus ^{18}F-fluorodeoxyglucose PET/CT for detecting metastases from pancreatic ductal adenocarcinoma: a proof-of-concept study. *Eur. J. Nucl. Med. Mol. Imaging* **46**, 810–820 (2019).
145. Robert, S. M. *et al.* SLC7A11 expression is associated with seizures, predicts poor survival in patients with malignant glioma. *Sci. Transl. Med.* **7**, (2015).
146. Beinat, C. *et al.* The characterization of 18F-hGTS13 for molecular imaging of xC-transporter activity with positron emission tomography. *J. Nucl. Med.* jnumed.119.225870 (2019). doi:10.2967/jnumed.119.225870
147. Kavanaugh, G. *et al.* Utility of [18F]FSPG PET to Image Hepatocellular Carcinoma: First Clinical Evaluation in a US Population. *Mol. Imaging Biol.* **18**, 924–934 (2016).
148. Stewart, B. W. & Wild, C. P. *World Cancer Report 2014*. *World Health Organization* (2014). doi:9283204298
149. Allred, D. C. Ductal carcinoma in situ: Terminology, classification, and natural history. *J. Natl. Cancer Inst. - Monogr.* 134–138 (2010). doi:10.1093/jncimonographs/lgq035
150. Lodish, H., Berk, A., Zipursky, S. & Al., E. Tumor Cells and the Onset of Cancer. in *Molecular Cell Biology* 21590 (New York: W.H. Freeman, 2000).
151. Karamouzis, M. V., Papavassiliou, K. A., Adamopoulos, C. & Papavassiliou, A. G. Targeting Androgen/Estrogen Receptors Crosstalk in Cancer. *Trends in Cancer* **2**, 35–48 (2016).
152. Yersal, O. Biological subtypes of breast cancer: Prognostic and therapeutic implications. *World J. Clin. Oncol.* **5**, 412 (2014).
153. Prat, A. *et al.* Clinical implications of the intrinsic molecular subtypes of breast cancer. *Breast* **24**, S26–S35 (2015).
154. Scholzen, T. & Gerdes, J. The Ki-67 protein: from the known and the unknown. *J.Cell Physiol* **182**, 311–322 (2000).

155. Li, H., Han, X., Liu, Y., Liu, G. & Dong, G. Ki67 as a predictor of poor prognosis in patients with triple-negative breast cancer. *Oncol. Lett.* **9**, 149–152 (2015).
156. Manning, H. C., Buck, J. R. & Cook, R. S. Mouse Models of Breast Cancer: Platforms for Discovering Precision Imaging Diagnostics and Future Cancer Medicine. *J. Nucl. Med.* **57**, 60S-68S (2016).
157. Stover, D. G., Bell, C. F. & Tolaney, S. M. Neoadjuvant and Adjuvant Chemotherapy Considerations for Triple-Negative Breast Cancer. *Am. J. Hematol. Oncol.* **12**, 6–12 (2016).
158. Lin, N. U. *et al.* Clinicopathologic features, patterns of recurrence, and survival among women with triple-negative breast cancer in the National Comprehensive Cancer Network. *Cancer* **118**, 5463–5472 (2012).
159. Keam, B. *et al.* Prognostic impact of clinicopathologic parameters in stage II/III breast cancer treated with neoadjuvant docetaxel and doxorubicin chemotherapy: Paradoxical features of the triple negative breast cancer. *BMC Cancer* **7**, 1–11 (2007).
160. Pantel, A. R. & Mankoff, D. A. Molecular imaging to guide systemic cancer therapy: Illustrative examples of PET imaging cancer biomarkers. *Cancer Lett.* **387**, 25–31 (2017).
161. Gebhart, G. *et al.* 18F-FDG PET/CT for Early Prediction of Response to Neoadjuvant Lapatinib, Trastuzumab, and Their Combination in HER2-Positive Breast Cancer: Results from Neo-ALTTO. *J. Nucl. Med.* **54**, 1862–1868 (2013).
162. Gradishar, W. J. *et al.* Invasive Breast Cancer Version 1.2016: Clinical Practice Guidelines in Oncology. *JNCCN J. Natl. Compr. Cancer Netw.* **14**, 324–354 (2016).
163. Ulaner, G. A. *et al.* 18F-FDG-PET/CT for systemic staging of newly diagnosed triple-negative breast cancer. *Eur. J. Nucl. Med. Mol. Imaging* **43**, 1937–1944 (2016).
164. Tchou, J. *et al.* Degree of tumor FDG uptake correlates with proliferation index in triple negative breast cancer. *Mol. Imaging Biol.* **12**, 657–662 (2010).
165. Herrera, A. C. S. A. *et al.* Molecular subtype is determinant on inflammatory status and immunological profile from invasive breast cancer patients. *Cancer Immunol. Immunother.* **61**, 2193–2201 (2012).
166. Mencalha, A., Victorino, V. J., Cecchini, R. & Panis, C. Mapping oxidative changes in breast cancer: Understanding the basic to reach the clinics. *Anticancer Res.* **34**, 1127–1140

(2014).

167. Huang, C. & McConathy, J. Radiolabeled Amino Acids for Oncologic Imaging. *J. Nucl. Med.* **54**, 1007–1010 (2013).
168. Wagner, C. A., Lang, F. & Broer, S. Function and structure of heterodimeric amino acid transporters. *Am J Physiol Cell Physiol* **281**, C1077–C1093 (2001).
169. McConathy, J. & Goodman, M. Non-natural amino acids for tumor imaging using positron emission tomography and single photon emission computed tomography. *Cancer Metastasis Rev* **27**, 555–57 (2008).
170. Altan, B. *et al.* Relationship between LAT1 expression and resistance to chemotherapy in pancreatic ductal adenocarcinoma. *Cancer Chemother. Pharmacol.* **0**, 0 (2017).
171. Huang, S., Stout, D., Yee, R., Satyamurthy, N. & Barrio, J. Distribution volume of radiolabeled large neutral amino acids in brain tissue. *J. Celebr. Blood Flow Metab.* **18**, 1288–1293 (1998).
172. Weber, T. & Luster, M. C-11-Methionin-PET/CT zur Lokalisation von Nebenschilddrusenadenomen. *Chirurg* **85**, 601–606 (2014).
173. Langen, K. J. *et al.* O-2-([18F]fluoroethyl)-L-tyrosine: uptake mechanisms and clinical applications. *Nucl. Med. Biol.* **33**, 501–508 (2006).
174. Floeth, F. *et al.* 18F-FET PET differentiation of ring-enhancing brain lesions. *J. Nucl. Med.* **47**, 776–782 (2006).
175. Nye, J. A. *et al.* Biodistribution and Radiation Dosimetry of the Synthetic Nonmetabolized Amino Acid Analogue Anti-18 F-FACBC in Humans. *J Nucl Med* **48**, 1017–1020 (2007).
176. Li, Z. & Conti, P. S. Radiopharmaceutical chemistry for positron emission tomography. *Adv. Drug Deliv. Rev.* **62**, 1031–1051 (2010).
177. Snyder, S. R. & Kilbourn, M. R. Chemistry of Fluorine-18 radiopharmaceuticals. in *Handbook of Radiopharmaceuicals Radiochemistry and Applications* (eds. Welch, M. J. & Redvanly, C. S.) 195–227 (John Wiley & Sons Ltd., 2003).
178. Cal-González, J. *et al.* Positron range effects in high resolution 3D PET imaging. *2009 IEEE Nucl. Sci. Symp. Conf. Rec.* 2788–2791 (2009). doi:10.1109/NSSMIC.2009.5401950
179. Gillis, E. P., Eastman, K. J., Hill, M. D., Donnelly, D. J. & Meanwell, N. A. Applications

of Fluorine in Medicinal Chemistry. *J. Med. Chem.* **58**, 8315–8359 (2015).

180. Lee, E. *et al.* A Fluoride-Derived Electrophilic Late-Stage Fluorination Reagent for PET Imaging. *Science (80-.).* **334**, 639–642 (2011).
181. Roeda, D. & Dolle, F. Recent Developments in the Chemistry of [18F]fluoride for PET. *Chem. Mol. Imaging* **24**, 55–77 (2015).
182. Teare, H., Robins, E., Arstad, E., Luthra, S. & Gouverneur, V. Synthesis and reactivity of [^{18}F]–fluorobenzenesulfonimide. *Chem. Commun.* 2330–2332 (2007). doi:10.1103/PhysRevB.67.092509
183. Wang, Q. & Holst, J. L-type amino acid transport and cancer: Targeting the mTORC1 pathway to inhibit neoplasia. *Am. J. Cancer Res.* **5**, 1281–1294 (2015).
184. Bröer, S. & Bröer, A. Amino acid homeostasis and signalling in mammalian cells and organisms. *Biochem. J.* **474**, 1935–1963 (2017).
185. Saxton, R. A. *et al.* Structural basis for leucine sensing by the Sestrin2-mTORC1 pathway. *Science (80-.).* **351**, 53–58 (2016).
186. Geier, E. G. *et al.* Structure-based ligand discovery for the Large-neutral Amino Acid Transporter 1, LAT-1. *Proc. Natl. Acad. Sci.* **110**, 5480–5485 (2013).
187. Nodwell, M. B. *et al.* ^{18}F-Fluorination of Unactivated C-H Bonds in Branched Aliphatic Amino Acids: Direct Synthesis of Oncological Positron Emission Tomography Imaging Agents. *J. Am. Chem. Soc.* **139**, (2017).
188. Piroth, M. D. *et al.* Prognostic value of early [18F]fluoroethyltyrosine positron emission tomography after radiochemotherapy in glioblastoma multiforme. *Int. J. Radiat. Oncol. Biol. Phys.* **80**, 176–184 (2011).
189. McConathy, J. 18F-Fluciclovine (FACBC) and Its Potential Use for Breast Cancer Imaging. *J. Nucl. Med.* **57**, 1329–1330 (2016).
190. Ulaner, G. A. *et al.* Prospective Clinical Trial of ^{18} F-Fluciclovine PET/CT for Determining the Response to Neoadjuvant Therapy in Invasive Ductal and Invasive Lobular Breast Cancers. *J. Nucl. Med.* **58**, 1037–1042 (2017).
191. Tade, F. I. *et al.* Anti-3-18F-FACBC (18F-Fluciclovine) PET/CT of Breast Cancer: An Exploratory Study. *J. Nucl. Med.* **57**, 1357–1363 (2016).
192. Yanagisawa, N. *et al.* High expression of L-type amino acid transporter 1 (LAT1) predicts

poor prognosis in pancreatic ductal adenocarcinomas. *J. Clin. Pathol.* **65**, 1019–1023 (2012).

193. Saxton, R. A. & Sabatini, D. M. mTOR Signaling in Growth, Metabolism, and Disease. *Cell* **168**, 960–976 (2017).
194. Hodson, N. *et al.* Characterisation of L-type amino acid transporter 1 (LAT1) expression in human skeletal muscle by immunofluorescent microscopy. *Nutrients* **10**, (2018).
195. Yang, H. *et al.* Addressing Chirality in the Structure and Synthesis of [^{18}F]5-Fluoroaminosuberic Acid ([^{18}F]FASu). *Chem. - A Eur. J.* **23**, (2017).
196. Gambhir, S. S. *et al.* A Tabulated Summary of the FDG PET Literature. *J. Nucl. Med.* **42**, 1S-93S (2001).
197. Almuhaideb, A., Papathanasiou, N. & Bomanji, J. 18 F-FDG PET/CT Imaging In Oncology. *Ann. Saudi Med.* **31**, 3–13 (2011).
198. Avril, S. *et al.* 18F-FDG PET/CT for Monitoring of Treatment Response in Breast Cancer. *J. Nucl. Med.* **57**, 34S-39S (2016).
199. Rosen, E. L., Eubank, W. B. & Mankoff, D. a. FDG PET, PET/CT, and breast cancer imaging. *Radiographics* **27 Suppl 1**, S215–S229 (2007).
200. Nakatani, K. *et al.* Roles and limitations of FDG PET in pediatric non-Hodgkin lymphoma. *Clin. Nucl. Med.* **37**, 656–662 (2012).
201. Jadvar, H. Imaging evaluation of prostate cancer with 18F-fluorodeoxyglucose PET/CT: utility and limitations. *Eur J Nucl Med Mol Imaging* **40**, 5–10 (2013).
202. Van Liefferinge, J. *et al.* Comparative analysis of antibodies to xCT (Slc7a11): Forewarned is forearmed. *J. Comp. Neurol.* **524**, 1015–1032 (2016).
203. Massie, A. *et al.* Time-dependent changes in striatal xCT protein expression in hemi-Parkinson rats. *Neuroreport* **19**, 1589–1592 (2008).
204. Burdo, J., Dargusch, R. & Schubert, D. Distribution of the cystine/glutamate antiporter system xc-in the brain, kidney, and duodenum. *J. Histochem. Cytochem.* **54**, 549–557 (2006).
205. Shih, A. Y. *et al.* Cystine/Glutamate Exchange Modulates Glutathione Supply for Neuroprotection from Oxidative Stress and Cell Proliferation. *J. Neurosci.* **26**, 10514–10523 (2006).

206. La Bella, V., Valentino, F., Piccoli, T. & Piccoli, F. Expression and developmental regulation of the cystine/glutamate exchanger (Xc-) in the rat. *Neurochem Res* **32**, 1081–1090 (2007).

207. Liu, Z. *et al.* Boramino acid as a marker for amino acid transporters. *Sci. Adv.* **1**, e1500694–e1500694 (2015).

208. Liu, H. *et al.* ^{18}F-Alanine Derivative Serves as an ASCT2 Marker for Cancer Imaging. *Mol. Pharm.* **15**, 947–954 (2018).

209. Yang, X. *et al.* Preclinical evaluation of an ^{18}F-trifluoroborate methionine derivative for glioma imaging. *Eur. J. Nucl. Med. Mol. Imaging* **45**, 585–592 (2018).

210. Kai, K., Takeuchi, J., Kataoka, T., Yokoyama, M. & Watanabe, N. Structure-activity relationship study of flowering-inducer FN against Lemna paucicostata. *Tetrahedron* **64**, 6760–6769 (2008).

211. Lin, K. S. *et al.* In vivo radioimaging of bradykinin receptor B1, a widely overexpressed molecule in human cancer. *Cancer Res.* **75**, 387–393 (2015).

212. Zhang, Z. *et al.* Design, synthesis and evaluation of ^{18}F-labeled cationic carbonic anhydrase IX inhibitors for PET imaging. *J. Enzyme Inhib. Med. Chem.* **32**, 722–730 (2017).

213. Yang, H. *et al.* ^{18}F-5-Fluoroaminosuberic Acid as a Potential Tracer to Gauge Oxidative Stress in Breast Cancer Models. *J. Nucl. Med.* **58**, 367–373 (2017).

214. Beenen, M. A., An, C. & Ellman, J. A. Asymmetric copper-catalyzed synthesis of α-amino boronate esters from N-tert-butanesulfinyl aldimines. *J. Am. Chem. Soc.* **130**, 6910–6911 (2008).

215. Liu, Z. *et al.* Preclinical Evaluation of a High-Affinity ^{18}F-Trifluoroborate Octreotate Derivative for Somatostatin Receptor Imaging. *J. Nucl. Med.* **55**, 1499–1505 (2014).

216. Pourghiasian, M. *et al.* ^{18}F-AmBF$_3$-MJ9: A novel radiofluorinated bombesin derivative for prostate cancer imaging. *Bioorganic Med. Chem.* **23**, 1500–1506 (2015).

217. Liu, Z. *et al.* ^{18}F-trifluoroborate derivatives of [des-Arg10]kallidin for imaging bradykinin B1 receptor expression with positron emission tomography. *Mol. Pharm.* **12**, 974–982 (2015).

218. Lau, J. *et al.* Trimeric Radiofluorinated Sulfonamide Derivatives to Achieve In Vivo

Selectivity for Carbonic Anhydrase IX–Targeted PET Imaging. *J. Nucl. Med.* **56**, 1434–1440 (2015).

219. Zhang, Z. *et al.* Synthesis and evaluation of ^{18}F-trifluoroborate derivatives of triphenylphosphonium for myocardial perfusion imaging. *Bioorganic Med. Chem. Lett.* **26**, 1675–1679 (2016).
220. Kumar, B., Koul, S., Khandrika, L., Meacham, R. B. & Koul, H. K. Oxidative stress is inherent in prostate cancer cells and is required for aggressive phenotype. *Cancer Res.* **68**, 1777–1785 (2008).
221. Shikano, N., Kanai, Y., Kawai, K., Ishikawa, N. & Endou, H. Transport of ^{99m}Tc-MAG3 via rat renal organic anion transporter 1. *J. Nucl. Med.* **45**, 80–85 (2004).
222. Toyoda, M. *et al.* Prognostic significance of amino-acid transporter expression (LAT1, ASCT2, and xCT) in surgically resected tongue cancer. *Br. J. Cancer* **110**, 2506–2513 (2014).
223. Qu, W. *et al.* Synthesis of optically pure 4-fluoro-glutamines as potential metabolic imaging agents for tumors. *J. Am. Chem. Soc.* **133**, 1122–1133 (2011).
224. Liu, F. *et al.* PET Imaging of ^{18}F-(2S,4R)4-Fluoroglutamine Accumulation in Breast Cancer: From Xenografts to Patients. *Mol. Pharm.* **15**, 3448–3455 (2018).
225. Urakami, T. *et al.* Evaluation of O-[^{18}F]fluoromethyl-d-tyrosine as a radiotracer for tumor imaging with positron emission tomography. *Nucl. Med. Biol.* **36**, 295–303 (2009).
226. Čolović, M. *et al.* Non-invasive Use of Positron Emission Tomography to Monitor Diethyl maleate and Radiation-Induced Changes in System x_C^- Activity in Breast Cancer. *Mol. Imaging Biol.* **21**, 1107–1116 (2019).
227. Čolović, M. *et al.* Synthesis and evaluation of an ^{18}F-labeled boramino acid analog of aminosuberic acid for PET imaging of the antiporter system x_C^-. *Bioorganic Med. Chem. Lett.* **28**, 3579–3584 (2018).
228. Heiss, P. *et al.* Investigation of transport mechanism and uptake kinetics of O-(2-[^{18}F]fluoroethyl)-L-tyrosine in vitro and in vivo. *J. Nucl. Med.* **40**, 1367–73 (1999).
229. Langen, K. J. *et al.* Preferred stereoselective transport of the D-isomer of cis-4-[^{18}F]fluoro-proline at the blood-brain barrier. *J. Cereb. Blood Flow Metab.* **25**, 607–616 (2005).

230. Tsukada, H., Sato, K., Fukumoto, D. & Kakiuchi, T. Evaluation of D-isomers of O-^{18}F-fluoromethyl, O-^{18}F-fluoroethyl and O-^{18}F-fluoropropyl tyrosine as tumour imaging agents in mice. *Eur. J. Nucl. Med. Mol. Imaging* **33**, 1017–1024 (2006).

231. Kersemans, V. *et al.* $^{123/125}$I-labelled 2-iodo-L-phenylalanine and 2-iodo-D-phenylalanine: Comparative uptake in various tumour types and biodistribution in mice. *Eur. J. Nucl. Med. Mol. Imaging* **33**, 919–927 (2006).

232. Bauwens, M. *et al.* Intra-individual comparison of the human biodistribution and dosimetry of the D and L isomers of 2-[I]iodo-phenylalanine. *Nucl. Med. Commun.* **28**, 823–828 (2007).

233. Martarello, L. *et al.* Synthesis of syn- and anti-1-amino-3-[18 F]fluoromethyl-cyclobutane-1-carboxylic acid (FMACBC), potential PET ligands for tumor detection. *J. Med. Chem.* **45**, 2250–2259 (2002).

234. Zhang, Z. *et al.* Radiosynthesis and preliminary biological evaluation of the 2-[^{18}F]fluoropropionic acid enantiomers for tumor PET imaging. *J. Radioanal. Nucl. Chem.* **316**, 153–159 (2018).

235. Kreissl, M. C. *et al.* Influence of dietary state and insulin on myocardial, skeletal muscle and brain [^{18}F]- fluorodeoxyglucose kinetics in mice. *EJNMMI Res.* **1**, 1–9 (2011).

236. Fueger, B. J. *et al.* Impact of animal handling on the results of 18F-FDG PET studies in mice. *J. Nucl. Med.* **47**, 999–1006 (2006).

237. Ogunrinu, T. A. & Sontheimer, H. Hypoxia increases the dependence of glioma cells on glutathione. *J. Biol. Chem.* **285**, 37716–37724 (2010).

238. Rouschop, K. M. *et al.* PERK/eIF2 signaling protects therapy resistant hypoxic cells through induction of glutathione synthesis and protection against ROS. *Proc. Natl. Acad. Sci.* **110**, 4622–4627 (2013).

239. Martin, L. & Gardner, L. B. Stress-induced inhibition of nonsense mediated RNA decay regulates intracellular cystine transport and intracellular glutathione through regulation of the cystine/glutamate exchanger SLC7A11. **34**, 4211–4218 (2015).

240. Lu, H. *et al.* Chemotherapy triggers HIF-1–dependent glutathione synthesis and copper chelation that induces the breast cancer stem cell phenotype. *Proc. Natl. Acad. Sci.* **112**, E4600–E4609 (2015).

241. Hyde, R., Taylor, P. M. & Hundal, H. S. Amino acid transporters: roles in amino acid sensing and signalling in animal cells. *Biochem. J.* **373**, 1–18 (2003).
242. Neale, S. A., Copeland, C. S. & Salt, T. E. Effect of VGLUT inhibitors on glutamatergic synaptic transmission in the rodent hippocampus and prefrontal cortex. *Neurochem. Int.* **73**, 159–165 (2014).
243. Lewerenz, J., Klein, M. & Methner, A. Cooperative action of glutamate transporters and cystine/glutamate antiporter system Xc-protects from oxidative glutamate toxicity. *J. Neurochem.* **98**, 916–925 (2006).
244. Haase, C., Bergmann, R., Fuechtner, F., Hoepping, A. & Pietzsch, J. L-Type Amino Acid Transporters LAT1 and LAT4 in Cancer: Uptake of 3-O-Methyl-6- 18F-Fluoro-L-Dopa in Human Adenocarcinoma and Squamous Cell Carcinoma In Vitro and In Vivo. *J. Nucl. Med.* **48**, 2063–2071 (2007).
245. Kim, C. S., Cho, S. H., Chun, H. S., Lee, S. y & Ndou, H. E. BCH, an inhibitor of system L amino acid transporters, induces apoptosis in cancer cells. *Biol. Pharm. Bull.* **31**, 1096–100 (2008).
246. Pietrancosta, N. *et al.* Rose Bengal analogs and vesicular glutamate transporters (VGLUTs). *Bioorganic Med. Chem.* **18**, 6922–6933 (2010).
247. Mu, F., Mangner, T. & Chugani, H. Facile synthesis of L-[1-C-11]leucine as a PET radiotracer for the measurement of cerebral protein synthesis. *J. Label. Compd. Radiopharm.* **48**, S189–S189 (2005).
248. Schuster, D. M. *et al.* Anti-1-Amino-3-18F-Fluorocyclobutane-1-Carboxylic Acid: Physiologic Uptake Patterns, Incidental Findings, and Variants That May Simulate Disease. *J. Nucl. Med.* **55**, 1986–1992 (2014).
249. Firnau, G., Chirakal, R. & Garnett, E. S. Aromatic radiofluorination with [18F]fluorine gas: 6-[18F]fluoro-L-dopa. *J. Nucl. Med.* **25**, 1228–1233 (1984).
250. Halperin, S. D., Fan, H., Chang, S., Martin, R. E. & Britton, R. A convenient photocatalytic fluorination of unactivated C-H bonds. *Angew. Chemie - Int. Ed.* **53**, 4690–4693 (2014).
251. Halperin, S. D. *et al.* Development of a Direct Photocatalytic C-H Fluorination for the Preparative Synthesis of Odanacatib. *Org. Lett.* **17**, 5200–5203 (2015).

252. Nodwell, M. B. *et al.* Direct photocatalytic fluorination of benzylic C–H bonds with N-fluorobenzenesulfonimide. *Chem. Commun.* **51**, 11783–11786 (2015).
253. Renneke, R. F., Pasquali, M. & Hill, C. L. Polyoxometalate Systems for the Catalytic Selective Production of Nonthermodynamic Alkenes from Alkanes. Nature of Excited-State Deactivation Processes and Control of Subsequent Thermal Processes in Polyoxometalate Photoredox Chemistry. *J. Am. Chem. Soc.* **112**, 6585–6594 (1990).
254. Rueda-Becerril, M. *et al.* Fluorine transfer to alkyl radicals. *J. Am. Chem. Soc.* **134**, 4026–4029 (2012).
255. Teare, H., Robins, E. G., Årstad, E., Luthra, S. K. & Gouverneur, V. Synthesis and reactivity of [18F]-N-fluorobenzenesulfonimide. *Chem. Commun.* 2330–2332 (2007). doi:10.1039/B701177F
256. Buckingham, F. *et al.* Organomediated Enantioselective ^{18}F Fluorination for PET Applications. *Angew. Chemie* **127**, 13564–13567 (2015).
257. Buckingham, F. & Gouverneur, V. Asymmetric ^{18}F-fluorination for applications in positron emission tomography. *Chem. Sci.* **7**, 1645–1652 (2016).
258. Teare, H. *et al.* Radiosynthesis and evaluation of [18F]Selectfluor bis(triflate). *Angew. Chemie - Int. Ed.* **49**, 6821–6824 (2010).
259. Padmakshan, D., Bennett, S. A., Otting, G. & Easton, C. J. Stereocontrolled synthesis of (S)-γ-fluoroleucine. *Synlett* 1083–1084 (2007). doi:10.1055/s-2007-977420
260. Nodwell, M. B. *et al.* 18F-Fluorination of Unactivated C-H Bonds in Branched Aliphatic Amino Acids: Direct Synthesis of Oncological Positron Emission Tomography Imaging Agents. *J. Am. Chem. Soc.* **139**, 3595–3598 (2017).
261. Nodwell, M. B. *et al.* 18F-branched-chain amino acids: Structure-activity relationships and PET imaging potential. *J. Nucl. Med.* **60**, 1003–1009 (2019).
262. Demling, J., Langer, K. & Yusufu, V. Individual day-to-day variations in plasma amino acid levels in healthy persons. *Amino Acids* **5**, 253–262 (1993).
263. Chin, B. B. *et al.* Synthesis and Preliminary Evaluation of 5-[18F]fluoroleucine. *Curr. Radiopharm.* **10**, 41–50 (2017).
264. Barretina, J. *et al.* The Cancer Cell Line Encyclopedia enables predictive modelling of anticancer drug sensitivity. *Nature* **483**, 603–607 (2012).

265. Limanto, J. *et al.* An efficient chemoenzymatic approach to (S)-γ-fluoroleucine ethyl ester. *J. Org. Chem.* **70**, 2372–2375 (2005).
266. Galli, C., Illuminati, G., Mandolini, L. & Tamborra, P. Ring-Closure Reactions. 7.1 Kinetics and Activation Parameters of Lactone Formation in the Range of 3- to 23-Membered Rings. *J. Am. Chem. Soc.* **99**, 2591–2597 (1977).
267. Nagamori, S. *et al.* Structure-activity relations of leucine derivatives reveal critical moieties for cellular uptake and activation of mTORC1-mediated signaling. *Amino Acids* **48**, 1045–1058 (2016).
268. Berg, J., Tymoczko, J. & Stryer, L. Section 3.2, Primary Structure: Amino Acids Are Linked by Peptide Bonds to Form Polypeptide Chains. in *Biochemistry 5th Edition* (ed. Freeman, W.) (2002).
269. Chenault, H. K., Dahmer, J. & Whitesides, G. M. Kinetic Resolution of Unnatural and Rarely Occurring Amino Acids: Enantioselective Hydrolysis of N-Acyl Amino Acids Catalyzed by Acylase I. *J. Am. Chem. Soc.* **111**, 6354–6364 (1989).
270. Freeman, T. L., Ngo, H. Q. & Mailliard, M. E. Inhibition of system A amino acid transport and hepatocyte proliferation following partial hepatectomy in the rat. *Hepatology* **30**, 437–444 (1999).
271. Li, Z. *et al.* Pregabalin is a potent and selective ligand for α 2 δ- 1 and α 2 δ-2 calcium channel subunits. *Eur. J. Pharmacol.* **667**, 80–90 (2011).
272. Roy, A. *et al.* Induction of mitochondrial apoptotic pathway in triple negative breast carcinoma cells by methylglyoxal via generation of reactive oxygen species. *Mol. Carcinog.* **56**, 2086–2103 (2017).
273. Okuno, S. *et al.* Role of cystine transport in intracellular glutathione level and cisplatin resistance in human ovarian cancer cell lines. *Br. J. Cancer* **88**, 951–956 (2003).
274. Narang, V. S., Pauletti, G. M., Gout, P. W., Buckley, D. J. & Buckley, A. R. Sulfasalazine-induced reduction of glutathione levels in breast cancer cells: Enhancement of growth-inhibitory activity of doxorubicin. *Chemotherapy* **53**, 210–217 (2007).
275. Huang, Y., Dai, Z., Barbacioru, C. & Sadée, W. Cystine-glutamate transporter SLC7A11 in cancer chemosensitivity and chemoresistance. *Cancer Res.* **65**, 7446–7454 (2005).
276. Lo, M., Ling, V., Wang, Y. Z. & Gout, P. W. The xc- cystine/glutamate antiporter: A

mediator of pancreatic cancer growth with a role in drug resistance. *Br. J. Cancer* **99**, 464–472 (2008).

277. Siolas, D. & Hannon, G. J. Patient-derived tumor xenografts: Transforming clinical samples into mouse models. *Cancer Res.* **73**, 5315–5319 (2013).

278. Lam, K., Chan, C., Done, S. J., Levine, M. N. & Reilly, R. M. Preclinical pharmacokinetics, biodistribution, radiation dosimetry and acute toxicity studies required for regulatory approval of a Clinical Trial Application for a Phase I/II clinical trial of111In-BzDTPA-pertuzumab. *Nucl. Med. Biol.* **42**, 78–84 (2015).

Appendices

Appendix A

qPCR Parameters

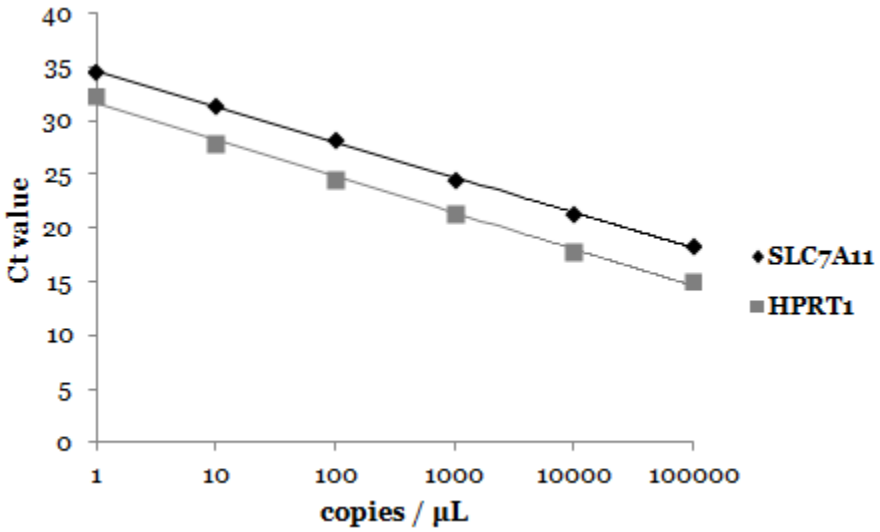

Figure A1. Representative standard curves for absolute quantification qPCR experiments.

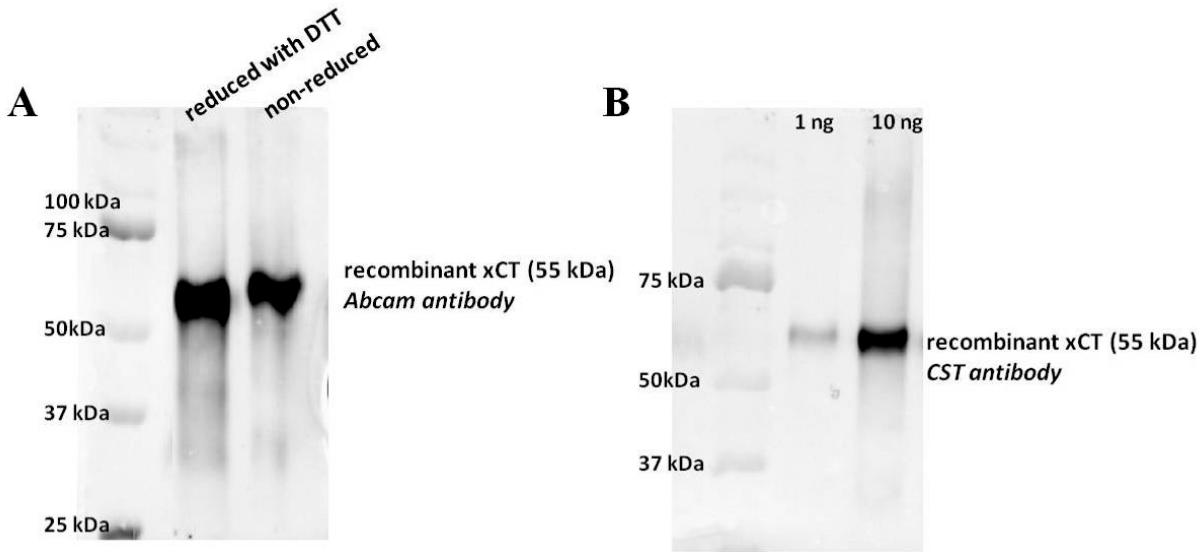

Figure A2. Western blot of recombinant human xCT protein anti-human xCT/*SLC7A11* rabbit monoclonal (CST) or rabbit polyclonal (Abcam) antibody.

Table A1. qPCR standard curve parameters from a sample reaction. Each sample was run in triplicates and each standard curve was generated at least three separate times.

Standard Curve Parameters

Target	Efficiency (%)	Curve Fit (R^2)
SCL7A11	97.62	0.998
HPRT1	95.99	0.995

Table A2. PCR cycling conditions.

PCR cycling conditions

Denaturation	98 °C	30 sec
40 cycles :		
Denaturation	98 °C	10 sec
Annealing		10 sec
	SLC7A11: 60 °C	
	HPRT1: 58°C	
Extension	72 °C	20 sec
Final Extension	72 °C	2 min
Hold	4 °C	

Table A3. qPCR cycling conditions.

qPCR cycling conditions

Hot Start	95 °C	15 sec
40 cycles :		
Denaturation	95 °C	10 sec
Annealing		60 sec
/Extension	*SLC7A11:* 60 °C	
	HPRT1: 58°C	

Appendix B

Table B1 Biodistribution of [^{18}F]FASu formulated in TFA and HCl.

	[^{18}F]FASu-TFA		**[^{18}F]FASu-HCl**	
organ	**(n ≥ 6)**	**100 mg/kg ASu[a] (n ≥ 7)**	**(n ≥ 4)**	**100 mg/kg ASu[a] (n ≥ 3)**
blood	0.74 ± 0.31	0.61 ± 0.37	0.84 ± 0.50	1.13 ± 0.61
fat	0.05 ± 0.02	0.06 ± 0.05	0.04 ± 0.02	0.05 ± 0.02
ovaries	3.93 ± 2.19	1.05 ± 0.47[b]	3.07 ± 1.48	0.90 ± 0.22
uterus	10.34 ± 8.11	0.90 ± 0.37	5.97 ± 3.08	0.80 ± 0.12
small intestine	2.48 ± 0.29	0.53 ± 0.22[b]	1.83 ± 0.64	0.68 ± 0.18
stomach	1.75 ± 0.43	0.30 ± 0.12[b]	1.66 ± 1.13	0.54 ± 0.25
pancreas	26.64 ± 4.59	3.93 ± 1.15[b]	26.42 ± 11.59	4.53 ± 0.29
spleen	6.43 ± 1.89	0.78 ± 0.39[b]	4.47 ± 1.65	1.18 ± 0.15
adrenal glands	0.81 ± 0.48	0.86 ± 0.85	0.46 ± 0.15	0.73 ± 0.13
kidneys	20.21 ± 2.99	19.24 ± 11.95	17.79 ± 7.20	24.08 ± 9.98
liver	0.96 ± 0.38	0.74 ± 0.10	0.95 ± 0.44	1.07 ± 0.19
heart	0.31 ± 0.10	0.23 ± 0.07	0.36 ± 0.21	0.48 ± 0.20
lungs	1.74 ± 0.14	3.10 ± 1.72	3.41 ± 2.20	2.77 ± 0.61
muscle	0.23 ± 0.10	0.14 ± 0.03	0.26 ± 0.11	0.23 ± 0.06
bone	1.45 ± 0.67	0.96 ± 0.67	0.76 ± 0.46	0.47 ± 0.06
brain	0.16 ± 0.07	0.09 ± 0.04	0.16 ± 0.09	0.13 ± 0.04
tail	2.08 ± 0.70	0.86 ± 0.39[b]	1.81 ± 0.90	0.78 ± 0.20
U-87 tumour	**4.96 ± 2.02**	**1.76 ± 0.59[b]**	**6.05 ± 2.40**	**2.87 ± 0.55**

Biodistributions and ratios are at 1 h p.i. Values (%ID/g) are presented as mean ± standard deviation.
[a]Blocked with co-injection of the cold standard, aminosuberic acid (ASu).
[b]Co-injection significantly reduced uptake of the same organ for the tracer ($p < 0.05$).

Appendix C

This appendix lists awards received, published manuscripts and both peer-reviewed and non-peer reviewed presentations in forms of oral talks or posters, of the research that I have conducted for my graduate degree.

C.1 AWARDS AND SCHOLARSHIPS

2019	Interdisciplinary Oncology Program Outstanding Student Award
2019	UBC Interdisciplinary Oncology Program Travel Award
2017	UBC Faculty of Medicine Graduate Award
2017	UBC Interdisciplinary Oncology Program Travel Award
2016	UBC Interdisciplinary Oncology Program Travel Award
2016	UBC Graduate Student Travel Award
2016	UBC Faculty of Medicine Graduate Award
2015-2017	IsoSiM CREATE NSERC Scholarship
2015	UBC International Tuition Award
2015	UBC Faculty of Medicine Graduate Award

C.2 PUBLICATIONS

Published journal articles

1) **Čolović M**, Yang H, Merkens H, Colpo N, Bénard F, Schaffer P, "The effect of chirality on the application of [^{18}F]5-fluoro-aminosuberic acid ([^{18}F]FASu) for oxidative stress imaging", *Molecular Imaging and Biology*, 2019 Dec 2. doi: 10.1007/s11307-019-01450-2. [Epub ahead of print].
2) Lim JKM, Delaidelli A, Minaker SW, Zhang HF, **Čolović M**, Yang H, Negri GL, von Karstedt S, Lockwood WW, Schaffer P, Leprivier, Sorensen PH. "Cystine/glutamate antiporter xCT (SLC7A11) facilitates oncogenic RAS transformation by preserving intracellular redox balance", *Proceedings of the National Academy of Sciences of the United States of America*, May 2019, 116 (19) 9433-9442.

3) **Čolović M**, Yang H, Merkens H, Colpo N, Schaffer P, Bénard F, Lin KS, "Non-invasive use of positron emission tomography to monitor chemo- and radiation- induced changes in system x_C^- expression in breast cancer", *Molecular Imaging and Biology*, (2019) 21: 1107.
4) Yuan Z, Yang H, Malik N, **Čolović M**, Weber DS, Wilson D, Bénard F, Martin RE, Warren JJ, Schaffer P, Britton R, "Electrostatic Effects Accelerate Decatungstate-Catalyzed C–H Fluorination Using [^{18}F]- and [^{19}F]NFSI in Small Molecules and Peptide Mimics", *ACS Catalysis*. (2019) 9: 8276-8284.
5) Nodwell MB, Yang H, Merkens H, Malik N, **Čolović M**, Wagner B, Martin RE, Bénard F, Schaffer P, Britton R. "^{18}F-branched chain amino acids: structure-activity relationships and PET imaging potential", *Journal of Nuclear Medicine,* January 25, 2019 jnumed.118.220483
6) **Čolović M**, Rousseau E, Zhang Z, Lau J, Zhang CC, Kuo HT, Yang H, Schaffer P, Bénard F, Lin KS, "Synthesis and evaluation of ^{18}F-labeled boramino acid analog of aminosuberic acid for PET imaging of the antiporter system x_C^-", *Bioorganic and Medicinal Chemistry Letters* (2018) 3579-3584.
7) Rousseau J, Zhang Z, Wang X, Zhang CC, Lau J, Rousseau E, **Čolović M**, Hundal-Jabal N, Bénard F, Lin KS. "Synthesis and evaluation of bifunctional tetrahydroxamate chelators for labeling antibodies with ^{89}Zr for imaging with positron emission tomography", *Bioorganic and Medicinal Chemistry Letters*, 2018, 28, 899-905.
8) Yang H, Tam B, **Čolović M**, Southcott L, Merkens H, Bénard F, Schaffer P. "Addressing chirality in the structure and synthesis of [^{18}F]5-fluoroaminosuberic acid ([^{18}F]FASu)", *Chemistry - A European Journal*, 2017, 23, 11100 – 11107.
9) Nodwell MB, Yang H, **Čolović M**, Yuan ZL, Merkens H, Martin RE, Bénard F, Schaffer P, Britton R. "F-18-fluorination of Unactivated C-H Bonds in Branched Aliphatic Amino Acids: Direct Synthesis of Oncological Positron Emission Tomography Imaging Agents", *Journal of the American Chemical Society*, 2017, 139(10): 3595-3598.
10) Yang H, Jenni S, **Čolović M**, Merkens H, Poleschuk C, Rodrigo I, Miao Q, Johnson BF, Rishel MJ, Sossi V, Webster JM, Bénard F, Schaffer P. "[^{18}F]5-fluoro-aminosuberic acid (FASu) as a potential tracer to gauge oxidative stress in breast cancer models", *Journal of Nuclear Medicine,* 2016, 58(3): 367-373.

Accepted abstracts

1) **Čolović M**, Yang H, Merkens H, Colpo N, Bénard F, Schaffer P, "In vivo evaluation of [^{18}F]5-fluoroaminosuberic acid ([^{18}F]FASu) isomers as PET imaging agents for different cancer types", accepted to *The Annual Congress of the European Association of Nuclear Medicine*, Barcelona, Spain, 2019.
2) **Čolović M**, Yang H, Merkens H, Colpo N, Schaffer P, Bénard F, Lin KS, "[^{18}F]FASu as a gauge to monitor ocidative stress fluctuations in breast cancer", accepted to *The Annual Meeting of the World Molecular Imaging Congress*, Montreal, Quebec, Canada, 2019.
3) Nodwell MB, Yang H, **Čolović M**, Yuan ZL, Merkens H, Fu W, Martin RE, Bénard F, Schaffer P, Britton R. "Photo-catalyzed ^{18}F-fluorination of leaucine and leaucine analogues for system L imaging", accepted to *The Annual Meeting of the Society of Nuclear Medicine and Molecular Imaging*, Philadelphia, Pennsylvania, USA, 2018.
4) **Čolović M**, Rousseau E, Zhang ZX, Lau J, Zhang CC, Kuo HT, Yang H, Schaffer P, Bénard F, Lin KS, "Synthesis and evaluation of ^{18}F-labeled trifluoroborate derivative of aminosuberic acid for PET imaging of the antiporter system x_C^-", accepted to *The Annual Meeting of the Society of Nuclear Medicine and Molecular Imaging*, Philadelphia, Pennsylvania, USA, 2018.
5) Rousseau J, Zhang ZX, Wang XZ, Zhang CC, Lau J, Rousseau E, **Čolović M**, Hundal-Jabal N, Bénard F, Lin KS. "Synthesis and evaluation of bifunctional tetrahydroxamate chelators for labelling antiobides with ^{89}Zr for imaging with positron emission tomography", accepted to *The Annual Meeting of the Society of Nuclear Medicine and Molecular Imaging*, Philadelphia, Pennsylvania, USA, 2018.
6) **Čolović M**, Yang H, Merkens H, Bénard F, Schaffer P. "Oxidative stress level monitoring using a novel positron emission tomography imaging agent [^{18}F]-5-fluoroaminosuberic acid", accepted to *Western Regional Meeting of the Society of Nuclear Medicine and Molecular Imaging*, Vancouver, Canada, 2017.
7) **Čolović M**, Yang H, Merkens H, Southcott L, Colpo N, Rousseau J, Bénard F, Schaffer P. "[^{18}F]-5-fluoroaminosuberic acid ([^{18}F]FASu) superior to [^{18}F]FDG in small animal PET/CT imaging of human xenografts", accepted to *The Annual Congress of the European Association of Nuclear Medicine*, Vienna, Austria, 2017.

8) Yang H, Tam B, **Čolović M**, Merkens H, Bénard F, Schaffer P. "Addressing the chirality of an amino acid tracer ^{18}F-fluoro-aminosuberic acid", accepted to *The Annual Meeting of the Society of Nuclear Medicine and Molecular Imaging*, Denver, Colorado, USA, 2017.
9) **Čolović M**, Yang H, Merkens H, Zhang CC, Lin KS, Bénard F, Schaffer P. "xCT as molecular target for oxidative stress imaging in PET", accepted to *The Annual Congress of the European Association of Nuclear Medicine*, Barcelona, Spain, 2016.
10) Yang H, Merkens H, **Čolović M**, Jenni S, Lazarakos M, Rodrigo I, Miao Q, JM Webster JM, Bénard F, Schaffer P. "The effect of chirality on the application of [^{18}F]-5-fluoroaminosuberic acid ([^{18}F]FASu) for oxidative stress imaging", accepted to *The Annual Meeting of the Society of Nuclear Medicine and Molecular Imaging*, San Diego, California, USA, 2016.
11) Yang H, Merkens H, **Čolović M**, Jenni S, Lazarakos M, Rodrigo I, Miao Q, Bénard F, Webster JM, Schaffer P. "*D*- and *L*-[^{18}F]5-fluoroaminosuberic acid ([^{18}F]5-FASu) for oxidative stress imaging", accepted to *The International Chemical Congress of Pacific Basin Societies*, Honolulu, Hawaii, 2015.
12) Yang H, Miao Q, Jenni S, **Čolović M**, Johnson BF, Rishel MJ, Yapp D, Webster JM, Bénard F, Schaffer P. "[^{18}F]5-fluoroaminosuberic acid (FASu) for oxidative stress imaging in breast cancer", accepted to *The Annual Meeting of the Society of Nuclear Medicine and Molecular Imaging*, Baltimore, USA, 2015.

Oral presentations

1) "*In vivo* evaluation of [^{18}F]5-fluoroaminosuberic acid ([^{18}F]FASu) isomers as PET imaging agents for different cancer types", European Association of Nuclear Medicine Annual Meeting, Barcelona, Spain, October 14th 2019.
2) "^{18}F-labelled cystine analog [^{18}F]5-fluoroaminosuberic acid ([^{18}F]FASu), for oxidative stress imaging with positron emission tomography", Thursday Oncology Training Seminars, BC Cancer Research Centre, Vancouver, Canada, 17 January 2019
3) "Non-invasive use of positron emission tomography to monitor chemo- and radiation-induced changes in system x_C^- expression in breast cancer", Thursday Oncology Training Seminars, BC Cancer Research Centre, Vancouver, Canada, 30 November 2017.
4) "Oxidative stress level monitoring in breast cancer using a novel positron emission tomography imaging agent [^{18}F]5-fluoroaminosuberic acid", Thursday Oncology Training Seminars, BC Cancer Research Centre, Vancouver, Canada, 1 June 2017.
5) "xCT as molecular target for oxidative stress PET imaging in breast cancer models", B.I.G. Research Day, UBC, Vancouver, Canada, 7 March 2017.
6) "Radiolabelled amino acids as probes for PET imaging of cancer", IsoSiM / HGS-HIRe Summer School, Schmitten, Germany, 25-30 July, 2016.
7) "Oxidative stress imaging in breast cancer", Graduate and Postdoctoral Society, TRIUMF, Vancouver, Canada, 17 March 2016.